TECHNISCHE UNIVERSITÄT MÜNCHEN
LEHRSTUHL FÜR AERODYNAMIK UND STRÖMUNGSMECHANIK

Aerodynamic Analyses of Novel Helicopter Engine Air Intakes

Florian Knoth

Vollständiger Abdruck der von der Fakultät für Maschinenwesen der Technischen Universität München zur Erlangung des akademischen Grades eines Doktor-Ingenieurs genehmigten Dissertation.

Vorsitzender:	Prof. Dr.-Ing. Manfred Hajek
Prüfer der Dissertation:	1. apl. Prof. Dr.-Ing. Christian W. M. Breitsamter
	2. Prof. Dr.-Ing. Volker Gümmer

Die Dissertation wurde am 30.04.2019 bei der Technischen Universität München eingereicht und durch die Fakultät für Maschinenwesen am 03.02.2020 angenommen.

Vorwort

Die folgende Doktorarbeit entstand im Laufe meiner Tätigkeit am Lehrstuhl für Aerodynamik und Strömungsmechanik der Technischen Universität München, wo ich in den Jahren 2013 bis Ende 2017 beschäftigt war. Während dieser Zeit hatte ich das Vergnügen an einem sehr interessanten Thema im Bereich der Intake-Aerodynamik arbeiten zu können. Ich möchte mich an dieser Stelle ganz herzlich bedanken bei Herrn apl. Prof. Dr.-Ing. Christian Breitsamter, für seine aus fachlicher als auch organisatorischer Sicht jederzeit hervorragende Betreuung, Unterstützung, für die schöne Zeit und all die interessanten Erfahrungen, die ich machen durfte.

Ebenfalls bedanke ich mich bei Herrn Prof. Dr.-Ing. Volker Gümmer, der die Aufgabe des Zweitprüfers übernommen hat. Für die Übernahme des Prüfungsvorsitzes möchte ich Herrn Prof. Dr.-Ing. Manfred Hajek herzlich danken.

Für die erfolgreiche, jederzeit spannende Kooperation und Unterstützung im Cleansky Forschungsprojekt ATHENAI (Aerodynamic Testing of Helicopter Novel Air Intakes) in den Jahren 2013 bis 2015 möchte ich einen aufrichtigen Dank aussprechen an Dr. Alessandro D'Alascio und Thomas Kneisch von Airbus Helicopters.

Die Arbeit am Lehrstuhl zeichnete sich durch eine freundschaftliche Atmosphäre aus und dafür möchte ich mich herzlichst bei allen ehemaligen Kollegen bedanken.
Ganz herzlich danken möchte ich Andreas Hövelmann, Marco Stuhlpfarrer, Roman Ress, Benoît Béguin, Marc Förster, Moritz Grawunder, Patrick Pölzbauer, Stefan Pfnür, Vladyslav Rozov, Florian Heckmeier, Andrei Buzica und Marcus Giglmaier, für die gemeinsame Zeit am Lehrstuhl sowie Lisa Debschütz, Tobias Chemnitz und Maximilian Pulfer für ihre hervorragende Unterstützung in ihren Studienarbeiten.
Auch den Kollegen Wolfgang Lützenburg, Hans-Gerhard Frimberger und Martin Banzer gebührt mein Dank für ihre Unterstützung, da es ohne sie keine Windkanalmodelle für die Intake Versuche gegeben hätte.
Ein weiterer besonderer Dank geht an Benjamin Anstett, Robert Lukesch, David Schwalb, Maximilian Winter und Jakob Sparrer, da sie mir immer gute Freunde waren und sind.
Ich bedanke mich von Herzen bei meiner Freundin Greta für all Ihre Unterstützung.
Zuletzt geht mein größter Dank an meine Eltern Sigrid und Alois sowie an meine Schwester Rosa, die mich bis zu meiner Promotion stets und unermüdlich unterstützt haben.

München, im Sommer 2020 Florian Knoth

Abstract

The main aim of the current thesis is the aerodynamic investigation of plenum chamber type side intake configurations for application in light weight utility helicopters is analyzed. As a main portion in typical helicopter missions, a focus is on fast forward flight condition. For that purpose, a full-scale engine air intake wind tunnel setup was designed to achieve realistic flight Mach and Reynolds numbers. With this setup, engine air intakes are analyzed, incorporated in a truncated fuselage section model. For the simulation of inflight engine mass flow rates, a fan and a Venturi meter are connected to the intake duct. A rake of four five-hole probes is integrated and can be adjusted automatically in circumferential direction. With the five-hole probe measurement system, engine inflow conditions in the aerodynamic interface plane are quantified, namely the total pressure recovery, total pressure distortion and swirl. To characterize the intake and upstream flow field, static surface pressure as well as particle image velocimetry measurements are applied.

Comprehensive experimental studies are performed using the wind tunnel setup and complemented by numerical investigations. The validity of the truncation assumption is substantiated by a numerical comparison of the complete fuselage in free flight condition and the truncated fuselage section, flush mounted to the wind tunnel floor.

The comprehensive experimental data set includes different plenum chamber types combined with several side intake configurations. The tested geometries are sub-divided into "basic" intakes and intakes including "retrofit" modifications. Of the "basic" intakes, the first intake (baseline) is a "static" side intake geometry, the second intake is denoted as "semi-dynamic" intake due to the cowling approach ramp and the third intake is specified as "dynamic" intake, due to its scoop. A detailed investigation of the first intake identifies the main flow phenomena, that originate a distorted aerodynamic interface plane total pressure distribution. Subsequently, the main aerodynamic characteristics of the "basic" intakes are compared. Based on the second "basic" intake (reference), retrofit modifications are analyzed such as a rear spoiler and an inlet guide vane to assess the aerodynamic optimization potential for existing intake geometries. Two sets of best retrofit modifications are identified, that improve the engine inflow conditions in fast forward conditions while only modestly deteriorating the engine inflow conditions in low freestream velocity flight.

To complement the experimental results and to find better solutions in terms of overall helicopter performance in fast forward flight conditions, further parameter studies and numerical optimization are performed for three different cases.

The first two cases reflect simplified geometries to identify improvement potential of the total pressure recovery due to variations in the ramp incidence and planform as well as due to the scoop height and forward protrusion. In the third case, a parameter study is conducted for an intake which is derived from the reference intake and integrated into the full helicopter fuselage. Hereby, the engine power output changes due to pressure recovery and total pressure distortion are taken into account, as well as changes in power demands due to intake related drag. A best parameter configuration is found that optimizes the excessive shaft output power compared to the reference configuration.

Zusammenfassung

Die vorliegende Arbeit beschäftigt sich mit aerodynamischen Untersuchungen von lateralen Triebwerkslufteinlässen für eine leichte Hubschrauberkonfiguration. Alle behandelten Lufteinlässe beinhalten eine Plenumskammer stromauf des Triebwerks. Da der schnelle Geradeausflug einen Großteil typischer Missionsprofile ausmacht, wird darauf ein Hauptaugenmerk gelegt. Um realistische Mach- und Reynoldszahlen im Windkanalversuch darzustellen, wurde ein Windkanalmodel im Originalmaßstab entworfen und gebaut. Das modulare Model stellt eine Sektion eines Hubschrauberrumpfes dar, zum Testen unterschiedlicher Lufteinlässe. Ein Radialgebläse und ein Venturirohr sind über ein Rohrsystem an den Lufteinlass angeschlossen und ermöglichen die Simulation von realistischen Luftmassenströmen des Triebwerkes im Versuch. Für die Ermittlung der Triebwerkseintrittsbedingungen im Windkanalversuch wird ein Messrechen verwendet, der vier 5-Lochsonden enthält und automatisch in Umfangsrichtung verstellbar ist. Zur quantitativen Bewertung werden in der Triebwerseintrittsebene ein Totaldruckverhältnis, die Ungleichverteilung des Totaldrucks und ein gemittelter Drallwinkel analysiert. Weiterhin geben statische Druckverteilungen entlang der Einlaufkontur und laserbasierte Geschwindigkeitsfeldmessungen Aufschluss über das Strömungsfeld. Zusätzlich zu den umfangreichen experimentellen Untersuchungen werden noch komplementäre numerische Strömungssimulationen durchgeführt. Es wird eine numerische Untersuchung von einem Triebwerkseinlauf durchgeführt, einmal integriert in einen frei fliegenen kompletten Hubschrauberrumpf, und zusätzlich in eine Rumpfsektion. Hierbei wird gezeigt, dass für beide Fälle sehr ähnliche Triebwerkseintrittsbedingunen entstehen.

Als Teil der experimentellen Untersuchungen werden unterschiedliche Varianten von Plenumskammern und Einlaufgeometrien kombiniert. Hierbei lassen sich die Geometrien untergliedern in Basisvarianten und zusätzliche aerodynamische Modifikationen. Die erste Basisvariante stellt einen "statischen" lateralen Lufteinlass dar, die zweite Variante kann wegen der Rampenkontur stromauf des Lufteinlasses als "semi-dynamischer" Lufteinlass bezeichnet werden und die dritte Basisvariante wird als "dynamischer" Lufteinlass bezeichnet, da er zusätzlich zur Rampenkontur noch eine Hutze aufweist. Für die erste Basisvariante werden anhand einer Strömungssimulation die wichtigsten Strömungsphänomene erklärt, welche eine inhomogene Totaldruckverteilung am Triebwerkseintritt verursachen. Anschließend werden die aerodynamischen Charakteristika der Basisvarianten verglichen. Motiviert durch die gewonnenen Erkenntnisse werden auf Basis der zweiten Referenzgeometrie zusätzliche aerodynamische Modifikationen untersucht, nämlich Spoiler und ein Luftleitblech. Zwei Konfigurationen werden identifiziert, die die Triebwerksbedingungen im schnellen Geradeausflug deutlich verbessern und nur mäßige Einbußen im Langsamflug bewirken. Zusätzlich zu den experimentellen Untersuchungen werden numerische Parameterstudien und eine Optimierung durchgeführt, die für den schnellen Geradeausflug weitere potenzielle Leistungsverbesserungen für Triebwerkseinlässe von Hubschraubern aufzeigen sollen. Anhand der ersten beiden Fälle werden Parameter variiert, die die Einlauframpe und die Hutze beschreiben, um das Verbesserungspotential im Totaldruckverhältnis zu untersuchen. Im dritten Fall wird eine Parameterstudie durchgeführt für eine von der Referenzgeometrie abgeleiteten Einlassgeometrie, integriert im kompletten frei fliegenden Hubschrauberrumpf. Innerhalb dieser Studie wird die Triebwerksüberschussleistung bewertet. Diese wird einerseits durch das Totaldruckverhältnis und eine inhomhogene Totaldruckverteilung im Triebwerkseintritt beinflusst, andererseits wird der Leistungsbedarf auch beeinflusst durch den Widerstand, der sich durch die Einlaufströmung ergibt. Final wird eine Konfiguration identifiziert, die ein Optimum der resultierenden Triebwerksüberschussleistung darstellt.

Contents

List of Figures **ix**

List of Tables **xi**

Nomenclature **xiii**

1 Introduction **1**
- 1.1 Motivation . . . 1
- 1.2 State of the Art . . . 3
  - 1.2.1 Submerged Intakes . . . 3
  - 1.2.2 S-Duct Intakes . . . 4
  - 1.2.3 Helicopter Intakes . . . 4
  - 1.2.4 Intake Optimization . . . 6
- 1.3 Research Objectives . . . 8
- 1.4 Thesis Outline . . . 9

2 Air Intake Research **11**
- 2.1 Intake Total Pressure Distortion and Swirl . . . 13
  - 2.1.1 Stable Engine Operation . . . 13
  - 2.1.2 Parallel Compressor Theory . . . 14
  - 2.1.3 Intake Shape and Operating Condition . . . 16
  - 2.1.4 Engine Performance . . . 18
  - 2.1.5 Intake Swirl . . . 19
- 2.2 Further Performance Parameters . . . 20
  - 2.2.1 Intake Pressure Recovery . . . 20
  - 2.2.2 Intake Drag . . . 23

3 Wind-Tunnel Testing **25**
- 3.1 Model Design . . . 26
  - 3.1.1 Outer Components and Chassis . . . 26
  - 3.1.2 Inner Components . . . 27
  - 3.1.3 Circumferential Five-Hole Probe Adjustment System . . . 29
  - 3.1.4 Duct System, Venturi Meter and Fan . . . 31
- 3.2 Geometric Variants . . . 32
- 3.3 Measurement Techniques and Instrumentation . . . 34

3.3.1 Massflow Measurement . . . 34
3.3.2 Aerodynamic Interface Plane Measurement . . . 35
3.3.2.1 Five-Hole Probe Measurement . . . 36
3.3.2.2 Aerodynamic Interface Plane Coefficients . . . 38
3.3.3 Surface Pressure Measurement . . . 39
3.3.4 Stereo Particle Image Velocimetry . . . 41

4 Numerical Simulations 43
4.1 Numerical Setup . . . 43
4.2 Computational Mesh . . . 45
4.3 Mesh Sensitivity Study . . . 48

5 Analysis of the Baseline Case 49
5.1 Sectional Fuselage Characteristics . . . 49
5.1.1 Surface Pressure Distributions . . . 49
5.1.2 Flow Field Investigations . . . 52
5.2 Comparison of Sectional and Full Fuselage Case . . . 55
5.3 Synthesis . . . 59

6 Analysis of Side Intake Configurations 61
6.1 Basic Intakes . . . 61
6.2 Grid and Plenum Splitter . . . 66
6.3 Cowling Ramp and Plenum Chamber . . . 71
6.4 Retrofit Geometric Variants . . . 75
6.5 Comparison of Basic and Best Retrofit Variants . . . 80
6.5.1 AIP Detail Investigation . . . 81
6.5.2 Surface Pressures . . . 83
6.6 Angle of Attack . . . 87
6.7 Synthesis . . . 89

7 Numerical Optimization and Parameter Studies 92
7.1 Methods . . . 92
7.1.1 Workbench Environment . . . 93
7.1.2 Automated Aerodynamic Shape Development Environment . . . 94
7.2 Optimization and Parameter Study Cases . . . 95
7.2.1 Optimization of a quasi two-dimensional Side Intake Geometry . . . 95
7.2.2 Submerged Intake Parameter Case . . . 98
7.2.3 Parameter Study of a Side Intake Geometry . . . 102
7.3 Synthesis . . . 117

8 Conclusions 120

Bibliography 126

List of Figures

1.1 a) Airbus Helicopters Super Puma, b) Bell 430, and c) Airbus Helicopters Bluecopter Demonstrator, Refs. [4], [5]. 2

1.2 North American YF-93A intake flight tests a) equipped with submerged intake and b) equipped with scoop intake, Ref. [62]. 4

1.3 EIKON intake investigations a) transsonic wind tunnel tests and b) instantaneous flow field in the symmetry plane and in the AIP (ONERA ZDES computation), Ref. [24]. . . 5

1.4 a) Schematic of scavenger, [12] , b) Eurocopter EC135 inlet barrier filter, [83], c) icing test of KAI surion helicopter intake, Ref. [23]. 5

1.5 a) Aérospatiale AS 360 Dauphin with static intake, and b) Eurocopter AS 365 Dauphin with dynamic intake, Ref. [84]. 6

1.6 a) ERICA nacelle, Ref. [21] and b) nacelle model installation in the POLIMI wind tunnel, Ref. [19]. 7

1.7 a) AIP η distribution for baseline and optimized as well as b) longitudinal cut shape optimization, [28]; $\eta = p_{t,AIP}/p_{t,\infty}$. 7

1.8 a) Agusta Westland AW101 external geometry and b) AIP η-distribution of baseline and optimized cases, fast forward flight, Intake#1, Ref. [27]. 8

2.1 Scheme of engine types and intake design depending on flight Mach number. 11

2.2 Eurofighter Typhoon intake (top) and Lockheed SR71 Blackbird (bottom). 12

2.3 Airbus Helicopters Bluecopter Demonstrator with semi-dynamic intake at the ILA in Berlin. 12

2.4 Schematic compressor map, based on Ref. [18]. 14

2.5 Parallel compressor theory, based on Ref. [55]. 15

2.6 a) S-duct outlet η distribution, b) schematic of typical s-duct separation region, Ref. [81]. 16

2.7 a) Distortion level as function of throat Mach number, based on Ref. [7], b) distortion level as function of throat Mach number and relative duct length, based on Ref. [75]. . . 17

2.8 a) air intake distortion, wind tunnel tests Ref. [80], b) schematic of intake flow field (1) dynamic inlet at $U_\infty = 0$, (2) static inlet at $U_\infty = 0$, (3) dynamic inlet at $U_\infty > 0$, (4) static inlet at $U_\infty > 0$, Ref. [80]. 17

2.9 Helicopter intake computational simulations, $\mu = 0.198$ a) side intake, b) top intake, c) side intake streamlines and d) top intake streamlines, Ref. [33]. 18

2.10 Engine power loss due to total pressure distortion, based on Ref. [78]. 18

2.11 Pratt & Whitney PW200 series engines, a) insight into internal components of engine and b) side view of engine. 19

2.12 Swirl types, Bulk swirl (top), 1/rev paired swirl (middle) and 2/rev paired swirl (bottom), based on Ref. [16]. 20
2.13 NACA inlet planforms, Ref. [63], a) parallel walls, b) divergent walls, c) convergent walls, d) example of 7 deg ramp angle, standard curved divergence. 21
2.14 NACA inlets, Ref. [44], a) ramp angles, b) planforms, c) η progression for 5, 7 and 9 1/2 deg ramp angles and d) η progression for divergent and parallel planforms. 22
2.15 a) Typical pressure recoveries of helicopter intakes, based on Ref. [65], b) air intake efficiency, wind tunnel tests, Ref. [61]. 22

3.1 Overview of the W/T setup. 25
3.2 a) Truncation of the fuselage in front view, b) outer W/T model components, based on Ref. [36]. 25
3.3 a) Wind tunnel model in test section, b) angle of attack adjustment. 26
3.4 a) Chassis in side view, b) outer W/T model components and c) CAD display of chassis in W/T model, perspective longitudinal cut view. 27
3.5 Intake and retrofit modifications. 27
3.6 Inner model components. 28
3.7 Inner model components CAD, cut A-A. 28
3.8 a) EID front plate in top view and b) bottom view, c) EID outer (1) and inner (2) guide vanes and d) Plenum Chamber 1 in side view. 29
3.9 Schematic of traversing system. 30
3.10 a) CAD presentation of measurement rake including five hole probes b) measurement rake including five hole probes. 30
3.11 a) Radial fan, duct system and Venturi meter, b) flexible tube element. 31
3.12 Radial fan. 31
3.13 Overview of geometric variants. 32
3.14 Schematic cut view of intake 2 in upstream perspective, inner components: EPC, EID, AIP and plenum splitter. 33
3.15 Examples of retrofit modifications:
1) high and short rear spoiler,
2) low and long rear spoiler,
3) high and long rear spoiler, front intake guide vane. 33
3.16 a) Specified mass flow rate $\dot{m}_{corr}/\dot{m}_{corr,max}$ as a function of the specified relative freestream velocity $U_\infty/U_{\infty,max}$, Ref. [39], b) Venturi meter installation. 34
3.17 a) Upstream view in Y_{AIP} - Z_{AIP} plane, Ref. [38], b) cut view A-A in Y_{AIP} - Z_{AIP} plane of inner components: EPC, EID, outer guide vanes in EID, inner guide vanes and AIP, schematic overview of 5-hole-probe measurement locations in the AIP, circumferentially adjustable rake comprising four 5-hole probes. 35
3.18 a) Example of five-hole probe pressure port designation, b) five-hole probe coordinates and angle definitions based on Refs. [2, 74]. 36
3.19 a) top view of pressure tap positions on the outer geometry of BSL 1, b) cut view B-B in Y_{AIP} - Z_{AIP} plane, pressure tap positions on the inner geometry of BSL 1. 39
3.20 a) Local curve length coordinate S_2 for line 2 of I1 and I2, b) Local curve length coordinate S3 for line 3 of I1 and I2. 40

3.21 Side view of PIV setup, schematic display of laser sheet optic, downstream camera, light scheet and wind tunnel model. 41

4.1 Numerical setup and boundary conditions in perspective view a) of the sectional fuselage case, b) of the full fuselage case. 44

4.2 a) surface mesh of the W/T test section containing the interchangeable model mesh, b) blocking of the sectional fuselage mesh, including the intake mesh's outer surfaces. . . . 45

4.3 Surface mesh including the intake surface mesh of a) sectional fuselage case, b) full fuselage case. 46

4.4 a) blocking of intake I1, b) surface mesh of Intake I1. 46

4.5 a) blocking of EPC mesh, position of EID mesh and additional circular mesh, b) cut view of BSL1 - EPC, EID mesh and additional circular mesh. 47

4.6 a) detail of EID mesh section, b) complete EID mesh, AIP extension (schematically). . . 47

5.1 a) c_p distribution on line 2, b) c_p distribution on line 3. 50

5.2 a) c_p distribution on line 9, b) Sectional view through line 9 in EPC mid plane, characteristic flow regimes labelled from 1 to 5. 50

5.3 a) c_p distribution on line 12, b) c_p distribution on line 13. 51

5.4 a) X_{AIP}-Z_{AIP} cut view through EID, S_{EID} coordinates of conical planes (lines), b) perspective view of conical planes in the EID. 52

5.5 Distributions of a) normalized total pressure ratio vs. θ , b) relative freestream velocity ratio vs. θ for conical planes with constant S_{EID}. 53

5.6 a) surface streamlines on front intake lip, 4 different contours of constant $\omega_C \cdot l_I/U_\infty$ on radial-axial-planes ($\theta = 345°, 0°, 15°, 30°, 45°$), b) cut view through EID and intake region at $\theta = 30°$ showing the distribution of the normalized total pressure ratio together with projected streamlines. 53

5.7 a) sectional view of EPC mid plane, iso surface of a relative velocity ratio of 0.15 (schematic), surface streamlines, distribution of normalized total pressure ratio, cross section 1 at $\theta = 300°$, cross section 2 at $300° < \theta < 360°$, $0° < \theta < 60°$, cross section 3 at $\theta = 60°$, cylinder surface at $S_{EID} = 0$ (circle), cylinder surface at $S_{EID} = 0.5$ (dashed circle), b) distribution of normalized AIP total pressure ratio. 54

5.8 EID outer guide vane separation (left), EID inner guide vane separation (right). 54

5.9 Surface streamlines (CFD) and positions for BL investigations in top view for the SF case (left), FF case (right), the blue line represents the truncation line of the section, the yellow dash-dotted line represents the PIV measurement plane. 55

5.10 Boundary layer profiles for the sectional fuselage case (SF), full fuselage case (FF) and W/T PIV measurement in two lateral positions, a) relative freestream velocity, b) crossflow angle β_{BL}. 56

5.11 Back view of front intake lip, surface streamlines, a) sectional fuselage case, b) full fuselage case. 56

5.12 Cut view through EID and intake region at $\theta = 30°$ showing the distribution of the normalized total pressure ratio together with projected streamlines, a) sectional fuselage, b) full fuselage. 57

5.13 Distribution of the normalized total pressure ratio in the AIP (96 points) for a) CFD simulation of sectional fuselage case, medium mesh, b) CFD simulation of full fuselage case, medium mesh, c) wind tunnel experiment, maximum relative freestream velocity, maximum mass flow rate ratio. 58

6.1 Representation of basic intakes a) I1, b) I2, c) I3, and schematic cut view of d) I1, e) I2 and f) I3. 62
6.2 Aerodynamic characteristics vs. relative freestream velocity of the geometries I1 P1, I2 P3 and I3 P3 for the maximum mass flow rate ratio, a) normalized total pressure ratio and b) normalized distortion coefficient. 62
6.3 Distribution of normalized total pressure ratio in AIP for a) I1 P1, b) I2 P3, b) I3 P3, at maximum relative freestream velocity, maximum mass flow rate ratio. 63
6.4 Normalized swirl coefficient vs. relative freestream velocity of the geometries I1 P1, I2 P3 and I3 P3 for the maximum mass flow rate ratio. 64
6.5 Relative change of available engine power due to the total pressure ratio compared to the $I2P3$ configuration, vs. relative freestream velocity and mass flow rate ratio, a) I1 P1 and b) I3 P3. 64
6.6 Relative change of available engine power due to total pressure distortion compared to the I2 P3 configuration, vs. relative freestream velocity and mass flow rate ratio, a) I1 P1 and b) I3 P3. 65
6.7 Relative change of available engine power vs. relative freestream velocity and mass flow rate ratio, a) I1 P1, overall and b) I3 P3, overall. 65
6.8 a) I2 with intake grid, front view, b) plenum 3 (plenum 2 combined with plenum splitter). 66
6.9 a) Grid mount element installation, top view and b) grid mount element. 66
6.10 Normalized total pressure ratio vs. relative freestream velocity of the Intake 2 modifications for $\dot{m}_{corr}/\dot{m}_{corr,max} = 1$. 67
6.11 Relative difference in total pressure ratio due to intake grid vs. relative freestream velocity and mass flow rate ratio. 67
6.12 Normalized total pressure distortion vs. relative freestream velocity of the intake 2 plenum chamber and engine grid variants for the maximum mass flow rate ratio. 68
6.13 Relative difference in total pressure distortion due to plenum splitter vs. relative freestream velocity and mass flow rate ratio. 68
6.14 Normalized swirl coefficient vs. relative freestream velocity of the intake 2 plenum chamber and engine grid variants for $\dot{m}_{corr}/\dot{m}_{corr,max} = 1$. 68
6.15 Distribution of normalized total pressure ratio in AIP for a) I2 P2 IG2 EG1 RSP0 IGV0, b) I2 P3 IG2 EG1 RSP0 IGV0, maximum relative freestream velocity, maximum mass flow rate ratio. 69
6.16 Relative change of available engine power vs. relative freestream velocity and mass flow rate ratio, a) grid influence, due to the total pressure ratio, b) splitter influence, due to the total pressure ratio, c) grid influence, due to total pressure distortion and d) splitter influence, due to total pressure distortion, e) grid influence, overall and f) splitter influence, overall. 70
6.17 Geometry of I1 P1 and I2 P3 and its combinations, a) intake 1, top view, b) intake 2, top view, c) plenum 1 front view and d) plenum 3, front view. 71

6.18 Aerodynamic characteristics vs. relative freestream velocity of I1 P1, I2 P3 geometries and the combination I1 intake/ P3 plenum chamber, maximum mass flow rate ratio, a) normalized total pressure ratio and b) normalized distortion coefficient. 72

6.19 Normalized swirl coefficient vs. relative freestream velocity of the I1 P1, I2 P3 geometries and the combination I1 intake/ P3 plenum chamber for the maximum mass flow rate ratio. 72

6.20 Relative difference in total pressure ratio of I1 intake and I2 intake combined with P3 plenum chamber a) vs. relative freestream velocity and mass flow rate ratio and b) vs. relative freestream velocity, for the maximum mass flow rate ratio. 73

6.21 Relative change of available engine power vs. relative freestream velocity and mass flow rate ratio, a) ramp influence, due to the total pressure ratio, b) plenum influence, due to the total pressure ratio, c) ramp influence, due to total pressure distortion, d) plenum influence, due to total pressure distortion, e) ramp influence, overall and f) plenum influence, overall. 74

6.22 Schematic display of retrofit modifications and parametrization. 75

6.23 Relative difference in normalized total pressure ratio of retrofit variants compared to the I2 P3 configuration vs. relative freestream velocity, maximum mass flow rate ratio, a) rear spoilers and b) rear spoilers and intake guide vane. 76

6.24 Relative difference in normalized total pressure distortion of retrofit variants compared to the I2 P3 configuration vs. relative freestream velocity, maximum mass flow rate ratio, a) rear spoilers and b) rear spoilers and intake guide vane. 77

6.25 Relative difference in normalized swirl coefficient of retrofit variants compared to the I2 P3 configuration vs. relative freestream velocity, maximum mass flow rate ratio, a) rear spoilers and b) rear spoilers and intake guide vane. 77

6.26 Variation of intake guide vane position P_{IGV}, relative change of available engine power a) portion due to total pressure ratio, zero and maximum relative freestream velocity, maximum mass flow rate ratio and b) portion due to total pressure distortion, zero and maximum relative freestream velocity, maximum mass flow rate ratio. 78

6.27 Variation of rear spoiler overlapping ratio R, and relative height H_{rel}, relative change of available engine power a) portion due to total pressure ratio, zero relative freestream velocity, maximum mass flow rate ratio b) portion due to total pressure distortion, zero relative freestream velocity, maximum mass flow rate ratio, c) portion due to total pressure ratio, maximum relative freestream velocity, maximum mass flow rate ratio, d) portion due to total pressure distortion, maximum relative freestream velocity, maximum mass flow rate ratio, e) combined power change, zero relative freestream velocity, maximum mass flow rate ratio and f) combined power change, maximum relative freestream velocity, maximum mass flow rate ratio. 79

6.28 Normalized total pressure ratio vs. relative freestream velocity of the geometries I1 P1, I2 P3 and I3 P3 and best retrofit variants for maximum mass flow rate ratio. 80

6.29 Normalized total pressure ratio vs. mass flow rate ratio of the geometries I1 P1, I2 P3 and I3 P3 and best retrofit variants for $U_{\infty,max}$. 80

6.30 Normalized distortion coefficient vs. relative freestream velocity of the geometries I1 P1, I2 P3 and I3 P3 and best retrofit variants for maximum mass flow rate ratio. 81

6.31 Normalized distortion coefficient vs. mass flow rate ratio of the geometries I1 P1, I2 P3 and I3 P3 and best retrofit variants for maximum relative freestream velocity. 81
6.32 Distribution of normalized total pressure ratio in AIP for a) I2 P3 IG2 EG2 RSP0 IGV0, b) I2 P3 IG2 EG2 RSP3 IGV0 c) I2 P3 IG2 EG2 RSP3 IGV1, zero relative freestream velocity, maximum mass flow rate ratio. 82
6.33 Distribution of normalized total pressure ratio in AIP for a) I2 P3 IG2 EG2 RSP0 IGV0, b) I2 P3 IG2 EG2 RSP3 IGV0 c) I2 P3 IG2 EG2 RSP3 IGV1, maximum relative freestream velocity, maximum mass flow rate ratio. 83
6.34 a) Pressure distributions, line 2, basic intakes and best retrofit variants, maximum relative freestream velocity, maximum mass flow rate ratio and b) geometry and local curve length coordinate S_2 for line 2 of I1 and I2. 84
6.35 a) Pressure distributions, line 9, basic intakes and best retrofit variants, maximum relative freestream velocity, maximum mass flow rate ratio and b) geometry and coordinate S_9 for line 9 in plenum 1. 84
6.36 Pressure distributions, line 13, basic intakes and best retrofit variants, maximum relative freestream velocity, maximum mass flow rate ratio. 86
6.37 Influence of α variation on aerodynamic characteristics of I2 P3 IG2 EG2 RSP3 IGV1, relative freestream velocities of $0; 0.64; 1$, maximum mass flow rate ratio, a) total pressure ratio and b) distortion coefficient. 87
6.38 a) Influence of α on aerodynamic characteristics of I2 P3 IG2 EG2 RSP3 IGV1, relative freestream velocities of $0; 0.64; 1$, maximum mass flow rate ratio, normalized swirl coefficient, b) angle of attack adjustment. 88
6.39 Distribution of normalized total pressure ratio in AIP for I2 P3 IG2 EG2 RSP3 IGV1, a) $\alpha = -5°$, b) $\alpha = 0°$ and c) $\alpha = +5°$, relative freestream velocities of 0.64, maximum mass flow rate ratio. 89

7.1 Complete 2D optimization domain. 95
7.2 a) Assembly of domain A, B, C, D, and E, b) Parameter definition 96
7.3 Development of the final 2D optimization run, a) η_{rel}, b) φ_{rel}, c) R and d) H_{rel}. 97
7.4 Distribution of η for a) reference geometry and b) optimized geometry. 98
7.5 Boundary conditions of the submerged intake optimization case. 99
7.6 Parametrization of the submerged intake optimization case, a) side view, b) top view. . . 99
7.7 Main parameter trends of the submerged intake case, a) $\eta(\varphi, \psi), dx_2 = 0.4$, b) dx_2 influence on $\eta(\varphi, \psi)$. 100
7.8 Side intake parameter study, domain representation. 102
7.9 Side intake parameter study, fuselage and intake surface meshes. 103
7.10 Back view of a) Original EID mesh combined with EPC mesh and additional circular mesh, b) Simplified EID mesh combined with EPC mesh. 103
7.11 Cut view of a) Original EID mesh combined with EPC mesh and additional circular mesh, b) Simplified EID mesh combined with EPC mesh. 104
7.12 Decomposition of the drag coefficient for a lightweight helicopter configuration, Ref. [30]. 105
7.13 Total pressure iso surfaces for $\eta_{norm} = 0.988$, a) top view of the original reference geometry, b) top view of the simplified reference geometry, c) back view of the original reference geometry and d) back view of the simplified reference geometry. 106

7.14 Normalized total pressure ratio distribution, a) sectional cut view in X_{AIP} $Z_{AIP}-$ plane of the original reference geometry, b) sectional cut view at $\theta = 15°$ of the original reference geometry and c) sectional cut view in X_{AIP} $Z_{AIP}-$ plane of the simplified reference geometry. 107
7.15 Normalized total pressure ratio distribution, a) AIP back view of the original reference geometry and b) AIP back view of the simplified reference geometry. 107
7.16 Display of aft-body separation regions at helicopter fuselage, indicated by green iso surfaces of the axial velocity $U = -0.5\ m/s$, a) perspective view of the original reference geometry and b) perspective view of the simplified reference geometry. 108
7.17 Exemplary side intake geometry in a) isometric, b) front, c) top and d) side view. 109
7.18 Parametrization of side intake geometry a) ramp and scoop geometry in sectional view, b) ramp parametrization in top view. 109
7.19 Variation of the relative scoop height H_{rel} and the scoop overlapping ratio R, $\varphi_{rel} = 0.88$, $r_{rel} = 2$, $\psi = 0\ deg$, relative change of the available engine power a) total change, b) portion due to η, c) portion due to $DC60$ and d) portion due to fuselage drag. 111
7.20 Variation of the relative ramp angle φ_{rel} and the relative ramp radius r_{rel}, $H_{rel} = 1.94$, $R = 1.0$, $\psi = 0\ deg$, relative change of the available engine power a) total change, b) portion due to η, c) portion due to $DC60$ and d) portion due to fuselage drag. 112
7.21 Variation of the ramp side angle ψ and the scoop overlapping ratio R, $H_{rel} = 1.94$, $\varphi_{rel} = 0.88$, $r_{rel} = 2$, relative change of the available engine power a) total change, b) portion due to η, c) portion due to $DC60$ and d) portion due to fuselage drag. 113
7.22 Geometric display of the configuration defined by $R = 1.0$, $H_{rel} = 1.94$, $\varphi_{rel} = 0.88$, $r_{rel} = 2$ as well as $\psi = 0 deg$ a) front view, b) top view and c) side view. 114
7.23 Total pressure iso surfaces for $\eta_{norm} = 0.988$, a) top view of the reference geometry, b) top view of the best parameter case, c) back view of the reference geometry and d) back view of the best parameter case. 115
7.24 Normalized total pressure ratio distribution, a) sectional cut view in $X_{AIP}-Z_{AIP}-$ plane of the reference geometry, b) sectional cut view in $X_{AIP}-Z_{AIP}-$ plane of the best parameter case, c) AIP back view of the reference geometry and d) AIP back view of the best parameter case. 116
7.25 Display of aft-body separation regions at the helicopter fuselage, indicated by green iso surfaces of axial velocity $U = -0.5\ m/s$, a) perspective view of the reference geometry and b) perspective view of the best parameter case. 116

List of Tables

3.1 Components of the W/T setup, based on Ref. [36]. 25

4.1 Comparison of intake coefficients for mesh refinement levels of the sectional/full fuselage case 48

6.1 Rear spoiler parameter values and intake guide vane positioning. 75

7.1 Limits for the parametrizations, relative to the baseline configuration. 97
7.2 Parameter limits of parameter studies, relative to the reference configuration, only ψ presented as absolute value. 110

Nomenclature

Arabic Characters

A	$\left[m^2\right]$	Cross section area.
B	$[m]$	Width.
C	$[-]$	Total pressure loss indicator in Venturi meters.
C_D	$[-]$	Drag coefficient.
c_p	$[-]$	Pressure coefficient.
d, D	$[m]$	Diameter.
$dx1$	$[m]$	Length of the cowling approach ramp.
$dx2$	$[m]$	Relative position of ramp inflection point, measured upstream from final ramp section.
DC_{60}	$[-]$	Distortion coefficient, describing total pressure distortion, based on 60deg sector with lowest average total pressure.
F	$[-]$	Objective function for the evaluation of the design points in the parameter study.
F_X	$[N]$	Force in X coordinate direction.
h, H	$[m, km]$	Height.
H_{rel}	$[-]$	Rear spoiler and scoop height, relative to reference case.
K	$[-]$	Sensitivity factor for shift of the surge line calculation.
l, L	$[m]$	Length.
$\dot{m}$	$[kg/s]$	Mass flow rate.
Ma	$[-]$	Mach number, multiple of the sound speed, measure of flow compressibility.
p	$[Pa]$	Air pressure.
P_{avail}	$[W]$	Available engine power.
P_{engine}	$[W]$	Engine power.

P_{IGV}	$[-]$	Intake guide vane position, relative to intake opening.
P_o	$[W]$	Profile power.
P_p	$[W]$	Parasite power.
P_{TOT}	$[W]$	Total required engine power.
P_{TR}	$[W]$	Tail rotor power.
q	$[Pa]$	Air dynamic pressure.
r_{rel}	$[-]$	Ramp radius at the end of the cowling approach ramp, relative to the reference case.
R	$[-]$	Overlapping ratio of rear spoiler or scoop, relative to intake opening.
Re	$[-]$	Reynolds number, relation of momentum and viscous forces.
S	$[-]$	General coordinate in main flow direction.
S_{EID}	$[-]$	General coordinate in main flow direction, dedicated to engine intake duct flow investigations.
S_{norm}	$[-]$	Swirl coefficient, describing mean deviation of flow direction from engine axis.
SC_{60}	$[-]$	Swirl coefficient, describing deviation of flow direction from engine axis, based on 60deg sector.
SM	$[-]$	Surge margin, coefficient describing margin to surge pressure ratio.
t	$[s]$	Time.
T	$[K]$	Air temperature.
u	$[m/s]$	Velocity component.
u_c	$[m/s]$	Local circumferential cross flow velocity component.
U	$[m/s]$	Resulting Velocity.
x	$[-]$	Design point, set of geometric variables.
X	$[-]$	Cartesian X coordinate direction.
Y	$[-]$	Cartesian Y coordinate direction.
y^+	$[-]$	Dimensionless wall distance.
Z	$[-]$	Cartesian Z coordinate direction.

Greek Characters

α	$[°]$	Angle of attack, local flow angle, pitch angle.
α_{swirl}	$[°]$	Local circumferential flow angle, calculated from local circumferential velocity component u_c and axial velocity U.
β	$[°]$	Sideslip or yaw angle, local flow angle at the edge of the boundary layer.
β	$[-]$	Area contraction ratio in Venturi meter.
δ	$[m]$	Boundary layer normal coordinate and height.
δ_{99}	$[m]$	Boundary layer height, defined at 99% freestream velocity.
ε	$[-]$	Expansion parameter for pressure calculation in Venturi meter, indicates compressibility.
η	$[-]$	Total pressure ratio, coefficient describing efficiency of the intake's ram compression.
η_σ	$[-]$	Pressure recovery coefficient.
κ	$[-]$	Isentropic expansion factor.
μ	$[Pa \cdot s]$	Dynamic viscosity of air.
μ	$[-]$	Advance ratio, ratio of forward flight speed in relation to propeller/rotor tip speed.
μ_σ	$[-]$	Inverse flow ratio, ratio of intake entry cross section relative to related upstream streamtube cross section in infinity.
ν	$\left[m^2/s\right]$	Kinematic viscosity.
ω	$[1/s]$	Vorticity.
φ	$[°]$	Incidence angle of cowling approach ramp.
φ_{rel}	$[-]$	Incidence angle of cowling approach ramp, relative to reference case.
π	$[-]$	Operating pressure ratio of compressor.
ψ	$[°]$	Ramp side wall angle.
ρ	$\left[kg/m^3\right]$	Air density.
τ	$[-]$	Pressure ratio in Venturi meter.
θ	$[°]$	Measure of the circumferential angle in the aerodynamic interface plane.

Subscripts, Superscripts and Prefixes

AIP	Condition in the aerodynamic interface plane.
$avail$	Denotes available engine power due to DC_{60}, η or intake related drag.
BSL	Related to baseline configuration.
c	Circumferential.
$corr$	Corrected values, resulting from reduced values, made dimensionless by referencing to reference values of temperature and pressure.
$Dist$	Value corresponding to "distorted" surge line.
err	Related to uncertainty of measurement value.
F	Indicating fuselage.
i, j	Indices.
i	Induced component.
$inlet$	Value related to domain inlet.
I	Value related to intake entry section.
IGV	Value related to intake guide vane.
$I2$	Value related to intake 2, the reference geometry.
low	Lowest value.
m	Average value.
max	Maximal value.
$norm$	Value, normalized with certain reference value.
$outlet$	Value related to domain outlet.
p	Indicating coefficient based on pressure.
p	Indicating coefficient in probe-fixed coordinate frame.
$probetip$	Value related to tip of probe.
r	Radial.
red	Reduced value, made independent of ambient air temperature and pressure, solely dependent on flight Mach number.
Ref	Reference value.
rel	Relative value, compared to reference value.
RSP	Value related to rear spoiler.
s	Surge line value.
Sc	Related to the scoop.
t	Total value.
$throat$	Condition at duct throat.

TOT	Total value.
$Wall$	Condition at wall.
$1,2$	Stations in Venturi meter.
60	Average value of AIP 60° sector.
∞	Ambient or freestream condition.
Δ	Difference, relative or absolute.
$\bar{\ }$	Mean value.

Acronyms

AASD	Automated Aerodynamic Shape Development
AER	Chair of Aerodynamics and Fluid Mechanics of the TUM
AIP	Aerodynamic Interface Plane
APU	Auxiliary Power Unit
AR	Aspect Ratio, of flow ducts.
ATHENAI	Aerodynamic Testing of HElicopter Novel Air Intakes
CAD	Computer Aided Design
CFD	Computational Fluid Dynamics
CFRP	Carbon Fibre Reinforced Plastics
CFX	comercial CFD solver of ANSYS
CNC	Computerized Numerical Control
CR	Contraction Ratio, of flow ducts.
DFS	Distance From Surge
EG	Engine Grid
EID	Engine Intake Duct
EPC	Engine Plenum Chamber
ERICA	Enhanced Rotorcraft Innovative and Achievement
FF	Full Fuselage, referring to a helicopter fuselage in free flight conditions.
FOD	Foreign Object Damage
FOI	Totalförsvarets forskningsinstitut, Swedish Defence Research Agency
GARTEUR	Group for Aeronautical Research and Technology in Europe
GDEA	Genetic Diversity Evolutionary Algorithm
GGI	General Grid Interface
HEAVYcOPTer	Contribution to OPTimisation of HEAVY helicopter engine installation design
HWA	Hot Wire Anemometry

I	Intake variant
IBF	Inlet Barrier Filter
IG	Intake Grid
IGV	Intake Guide Vane
ISA	International Standard Atmosphere
NACA	National Advisory Comittee for Aeronautics
NASA	National Aeronautics Space Administration
ONERA	Office Nnational d' Etudes et de Recherches Aérospatiales
P	Plenum chamber variant
PIV	Particle Image Velocimetry
PRS	Pressure Ratio of Surge line
RANS	Reynolds Averaged Navier-Stokes (equations)
RSP	Rear SPoiler
SAR	Search And Rescue (mission)
SF	Sectional Fuselage, referreing to truncated fuselage section as tested in the wind tunnel.
SFC	Specific Fuel Consumption
SST	Shear Stress Transport (turbulence model)
TILTOp	Efficient Shape Optimization of Intake and Exhaust of a Tiltrotor Nacelle
TUM	Technische Universität München
UAV	Unmaned Aerial Vehicle
URANS	Unsteady Reynolds Averaged Navier-Stokes (equations)
VTOL	Vertical Take Off and Landing
W/T	Wind Tunnel
ZDES	Zonal Detached Eddy Simulation

1 Introduction

1.1 Motivation

The research in the field of engine air intakes has always been strongly connected to the development and progress of aircraft design. The increase in flight velocities and development of jet engines implicitly necessitated analyses of the engine airframe interaction and integration. Hereby, the engine air intake couples the requirements of two research fields. The first is the aerodynamics of an aircraft's external parts: fuselage, wing and control surfaces. The second is the field of gas turbine aerodynamics and thermodynamics. Especially in early design stages of a new aircraft, the knowledge of their interactions is essential to save development times, reduce cost and uncertainties as well as enhance the aircraft's performance. The interaction of an aircraft airframe and engine is qualified by evaluating the engine inflow conditions, usually in the aerodynamic interface plane (AIP). Hereby, main aims are reduction of emissions, increase of engine thrust, stable engine operation and avoidance of additional drag. Often a mismatch of the freestream velocity and the required engine entry velocity exists for different operation conditions. Compatibility of an aircraft's airframe with the installed engine requires that the engine operates stably when subjected to the complex inlet flow conditions at the inlet/engine interface, which are characterized by total pressure and total temperature variations in both space and time. Homogeneity with respect to the AIP total pressure distribution is commonly assessed by a distortion parameter DC_{60}. Engine thrust is strongly influenced by the efficiency of the intake's ram compression, which is often described by the ratio η of the mean AIP total pressure and free stream total pressure. The efficieny of the compressor is dependent on local blade incidence angles at its entry face relative to the blades leading edge. Therefore, a swirl coefficient SC_{60} is often evaluated to account for the deviation of local flow direction in relation to the engine axis.

In the subsonic flight regime, helicopters play an essential role in air transport on the basis of their unique vertical take-off and landing (VTOL) abilities. Thus, in certain situations and applications such as search and rescue (SAR) missions, they prevail over other aircraft. Here particularly typical lightweight utility helicopters are addressed. Also in this sector the reduction of emissions is a crucial aim. To address this purpose, aerodynamically optimized engine installation is beneficial for fuel-efficient engine operation. Besides classical intake optimization targets concerning intake related drag, pressure recovery and distortion, several constraints and requirements can lead to significantly different intake shapes as applied for fixed-wing aircraft. The inflow direction at the intake entry completely changes from hover flight over transition flight to level flight. Highest demands on engine power output and stability are imposed in hover and transition flight. In these cases a non-negligible influence exists due to the main

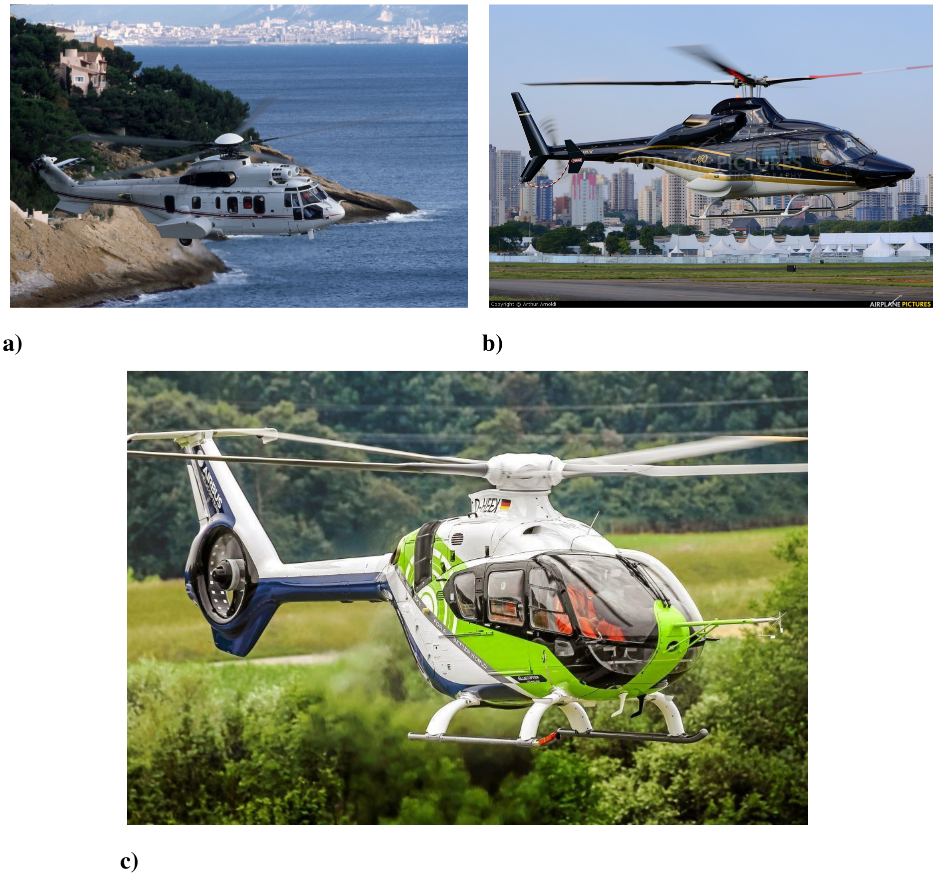

Figure 1.1: a) Airbus Helicopters Super Puma, b) Bell 430, and c) Airbus Helicopters Bluecopter Demonstrator, Refs. [4], [5].

rotor's downwash. In level flight induced downwash is rather small. One usual characteristic of rotorcraft intakes is an area-contraction between the intake entry and the engine entry face. It helps to achieve low loss and stable engine operation in hover and maneuver flight conditions. Widespread helicopter intake designs, as illustrated in Figure 1.1, are pitot intakes (cf. Airbus Helicopters H225 Super Puma), forward facing side intakes (cf. Bell 430), and sideways facing plenum chamber type intakes (also known as static intakes, cf. Airbus Helicopters Bluecopter demonstrator). Especially in fast forward flight, pitot intakes and forward facing side intakes prevail over their sideways facing counterparts in terms of pressure recovery. In several helicopter configurations, pitot intakes are not applicable as they require installation in front of the gearbox. Further analyses and benefits of various intake shapes are presented as part of the current research.

Helicopters have to perform missions in dirty and cold environments. To ensure safe engine operation in such conditions, particle separators such as inlet barrier filters (IBF), scavengers, foreign object damage grids or vortex tubes are indispensable. Foreign object damage grids are applied also to protect the engine when ice accretion occurs. Plenum chamber type side intake geometries are applied for various reasons. These intakes can work as particle separators while in some cases reducing the additional drag of the engine airframe integration. Further reasons are the intakes' positioning aft of the rotor axis, maintainability and spatial limitations in the engine compartement. Especially for s-duct and pitot type intake shapes, the influence of the main parameters on flow topologies and the resulting inflow conditions at the AIP is well understood and documented in the literature. For plenum chamber type intakes with forward or sideward facing intake entries, which are often applied for helicopter configurations, only little research has been published. For this reason, selected plenum chamber type side intake configurations are investigated in the context of the current research. The investigation results of submerged and s-duct intakes can be transferred to helicopter intakes in some cases. Therefore, these configurations are also addressed in this thesis.

1.2 State of the Art

Several intake wind tunnel and numerical investigations for fixed-wing as well as rotorcraft configurations have been performed for a variety of flight Mach numbers, amongst others as part of Refs. [6, 44, 48, 64, 80, 82].

The purpose and especially the flight Mach number strongly influence the intake shape. Flight Mach numbers of modern and future fast rotorcraft are increasing. Hereby addressed are novel concepts such as tilt-rotors and hybrid transitioning vertical take-off and landing (VTOL) aircraft, which interfuse the clear separation between classical helicopter and fixed-wing configurations. Thus, in dependence of the mission envelope and integration, also s-duct and submerged intake shapes have to be considered. Therefore, subsequently not only classical helicopter intakes but also submerged intakes and s-duct intakes are regarded.

1.2.1 Submerged Intakes

Already in the 1940s, an extensive intake wind tunnel testing program was launched by NASA's predecessor, the NACA. Corresponding to the typical flight Mach numbers achieved by fighter or reconnaissance aircraft configurations of the time, especially intakes suitable to the subsonic flight regime were investigated applying large-scale wind tunnel models of aircraft including the engine air intake. Among the tested configurations were pitot intakes, submerged side intakes (a specific kind later often related to as "NACA intake"), scoop side intakes and several more. As part of Ref. [44], for low Mach numbers the effectiveness of a divergent planform over parallel side walls was only found for low inlet-velocity-ratios, cf. chapter 2.2.1. Hereby, a vortex-pair is created to support transport of high-energetic air from the freestream flow to the wall. The tests revealed considerable errors in terms of total pressure recovery of the intakes comparing a 1/4-scale model to a full scale model. In flight tests, performed with a North American YF-93A as part of Ref. [62], for a range of subsonic flight Mach numbers and engine mass flow rates, submerged and scoop side intakes were compared in terms of pressure recovery and drag, see Figure 1.2. Hereby, higher pressure recoveries were obtained for the submerged intake at lower flight Mach numbers ($Ma < 0.87$) whereas at higher flight Mach numbers ($Ma > 0.89$), the pressure recovery as well as the drag corresponding to the scoop intake was higher than that of the submerged intake.

In Ref. [32], further investigations for different Mach numbers, boundary layer heights, angles of attack as well as intake positioning along the fuselage were conducted. In Ref. [47], the application of boundary-layer control was tested for a submerged scoop intake featuring a steep approach ramp ($\varphi = 19deg$). The use of one or more slots with active suction led to a significant increase in pressure recovery over the entire tested inlet-velocity-ratio range.

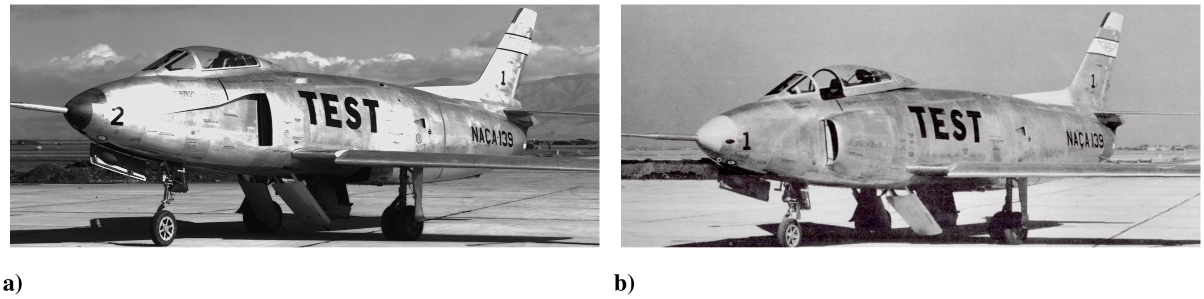
a) b)

Figure 1.2: North American YF-93A intake flight tests a) equipped with submerged intake and b) equipped with scoop intake, Ref. [62].

The research performed in the field of supersonic fighter intakes has always been of high interest since aircraft are capable of exceeding flight Mach numbers of 1. Investigations of such configurations are part of Ref. [82] and Ref. [66] amongst others. Since the main interest of the current research is in subsonic intake aerodynamics, it is not discussed further.

1.2.2 S-Duct Intakes

In the last decades, a main interest was in the investigation of s-duct intake configurations as they are important in the field of unmanned (combat) aerial vehicles U(C)AV and auxiliary power unit (APU) applications. As flight Mach numbers of novel helicopter and tilt-rotor designs increase, such geometries could play a more important role also in this field. The flow field of such configurations was investigated in detail both numerically and experimentally at the example of the M2129 s-duct geometry in Ref. [22, 81]. Especially as part of Ref. [81] the topology in the separation region of s-duct geometries was studied by means of oil flow visualization and in complementary numerical simulations. The research of Ref. [6] confirmed the applicability of vortex generators in s-duct geometries for an effective reduction of total pressure distortion in the AIP. In UAV s-duct configurations boundary layer ingestion is a crucial factor and has been studied in Ref. [13]. The research as part of the GARTEUR (Group for Aeronautical Research and Technology in Europe) project "GARTEUR AD/AG-46 Highly Integrated Subsonic Air Intakes", investigations of strongly curved ducts (highly integrated s-ducts) have been performed, Ref. [31]. The intake which represents a typical UAV intake geometry, is also referred to as EIKON FOI-EIC-01. Main aims of the research were on numerical predictions and experimental studies of steady/dynamic intake distortion in the complex intake flow fields due to a compact s-shaped intake (Ref. [24]), effects of forebody boundary layer ingestion (Ref. [56]), intake (entry) shape design and optimization (Ref. [75]), active and passive flow control (vortex generators and micro jets, Ref. [76]). The wind tunnel model of the intake is illustrated in Figure 1.3a. The major components of the wind tunnel model are a simplified U(C)AV forebody geometry, the intake duct geometry and the devices necessary to simulate the engine mass flow. Figure 1.3b represents the complex instantaneous internal flow field, simulated applying a ZDES computation.

1.2.3 Helicopter Intakes

Typical design requirements for fixed wing aircraft, Refs. [64, 82], greatly differ from those for rotorcraft. The often applied area-contraction between the intake entry and the engine entry face is an example

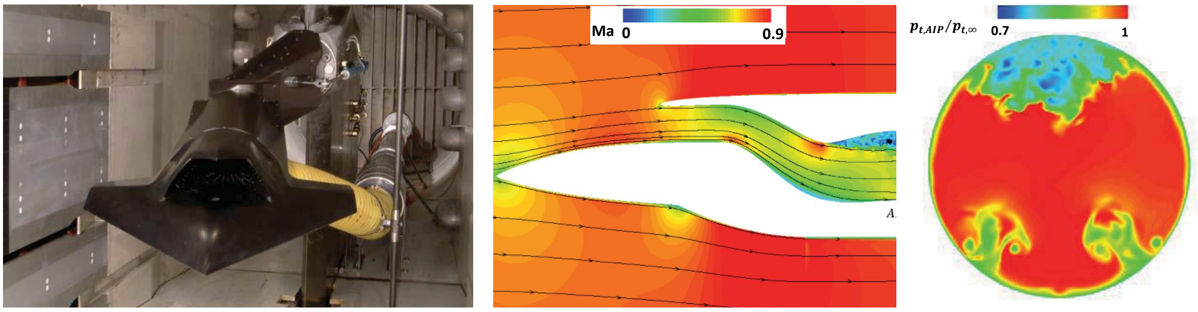

a) b)

Figure 1.3: EIKON intake investigations a) transsonic wind tunnel tests and b) instantaneous flow field in the symmetry plane and in the AIP (ONERA ZDES computation), Ref. [24].

which fosters good pressure recovery in hover and manoeuver flight, Refs. [33, 65]. Stable engine operation has to be ensured in a variety of off-design operation points. Furthermore, helicopter engine intakes are exposed to special operation conditions, that can significantly reduce engine power in the long term, Ref. [77]. Thus, stable and efficient engine operation was tested applying inlet barrier filters, Ref. [15], engine inlet particle separators such as scavengers, Refs. [12, 14], or foreign object damage grids for dusty environments or where icing is possible. Some examples of such devices are depicted in Figure 1.4. In Refs. [3, 23], ice accretion at realistic Reynolds numbers and temperatures was both experimentally tested in full-scale intake icing wind tunnel tests (see Fig 1.4 c) and in complementary numerical simulations.

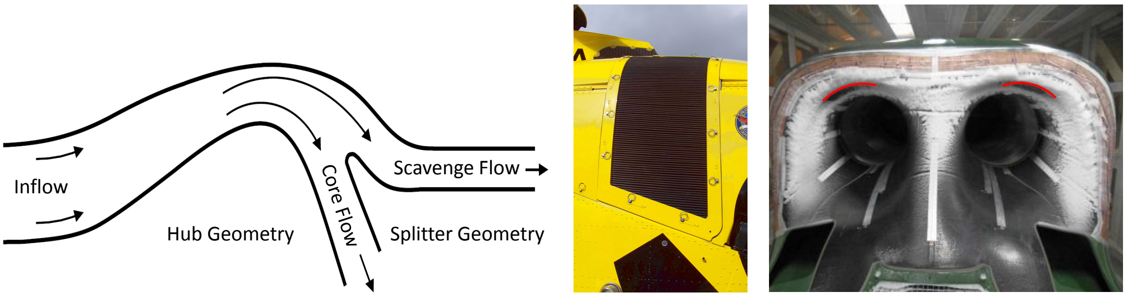

a) b) c)

Figure 1.4: a) Schematic of scavenger, [12] , b) Eurocopter EC135 inlet barrier filter, [83], c) icing test of KAI surion helicopter intake, Ref. [23].

Due to the use of a full-scale helicopter part model, icing was reproduced as accurately as possible and an anti-icing system was qualified prior to certification flight testing. Large scale intake test facilities are benefitial for realistic representation of flight conditions, as scaling can lead to errors in the measurement results, Ref. [68]. Large or full-scale wind tunnel testing is the best method to investigate the effect of geometric details such as intake grids, for a minimization of uncertainties before flight certification, especially with respect to safe engine operation. As part of the further development of the Aérospatiale AS 360/365 Dauphin, the aerodynamic charcteristics of different helicopter static, dynamic and pitot intakes were analyzed in wind tunnel tests applying a half-scale model, Refs. [61, 80]. The Aérospatiale AS 360 Dauphin with a static top intake is depicted in Figure 1.5a and the Aérospatiale AS 365 Dauphin with a dynamic intake is depicted in Figure 1.5b.

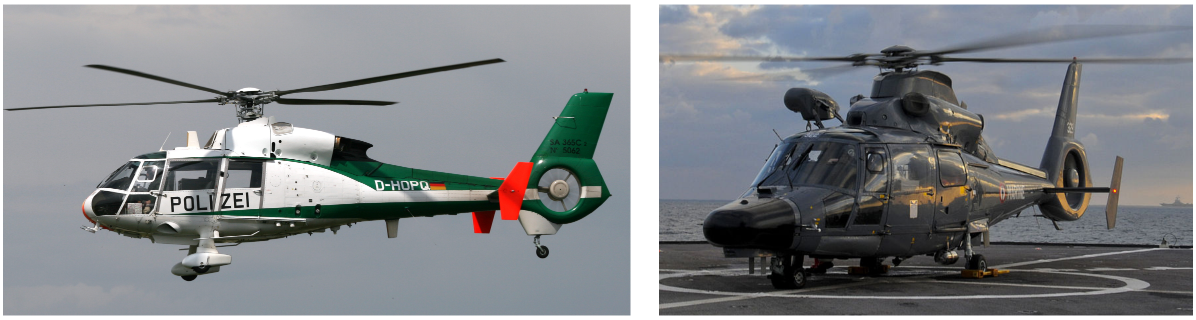

a) **b)**

Figure 1.5: a) Aérospatiale AS 360 Dauphin with static intake, and b) Eurocopter AS 365 Dauphin with dynamic intake, Ref. [84].

As discussed in more detail in chapter 2, the static intake is beneficial in the lower velocity regime, whereas a dynamic intake is advantageous in high velocity fast forward flight conditions. Experimental full-scale studies of static and semi-dynamic as well as dynamic helicopter intake configurations have been performed as part of Refs. [37, 39]. In Ref. [33], detailed investigations of different static and semi-dynamic top and side intakes have been conducted numerically, taking into account the influence of the rotor downwash for different flight velocities. Some of the important findings are also discussed in chapter 2.

1.2.4 Intake Optimization

Aerodynamic shape optimization has always been an important part of intake research. Nevertheless, the main portion of the findings of all aerodynamic optimization activities has not been published due to confidentiality. The performance of aircraft is strongly dependent on its outer shape as well as the shape of the geometry related to airframe engine integration, namely the engine air intake. As aerodynamic shape optimization of a side air intake geometry is conducted in the context of this thesis, some relevant intake optimization studies are briefly presented in the following. Within the CleanSky initiative, the project *TILTOp* (Efficient Shape Optimization of Intake and Exhaust of a Tiltrotor Nacelle) was dedicated to the investigation and optimization of the intake and exhaust integration within the ERICA (Enhanced Rotorcraft Innovative Achievement) tilt-rotor engine nacelle. As part of Ref. [28], an aerodynamic optimization for the aforementioned geometry was performed. The geometry is presented in Figure 1.6a. The CFD results were validated with wind tunnel measurements performed on a 1:2.5 scale model, see Figure 1.6b.

Due to the propeller shaft position, the baseline intake is strongly curved. This fosters flow separation and a distorted AIP total pressure distribution, see Figure 1.7a left. The optimization was run applying an in-house optimization code including the Genetic Diversity Evolutionary Algorithm (GDEA). Of the achieved pareto optimal frontier, one result was chosen as best suitable. The corresponding distribution of the total pressure ratio (η) in the AIP is depicted in Figure 1.7a right and the associated geometrical modification is illustrated in Figure 1.7b.

The achieved optimal shape was thereafter evaluated in terms of its effect on the specific fuel consumption (SFC) and improvement of the surge margin in different operation conditions using the engine simu-

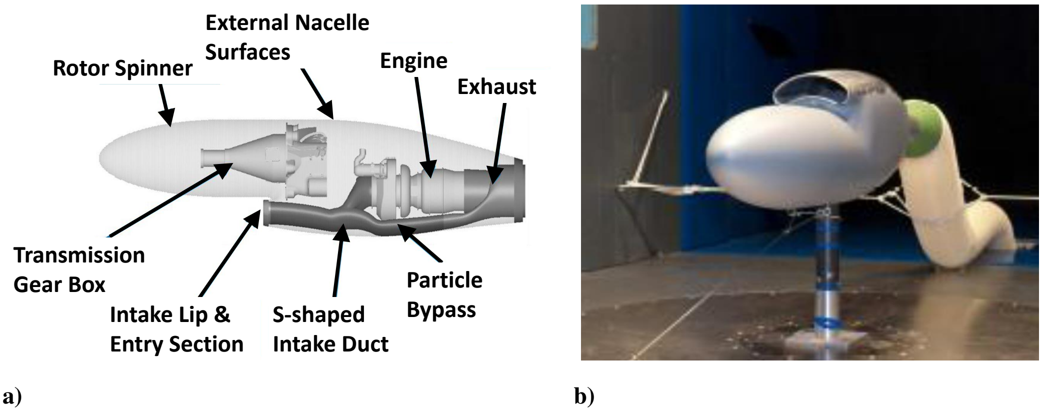

Figure 1.6: a) ERICA nacelle, Ref. [21] and b) nacelle model installation in the POLIMI wind tunnel, Ref. [19].

lation tool TSHAFT, cf. [46]. Especially in cruise flight, a significant specific fuel consumption reduction of $\Delta SFC \approx 1.5\%$ was achieved, comparing the baseline and optimized geometrical cases.

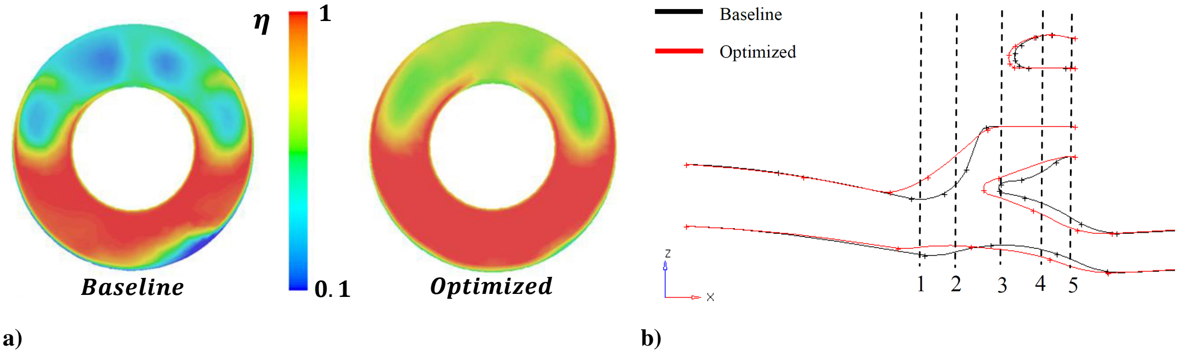

Figure 1.7: a) AIP η distribution for baseline and optimized as well as b) longitudinal cut shape optimization, [28]; $\eta = p_{t,AIP}/p_{t,\infty}$.

As part of the *HEAVYcOPTer* project (Contribution to optimisation of heavy helicopter engine installation design) within the CleanSky initiative, the inner geometry of the static side intakes and exhaust were optimized for a heavy class helicopter configuration (cf. Figure 1.8a, namely the Agusta Westland AW101, Ref. [27]. Hereby, the same automatic optimization algorithm was applied as in *TILTOp*. Considerable improvement in η-levels was achieved for the two intakes, especially in fast forward flight, cf. Figure 1.8b. while not increasing AIP total pressure distortion. At the same time, the exhaust back pressure could be significantly decreased thus increasing engine power output. Another optimization study for submerged inlets was performed in Refs. [72, 73]. Hereby, a fin was inserted in the duct bend region in the vicinity of the duct side walls. The swirl created by the fin is meant to counteract the intake discharge swirl and leads to a more homogeneous total pressure distribution at the duct exit. The incidence angle, fin height and length were varied to find pareto optimal solutions for the swirl and distortion coefficients SC and DC. The gradient based optimizer CFQSP (C code for Feasible Sequential Quadratic Programming) found two pareto optimal sets for the objective function, namely a weighted sum of SC and DC. Each set either featured a strong decrease in discharge swirl or distortion coefficients compared to the baseline case. Resulting total pressure ratios were not regarded in the optimization.

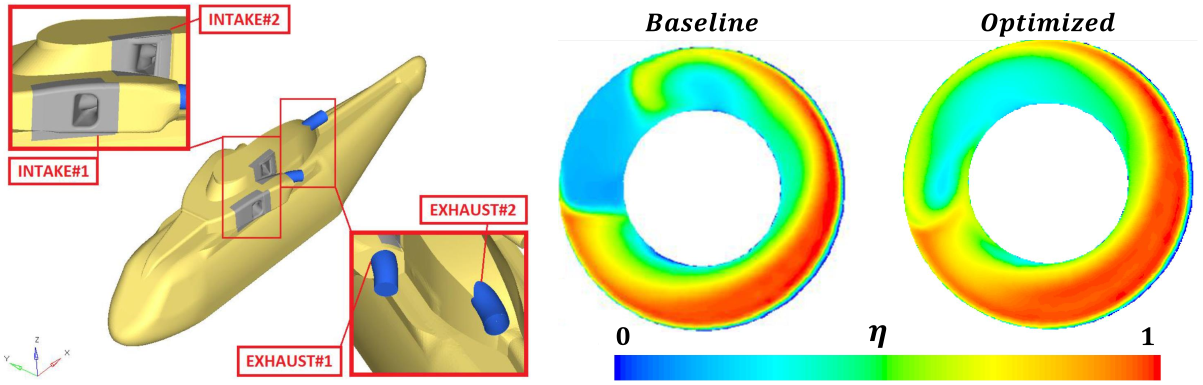

a) b)

Figure 1.8: a) Agusta Westland AW101 external geometry and b) AIP η-distribution of baseline and optimized cases, fast forward flight, Intake#1, Ref. [27].

1.3 Research Objectives

In contrast to s-duct and pitot type intake shapes, the characteristics of the flow field is not as well understood and documented in the literature for typically more complex helicopter intake geometries. This thesis and the corresponding research specifically addresses the investigation of plenum chamber type side intakes for helicopters. Hereby, the focus is on several research objectives. Some of them originate from the milestones and goals within the ATHENAI (Aerodynamic Testing of HElicopter Novel Air Intakes) project, Ref. [57]. The project was part of the technology demonstrator *Green Rotorcraft* within the *Cleansky Joint Technology Initiative*, Ref. [58]. The main aim was to increase the competitiveness of the European aviation industry while reducing the environmental impact due to increasing air traffic. Until 2020, carbon dioxide emissions should be reduced by 50 percent, emissions of nitrogen dioxide by 80 percent and noise pollution by 50 percent. At the same time, a sustainable live cycle should be realized for all components of air transport. Cleansky was funded by the *7th Framework Programme for Research and Technological Development* (2007 - 2013), Ref. [60]. The purpose of the Green Rotorcraft technology demonstrator was directly coupled with the aims of emission reduction in air transport. Thus, a decrease of parasite and induced drag and aerodynamic improvement of the engine integration for means of higher engine efficiency was desired. Therefore, one goal of the current research is the understanding of the aerodynamic characteristics of helicopter engine side air intakes as well as their shape optimization for fuel and emission reduction. This is particularly addressed by comprehensive experimental wind tunnel testing as well as by means of numerical shape optimization. To reach the goal of conducting comprehensive experimental investigations, implicitely another research objective arised. Namely, the realization of a reliable, adaptive and modular full-scale engine intake wind tunnel setup, including a fan for realistic reproduction of engine mass flow rates in the experiment. The verification of the truncation assumption, thus, testing a sectional fuselage model instead of a full fuselage model was another essential research objective. To reach this goal, numerical simulations of two cases were compared to each other, namely one including the sectional model geometry and all essential wind tunnel components and a second case representing the full fuselage geometry in free flight.

In order to create a basis for the experimental and numerical optimization, a detailed numerical investigation complemented the experimental results by providing more insight into the flow field characteristics of the baseline intake geometry.

1.4 Thesis Outline

Subsequently, a short overview of the thesis is presented. In *Chapter 2: Air Intake Research*, basic principles of air intakes are illustrated. An emphasis is put on typical intake shapes that are applied in subsonic flight, namely submerged NACA, s-duct, pitot and sideways-/forward-facing side intakes. Hereby, several aims are addressed. Airframe/Intake compatibility and performance are discussed and the related commonly used evaluation parameters like pressure recovery and distortion descriptors are regarded. Flow phenomena and total pressure as well as distortion coefficient tendencies for the aforementioned intake types are presented in dependence of influential parameters such as throat and freestream Mach numbers or velocitiy ratios etc. As part of *Chapter 3: Wind-Tunnel Testing*, the wind tunnel model and the experimental setup is described. The main assumptions are discussed that allow for the testing of a full-scale helicopter fuselage part model and realization of realistic flight Reynolds and Mach numbers. Furthermore, an overview is given of the tested configurations and the applied measurement techniques. The purpose of *Chapter 4: Numerical Simulations* is the presentation of the numerical setup and computational grids. Hereby, two cases are considered to evaluate the boundary layer and local flow directions' influence on the intake flow field. The first case reflects the conditions of the wind tunnel tests including a sectional fuselage model flush-mounted to the wind tunnel floor. Herein, the relevant wind tunnel parts like the nozzle, floor and collector are included. The second case represents a flight case constituted by a symmetric half of the full fuselage. The high quality block-structured meshing approach is illustrated for the study. In both cases the *baseline* intake geometry is incorporated. Unsteady Reynolds Averaged Navier-Stokes Equations are solved using ANSYS CFX and the shear-stress-transport model. In *Chapter 5: Analysis of the Baseline Case*, first a detailed investigation of the intake flow field of the baseline geometry is presented. In the second sub-chapter, the sectional fuselage case is compared to the full fuselage case in terms of upstream boundary layer, flow directions and AIP total pressure distributions. This investigation is substantial for the thesis as it compares wind tunnel against free flight conditions. The numerical method is validated by comparison of AIP total pressure distributions and incoming flow PIV data.

The experimental investigations and results of this thesis constitute *Chapter 6: Analysis of Side Intake Configurations*. On the full scale model of a helicopter fuselage section, a comprehensive data set is obtained. Various plenum chamber types along with static side intake and semi-dynamic side intake configurations are analyzed. Hereby, engine mass flow rates reflect the power requirements of real helicopter operating conditions. For different freestream velocities and mass flow rates, AIP five-hole pressure probe data and surface pressure distributions are compared for the intake shapes.

The geometries are sub-structured as "basic" intakes and intakes including "retrofit" modifications. Hereby, on the basis of the second "basic" intake (reference intake), retrofit modifications were tested such as a rear spoiler (small scoop) and an inlet guide vane to assess the aerodynamic optimization potential for existing intake geometries. *Chapter 7: Numerical Optimization and Parameter Studies* deals with numerical optimization and extensive parameter studies for sideways- and forward- facing side intake geometries. The chapter is subdivided into a first part that focuses on the description of the methods and optimization tool-chains involved. The second part comprises parameter studies and optimization results of three cases. The first case is a 2D case which reflects the intake cowling ramp and scoop influence on AIP total pressure levels, the second case is based on NACA submerged intake investigations and represents the plan form effects on AIP total pressure levels. The third case involves parameter studies of an intake based on the reference intake, integrated in the full helicopter fuselage. This case interconnects the previous numerical parameter studies. It is highly relevant for the application in a real helicopter, as the excessive shaft output power is investigated taking into account the power gains due to changes in pressure recovery and total pressure distortion but further involves the detrimental effect of fuselage drag induced by the engine air intake. The thesis is concluded by *Chapter 8: Conclusions*. The experimental and numerical methods are recapitulated and the key outcomes of the research are summarized.

2 Air Intake Research

For aircraft with air-breathing propulsion systems, the design and integration of the engine air intake is an essential part of the aircraft design. Engine air intake shapes are strongly influenced by the purpose of the aircraft, i.e. the application which it is designed for and the projected flight regime and envelope. In the subsequent chapter, the research of different intake shapes is presented together with their application as well as main influencial parameters. The flight Mach number is very important in terms of the integration and overall geometry of an intake. Four main regimes are distinguished, related to subsonic, transsonic and supersonic flight. The corresponding engine types used and typical intake shapes are presented schematically in Figure 2.1.

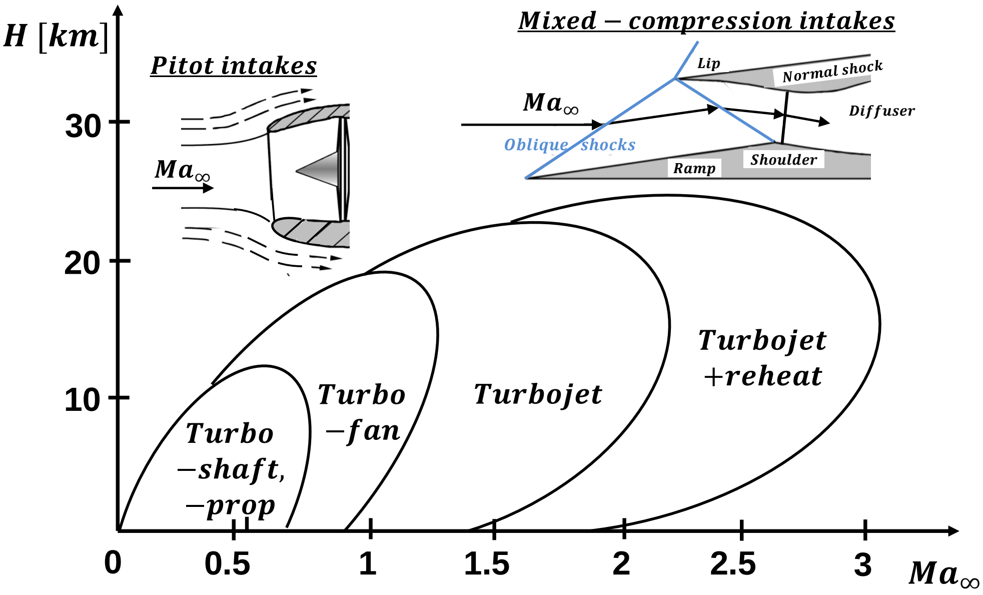
H [km]
30
20
10
0
0.5
1
1.5
2
2.5
3
Ma_∞
Pitot intakes
Ma_∞
Mixed – compression intakes
Ma_∞
Lip
Normal shock
Diffuser
Oblique shocks
Ramp
Shoulder
Turbo –shaft, –prop
Turbo –fan
Turbojet
Turbojet +reheat

Figure 2.1: Scheme of engine types and intake design depending on flight Mach number.

Especially for fixed wing aircraft, in the subsonic and transsonic flight regime often a diffuser is employed to recover dynamic to static pressure up to the engine entry face. Operation at low flight speeds and in cross flow conditions requires blunt intake lips, to avoid flow separation on the inside and outside walls. Engine nacelles are usually applied to guarantee optimal inflow conditions thus fostering engine operation at the design speed of current transport aircraft (e.g. Airbus A350, Boeing 787). In case of supersonic flight, external or mixed compression intakes including oblique shocks at the intake entry are applied to reduce total pressure losses to a minimum while decelerating the flow up to the engine entry. Aircraft like the Eurofighter Typhoon and the Aérospatiale-BAC Concorde 101/102 use(d) "2D" intakes with adaptive ramps to be able to fly the A/C in the entire envelope includinge the envisaged AoA and flight Mach number ranges. The Lockheed SR71 *Blackbird* used an axially movable cone to serve the same purpose for it's mixed-compression intake, see Figure 2.2.

In the supersonic flight regime, shock boundary layer interaction and shock oscillation are also important topics that can compromize an intakes' performance. Usually, the ingestion of the low energetic boundary layer is prevented by means of a diverter, Figure 2.2 top. A bleed system is often applied to reduce the low momentum boundary layer fluid close to the intake walls and thereby, among other aspects, to stabilize the shock system. For highly maneuverable fighter configurations, engine positioning in or close to an axis through the center of gravity is beneficial. Due to radar system positioning and signature, nose-mounted pitot intakes (F-86A Sabre, 1947) have been substituted for side or underbelly intakes often combined with s-duct geometries. Already in the 1940s and 50s, scoop and submerged intakes where investigated by NACA (National Advisory Committee for Aeronautics). The latter, commonly known as NACA intakes, originate low intake related drag levels at relatively high ram compression and are therefore often applied in low speed applications. Some main design aspects and characteristics of engine air intakes are discussed in the following. Hereby, an emphasis is put on aircraft operating within a subsonic flight envelope.

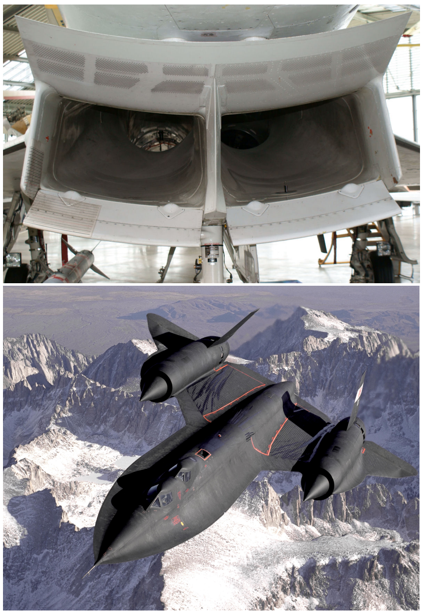

Figure 2.2: Eurofighter Typhoon intake (top) and Lockheed SR71 Blackbird (bottom).

Figure 2.3: Airbus Helicopters Bluecopter Demonstrator with semi-dynamic intake at the ILA in Berlin.

Effects related to intake-boundary layer interaction are not addressed here, as for the combination of freestream dynamic pressures and the bluntness of the intake shapes of sideways-facing helicopter intakes (Figure 2.3), the importance is assessed to be not as high as for high Ma number fixed-wing flight.
For configurations such as classical s-duct or pitot intakes, operated at flight Ma numbers in the high subsonic, transsonic or supersonic regime, the impact on engine performance is much more critical.
The investigations in chapter 5.2 of a sectional and full fuselage case including the baseline configuration showed, that the effect on the total pressure distributions in the AIP are insignificant in the current case, even for some change in the boundary layer heights.

2.1 Intake Total Pressure Distortion and Swirl

Engine intake distortion parameters describe the homogeneity of the flow field at the intake-engine interface in terms of total pressure and temperature. Total temperature distortion can occur due to exhaust gas re-ingestion in VTOL or helicopter hover flight. Total pressure distortion originates from asymmetric flow separation and vortex systems which occur in the intake region. Some examples are presented subsequently referring to Ref. [55].

Flow separation in the intake region appears:

- at the intake lips at high angles of attack or side slip angles
- in curved intake ducts
- due to operation away from design velocity-ratios (spillage)
- as an effect of boundary layer ingestion
- resulting from shock-boundary-layer interaction

Vortex structures in the intake region emanate from:

- curved intake geometries
- ingestion of ground vortices, leading-edge/strake vortices

In the current research, an emphasis is put on helicopter fast forward flight, for which the influence of total pressure distortion dominates over that of total temperature distortion. A more detailed examination of combined total pressure and total temperature distortion effects is presented in Ref. [17]. In the following, stability and efficiency influencing engine operation due to total pressure distortion is discussed. Inhomogeneous AIP total pressure distributions lead to a deterioration of engine power output and surge margin loss. Effects of time-dependent distortion are not regarded in the current research.

2.1.1 Stable Engine Operation

For the design of a compressor, the realization of a range of operating conditions along the operating line is mandatory to cover the entire aircraft flight envelope, cf. Figure 2.4. Stable engine operation requires the compressor to operate below the surge line to avoid rotating stall that can lead to periodic compressor flow reversal (surge). For each operating condition along the steady state operating line, a surge/stability margin ensures stable engine operation, also during engine transients, Ref.[69]. As depicted in Figure 2.5, the surge margin represents the relative distance of the operating pressure ratio π and the surge line total pressure ratio π_s. A common definition is $SM = |(\pi_s - \pi)/\pi|_{const.\ mass\ flow} \cdot 100$ [%], Ref. [67]. Inhomogeneous total pressure distributions at the AIP lead to an effective shift of the surge line closer to the operating line and thus reduction of the surge margin, Ref. [65].

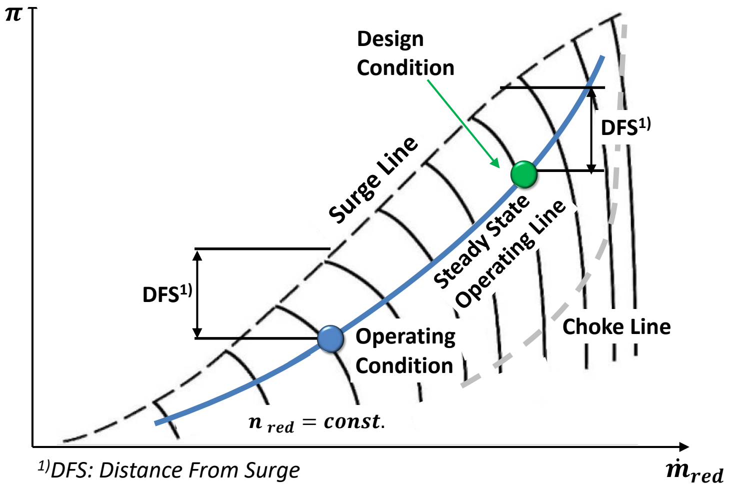

Figure 2.4: Schematic compressor map, based on Ref. [18].

Commonly, for a categorization of flow inhomogeneities, radial and circumferential patterns of lowered total pressure regions are distinguished. So-called "square-wave" spoiling patterns of nearly constant lowered total pressures in circumferential or radial direction can be achieved in rig testing by placing stationary gauzes upstream of the AIP. Circumferential patterns lead to significantly higher surge margin loss than radial patterns, Ref. [55]. Furthermore, angular AIP sections of low total pressure with an extent of $60^\circ < \theta < 90^\circ$ reduce surge margins significantly. Further increase of the circumferential low total pressure region have lower impact. As part of Ref. [55], the effect of different partitions of circumferential low total pressure regions was examined. It was found that a single 90° low total pressure region (single-per-revolution distortion pattern) was more detrimental in terms of surge margin loss as that of two 45° sectors or four 22.5° sectors (multiple-per-revolution distortion patterns). The stall of single blades is dependent on their individual continuous operating time in the low pressure region. Thus leading to higher tendency of stall in a connected low total pressure region. The critcal circumferential sector angle of lowered total pressures may vary depending on the blade partition and other geometrical parameters, but a critical angle of 60° was found to be a sound assumption in many cases, Ref. [55]. A further important finding of the same research was the nearly direct proportionality of the average total pressure level in a region of low total pressure ($p_{t,low}$) and the reduction in surge margin. Based on the latter findings, for the evaluation of total pressure distortions often the DC_{60} coefficient is applied. The DC_{60} is a circumferential distortion coefficient which is defined as $DC_{60} = (p_{t,AIP} - p_{t,low,60})/q_{AIP}$. It represents the difference of the lowest average total pressure $p_{t,low,60}$ segment with an extent of $\theta = 60^\circ$ and the mean total pressure $p_{t,AIP}$ divided by the mean AIP dynamic pressure q_{AIP}. A detailed assessment of the distortion's influence on surge margins is only possible in combination with the specific compressor performance map as well as information about the characteristic gradient of the loss-of-surge-margin-curve as function of a distortion parameter, Ref. [20]. Nevertheless, estimation methods exist to predict relative changes in surge margin loss. One method is shortly presented subsequently.

2.1.2 Parallel Compressor Theory

As illustrated in Figure 2.5, the parallel compressor theory is a simple but common model which is used to explain and predict compressor surge, Ref. [50]. It is based on the assumption, that a critical mainly circumferentially orientated area of reduced total pressures is responsible for an effective shift of the surge line.

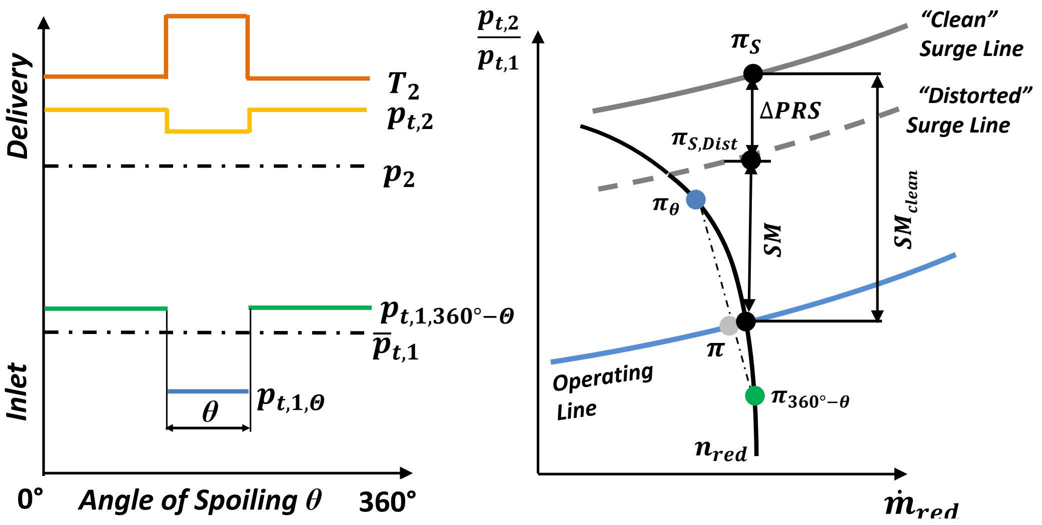

Figure 2.5: Parallel compressor theory, based on Ref. [55].

The real compressor is modeled as two fictional compressors operating in parallel with identical non-dimensional rotary speed (n_{red}) and identical discharge static pressure (p_2). One compressor is subjected to the decreased inflow total pressure of the "spoiled" sector ($p_{t,1,\theta}$), whereas the other one operates under "undisturbed" total pressure inflow condition ($p_{t,1,360°-\theta}$). Applying the characteristic and the compressor pressure ratio (i.e. operating condition) of the completely "undisturbed" compressor, together with the mass flow fractions of each of the two compressors, new (fictional) total pressure ratios can be calculated. The fictional compressor subjected to lowered inflow total pressure consequently operates under a higher total pressure ratio $\pi_\theta = p_{t,2}/p_{t,1,\theta}$. If this total pressure ratio reaches the surge line, the entire compressor is assumed to be prone to surge, even if the operating pressure ratio of the real compressor $\pi = p_{t,2}/\bar{p}_{t,1}$ is away from the surge line. Consequently, the loss of surge pressure ratio and thus effective shift of the surge line can be estimated as $\Delta\mathrm{PRS} = |(\pi_s - \pi_{s,Dist})/\pi_s|_{const.\ mass\ flow} \cdot 100$ [%], Ref. [67]. An effective loss surge margin ΔSM is the consequence.

[Note: Figure 2.5 illustrates a general and not the surge case]. As part of Ref. [42], a coupling factor of multi-stage compressors is included to broaden the two-compressor theory to more complex cases in which the assumption of static pressure homogeneity between stages is not or only partly fulfiled. In such cases where downstream compressors are "close-coupled" with upstream compressors, the condition of equal static pressures can be substituted by a "no mass flow between sectors" condition. Due to a nearly linear behaviour, the loss of surge pressure ratio can also be expressed as the product of a sensitivity factor K and a descriptor of the distortion intensity (i.e. a distortion coefficient DC), $\Delta\mathrm{PRS} = K \cdot DC$, Ref. [29]. For complex distortion patterns, the loss of surge pressure ratio can be estimated by empirical correlations, Ref. [29]. Therefore, in rig tests, sensitivities K_c and K_r are obtained for circumferential and radial distortion patterns. The surge total pressure ratio loss results from a superposition of the individual losses due to circumferential and radial distortion, $\Delta\mathrm{PRS}_{mixed} = K_c \cdot DC_c + K_r \cdot DC_r + C$. Hereby, DC_c and DC_r describe circumferential and radial distortion coefficients and C is a superposition factor. A similar procedure is presented in Ref. [69].

2.1.3 Intake Shape and Operating Condition

Subsequently, for a better distinction of geometric and operating condition influences on the total pressure distortion, a short overview of DC_{60} levels is presented for different intake shapes and flight/engine operation conditions together with the corresponding flow phenomena. Besides variations in geometric shape, the most influential parameters on DC_{60} are the freestream Mach number, engine mass flow rate, throat Mach number and side slip angle β or angle of attack α. As depicted in Figure 2.6a, s-duct intakes often feature a region of low-momentum fluid in the lower and central part of the duct which increases the total pressure distortion in the AIP, Ref. [81]. Close to the inflection point of the duct's mid-axis, two counter-rotating vortices are created, which transport low-momentum boundary layer fluid to the center of the duct thus finally leading to the aforementioned total pressure distribution. The corresponding owl face separation topology near the lower duct surface was confirmed in Ref. [81] by means of oil flow visualization, cf. Figure 2.6b.

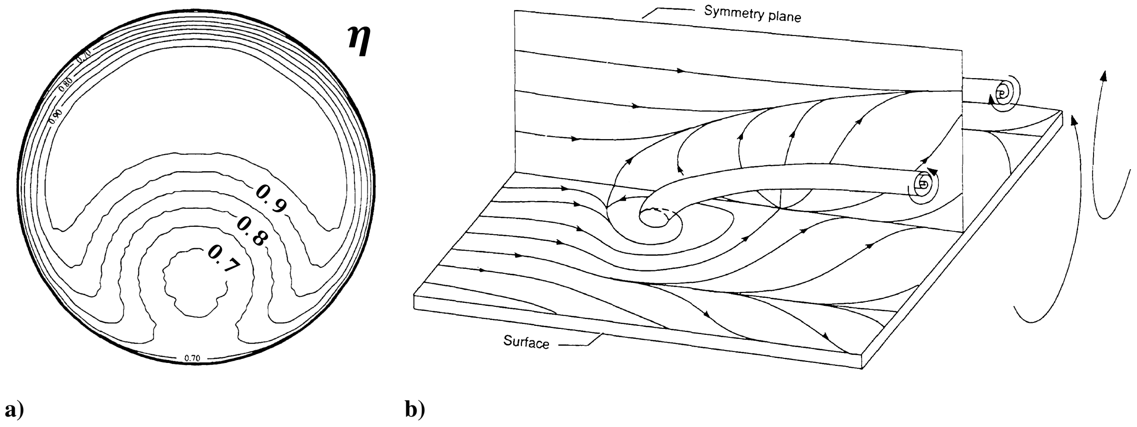

Figure 2.6: a) S-duct outlet η distribution, b) schematic of typical s-duct separation region, Ref. [81].

At the exit face of s-duct geometries, the typical total pressure distribution leads to partly high DC_{60} levels, depending on cross section shapes, aspect ratios, duct length and curvature. In Ref. [7], the distortion characteristic in dependence of throat Mach number was examined for the M2129 s-duct geometry, as illustrated in Figure 2.7a. With an increase in throat Mach number, an upstream shift of the separation location as well as a thickening of the boundary layer is noticeable. Therefore, the region of lowered total pressure becomes increased, leading to higher DC_{60} levels. A similar trend is found as part of Ref. [75]. The corresponding parameter study for different s-duct geometries reveals a decrease in distortion levels with increase in duct length, see Figure 2.7b.

Generally, a great increase of DC_{60} occurs for $M_{throat} \rightarrow 1$ due to shocks. As shown in Ref. [6], the application of vortex generators to the configuration of Ref. [7] lead to an effective reduction of the distortion coefficient DC_{60} below levels of 0.1. For a low subsonic Mach number of $M_\infty = 0.17$, levels of $0.13 < DC_{60} < 0.22$ for a slightly curved pitot type intake are found in Ref. [82].

Different helicopter side and top intakes were analyzed as part of Refs. [33, 39, 61, 80]. The aerodynamic characteristics of a dynamic pitot type and static sideways-facing air intake configuration were experimentally investigated in Refs. [61, 80]. The static side air intake is mainly designed for low flight Mach numbers, for which DC_{60} is slightly lower compared to the dynamic intake, Figure 2.8a. This is

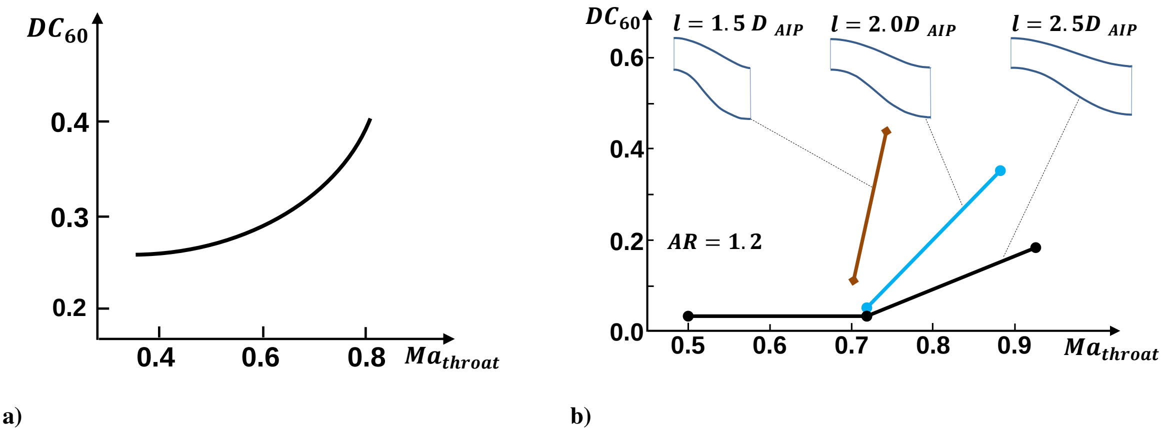

Figure 2.7: a) Distortion level as function of throat Mach number, based on Ref. [7], b) distortion level as function of throat Mach number and relative duct length, based on Ref. [75].

due to the fact, that in hover flight air is ingested from all sides and is deflected less around the intake lips in case of the static side intake, Figure 2.8b (1) and (2). A schematic illustration of the flow directions for fast forward flight is presented in Figure 2.8b (3) and (4).

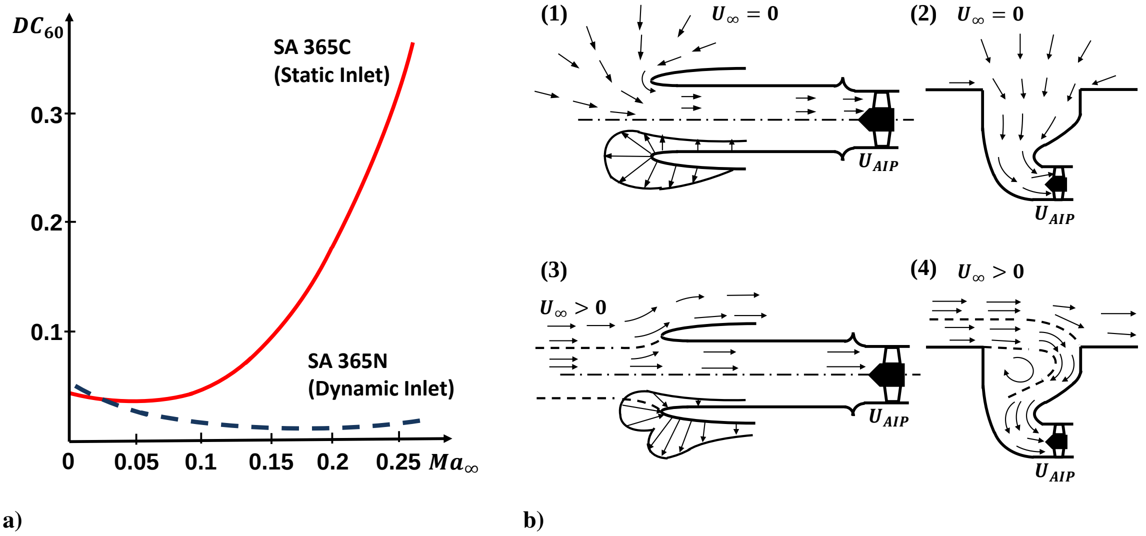

Figure 2.8: a) air intake distortion, wind tunnel tests Ref. [80], b) schematic of intake flow field (1) dynamic inlet at $U_\infty = 0$, (2) static inlet at $U_\infty = 0$, (3) dynamic inlet at $U_\infty > 0$, (4) static inlet at $U_\infty > 0$, Ref. [80].

As a consequence of the strong deflection around the front inlet lip, a region of separated flow occurs in case of the static intake, as shown in Figure 2.8b (4). This leads to increased distortion for fast forward flight (compare Figure 2.8a).

In Ref. [33], a 57°-side-facing side intake and a 55°-upward-facing top intake are investigated numerically in the presence of a main rotor and hub, compare Figure 2.9. Hereby, the main rotor is modeled with an actuator disc approach.

For both configurations, low total pressure distortion levels of $0.04 < DC_{60} < 0.1$ are found in the fan

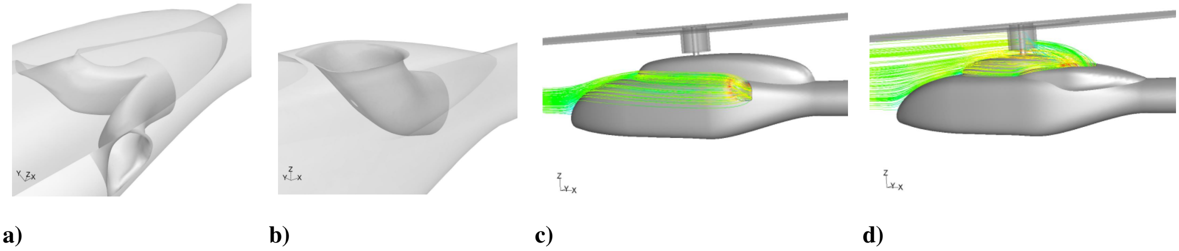

Figure 2.9: Helicopter intake computational simulations, $\mu = 0.198$ a) side intake, b) top intake, c) side intake streamlines and d) top intake streamlines, Ref. [33].

face for an inlet duct contraction ratio of $CR = 3$ as well as advance ratios $\mu < 0.1$. The influence of the rotor downwash was not significant in case of the top intake in hover flight due to rotor hub losses and reduced induced velocities in the region close to the intake. In fast forward flight ($\mu = 0.198$), DC_{60} levels of 0.25 and 0.15 are obtained for the side and top intake, respectively.

2.1.4 Engine Performance

In the literature, different estimates are presented for the impact of a deviation of engine inflow conditions from ideal conditions, thus zero total pressure losses, perfectly homogeneous total pressure distribution, low swirl angles and no increase in static temperature. The influence of the single parameters on engine power output are very specific for different engines and usually not published.

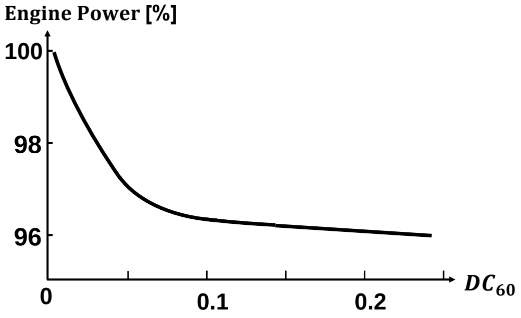

Figure 2.10: Engine power loss due to total pressure distortion, based on Ref. [78].

Some approximations are given in the following. In Ref. [80], a total pressure loss of 1% is estimated to create a decrease of engine power output of $\geq 2\%$. As part of Ref. [78], engine power loss in dependence of DC_{60} levels is measured for a Turbomeca Turmo IVB gas turbine. The decrease of the engine power output can be explained by a simple model such as the parallel compressor theory, as explained in Chapter 2.1.2. Due to an effective shift of the compressor operating point to a lower mass flow ratio in case of a spoiled total pressure inflow pattern, the power output of the entire engine is reduced. The effective reduction of the mean inflow pressure level usually also reduces the engine power output due to a detrimental change in the thermodynamic cycle. Both effects can only be evaluated with the specific compressor and turbine maps of the engine.

In the subsequent chapters, the effect of the AIP distortion on engine power output is approximated by the measured result of Ref. [78], even if the Pratt & Whitney PW206B2 engine, as installed in the Airbus Helicopters H135 could exhibit a different behaviour.

For the parameter studies of an engine side intake geometry in the current research (Chapter 7.2.3), the corresponding curve progression (cf. Figure 2.10) is approximated by a polynomial of sixth order and the original curve is linearly extrapolated to distortion levels of 0.4. Figure 2.11 gives an insight into PW200 series engines.

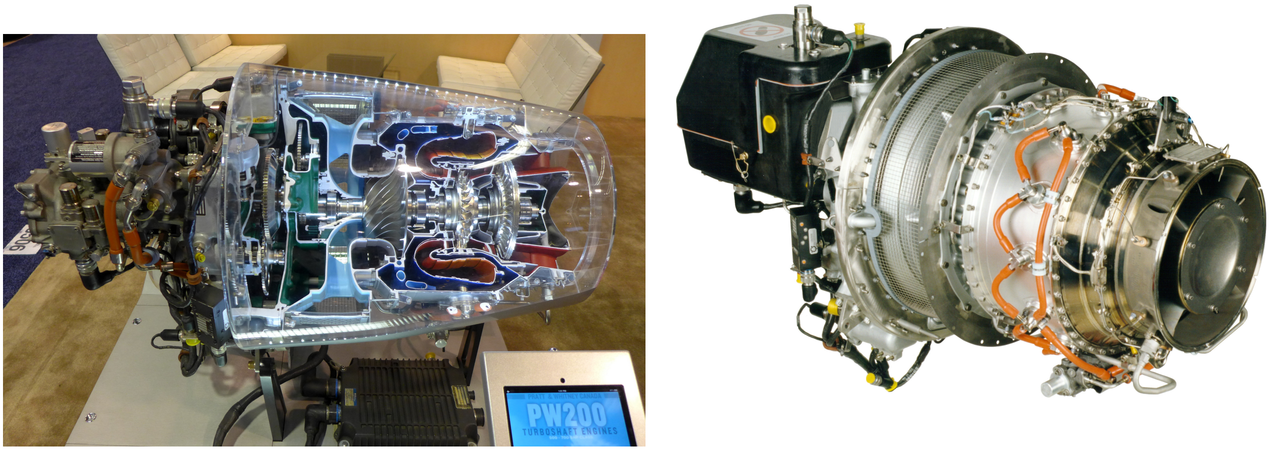

a) **b)**

Figure 2.11: Pratt & Whitney PW200 series engines, a) insight into internal components of engine and b) side view of engine.

2.1.5 Intake Swirl

Besides the steady-state and time dependent total pressure and total temperature distortions, intake swirl can also influence stable engine operation and performance. Hereby, swirl refers to deviations of the local flow directions from the axial direction in the AIP. More specifically, the swirl angle can be defined as the flow angle between the local circumferential velocity component u_C and the axial velocity component U, compare Equation 2.1.

$$\alpha_{swirl} = arctan\left(\frac{u_C}{U}\right) \tag{2.1}$$

Additionally, a swirl coefficient SC_{60} can be defined in analogy with the distortion coefficient DC_{60}. Hereby, as described in Equation 2.2, the highest average circumferential velocities 60 deg sector of the AIP corresponding to the highest average swirl angles $\bar{\alpha}_{swirl,60}$ is divided by the average axial AIP velocity, $\bar{U}_{AIP}$. Furthermore, a mean AIP swirl angle can be defined as $\bar{\alpha}_{swirl}$.

$$SC_{60} = \frac{max(\bar{u}_{c,60})}{\bar{U}_{AIP}} \tag{2.2}$$

Swirl can be classified as described in Ref. [16] in bulk swirl, two types of paired swirl, namely 1/rev paired swirl and 2/rev paired swirl, as well as other swirl types. In Figure 2.12, bulk swirl and the two kinds of paired swirl are depicted.

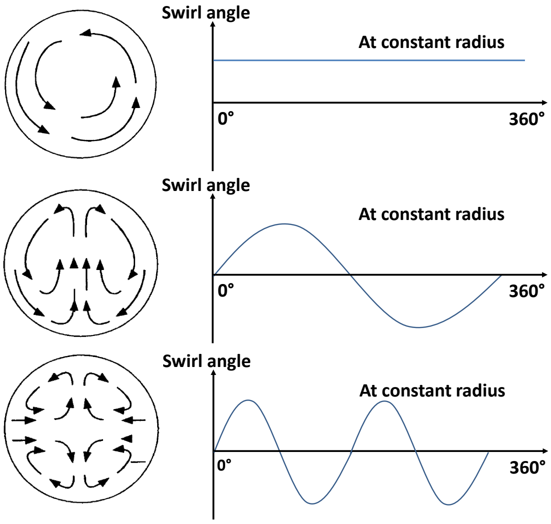

Figure 2.12: Swirl types, Bulk swirl (top), 1/rev paired swirl (middle) and 2/rev paired swirl (bottom), based on Ref. [16].

According to Ref. [16], the paired swirl types occur most commonly, for example in s-duct inlets. If the respective two or four vortices of the 1/rev paired swirl and 2/rev paired swirl types feature the same vorticity magnitude and extent, the resulting mean swirl angle is zero. Locally, three cases can be distinguished related to the local flow angle incidence of the compressor blades. The first is related to co-rotating swirl, which results in a decrease of the local blade incidence angles, whereas in case of counter-rotating swirl increased blade incidence angles are created. The last case of local zero swirl angles originates no change in blade incidence angles. The effect on surge margins due to the corresponding shift of the engine characteristics to lower pressure ratios (co-rotating swirl) or higher pressure-ratios (counter-rotating swirl) has to be evaluated for the specific compressor. In some cases of fighter aircraft, swirl has led to stability issues of the engine especially under high angle of attack flight conditions. For example as described in Ref. [11] for a twin engine fighter aircraft, due to local flow separation, counter-rotating swirl led to reduced surge margins of one engine. For aircraft with inlet guide vanes located upstream of the first compressore stage, swirl is not a significant performance or operability concern. According to Ref. [11], in terms of aircraft performance, a better measure to reduce bulk swirl at the engine entry is the application of upstream positioned fences due to the lower weight.

2.2 Further Performance Parameters

Two major parameters that are commonly used to quantify the influence of the intake on the performance of an aircraft are the intake pressure recovery and the intake related drag. For the second parameter, a detailed book-keeping has to be established for each aircraft, to distinguish between the contribution due to the intake, the airframe and the engine.

2.2.1 Intake Pressure Recovery

One main purpose of engine air intakes is to deliver air to the engine at the highest total pressure level to achieve high engine thrust or shaft power. Reductions of the total pressure along an intake duct can originate from friction losses in the boundary layer, flow separation or shocks. In Ref. [65], two coefficient definitions are presented for the intake's efficiency of the ram compression. One is a pressure recovery coefficient, defined as $\eta_\sigma = (\bar{p}_{t,AIP} - p_\infty)/q_\infty$. The most common definition is the total pressure ratio $\eta = \bar{p}_{t,AIP}/p_{t,\infty}$. Hereby, $p_{t,AIP}$ is the mean AIP total pressure, p_∞ and $p_{t,\infty}$ the static and total pressures of the freestream flow, and q_∞ the dynamic pressure of the freestream flow.

As part of the NACA large-scale wind tunnel tests of intakes for fighter/reconnaissance aircraft of the 1940s, submerged intakes were investigated, Ref. [44]. For such a submerged intake, a parameter study was conducted to assess the influence of approach ramp angles (5 - 9 1/2 deg) as well as different plan forms. The side wall orientation of submerged intakes leads to the distinction of three basic plan form types, see Figure 2.13.

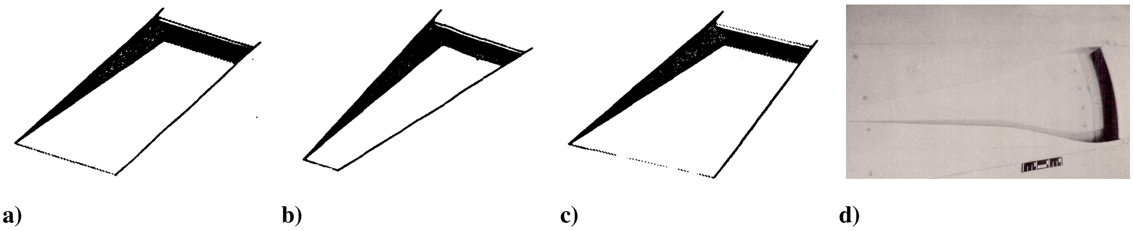

Figure 2.13: NACA inlet planforms, Ref. [63], a) parallel walls, b) divergent walls, c) convergent walls, d) example of 7 deg ramp angle, standard curved divergence.

The flow topologies occuring in the three plan form cases are considerably different. In the parallel side walls case, a 2D diffuser is realized. For attached flow, the static pressure is increased over the ramp until the intake entry face. In case of the divergent walls, at the top edge of each side wall a vortex is created due to the separation of the cowling boundary layer. The vortex axis is situated inboard of the side walls. A beneficial effect of this case is the transport of high energetic fluid from the outer flow to the near wall region due to the vortices. In the convergent side walls case, the two vortices, which are shed from the top edges of the side walls, are located on the cowling wall outboard of the inlet and therefore do not exhibit the same favorable behavior as found in the divergent walls case. In the following, some results of the research of Ref. [44] are summarized. Here, for a submerged intake, a parameter study was experimentally conducted in full-scale to assess the influence of approach ramp angles (5, 7 and 9 1/2 deg) as well as ramp planforms for the 7 *deg* ramp (divergent and parallel). An inlet-velocity-ratio U_{AIP}/U_∞ range of 0.2 to 1.6 was tested for Mach numbers < 0.34. Decreasing the ramp angle had a positive effect for $U_{AIP}/U_\infty > 0.5$ on total pressure recovery, below $U_{AIP}/U_\infty = 0.5$ no clear trend is obtained for the divergent walls case. The parallel planform was beneficial for inlet-velocity-ratios above 0.9, whereas divergent ramps were of advantage at low inlet-velocity ratios.

As depicted in Figure 2.15a, typical helicopter side intakes can be classified with the help of their pressure recovery progression according to Ref. [65]. For this purpose, the pressure recovery η_σ is plotted as a function of the inverse flow ratio $\mu_\sigma = A_I/A_\infty$. Hereby, A_I is the cross section area of the intake entry and A_∞ is the infinite stream tube cross section area of the ingested flow.

According to Ref. [65], the η_σ characteristics of the pitot and the forward facing side intake configurations are similar to their fixed wing counterparts. Globally, the pressure recovery η_σ is reduced with a decrease in freestream velocities ($A_\infty \to \infty$). The pitot type intake delivers best recompression with increased velocities due to the ram effect. Referring to Ref. [65], for plenum chamber type intake configurations a strong dependency exists on its inner geometry. In contrast to the forward facing intake shapes, the sideways facing intake (also static air intake) features its maximum pressure recovery at a relatively low optimum velocity and exhibits an asymptotic behavior towards a static pressure level imposed by the local pressure level on the engine cowling.

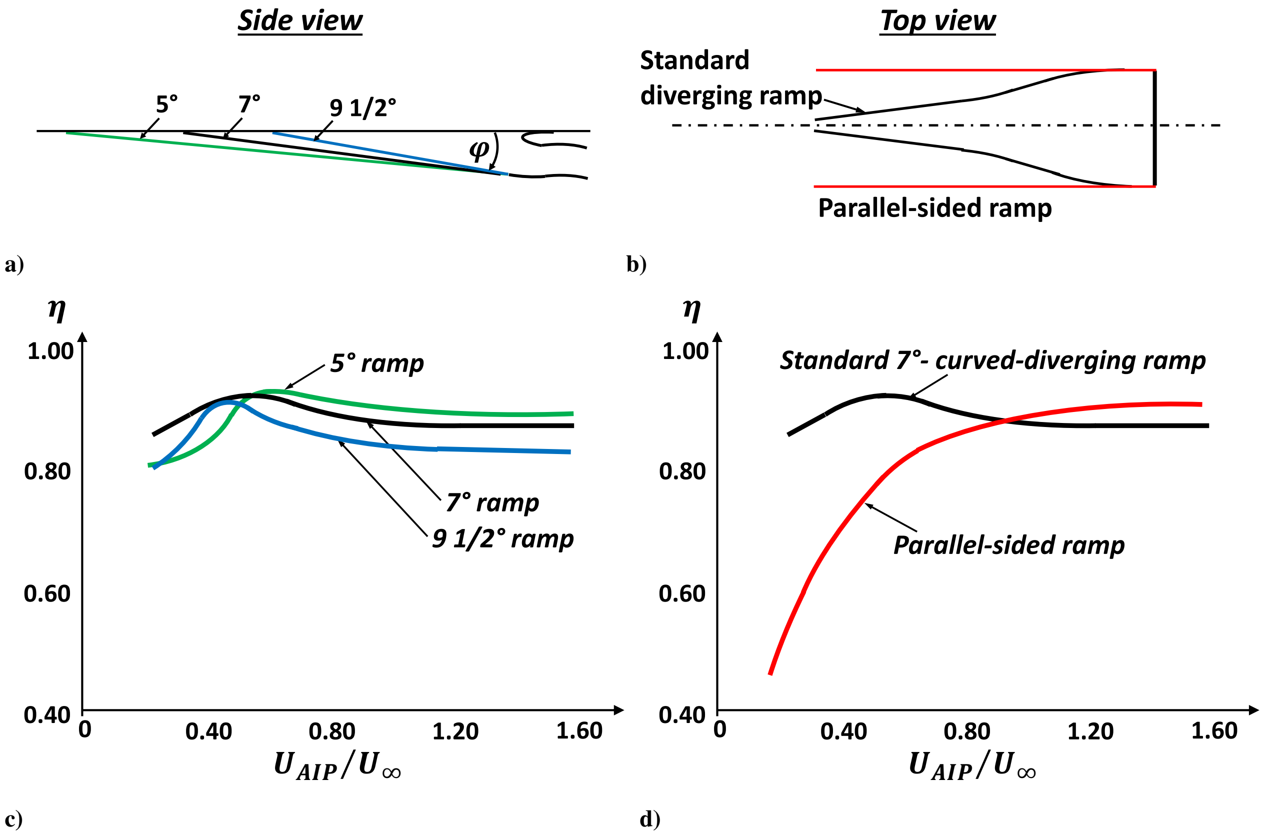

Figure 2.14: NACA inlets, Ref. [44], a) ramp angles, b) planforms, c) η progression for 5, 7 and 9 1/2 deg ramp angles and d) η progression for divergent and parallel planforms.

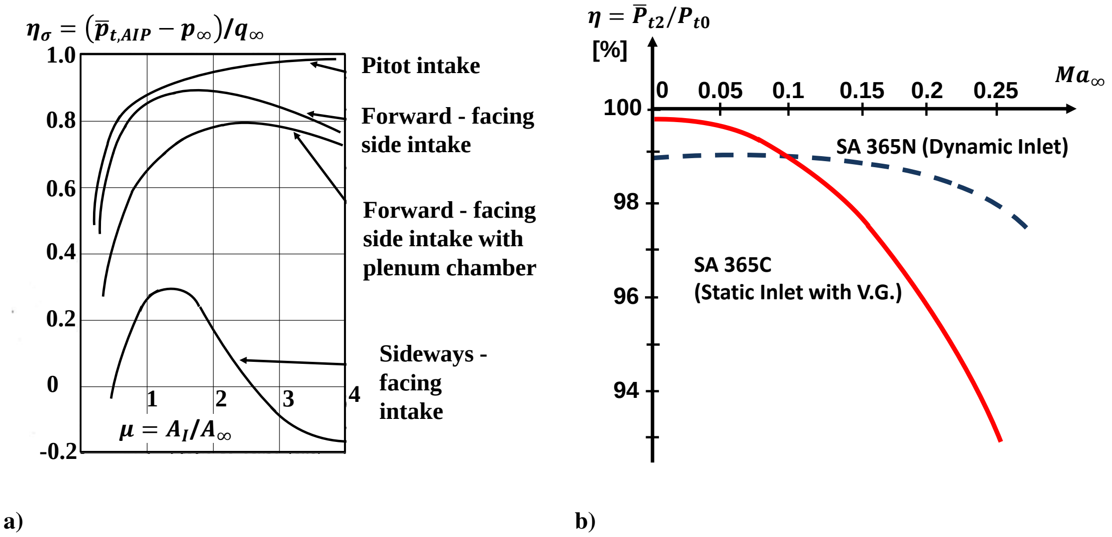

Figure 2.15: a) Typical pressure recoveries of helicopter intakes, based on Ref. [65], b) air intake efficiency, wind tunnel tests, Ref. [61].

2.2.2 Intake Drag

The sources of aerodynamic drag related to engine air intakes are of versatile nature. Due to the flight Mach numbers, intake drag is of higher importance for fixed wing aircraft, operating in the transsonic and supersonic flight speed regime, in contrast to helicopters which mainly operate in the pure subsonic regime. Typical intake drag phenomena of fixed-wing fighter configurations such as shock-induced drag or spillage drag are irrelevant for helicopter configurations incorporating sideways-facing side intakes. In the field of helicopter aerodynamics, depending on the publication, the drag originating from the intake is often classified in the category of "miscellaneous" and rather uncommonly as part of the category "fuselage drag". Hereby, the drag classification is mainly based on the geometric nature of its source. A different way of classifying drag is on the basis of its aerodynamic nature.

For helicopter intakes, amongst others, the following drag components and the corresponding sources exist:

- drag due to geometrical external/internal flow deflection, vortices, engine suction
- spillage drag in case of non-perfect matching of engine mass flow rate, freestream velocity and intake entry area
- drag due to flow separation
- interference drag
- viscous drag due to surface friction

The detail investigation and the distinction of the intake drag origin is out of scope for the current research and cannot be performed for the experimental cases due to lack of flow field and force data. Therefore, in Chapter 7.2.3 only integral drag differences for side intake configurations considering a reference case and distinct improved shapes are compared.

3 Wind-Tunnel Testing

A full scale model has been designed and investigated to fulfill local Mach and Reynolds number similarities simultaneously and to reproduce geometric details such as intake and engine grids in their original shape. The integration of the wind tunnel model is depicted with its subsystems and the adjacent W/T (wind tunnel) components in Figure 3.1. The corresponding components are listed in Table 3.1.

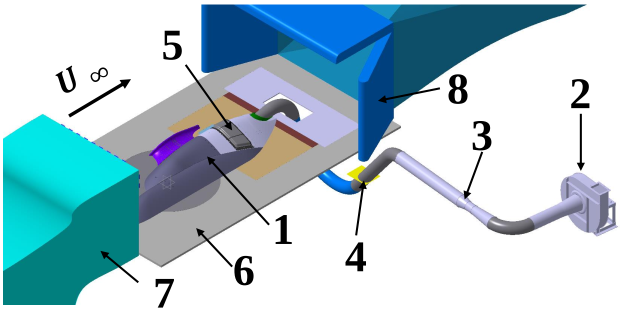

Figure 3.1: Overview of the W/T setup.

1	Fuselage section wind tunnel model
2	Radial fan
3	Venturi meter
4	Duct system
5	Air intake section
6	W/T floor
7	W/T nozzle
8	W/T collector

Table 3.1: Components of the W/T setup, based on Ref. [36].

The W/T model's outer geometry represents a fuselage part model, see front view in Figure 3.2a and top view in Figure 3.2b. The tail section influence on the intake flow topologies is considered to be small. The influence of the main rotor and its downwash in fast level flight are also small for the side part of the fuselage and for the intake section, Ref. [86].

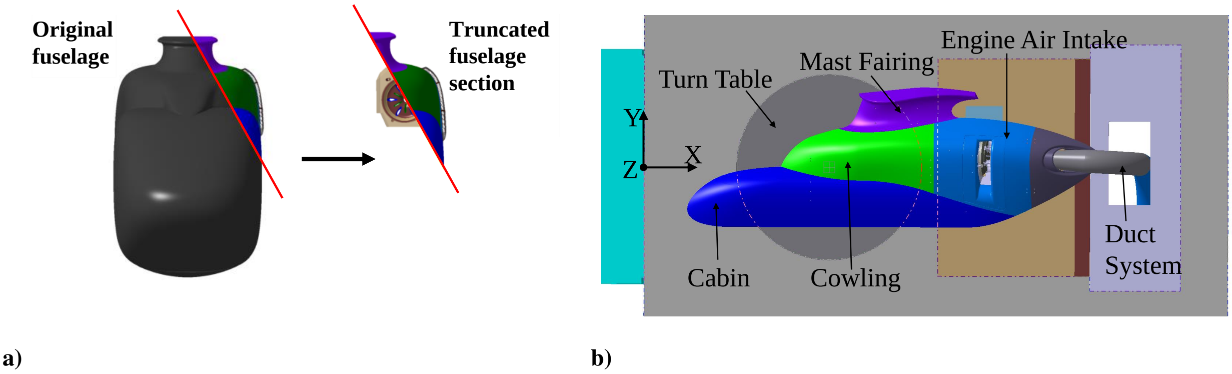

Figure 3.2: a) Truncation of the fuselage in front view, b) outer W/T model components, based on Ref. [36].

The outer geometry is smoothened, i.e., geometric details of the cabin and engine cowling like antennas, rivets, screws etc. are not considered. As proposed in Ref. [53] the blockage in the test section does not exceed a level of 7 – 8% to reduce measurement errors. To meet all spatial restrictions, a truncated

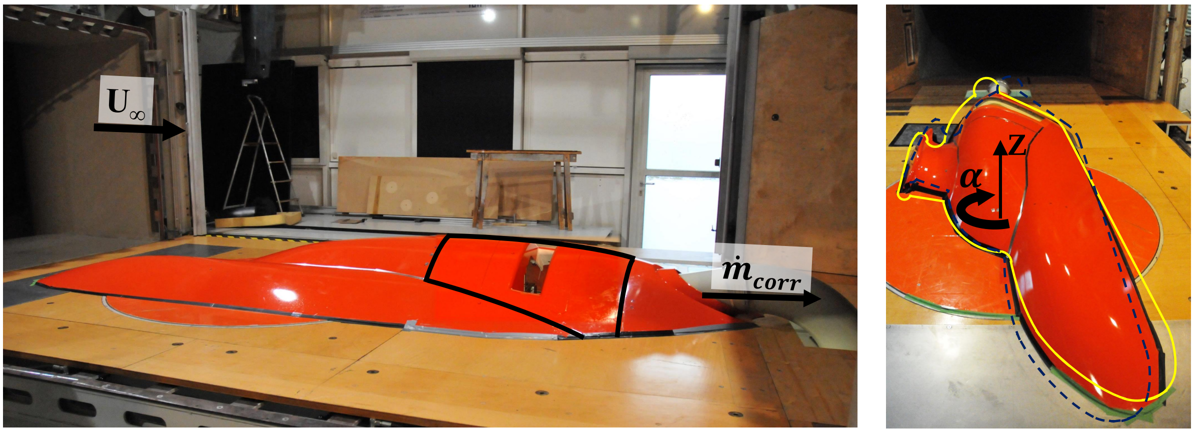

a)

b)

Figure 3.3: a) Wind tunnel model in test section, b) angle of attack adjustment.

section of the fuselage is investigated. The entire section, including all outer and inner components, is mounted on the turn table (cf. Figures. 3.2b and 3.3b) which allows testing the influence of angles of attack between $-5^\circ < \alpha < +5^\circ$ to cover typical fast forward flight operation conditions, Ref. [79]. The truncated fuselage section was derived from a comparison of the complete fuselage surface streamlines to those of the truncated section upstream of the air intake position resulting from numerical simulations, as presented in chapter 5.2. Small differences in flow angles and AIP total pressure distributions motivate the truncation of the fuselage. The experiments are conducted in the subsonic Göttingen-type wind tunnel facility A of TUM-AER, Ref. [59]. The wind tunnel test section measures 1.8 m x 2.4 m x 4.8 m (height x width x length). The maximum velocity in open test section operation is $U_\infty = 65\ m/s$. The freestream turbulence intensity is below 0.4 %. The uncertainty in the mean velocity distribution in time and space is lower than 0.7 %. The uncertainty in free stream direction is less than 0.2° and static pressure variations are less than 0.4 %. The wind tunnel model is depicted in Figure 3.3a.

3.1 Model Design

3.1.1 Outer Components and Chassis

A modular concept of the model components was realized. An alloy chassis was designed as the internal supporting structure for all model components as shown in Figure 3.4. All outer and inner components are connected directly or via connectors to the chassis. The model chassis is attached to the turn-table and the chassis of the wind tunnel underfloor balance which allows for angle adjustment of the complete wind tunnel model. Figure 3.4c illustrates the connection of the outer components to the chassis as well as the chassis' attachment to the turn table.

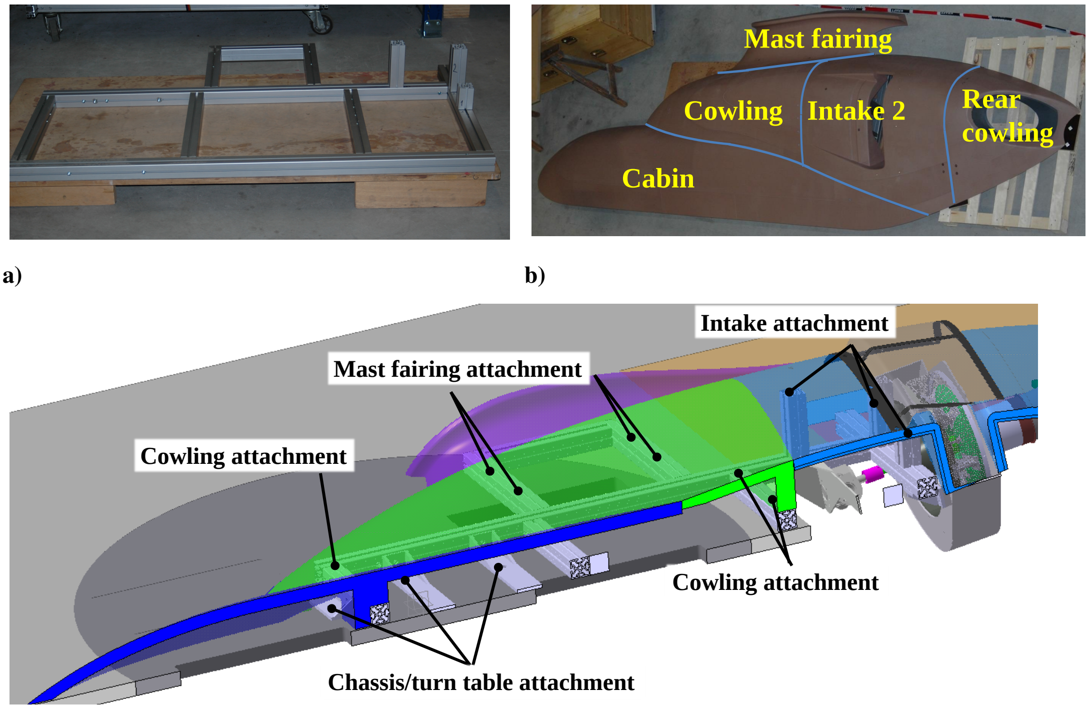
Mast fairing
Cowling
Intake 2
Rear cowling
Cabin
Intake attachment
Mast fairing attachment
Cowling attachment
Cowling attachment
Chassis/turn table attachment

a) b)

c)

Figure 3.4: a) Chassis in side view, b) outer W/T model components and c) CAD display of chassis in W/T model, perspective longitudinal cut view.

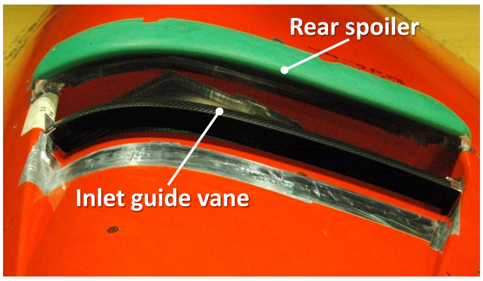
Rear spoiler
Inlet guide vane

Figure 3.5: Intake and retrofit modifications.

For the outer model components, including cabin, cowling, cowling rear, mast fairing and engine air intake, the choice of material was an Ureol model foam. To reduce undesired reflections of light with certain wavelengths when applying PIV for flow field measurements, the outer model surfaces are painted in a special shade of orange. The retrofit rear spoilers (see chapter 3.2) have been milled from model foam material. The intake guide vane was made of carbon fiber reinforced plastic (CFRP) to achieve high stiffness, compare Figure 3.5.

3.1.2 Inner Components

The geometry's inner components, which are connected to the engine air intake and the duct to the downstream positioned AIP, are shown in Figures 3.6 and 3.7. Hereby, the engine plenum chamber is attached to the engine air intake, which embeds the Engine Intake Duct (EID). The EID is a nozzle leading to the AIP. Downstream of the AIP, instead of the compressor, a circular duct is attached which is extruded in the direction of the engine axis in the experimental setup. The inner componentes are connected in such a way that the intake can be removed or mounted easily on the plenum chamber and the chassis while keeping all the inner components fixed. The EID consists of the EID front plate, the EID back plate as well as the inner and outer guide vanes.

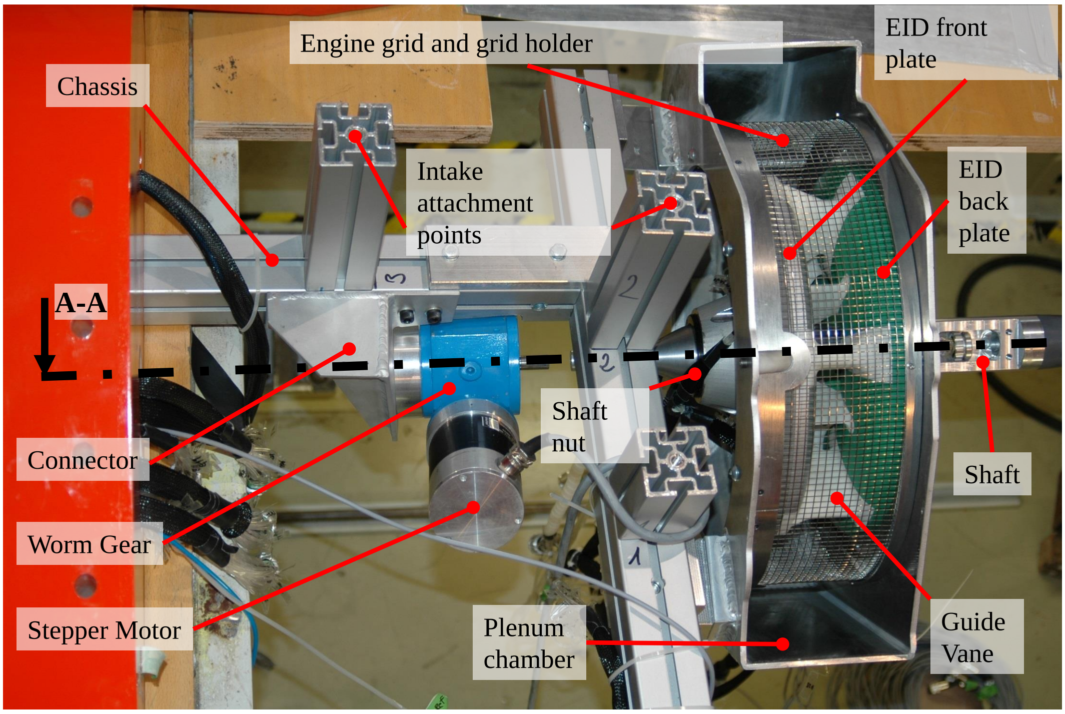
Chassis
Engine grid and grid holder
EID front plate
Intake attachment points
EID back plate
A-A
Connector
Worm Gear
Stepper Motor
Shaft nut
Shaft
Plenum chamber
Guide Vane

Figure 3.6: Inner model components.

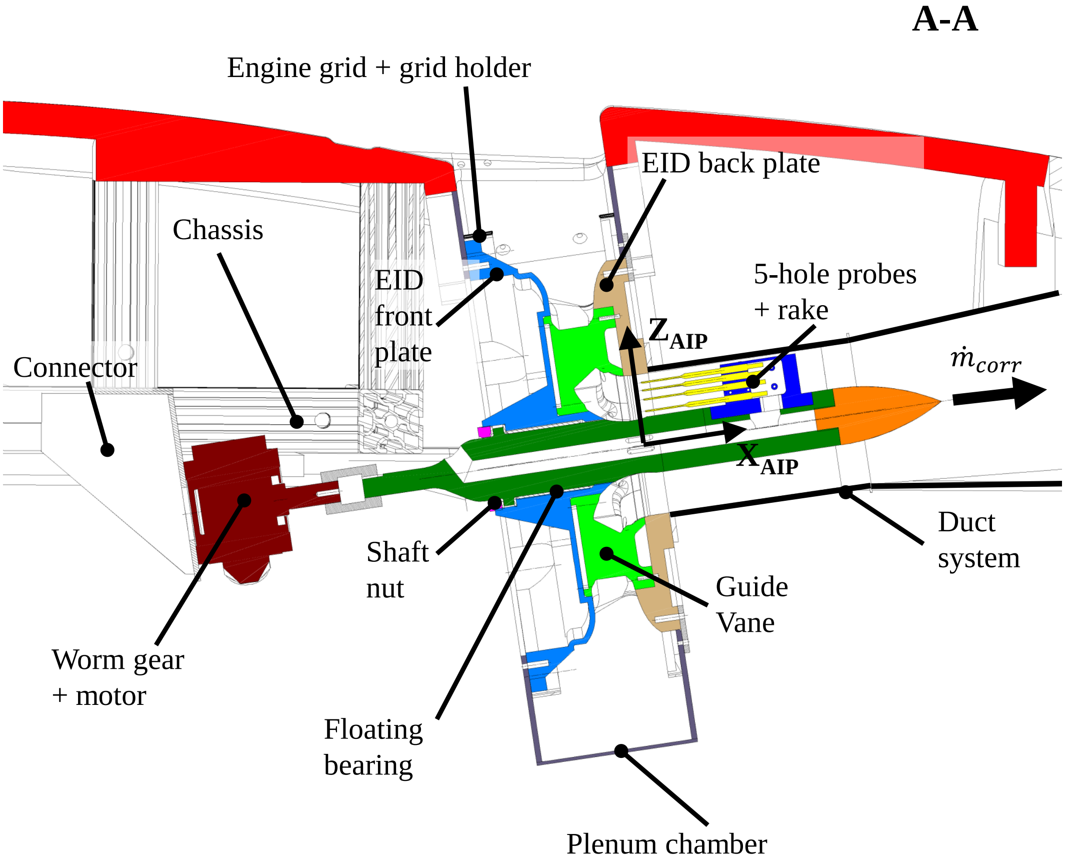
A-A
Engine grid + grid holder
EID back plate
Chassis
EID front plate
5-hole probes + rake
Z_{AIP}
Connector
$\dot{m}_{corr}$
X_{AIP}
Shaft nut
Duct system
Guide Vane
Worm gear + motor
Floating bearing
Plenum chamber

Figure 3.7: Inner model components CAD, cut A-A.

As the traversing system is mounted in the EID front plate, one main requirement for the component is stiffness. In order to cut costs while maintaining a good surface quality especially in the bearing seat region as well as saving weight, aluminum alloy was preferred to a composite structure. For the fixation of each of the six inner and six outer guide vanes, slots have been constructed in the front plates' surface. For further reduction of weight, the wall thickness was decreased to 5 mm. Figures 3.8a and 3.8b display the EID front plate.

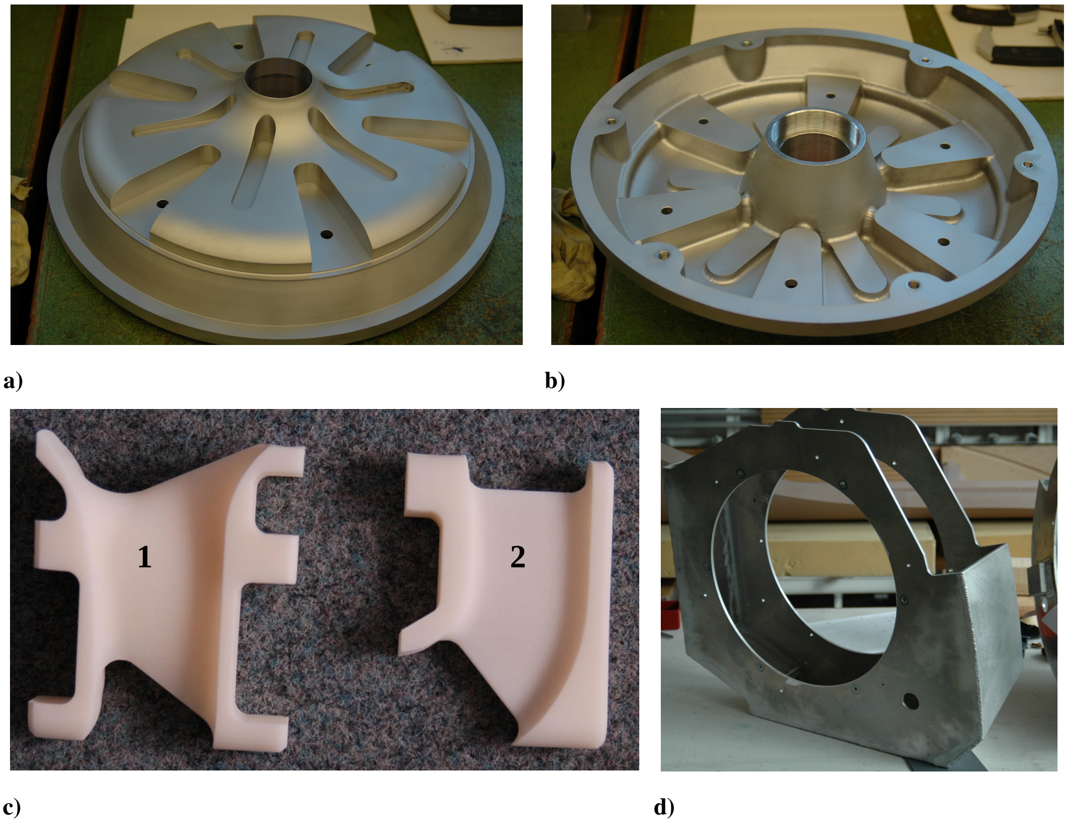

Figure 3.8: a) EID front plate in top view and b) bottom view, c) EID outer (1) and inner (2) guide vanes and d) Plenum Chamber 1 in side view.

The design of the back plate was derived from the front plate design also featuring slots for the inner and outer guide vanes. Because the forces impinging on the shaft are guided through the EID front plate, the requirements on the back plate regarding stiffness are not as high. Therefore, the EID back plate is made of Ureol model foam in order to save weight. The EID guide vanes (cf. Figure 3.8c) were produced as rapid prototyping components which is a better solution compared to machining and precision casting considering the complexity and the overall quantity of the parts. The engine plenum chamber P1 geometry is presented in Figure 3.8d. Taking the requirement of a adequate stiffness, lightweight design together with its rather simple geometry into account, the choice for manufacturing was welding laser-cut aluminum alloy sheet metal with a thickness of 5mm. The edge radii comprised in the surface geometry were added subsequently using a filler material after welding the laser-cut parts.

3.1.3 Circumferential Five-Hole Probe Adjustment System

The main purpose of the five-hole probe adjustment system is the angular adjustment of measurement positions in the AIP (cf. Figure 3.17). The system mainly consists of the components stepper motor, worm gear, shaft, 5-hole probe rake, bearing, shaft nut and shaft coupling. A schematic cut view of the design concept of the system is displayed in Figure 3.9. Figure 3.7 represents the system employed in the W/T measurements.

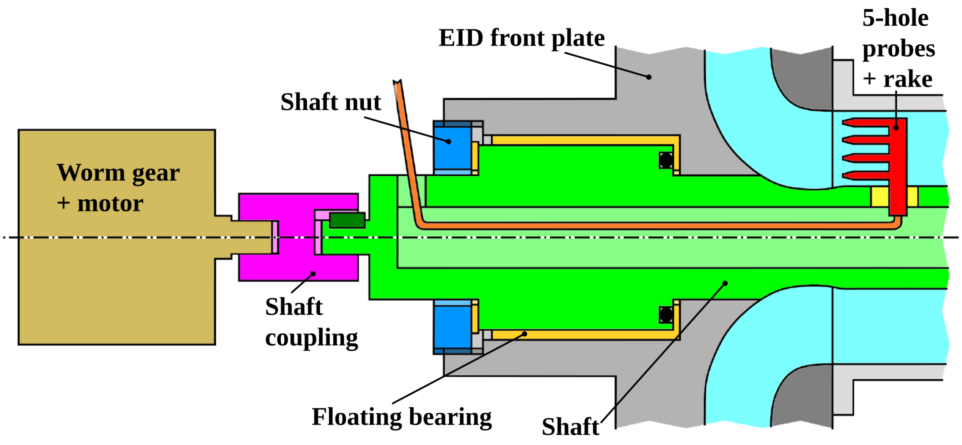

Figure 3.9: Schematic of traversing system.

An important requirement of the system is a high precision of the AIP five-hole probe angle adjustment. The combination of a Phytron RSH 2-phase stepper motor (resolution of 200 steps per revolution) and Zuerrer PSG1 G worm gear (transmission ratio of $i = 58/1$) fulfills the requirement of a high angle adjustment resolution. The motor-gear combination is self-locking due to the use of a worm gear which guarantees measurement at fixed positions. The angular tolerance of the worm gear is 0.13°. A stress analysis was conducted for the shaft and the bearings. The corresponding minimal safety factors were higher than $S_i = 23$. In Figure 3.10 the five-hole probe rake is depicted. The rake shape is derived from a $NACA0021$ profile section, intersecting the shaft. The material choice for the shaft as well as the rake is aluminum alloy.

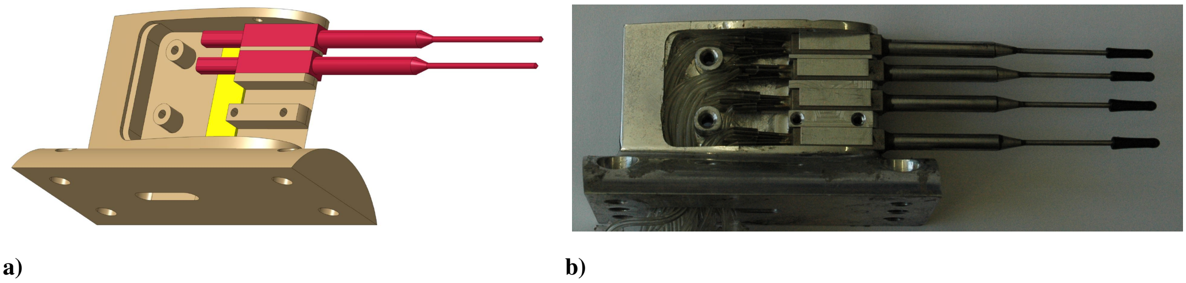

Figure 3.10: a) CAD presentation of measurement rake including five hole probes b) measurement rake including five hole probes.

3.1.4 Duct System, Venturi Meter and Fan

The duct system is integrated in the *W/T A* facility with as little influence on the flow field as possible, as illustrated in Figure 3.1. The model's angle of attack is adjustable between $-5° < \alpha < 5°$ while attached to the radial fan. The system is positioned in the vicinity of the wind tunnel facility and connected to the intake components using a flexible tube element (see Figure 3.11b) to account for the model angle adjustment.

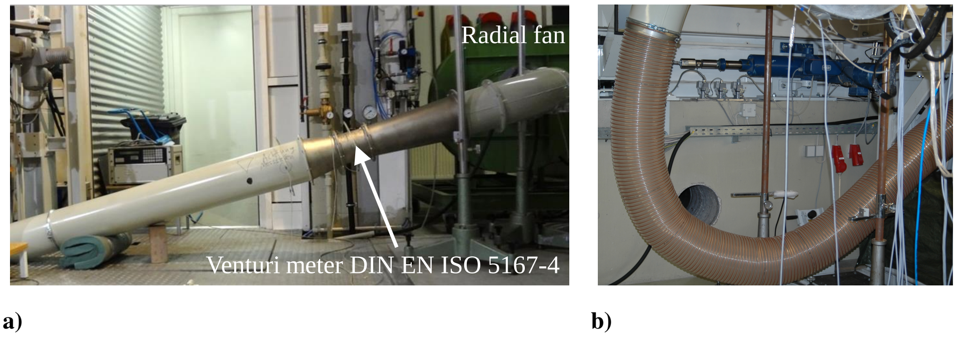

Figure 3.11: a) Radial fan, duct system and Venturi meter, b) flexible tube element.

The design requirements of the system are partly contradictory. The duct geometry is determined iteratively. Hereby, approximate duct total pressure losses are calculated for different combinations of duct diameters, tube lengths, cone angles and bending angles. Only discrete positions in the wind tunnel plenum are realizable thus leading to sets of combinations of the aforementioned parameters. Further parameters are the weight and cost of the duct system and Venturi meter, respectively. A requirement for the flexible tube element is the combination of sufficient flexibility for the angle adjustment while maintaining its shape when strongly decreased static pressures act on the tube's inner wall. For the simulation of engine massflow rates a radial fan of type Euroventilatori APRGc 801 is used.

Figure 3.12: Radial fan.

A maximum volume flow rate of 4 m^3/s can be adjusted and a maximum total pressure gain of 14500 Pa at an ambient temperature of 15 °C can be achieved. The fan creates a pressure suction at its entry face. The duct system is connected at the suction side of the fan and the air exits the fan at its pressure side. The fan compensates total pressure losses due to surface friction and separated flow in the upstream located duct system and intake. The exit section pressure level is equal to the ambient static pressure due to the free jet condition. Before the actual wind tunnel campaigns, the functionality of the complete system including the tube elements, the flexible tube element, Venturi meter and fan were tested, Figure 3.11. Therefore, the total pressure losses of the intakes were assessed using CFD investigations and reproduced by different orifices. The functionality of the Venturi meter was tested, which was designed according to Ref. [25]. The suitability of the fan for the expected total pressure losses could also be proven.

3.2 Geometric Variants

Figure 3.13 gives an overview of the intake geometries tested in the W/T campaigns, Refs. [37, 39]. Each component variant is indicated by a unique combination of component abbreviation letters and variant's number.

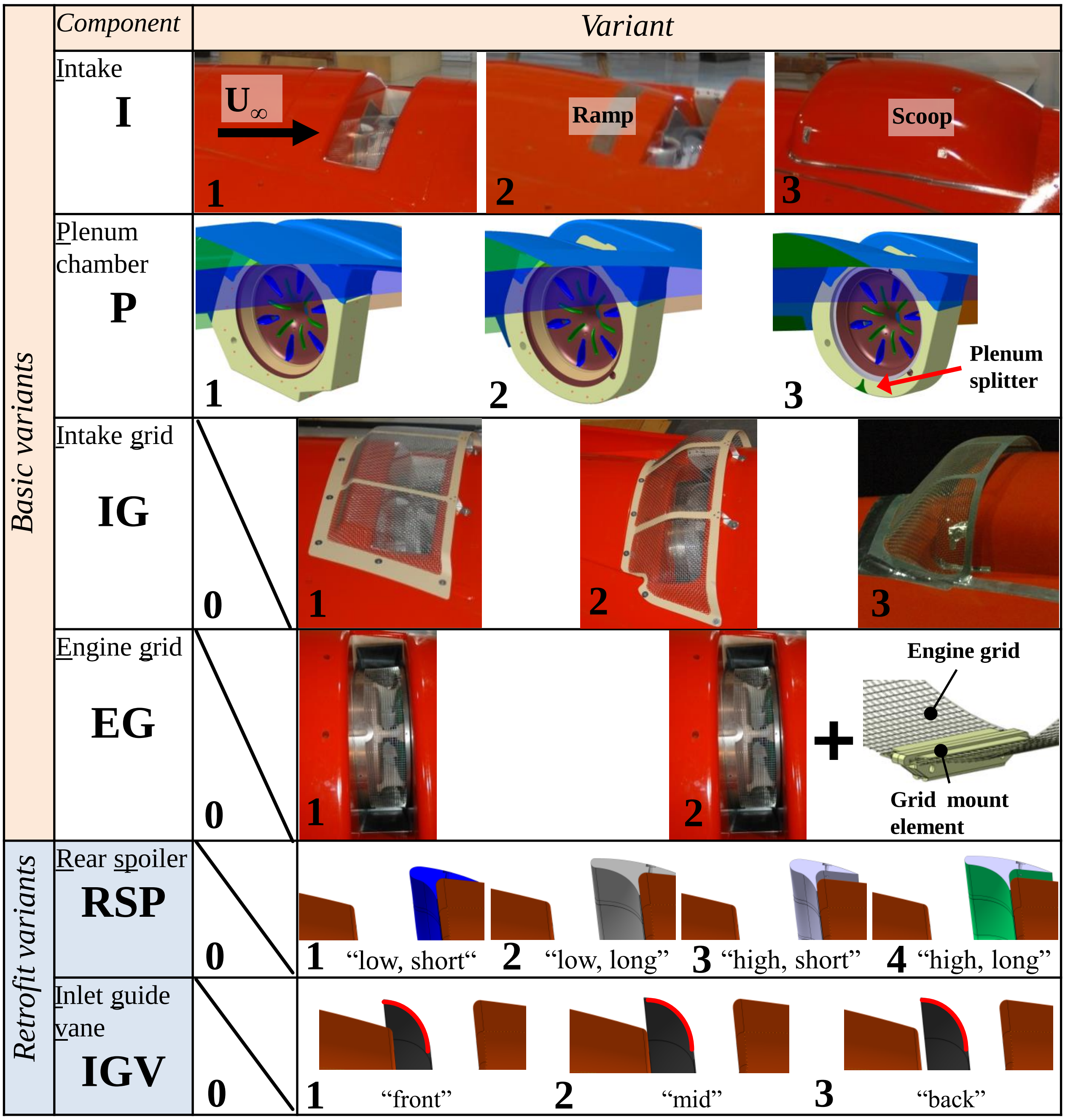
Basic variants
Retrofit variants
Component
Variant
Intake
I
U∞
Ramp
Scoop
1
2
3
Plenum chamber
P
1
2
3
Plenum splitter
Intake grid
IG
0
1
2
3
Engine grid
EG
0
1
2
+
Engine grid
Grid mount element
Rear spoiler
RSP
0
1 "low, short"
2 "low, long"
3 "high, short"
4 "high, long"
Inlet guide vane
IGV
0
1 "front"
2 "mid"
3 "back"

Figure 3.13: Overview of geometric variants.

An example of the nomenclature is as follows: I1 P1 IG1 EG1 RSP0 IGV0. This denotes the configuration of intake variant 1 (I1), plenum chamber 1 (P1), intake and engine grid installed (IG1 EG1), no rear spoiler (RSP0) as well as no intake guide vane (IGV0). Not all geometric combinations are possible. Intake variant 1 (I1) is designed as a static side intake. The intake variant 2 (I2) is designed as a "semi-dynamic" side intake comprising a cowling approach ramp to improve the recovery of dynamic pressure upstream of the intake opening. The third intake variant (I3) features the same cowling geometry of I2 and an additional scoop. All three intakes feature an area contraction from the intake opening to the engine face (AIP). Additionally, two basic engine plenum chamber (EPC) versions are tested. The P2 variant of the EPC is of an overall rounded shape compared to the square-edged P1 version. In addition to the geometries investigated in Ref. [39], some geometrical modifications are applied before testing retrofit geometries. Two foreign object damage grids are attached upstream of the engine entry section to protect the engine. The intake grid is mounted on the cowling, as depicted in Figure 3.13. The cylindrical engine grid is located at the EID entry, as shown in Figure 3.13 (engine grid). Additionally, a so-called "grid mount element" is integrated, which fixates the engine grid as in the real flight configuration. The grid mount element is situated at a AIP angular position of $\theta = 270°$ (compare Figure 3.13 and Figure 3.19b). The first retrofit modification to the basic geometric variants that has been applied is a plenum splitter, mounted at the bottom of the rounded plenum chamber, see Figure 3.13 and Figure 3.14.

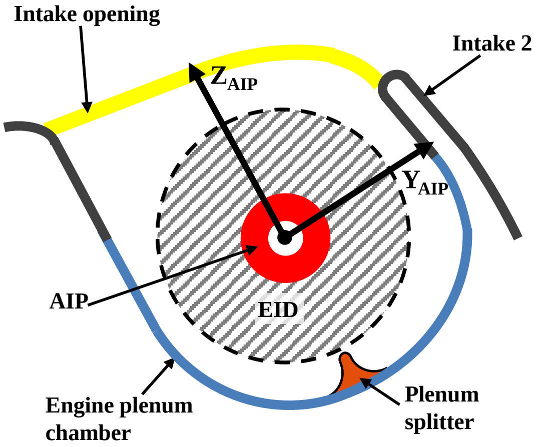

Figure 3.14: Schematic cut view of intake 2 in upstream perspective, inner components: EPC, EID, AIP and plenum splitter.

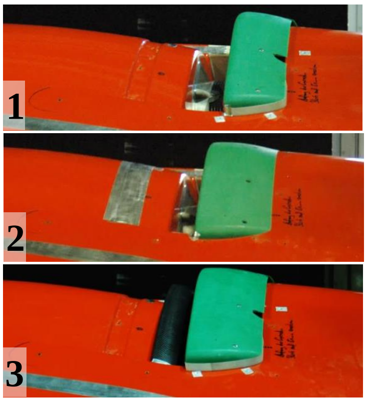

Figure 3.15: Examples of retrofit modifications:
1) high and short rear spoiler,
2) low and long rear spoiler,
3) high and long rear spoiler, front intake guide vane.

Thus, the plenum chamber variant P2 combined with the splitter results in the plenum chamber variant P3. The splitter's main purpose is to guide the air flow and deflect it from a circumferential to a radial direction. Different positions and heights have been tested. The most effective plenum splitter featuring the highest total pressures in the AIP is considered in the present work. The W/T data evaluation and analysis as part of Ref. [39] indicate that the I2 and I3 intake variant are superior to the I1 at different operation points. Therefore, a composition of both configurations is desired to cover all helicopter operation conditions. For this purpose, further retrofit variants, namely a rear spoiler (small scoop), intake guide vane and combinations of both are investigated. Some examples of the tested retrofit modifications are presented in Figure 3.15. The main results of the investigations of the retrofit modifications are presented in Chapter 6.4.

3.3 Measurement Techniques and Instrumentation

3.3.1 Massflow Measurement

Engine mass flow rates have a significant impact on the flow field upstream of the AIP. Therefore, realistic mass flow rates corresponding to flight operation conditions are reproduced in the wind tunnel measurements. To accomplish similarity of the Mach number for the W/T results with respect to inflight conditions, independent of ambient conditions due to flight altitude and weather, Ref. [18], the corrected mass flow rate $\dot{m}_{corr}$ is applied as defined in Equation (3.1).

$$\dot{m}_{corr} = \dot{m}\sqrt{\frac{T_t}{T_{ISA}}\frac{p_{ISA}}{p_t}} \tag{3.1}$$

Herein, $T_{ISA} = 288.15\ K$ and $p_{ISA} = 101325\ Pa$ are the ISA ambient conditions at sea level. For the representation of ambient flight conditions, the total temperature T_t and the total pressure p_t are measured at the wind tunnel nozzle exit. In Figure 3.16a, the mass flow rates are presented which are investigated in the W/T campaigns. The mass flow rates 1-3 are corresponding to different inflight power requirements, whereas mass flow rate 4 is a constant maximum mass flow rate.

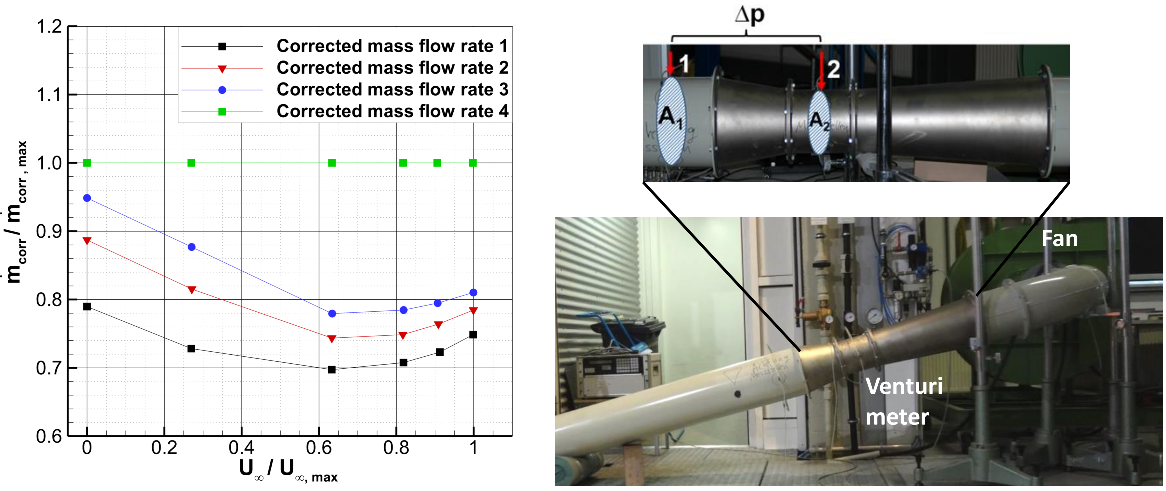

a) **b)**

Figure 3.16: a) Specified mass flow rate $\dot{m}_{corr}/\dot{m}_{corr,max}$ as a function of the specified relative freestream velocity $U_\infty/U_{\infty,max}$, Ref. [39], b) Venturi meter installation.

The mass flow rates are measured in accordance with Ref. [25] applying Equations 3.2 and 3.3.

$$\dot{m} = \frac{C}{\sqrt{1-\beta^4}}\varepsilon\frac{\pi}{4}d^2\sqrt{2\Delta p\rho} \tag{3.2}$$

$$\varepsilon = \sqrt{\left(\frac{\kappa\tau^{\frac{2}{\kappa}}}{\kappa-1}\right)\left(\frac{1-\beta^4}{1-\beta^4\tau^{\frac{2}{\kappa}}}\right)\left(\frac{1-\tau^{\frac{\kappa-1}{\kappa}}}{1-\tau}\right)} \tag{3.3}$$

Herein, Δp is the pressure difference which mainly results from the cross section contraction from A_1 to A_2 as depicted in 3.16b. The contraction ratio is $\beta = A_2/A_1$ and d is defined as $d = \sqrt{4A_2/\pi}$. Furthermore, the corresponding pressure ratio is $\tau = p_2/p_1$. The compressibility of the air is accounted for by the use of the expansion parameter ε. The flow parameter C reflects total pressure losses which arise between section 1 and 2. According to Ref. [25], for the applied Venturi meter and testing conditions, the parameter can be approximated as $C \approx 0.985$. The uncertainty in the measured mass flow rates is $|\dot{m}_{err}|/\dot{m} \leq 0.015$ for all measurements.

3.3.2 Aerodynamic Interface Plane Measurement

Four 5-hole pressure probes are employed to measure the total pressures and the three velocity components in the AIP. Consequently, based on this data, aerodynamic engine installation parameters, such as total pressure losses, pressure distortion and swirl are determined.

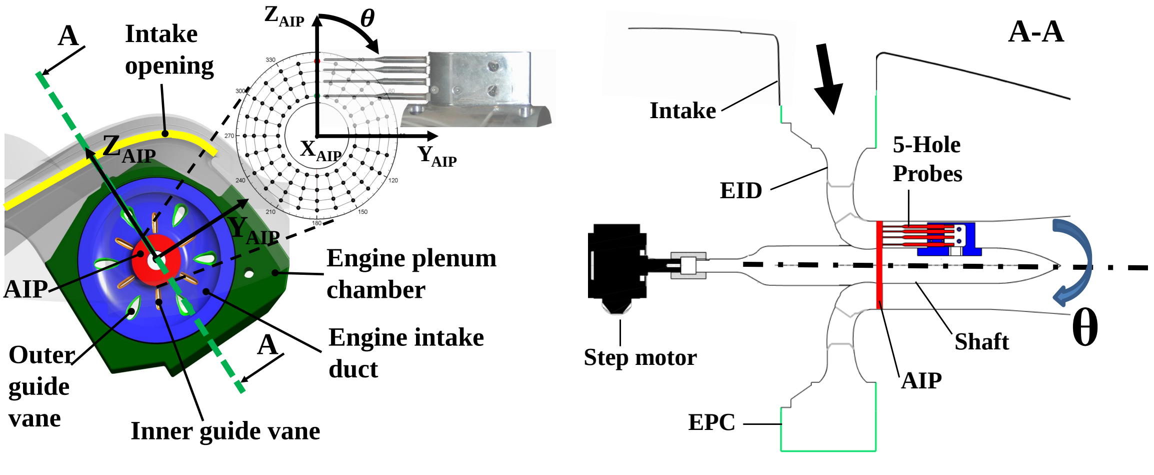

a) b)

Figure 3.17: a) Upstream view in Y_{AIP} - Z_{AIP} plane, Ref. [38], b) cut view A-A in Y_{AIP} - Z_{AIP} plane of inner components: EPC, EID, outer guide vanes in EID, inner guide vanes and AIP, schematic overview of 5-hole-probe measurement locations in the AIP, circumferentially adjustable rake comprising four 5-hole probes.

The circumferential and radial distribution of the 5-hole probe AIP measurement locations is depicted in Figure 3.17a. The AIP X-axis and the engine axis are collinear. The AIP Z-axis points at the outer guide vane, which is situated in the middle of the intake opening. The AIP Y-axis generates a right-hand system with the AIP X- and Z- axes. AIP θ angles are defined as positive in clockwise direction. Electronic pressure scanning modules of type Scanivalve ZOC17 are applied for data acquisition. The system's measurement accuracy is $\Delta p \approx \pm 0.001p$. Hereby, p is the pressure measured with a single 5-hole probe port.

3.3.2.1 Five-Hole Probe Measurement

Multi-hole probes are flow instruments that measure pressure along pressure ports situated on the probe tip. With prior calibration, from the measured pressures, static and dynamic pressures as well as the three components of the fluid velocity can be calculated at a measurement location. An advantage of multi-hole probe measurement compared to Hot-Wire Anemometry (HWA) is its robustness.Thus, it can be employed in harsh environments like high temperature conditions. In the following, five-hole probes with a conical tip shape are used.

The basic principle of 5-hole probe measurements is the calibrated relation of pressures, measured at five ports located at the tip of the probe, to the local flow direction and velocity magnitude. In Refs. [35, 49], the calculation method for obtaining the three velocity components as well as the total pressure based on the five pressures of a 5-hole pressure probe is explained. Subsequently, only a brief summary of the procedure is presented. Figure 3.18a depicts a 5-hole pressure probe in front view including the corresponding pressure ports.

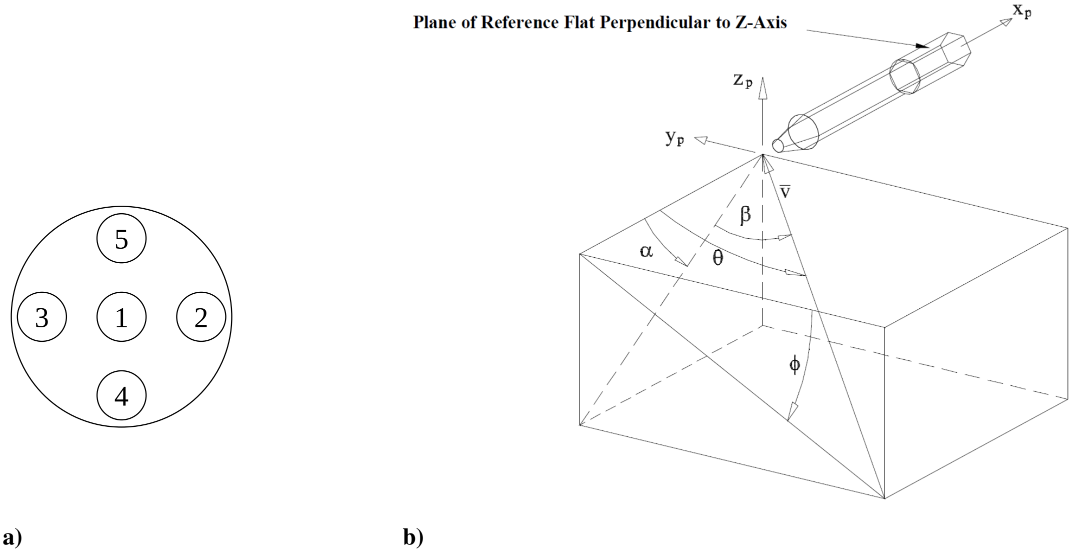

a) **b)**

Figure 3.18: a) Example of five-hole probe pressure port designation, b) five-hole probe coordinates and angle definitions based on Refs. [2, 74].

Five-hole probes are calibrated for the subsonic and supersonic flow regimes. For subsonic measurement conditions typically four coefficients are defined which are determined in each probes' calibration. The coefficients c_α and c_β are related to the pitch and yaw angle (α and β) of the flow in reference to the probe and the coefficients c_p as well as c_{pt} correspond to the static and total pressures (p and p_t). Various definitions exist for the coefficients which are calculated from the five pressures. In Equation 3.4, the coefficient definition based on Ref. [26] is presented for the port designation as depicted in Figure 3.18a.

$$c_\alpha = \frac{p_4 - p_5}{p_1 - p_m}, \qquad c_\beta = \frac{p_2 - p_3}{p_1 - p_m}, \qquad c_p = \frac{p_m - p_s}{p_1 - p_m}, \qquad c_{pt} = \frac{p_1 - p_t}{p_1 - p_m},$$
$$P_m = \frac{p_2 + p_3 + p_4 + p_5}{4} \tag{3.4}$$

Herein, the denominator of c_α, c_β, c_p as well as c_{pt} can be interpreted as a pseudo-dynamic pressure. To take compressibility and viscous effects into account, probes are calibrated over a range of Ma and Re numbers. In the course of the calibration, for each Ma number several hundred combinations of angles of pitch and yaw are adjusted and the port pressures recorded. Hereafter, all coefficient values are computed. Based on the calibration maps for c_α, c_β, c_p as well as c_{pt} of each Ma number, the angles of pitch and yaw as well as static and total pressures can be approximated, for an arbitrary combination of port pressures. Hereby, different techniques can be employed. Either global polynomial curve fits are calculated for the reduction procedure based on the data from entire calibration maps or sectional polynomial curve fits of a calibration map are applied, Ref. [54]. A local least-squares technique was presented by Ref. [35] which only takes into account the calibration points closest to the test point. To further increase prediction accuracy, measurement data can be reduced applying calibration maps of different Ma numbers followed by an interpolation of the results. For the applied 5-hole probes, the angle measurement accuracy of a single 5-hole probe is specified as $|\alpha_{err}| \leq 0.5°$ and the accuracy of the velocities is specified as $|u_{err}|/u \leq 0.01$, Ref [2]. Even if probe interference with the flow field is in principle calibrated out for the flow in freestream conditions, interaction cannot be entirely avoided in practical applications. Hereby, the tip dimensions and the local spatial variations of the flow have to be considered. Positioning of the 5-hole probes can strongly influence the measured pressures and thus originate deviations in measurement results. Especially, measuring close to solid walls should be avoided. Therefore, in the W/T experiments as part of this research, the smallest distance of the 5-hole probes to the AIP walls is $d_{Wall} \geq 3.5 \cdot d_{probetip}$. The same applies for the distance among the four probes. Extrapolating the results achieved in Ref. [71], this results in maximal induced measured local angles of attack of $|\alpha_i| \leq 0.7°$.

3.3.2.2 Aerodynamic Interface Plane Coefficients

Three coefficients are defined for the evaluation of the aerodynamic characteristics of the intakes depending on the engine operation conditions. A normalized total pressure ratio $\bar{\eta}_{norm}$ is defined, based on Ref. [65], to asses each intake's efficiency of the ram compression, Equation (3.5). Therefore, total pressure ratios $\eta = p_{t,AIP}/p_{t,\infty}$ are normalized using the total pressure ratio η_{Ref}. For the evaluation of the engine inflow conditions, the mean value $\bar{\eta}_{norm}$ of all $N = 96$ AIP measurement positions is calculated, cf. Figure 3.17a.

$$\begin{aligned}
&\eta_{norm} = \frac{\eta}{\eta_{Ref}}, \quad \bar{\eta}_{norm} = \frac{1}{N}\sum_{i=1}^{N}\eta_{norm}, \\
&\eta_{Ref} = \eta\left(BSL1,\ engine\ grid,\ \frac{U_\infty}{U_{\infty,max}} = 0,\ \frac{\dot{m}_{corr}}{\dot{m}_{corr,max}} = 0.79\right)
\end{aligned} \tag{3.5}$$

Hereby, $p_{t,AIP}$ is the mean total pressure in the AIP, whereas $p_{t,\infty}$ is the total pressure at the wind tunnel nozzle exit. Total pressure distortion in the AIP is an indicator for stable engine operation, see Ref. [17]. To assess the non-uniformity of the total pressure distribution in the AIP, the total pressure distortion is evaluated applying the DC_{60} coefficient, see chapter 2.1. The distortion parameter DC_{60} is further normalized using $DC_{60,Ref}$.

$$\begin{aligned}
&DC_{60,norm} = \frac{DC_{60}}{DC_{60,Ref}}, \\
&DC_{60,Ref} = DC_{60}\left(BSL1,\ engine\ grid,\ \frac{U_\infty}{U_{\infty,max}} = 0,\ \frac{\dot{m}_{corr}}{\dot{m}_{corr,max}} = 0.79\right)
\end{aligned} \tag{3.6}$$

For the evaluation of the flow angularity in the AIP, the normalized swirl coefficient S_{norm} is defined. Therefore, the mean AIP swirl angle $\bar{\alpha}_{swirl}$ of all 96 AIP measurement locations is divided by the reference mean swirl angle $\bar{\alpha}_{swirl,Ref}$, see Equation 3.7.

$$\begin{aligned}
&S_{norm} = \frac{\bar{\alpha}_{swirl}}{\bar{\alpha}_{swirl,Ref}}, \\
&\bar{\alpha}_{swirl,Ref} = \bar{\alpha}_{swirl}\left(BSL1,\ engine\ grid,\ \frac{U_\infty}{U_{\infty,max}} = 0,\ \frac{\dot{m}_{corr}}{\dot{m}_{corr,max}} = 0.79\right)
\end{aligned} \tag{3.7}$$

3.3.3 Surface Pressure Measurement

In the wind tunnel experiment, static surface pressure measurements at a total of 192 positions are conducted, of which twelve positions provide information about transient pressures. For the data acquisition, electronic pressure scanning modules of type Scanivalve ZOC33 are used. The measurement accuracy of the system is $|c_{p,err}| \leq 0.01$. In the following analyses, only mean surface pressure distributions are evaluated. For this purpose, pressure taps are located in eight lines along the surface of the outer geometry, as depicted in Figure 3.19a. Further pressure taps are situated on nine lines along the surface of the inner parts of the geometry, see Figure 3.19b. Line 9 is located in the mid-plane of the engine plenum chamber. For each of the circumferential positions $\theta = 45°, 135°, 225°$, and $288°$, two lines are positioned, one on the EID front side and one on the EID back side.

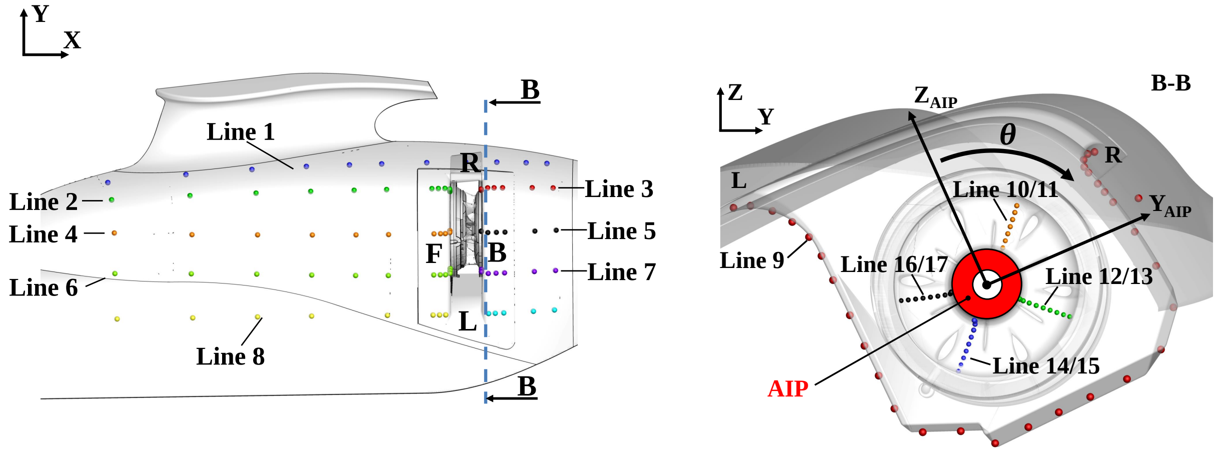

a) **b)**

Figure 3.19: a) top view of pressure tap positions on the outer geometry of BSL 1, b) cut view B-B in Y_{AIP} - Z_{AIP} plane, pressure tap positions on the inner geometry of BSL 1.

For a clear distinction between the four intake lips, in the following they are named as front (F), back (B), left (L) and right (R) intake lips as depicted in Figure 3.19a and 3.19b. A local curve length coordinate S is defined for each line of pressure measurement locations. The coordinate S ranges from 0 to 1 and is orientated along the surface in mainstream direction. For line 9, the curve length coordinate as well as the circumferential angle θ in the AIP is used, see Figure 3.19b. Due to the intake opening, θ ranges from 54° to 324° and S_9 from 0.15 to 0.9, respectively.

Exemplarily, longitudinal sections through the model at lines 2 and 3 are shown in Figure 3.20 (black for intake variant 1, red for intake variant 2), together with the corresponding coordinate S for the surface pressure tap locations (dots).

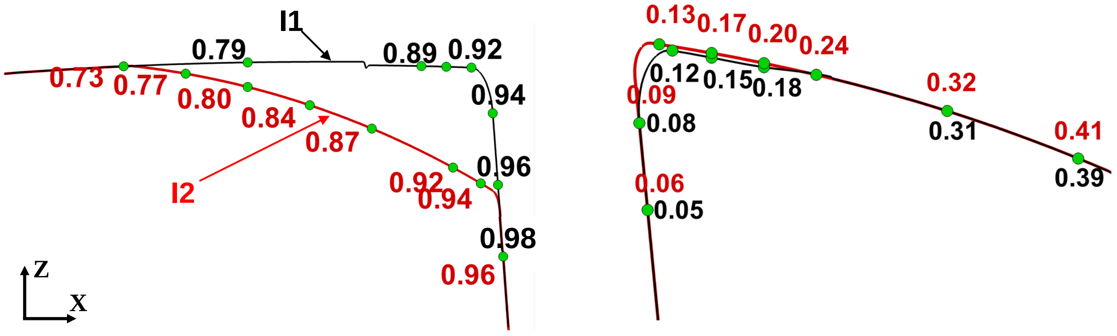
I1
0.79
0.89
0.92
0.94
0.96
0.98
0.73
0.77
0.80
0.84
0.87
I2
0.92
0.94
0.96
Z
X
0.13
0.17
0.20
0.24
0.12
0.15
0.18
0.09
0.08
0.06
0.05
0.32
0.31
0.41
0.39

a) b)

Figure 3.20: a) Local curve length coordinate S_2 for line 2 of I1 and I2, b) Local curve length coordinate S3 for line 3 of I1 and I2.

Surface pressure distributions of the pressure coefficient c_p are plotted along the local curve length coordinate S in chapters 5 and 6. For the definition of c_p, the freestream dynamic pressure $q_\infty = 0.5 \cdot \rho_\infty \cdot U_\infty^2$ is applied which is acquired with a Prandtl probe at the wind tunnel nozzle exit.

3.3.4 Stereo Particle Image Velocimetry

Stereo PIV measurements were performed to generate flow field data sets in two cross-flow sections upstream of the intake opening, Ref. Figure 3.21. The laser light sheets were generated using a double−pulse Nd:Yag laser with a wave length of $\psi = 532\ nm$. The employed laser sheet optic, incorporating a cylindrical lens, converts the laser beam to a sheet. Up- and downstream of the laser sheet optics, two high-speed sCMOS cameras with a resolution of 2560 × 2160 pixels were placed incorporating NIKON lenses with a focal length of $F = 135\ mm$. The use of two cameras enables instantaneous measurements of the three velocity components in the measurement plane. Scheimpflug adapters were mounted between the sCMOS sensor plane and the lens to render sharply the entire measurement plane. The grid spacing of each plane is $\Delta d = 3.4 - 3.7\ mm$. For a reduction of reflections, the model surface was covered with an orange laminate. For each measurement point, 400 samples were recorded at a sampling frequency of 13 Hz. The maximum velocity uncertainty estimate is $|u_{err}/U_\infty| = |v_{err}/U_\infty| = |w_{err}/U_\infty| \leq 0.02$, Ref. [34].

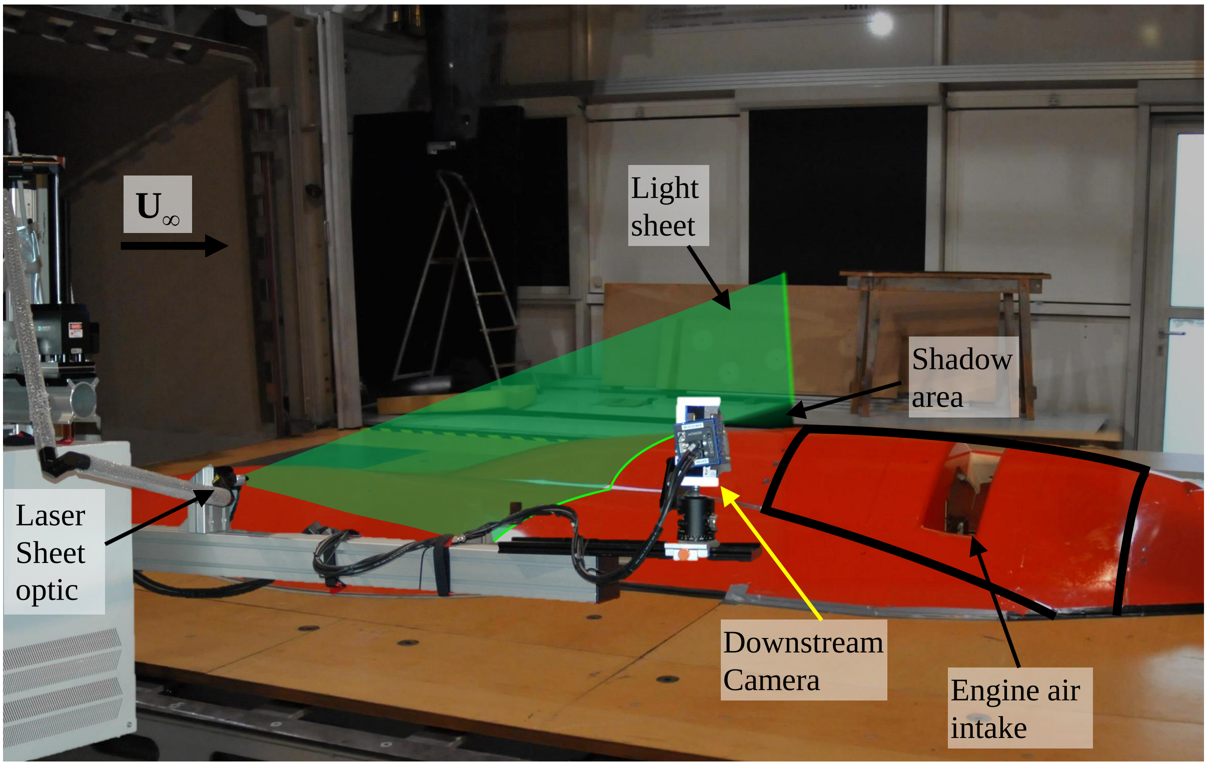

Figure 3.21: Side view of PIV setup, schematic display of laser sheet optic, downstream camera, light scheet and wind tunnel model.

4 Numerical Simulations

For the numerical investigations, two approaches are chosen to evaluate the effect of the boundary layer and local flow directions upstream of the intake entry. The geometry of the first numerical case is identical to that of the W/T setup, see Figure 3.1, Figure 3.2 and Figure 3.3. The essential parts of the W/T geometry are included. The radial fan, Venturi meter, and the parts of the duct system, which are situated outside of the wind tunnel test section, are not included in the numerical setup due to their negligible influence on the intake flow field. In the following the corresponding numerical case will be referred to as the sectional fuselage case (SF). The second approach refers to a real flight case incorporating one symmetric half of the entire helicopter fuselage without any wind tunnel parts. In the following it will be referred to as the full fuselage case (FF). The subsequent Sections 4.1, 4.2 and 4.3 are based on Ref. [40] and Ref. [38].

4.1 Numerical Setup

In Figure 4.1a and Figure 4.1b, the boundary conditions of the numerical simulation cases are presented. In the sectional fuselage case, the wind tunnel parts nozzle, collector blades and diffuser are exactly reproduced. The diffuser end section is prolongated to minimize interactions of the outlet boundary condition with the flow field of the intake. For the same purpose, a circular tube is attached to the AIP in the numerical simulations, compare Figure 4.6b. The mass flow rate boundary condition is set at the end of this tube. Hereby, the corrected engine mass flow rate of the W/T tests is simulated. A mass flow boundary condition is set on the inlet to reproduce the nozzle outflow velocity, measured with a Prandtl probe in the wind tunnel experiments. The Reynolds number based on the freestream velocity U_∞, reference length l_I and kinematic viscosity ν, is $Re = U_\infty \cdot l_I / \nu = 3.2 \cdot 10^6$. Additionally, for the static temperature a value of 306.26 K is adjusted, as measured close to the Prandtl probe position in the wind tunnel experiments. Also at the outlet of the domain, a mass flow boundary condition is set. For the outlet boundary condition, the difference of the inlet and engine mass flow rate is adjusted for the purpose of continuity in the entire domain. The part of the domain "Outer W/T region" is incorporated to simulate the surrounding ambient air outside of the wind tunnel test section. For the side and top surfaces of the outer W/T region a no slip wall boundary condition is chosen. The static ambient pressure of 96704 Pa which was obtained in the W/T test was defined as the reference pressure. The floor of the wind tunnel test section is modeled as a smooth wall. Identical to the W/T experiments, no gap exists between the model and the wind tunnel floor.

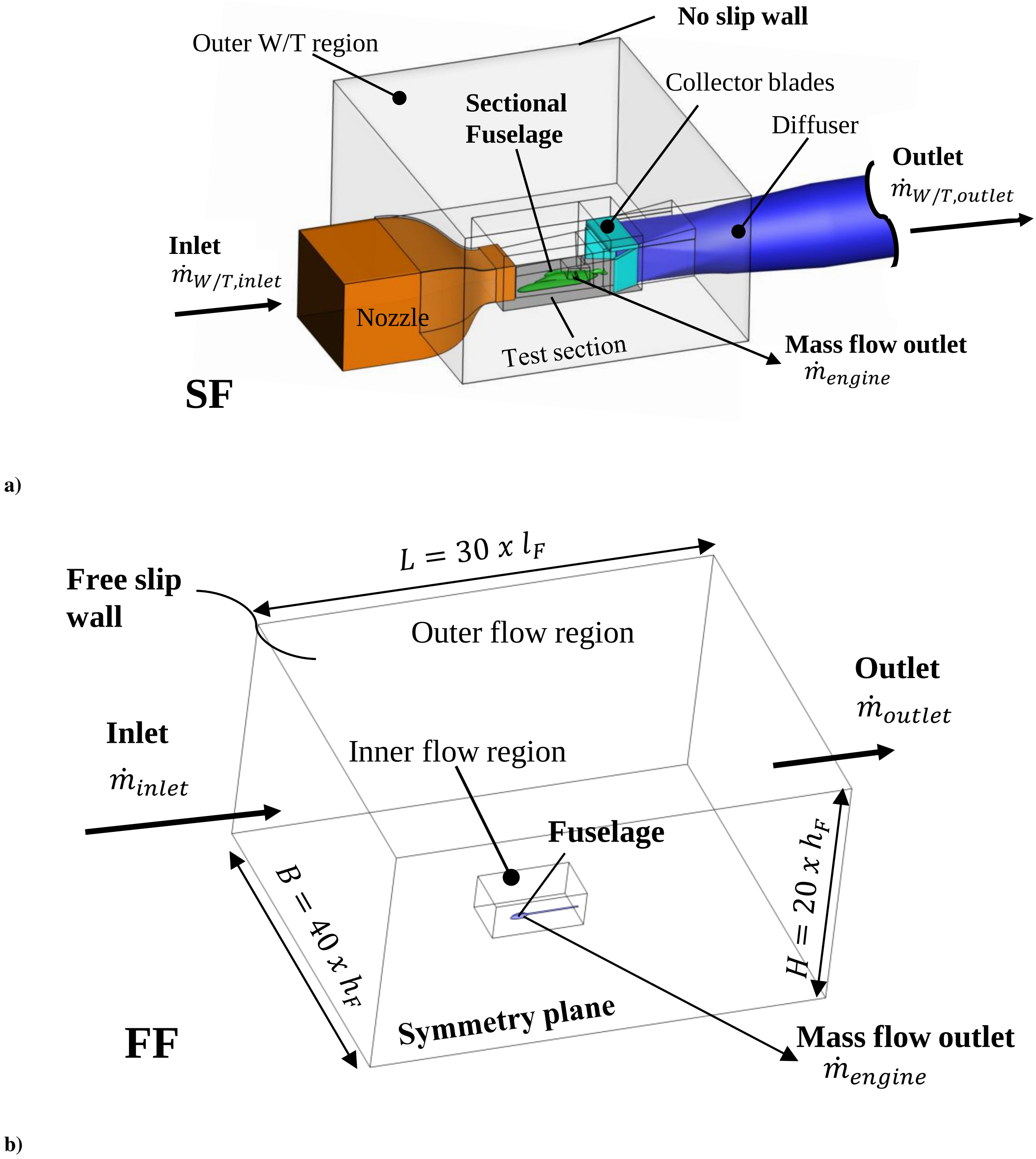
No slip wall
Outer W/T region
Sectional Fuselage
Collector blades
Diffuser
Outlet
$\dot{m}_{W/T,outlet}$
Inlet
$\dot{m}_{W/T,inlet}$
Nozzle
Test section
Mass flow outlet
$\dot{m}_{engine}$
SF
a)
$L = 30\ x\ l_F$
Free slip wall
Outer flow region
Outlet
$\dot{m}_{outlet}$
Inlet
$\dot{m}_{inlet}$
Inner flow region
Fuselage
$B = 40\ x\ h_F$
$H = 20\ x\ h_F$
Symmetry plane
Mass flow outlet
$\dot{m}_{engine}$
FF
b)

Figure 4.1: Numerical setup and boundary conditions in perspective view a) of the sectional fuselage case, b) of the full fuselage case.

As illustrated in Figure 4.1b, the full fuselage case incorporates one symmetric half of the original helicopter fuselage including the parts cabin, mast fairing, cowling and engine air intake. In the full fuselage case, mass flow boundary conditions are set at the inlet, outlet and mass flow outlet in analogy with the sectional fuselage case. The extent of the outer flow region is 15 times the fuselage length l_F in upstream and downstream direction and 20 times the fuselage height h_F in the left and right lateral as well as the vertical direction. Thereby, an interference of the fuselage flow field with the free slip wall conditions of the side and top surfaces is prevented. At the mid plane the symmetry option is selected to correctly simulate one half of the fuselage. The inlet static temperature and reference pressure are adjusted identically to the sectional fuselage case. The fluid is modeled as ideal gas air and, consequently, the ideal gas law is employed to relate the scalars temperature, pressure and density. A dynamic viscosity of $\mu = 1.831 \cdot 10^{-5}\ kg/ms$ and a thermal conductivity of $0.0261\ W/mK$ are chosen. The specific heat capacity at constant pressure is set to a value of $1004.4\ J/kgK$. For the numerical simulations of the sectional and full fuselage cases, the unsteady Reynolds Averaged Navier-Stokes Equations (URANS) are solved applying the flow solver ANSYS CFX 16.0 and the Shear-Stress-Transport (SST) turbulence model, Refs. [8, 45]. By application of a blending function, a blending between the $k-\omega$ model in the near wall flow regime to the $k-\varepsilon$ model starting in the wake region of the boundary layer is achieved. Therefore, a combination of the advantages of both formulations can be realised. Furthermore, the enthalpy-type of the energy equation is solved to account for compressibility effects upstream and in the AIP region, where Mach numbers of $Ma \approx 0.7$ occur locally. All boundary layers are simulated as fully turbulent. To resolve time dependent phenomena in the fluid domain, time-accurate simulations are performed. Therefore, a steady-state simulation serves as the initial solution for the subsequent time-accurate calculations. For the following investigations, only time-averaged results are considered. The spatial discretization is achieved through the application of the high resolution scheme, which incorporates a blending of a first and second order upwind scheme. For the temporal discretization the implicit backward-Euler-method with second order accuracy is selected. For the time-accurate simulations the timestep is set to $t = 10^{-4}$ s. A physical time of 0.1 s is reproduced and the mean results are achieved by averaging over a total of 1000 timesteps in the time-accurate simulations.

4.2 Computational Mesh

The complete fluid domain is subdivided into eight part meshes in the sectional fuselage case and seven part meshes in the full fuselage case which are all connected via general grid interfaces (GGIs). To achieve low numerical dissipation, for all part meshes a block-structured approach is chosen and all meshes exclusively comprise hexahedrons despite of the geometrical complexity. The meshes are created using ANSYS ICEM CFD and incorporate a total of 2432 blocks in the sectional fuselage case as well as 2297 blocks in the full fuselage case, respectively.

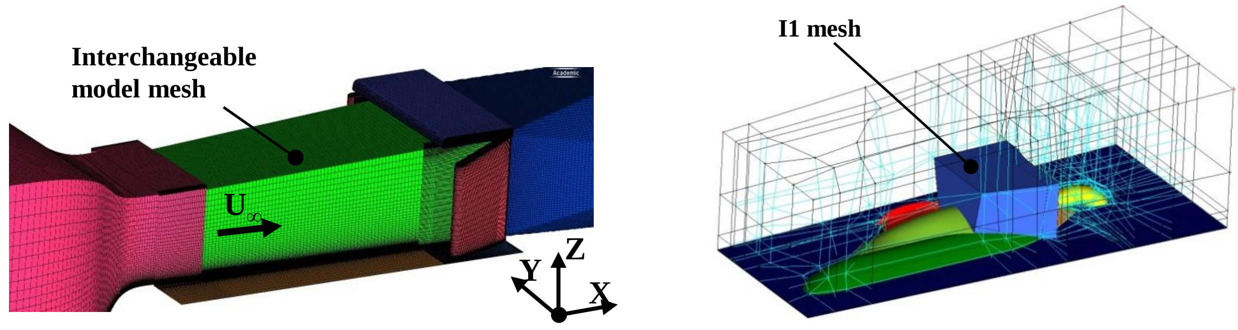

a)

b)

Figure 4.2: a) surface mesh of the W/T test section containing the interchangeable model mesh, b) blocking of the sectional fuselage mesh, including the intake mesh's outer surfaces.

In the entire domain O-grids are applied to allow local boundary layer mesh refinements close to the walls. The first layer element height of $h \approx 10^{-5}\ m$ leads to a dimensionless wall distance of $y+ < 1$.

Thus, combined with an expansion ratio of 1.2, the boundary layer including the viscous sublayer is accurately resolved without applying a wall function. Considering the sectional fuselage case, a block is cut out of the wind tunnel mesh in the test section, in between the nozzle exit and the collector blades (see Figure 4.2). The mesh of the sectional fuselage is embedded in the wind tunnel mesh. The box-shaped mesh topology also allows for the modular use of different model meshes, compare Figure 4.2. Consequently, in the concept of the W/T mesh a similar modularity as in the real W/T setup is achieved. The blocking of the sectional fuselage mesh is presented in Figure 4.2b. The blocking of the full fuselage case mesh which is nearly identical to the blocking of the sectional fuselage case is depicted in Figure 4.3b. It is connected to the outer flow region's mesh using a GGI, see Figure 4.1b. For both numerical cases, the mesh of the Intake 1 (I1) is situated inside the section mesh as well as the fuselage mesh, respectively. The blocking of the mesh is depicted in Figure 4.4a. In Figure 4.4b, the engine air intake mesh is presented in detail. Close to the intake entry the mesh is refined for an accurate prediction of the separation position and topologies, see Figure 4.4b.

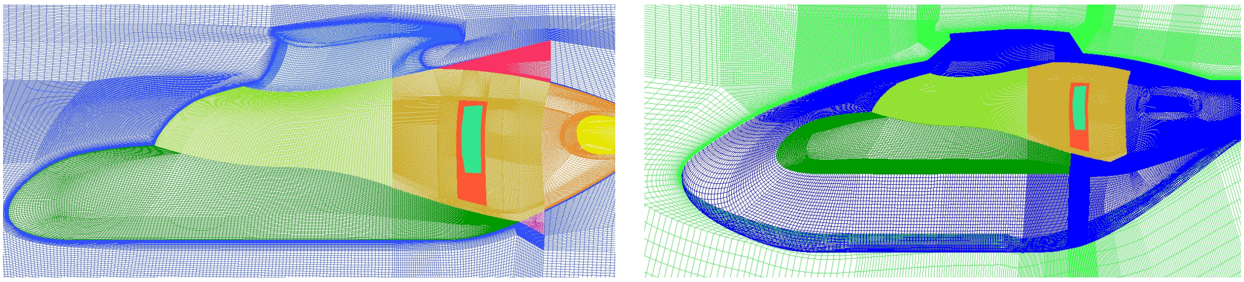

a) **b)**

Figure 4.3: Surface mesh including the intake surface mesh of a) sectional fuselage case, b) full fuselage case.

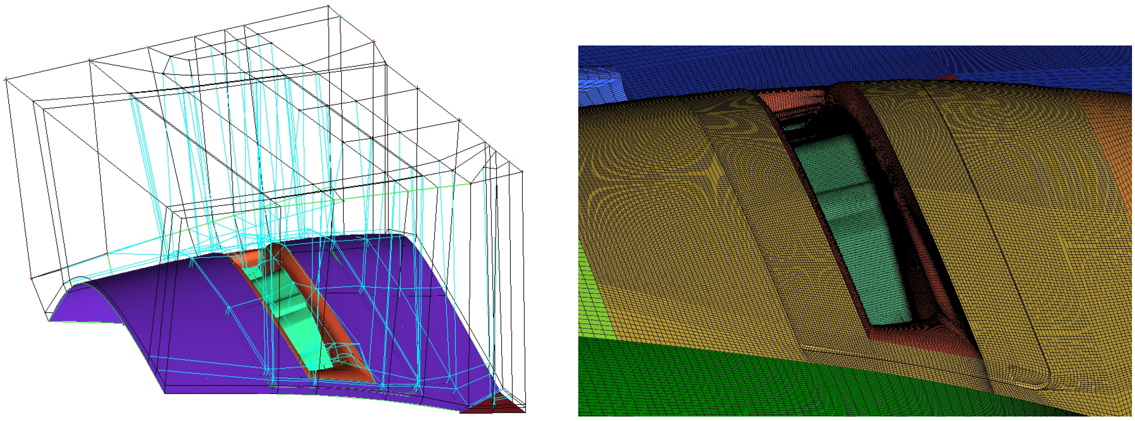

a) **b)**

Figure 4.4: a) blocking of intake I1, b) surface mesh of Intake I1.

Figure 4.5a presents the blocking of the engine plenum chamber (EPC) mesh. The top surface of the part mesh is connected to the I1 mesh (cp. Figure 3.17a and Figure 4.4a). The cylindrical inner surface of the EPC mesh embeds the mesh of the engine intake duct (EID), as shown in Figure 4.5a. A further circular mesh is situated between the EPC and the EID and is meant to connect both, as shown in the cut view in Figure 4.5b. In Figure 4.6a an EID 60 °-section is shown which comprises one outer and inner guide

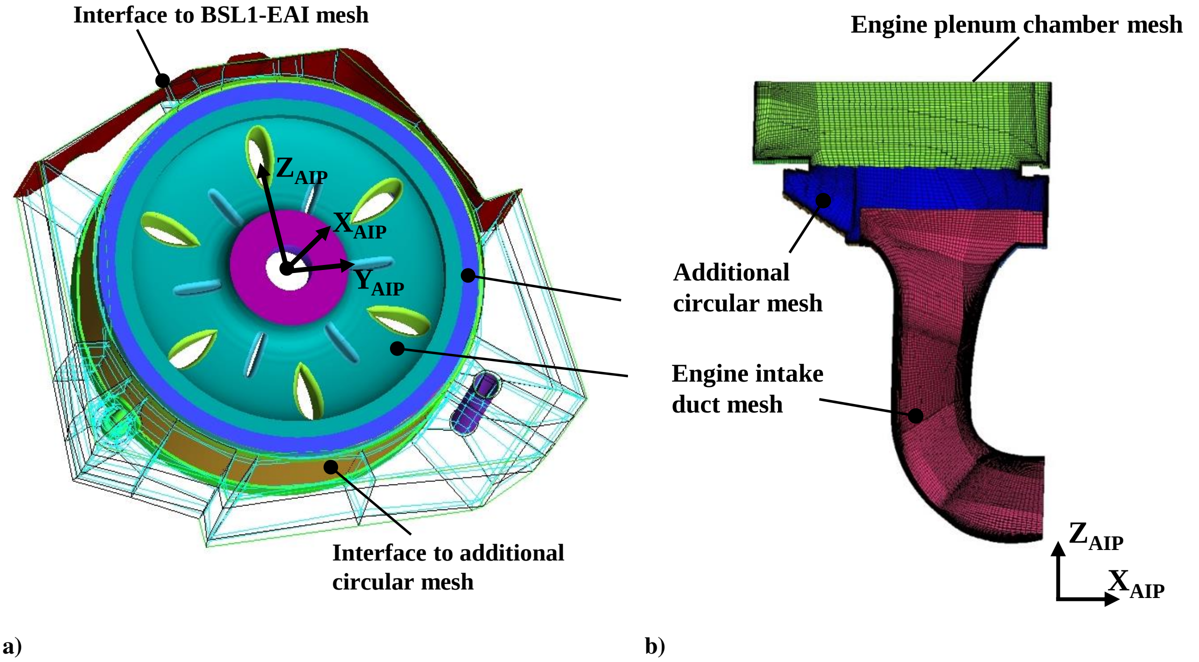
Interface to BSL1-EAI mesh
Z_{AIP}
X_{AIP}
Y_{AIP}
Interface to additional circular mesh
a)
Engine plenum chamber mesh
Additional circular mesh
Engine intake duct mesh
Z_{AIP}
X_{AIP}
b)

Figure 4.5: a) blocking of EPC mesh, position of EID mesh and additional circular mesh, b) cut view of BSL1 - EPC, EID mesh and additional circular mesh.

vane. The complete EID mesh is created by repeating six of these section meshes in circumferential direction around the X_{AIP} - axis and merging the nodes of the EID 60 °-sections.

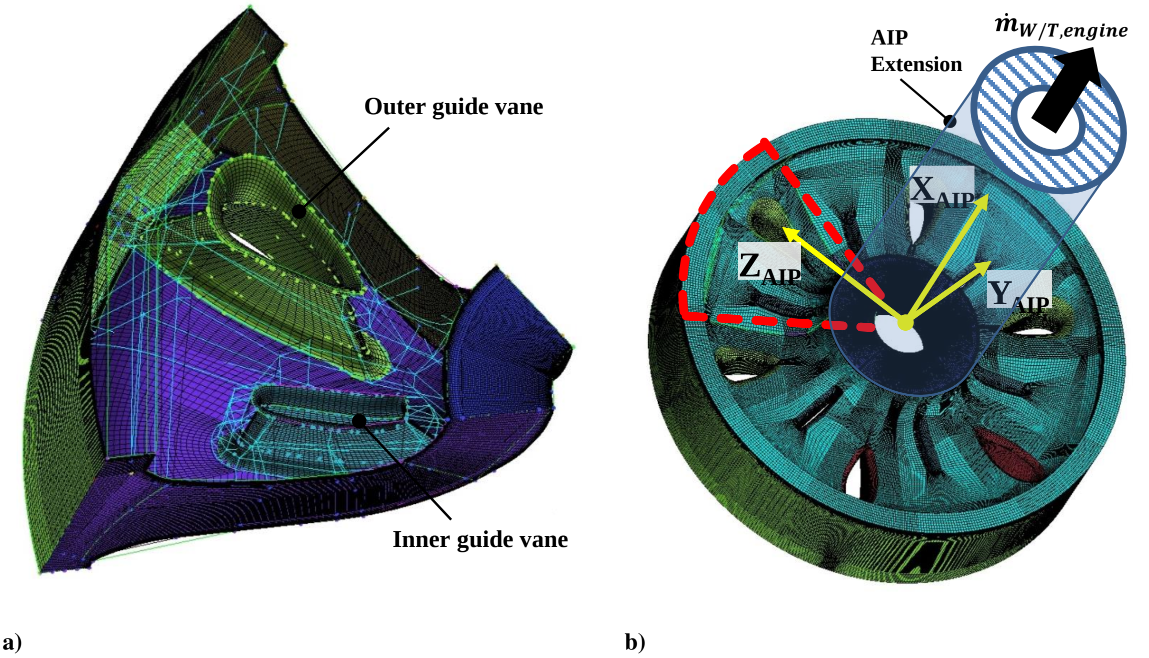
Outer guide vane
Inner guide vane
a)
AIP Extension
$\dot{m}_{W/T,engine}$
X_{AIP}
Z_{AIP}
Y_{AIP}
b)

Figure 4.6: a) detail of EID mesh section, b) complete EID mesh, AIP extension (schematically).

4.3 Mesh Sensitivity Study

A grid sensitivity study was performed for both the sectional fuselage and full fuselage case. Hereby, the results of meshes with three different global refinement levels are compared. Considering the sectional fuselage case, the coarse mesh comprises 18.6 Million nodes, the medium mesh 32.3 Million nodes and the fine mesh 58 Million nodes. Referring to the full fuselage case, the coarse, medium and fine meshes consist of 17.8 Million, 32 Million as well as 57 Million nodes, respectively. The dimensionless wall distance of $y+ < 1$ is achieved for all meshes. For the evaluation of the grid sensitivities of both cases, the coefficients $\bar{\eta}_{norm}$ and $DC_{60,norm}$ are applied (see 4.1).

Table 4.1: Comparison of intake coefficients for mesh refinement levels of the sectional/full fuselage case

Parameter	Coarse		Medium		Fine		W/T
	sectional f.	full f.	sectional f.	full f.	sectional f.	full f.	
$\bar{\eta}_{norm}$	0.9847	0.9828	0.9842	0.9836	0.9841	0.9837	0.984
$DC_{60,norm}$	2.3356	2.545	2.3215	2.3706	2.3136	2.348	2.1398

Considering the differences in $\bar{\eta}_{norm}$ of the sectional fuselage case, the result achieved with the coarse mesh differs by 0.05 % compared to the medium mesh, while the difference of the medium and fine mesh is only -0.01 %. Referring to the $DC_{60,norm}$, the difference of the coarse and medium mesh is 0.6 %. A decrease of the relative difference to -0.34 % is found for the comparison of the fine and medium meshes. Considering the full fuselage case, a relative difference in $\bar{\eta}_{norm}$ of -0.08 % appears comparing the coarse and medium meshes. The difference is reduced to 0.01 % for the fine mesh. Regarding the $DC_{60,norm}$, the relative difference of the coarse mesh is 7.36 % compared to the medium mesh. For the fine mesh a difference of only -0.95 % remains. For both numerical cases, the medium mesh is selected for the subsequent investigations as additional mesh refinements only slightly change the results of $\bar{\eta}_{norm}$ and $DC_{60,norm}$.

5 Analysis of the Baseline Case

To complement the experimental results, unsteady Reynolds-averaged Navier-Stokes (URANS) simulations of the helicopter fuselage section, including the baseline intake configuration, are performed using ANSYS CFX and the SST turbulence model. The baseline configuration (I1 P1 IG0 EG0 RSP0 IGV0) refers to the configuration comprising intake 1 (I1), plenum chamber 1 (P1), neither intake nor engine grid (IG0 EG0) and no retrofit modification (RSP0 IGV0), compare also Section 3.2. In the numerical simulations of the fuselage section, the complete inner structure of the engine air intake as well as the W/T nozzle, collector and test section geometry are modeled to reproduce the flow field around the fuselage section and intake parts in accordance with the experiments. In the first part of the chapter, the flow field of the sectional fuselage case is characterized. Furthermore, for the fast forward flight case, the influence on flow topologies due to the truncation of the original fuselage is analyzed. In the second part of the chapter two numerical cases are compared. The experimental data is considered as the reference. The presented methodology aims at the creation of a combined numerical and experimental testing facility for valuable early design-phase investigations of the engine airframe integration process, see also Refs. [36, 38, 40, 41].

5.1 Sectional Fuselage Characteristics

In the subsequent section, a detailed investigation on the flow characteristics of the Intake 1 configuration is presented. For fast forward-flight conditions, numerical and experimental surface pressure distributions as well as AIP total pressure data are analyzed and compared. Total pressure and velocity ratio distributions are discussed to give an insight to the flow phenomena of the static side intake configuration.

5.1.1 Surface Pressure Distributions

In the following section, the aerodynamic characteristics and flow patterns in the inflow area are regarded. Hereby, regions of attached and separated flow as well as local flow acceleration and deceleration are distinguished. Subsequently, the main flow phenomena are investigated employing surface pressure distributions. Pressure coefficient levels of the surface pressures are shown along the lines 2 and 3 (see Figure 5.1a and Figure 5.1b) which represent the cowling pressure distribution on the outer geometry. The numerical results of the sectional fuselage case are in very good agreement with the W/T measurements. The air is accelerated around the front intake lip of Intake 1's side intake. This leads to a pressure decrease for the range of $S_2 = 0.89 - 0.92$. The nearly constant pressure level that appears in between $S_2 = 0.94 - 0.98$ indicates a region of separated flow, which is discussed in more detail in

Chapter 5.1.2. In Figure 5.1b, the pressure distribution of line 3 is shown. On the back face of the intake, a stagnation point occurs close to $S_3 = 0.05 - 0.1$. The stagnation point separates the ingested fluid from the external flow.

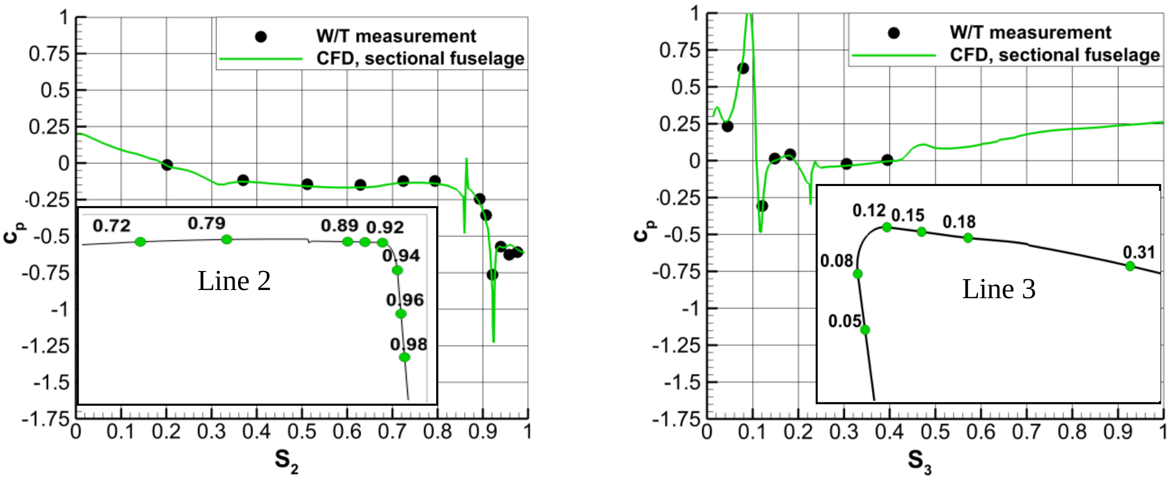

a) **b)**

Figure 5.1: a) c_p distribution on line 2, b) c_p distribution on line 3.

The external flow is accelerated around the back intake lip and leads to a decreased static pressure of $c_p \approx -0.45$ at the location $S_3 = 0.12$. The surface pressure distributions on the mid plane of the plenum chamber are compared for the numerical simulation of the sectional fuselage and the experiment in Figure 5.2a.

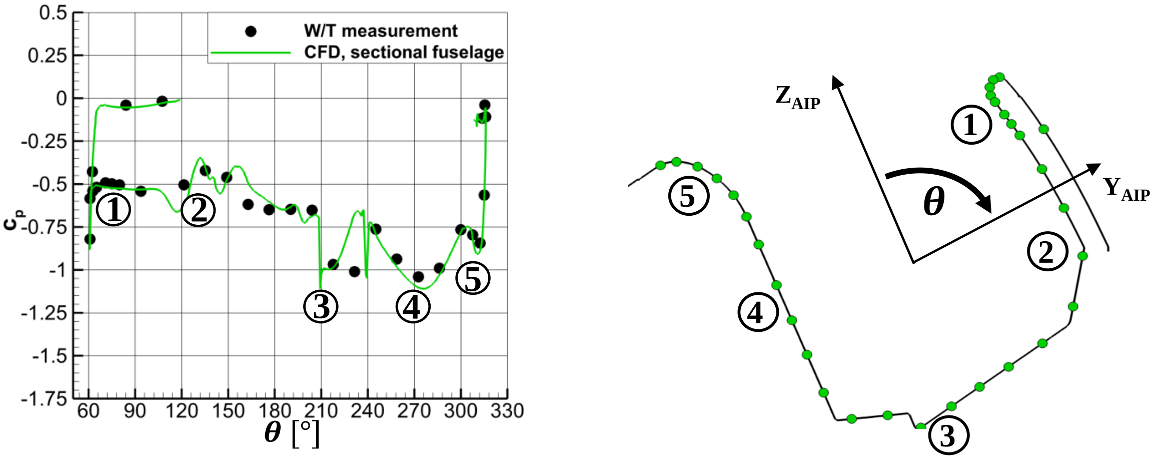

a) **b)**

Figure 5.2: a) c_p distribution on line 9, b) Sectional view through line 9 in EPC mid plane, characteristic flow regimes labelled from 1 to 5.

Globally, the surface pressure distributions indicate a very complex EPC flow field. The results are in good agreement with the experimental data for the prevailing portion of line 9. At the location $\theta = 61°$

the flow is accelerated around the right side intake lip resulting in a pressure drop to a level of nearly $c_p \approx -0.9$. As a consequence of the strong flow deflection, a separation occurs at the position $\theta = 63°$ (see label 1 in Figure 5.12a, Figure 5.2a). Starting at this location, a pressure plateau of $c_p \approx -0.5$ can be detected in Figure 5.2a. Subsequently, a separated flow region appears (label 2) which is characterized by low total pressures. On the left side intake lip, the flow stays attached (label 5) and lower c_p levels are observed for $180° < \theta < 320°$ caused by the high flow velocities on the EPC left side, cf. Chapter 5.1.2. The low pressure levels around $\theta = 270°$ are induced locally by the primary vortex which develops from the shear layer at the front intake lip and is ingested into the left side part of the EPC (label 4). At the back facing step at $\theta = 210°$, an additional small region of separated flow can be observed (label 3) which locally reduces c_p but is insignificant for the development of the flow field in the downstream located EID. In Figure 5.3a and Figure 5.3b the c_p-distributions are shown for lines 12 and 13, which are situated at the angular position $\theta = 135°$. These lines represent the rotationally symmetrical EID geometry. In the EID, the CFD results and the experimental data are in very good agreement.

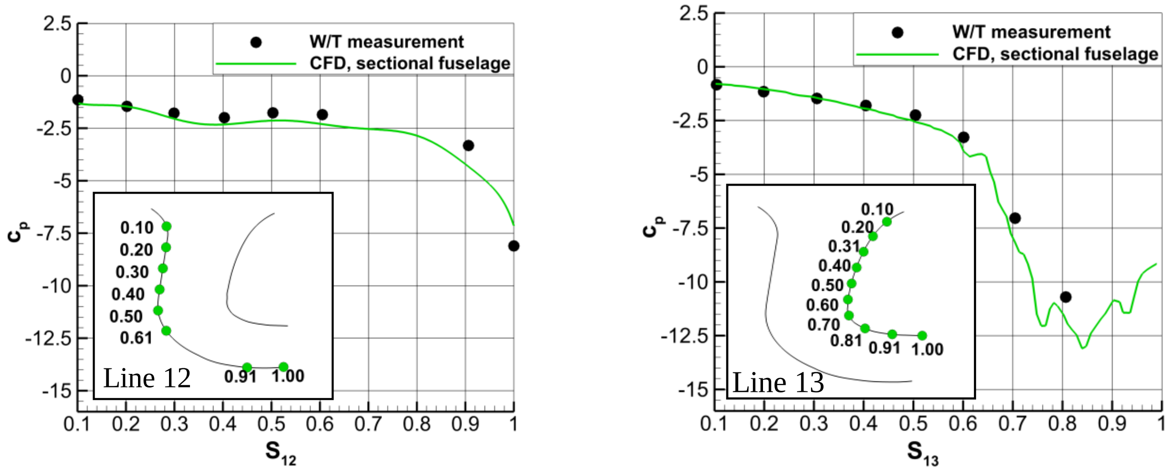

a) **b)**

Figure 5.3: a) c_p distribution on line 12, b) c_p distribution on line 13.

The EID operates as a nozzle with a strong area contraction from entry to exit plane (AIP). The contraction results in a significant acceleration as well as a static pressure drop of the fluid (consider also Figure 5.3b). The concave curvature of the front EID surface (line 12) diminishes the static pressure drop due to the area contraction. In contrast, due its convex curvature, the flow is accelerated significantly on the EID back surface, creating a more pronounced static pressure drop. Hence, a negative pressure gradient exists between the front and back sides of the EID.

5.1.2 Flow Field Investigations

In this chapter, the flow field in the intake region is discussed in more detail to analyze the source of the distorted total pressure distribution in the AIP. For a quantitative analysis of the total pressure loss development, conical surfaces are defined at five constant coordinates S_{EID}, see Figure 5.4a and Figure 5.4b. S_{EID} represents a generalized coordinate in main flow direction. It is locally identical with each of the curve length coordinates S_{10} - S_{17} (see last section). Subsequently, circumferential distributions of the total pressure ratio and the relative velocity ratio are analyzed. Therefore, angular distributions are generated by averaging the field quantities in the direction perpendicular to the coordinate direction S_{EID} for constant θ.

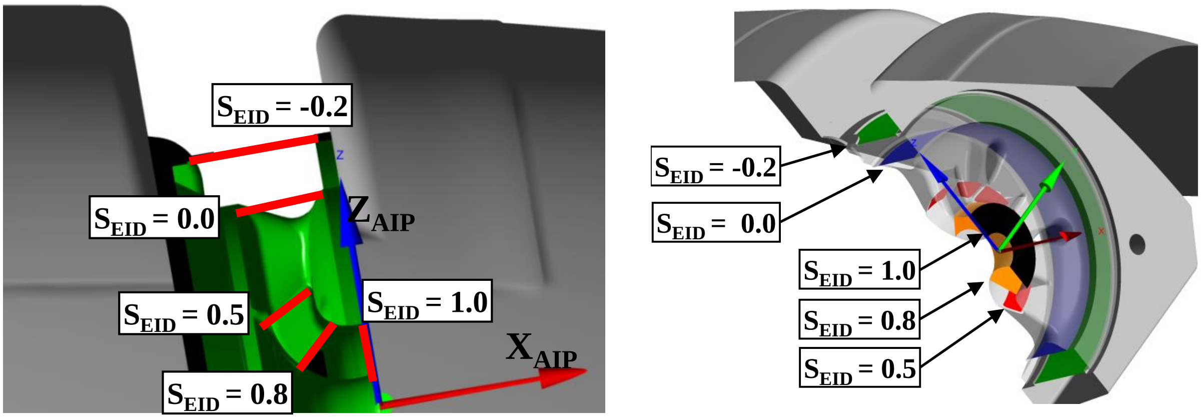

a) **b)**

Figure 5.4: a) X_{AIP}-Z_{AIP} cut view through EID, S_{EID} coordinates of conical planes (lines), b) perspective view of conical planes in the EID.

As depicted in Figure 5.5a, between $\theta = 300°$ and $\theta = 60°$, the highest total pressure levels persist in the entire EID. This can be observed from the grid holder position ($S_{EID} = -0.2$) to the AIP ($S_{EID} = 1$).

The origin of the high total pressure region can be explained by discussing the phenomena which appear directly downstream of the front intake lip (see Figure 5.6a and Figure 5.6b). Therefore, the circumferential vorticity ω_C is defined employing the reference length l_I and the freestream velocity at the nozzle exit U_∞. In the following, each flow phenomena is related to a number in Figure 5.6a and Figure 5.6b.

The boundary layer separates from the front intake lip (label 1) due to the strong surface curvature. Simultaneously, a velocity component in negative Z_{AIP} direction is induced due to the engine suction. As a result of this flow component and the main flow direction at the separation line, a vortex with high positive circumferential vorticity emanates from the shear layer (label 2). The primary vortex encounters the grid holder from the inside (label 8 in Figure 5.6b). As a consequence, a counter-rotating vortex with negative vorticity (label 3) is created. Due to the reattachment of the secondary vortex at the back-facing wall of the intake (label 5), a convergence of the surface streamlines can be detected. In between the shear layer and the secondary vortex, a small third vortex occurs locally (label 6), which also features positive vorticity. Due to its small extent, it is only shown in Figure 5.6b. Inside of the stagnation line on the back intake lip (label 4) air from the outer flow with high total pressure is ingested into the EID region between $\theta = 270°$ and 60°. The primary intake vortex and the backside EID grid vortex (label 7) support the transport of air with high total pressure to the inside of the EID, see Figure 5.6b.

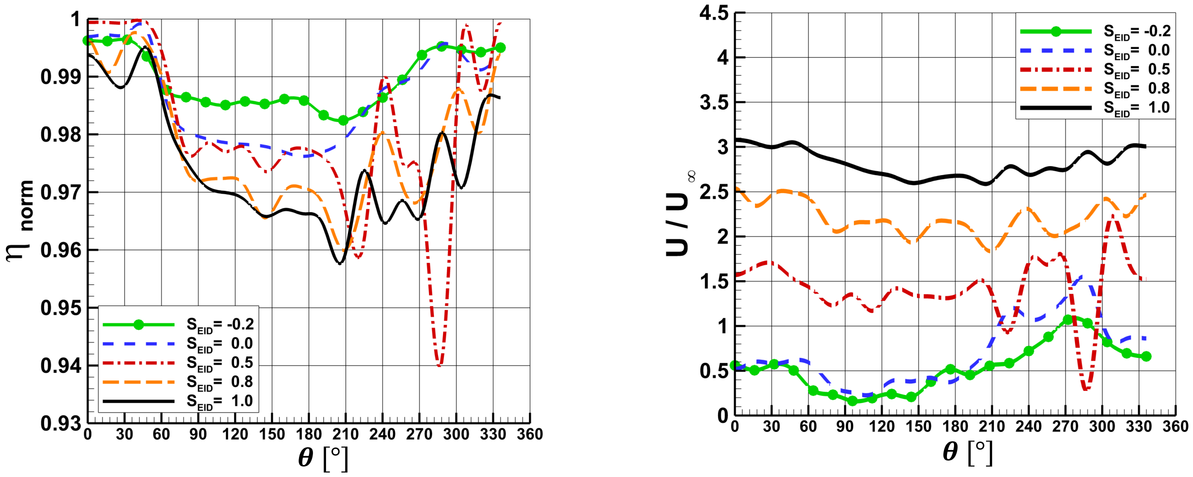

a) b)

Figure 5.5: Distributions of a) normalized total pressure ratio vs. θ , b) relative freestream velocity ratio vs. θ for conical planes with constant S_{EID}.

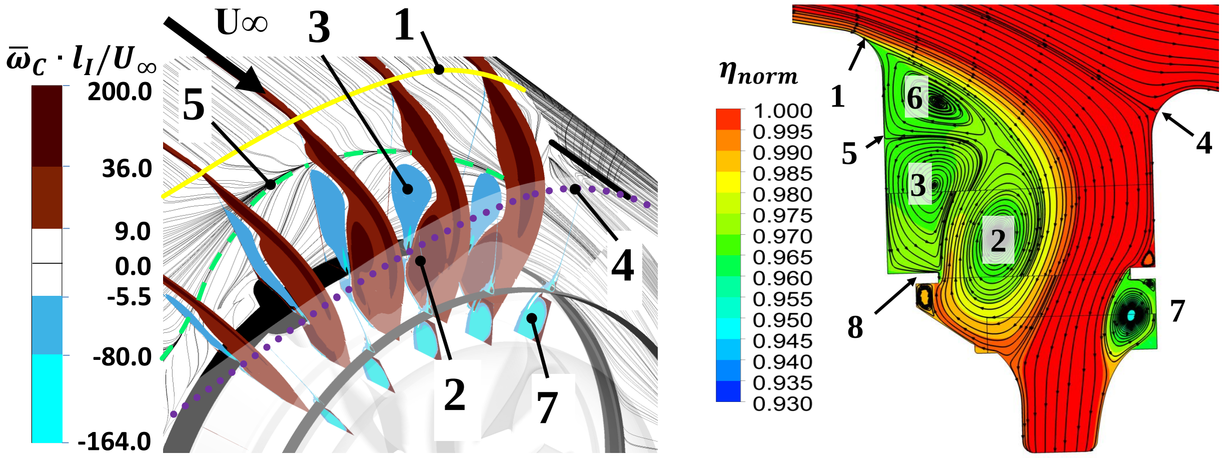

a) b)

Figure 5.6: a) surface streamlines on front intake lip, 4 different contours of constant $\omega_C \cdot l_I/U_\infty$ on radial-axial-planes ($\theta = 345°, 0°, 15°, 30°, 45°$), b) cut view through EID and intake region at $\theta = 30°$ showing the distribution of the normalized total pressure ratio together with projected streamlines.

For further analyzes, Figure 5.7a and Figure 5.7b are considered. A region of separated flow occurs in the EPC starting from a flow separation at the right intake lip, as shown before by means of the surface pressure distribution on line 9 (Figure 5.2b). The hatched surface in Figure 5.7a (label 4) indicates the region of reduced velocities and reduced total pressures. In an alleviated form, it can also be detected in Figure 5.5a and Figure 5.5b for $S_{EID} = 0$ and $60° < \theta < 180°$. Due to the region of separated flow, the ingested air is diverted to the left side of the EPC (negative Y_{AIP} values). This diversion is confirmed by determining the portion of the mass flow at three different cross sections at the top part of the EPC (labels 1, 2 and 3 in Figure 5.7a). An engine mass flow fraction of 46% is ingested into the central angle region (label 2 in Figure 5.7a), a portion of 44% enters the EPC at its left side (label 1 in Figure 5.7a) and only 10% pass through the EPC's right side (label 3 in Figure 5.7a).

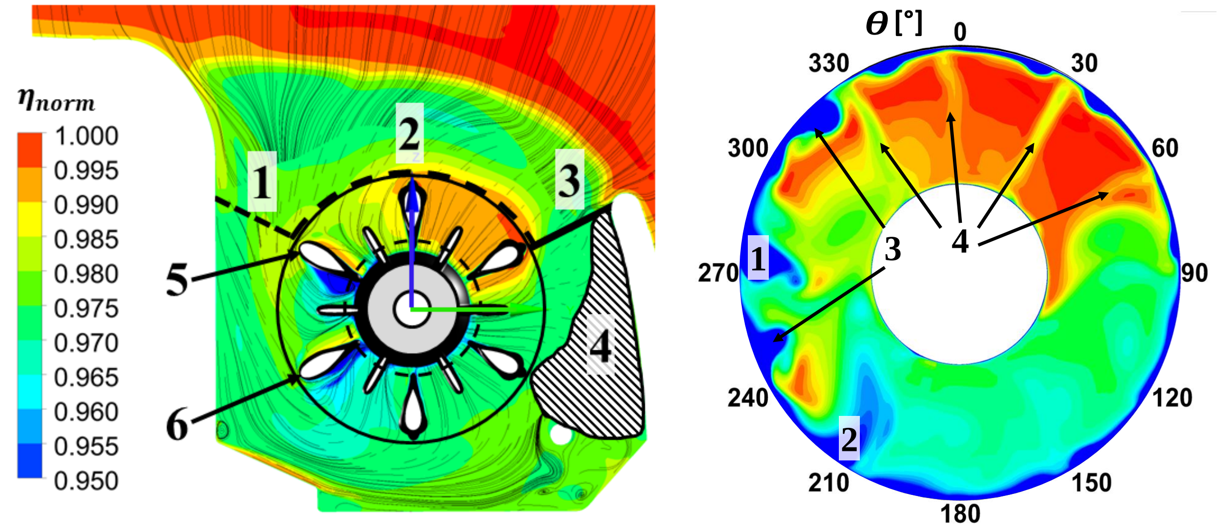

a) b)

Figure 5.7: a) sectional view of EPC mid plane, iso surface of a relative velocity ratio of 0.15 (schematic), surface streamlines, distribution of normalized total pressure ratio, cross section 1 at $\theta = 300°$, cross section 2 at $300° < \theta < 360°$, $0° < \theta < 60°$, cross section 3 at $\theta = 60°$, cylinder surface at $S_{EID} = 0$ (circle), cylinder surface at $S_{EID} = 0.5$ (dashed circle), b) distribution of normalized AIP total pressure ratio.

Increased velocities occur between $210° < \theta < 330°$ at the EID entrance ($S_{EID} = -0.2$) as depicted in Figure 5.5b due to the high mass flow portion entering the EPC's left side. Furthermore, high local angles of attack can be detected with respect to the outer guide vanes' symmetry plane (labels 5, 6 in Figure 5.7a). Thus, the flow separates at the EID guide vanes and further small regions of low total pressure and velocity occur at the angular positions $210° < \theta < 240°$ and $270° < \theta < 300°$, as illustrated by the curve of $S_{EID} = 0.5$ in Figure 5.5 and the streamlines in Figure 5.8.

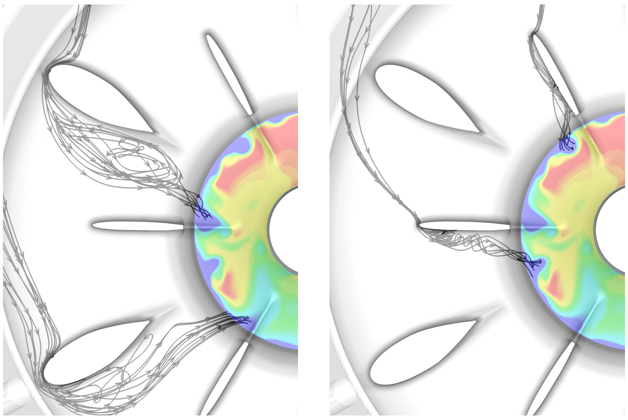

Figure 5.8: EID outer guide vane separation (left), EID inner guide vane separation (right).

In Figure 5.7b, the η_{norm} distribution in the AIP is presented. The location of the high total pressure region in the AIP is almost unchanged compared to the upstream positions. Still, the highest levels of η_{norm} appear for $300° < \theta < 360°$ and $0° < \theta < 60°$. The flow separations at the guide vanes lead to a considerable reduction of the AIP total pressure level for the region of $210° < \theta < 330°$. The low momentum fluid from the separation region which originates from the guide vane at $\theta = 300°$ is convected to a circumferential position of $\theta \approx 270°$ as a result of the local main flow direction (see label 1, Figure 5.7b). Due to the negative pressure gradient between the EID front and back surfaces caused by the different curvatures (see Figure 5.6) a concentration of fluid with low total pressure at the EID back side occurs. As a consequence, particularly at the outer wall of the AIP, low total pressure regions appear which originate from the outer guide vane separation regions (labels 1 and 2 in Figure 5.7b) and the inner guide vane separation regions (label 3 in Figure 5.7b). The wakes of the guide vanes at the angular positions $\theta \approx 330°$, 0°, 30° and 60° are not transported in circumferential direction (label 4 in Figure 5.7b). In the flow regime between $60° < \theta < 210°$, no wakes can be distinguished as an effect of the predominately low total pressures. In the EID, no further flow separations are noticeable besides the guide vane separations. This is a result of the strong negative pressure gradient in main flow direction due to the cross section contraction (Figure 5.6). Generally, the EID guide vanes are developed to straighten the flow and improve the engine inflow conditions by reduction of swirl and inhomogeneous total pressure distributions. The design has to cover a wide range of combinations of engine mass flow rates and flight speeds. Therefore, without application of variable guide vanes, small regions of separated flow can occur at the EID guide vanes in parts of the flight envelope.

5.2 Comparison of Sectional and Full Fuselage Case

Two numerical cases are compared to evaluate the influence of the boundary layer and local flow directions upstream of the intake opening. The first case represents the W/T setup, including essential W/T parts (nozzle, collector blades and diffuser). It is denominated the sectional fuselage case (SF). The second case incorporates one symmetric half of the original helicopter fuselage without W/T parts and reflects a real flight case. It is referred to as the full fuselage case (FF). The related boundary conditions of the numerical simulations are depicted in Figure 4.1. A comparison of the near-wall flow field upstream of the intake opening is performed for the sectional (SF) and full fuselage (FF) cases. Firstly, the incoming flow upstream of the intake opening is analyzed. Secondly, flow topologies are compared downstream of the front intake lip. Finally, differences in the engine inflow conditions are presented. Surface streamlines are depicted in Figure 5.9 for both cases.

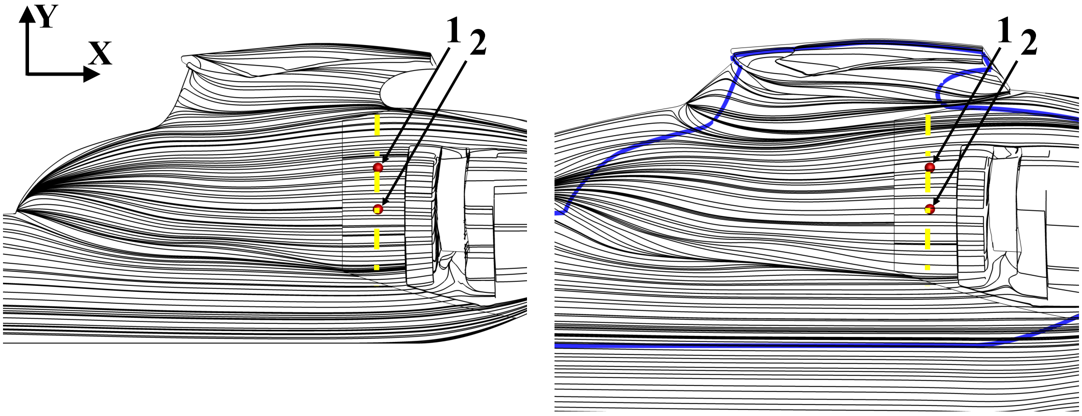

Figure 5.9: Surface streamlines (CFD) and positions for BL investigations in top view for the SF case (left), FF case (right), the blue line represents the truncation line of the section, the yellow dash-dotted line represents the PIV measurement plane.

Only slight deviations of the flow directions are found upstream of the intake opening. In two lateral locations, the boundary layer profiles of the SF and FF cases are compared to the PIV data (Figure 5.10).

Two red dots indicate the measurement positions in Figure 5.9.

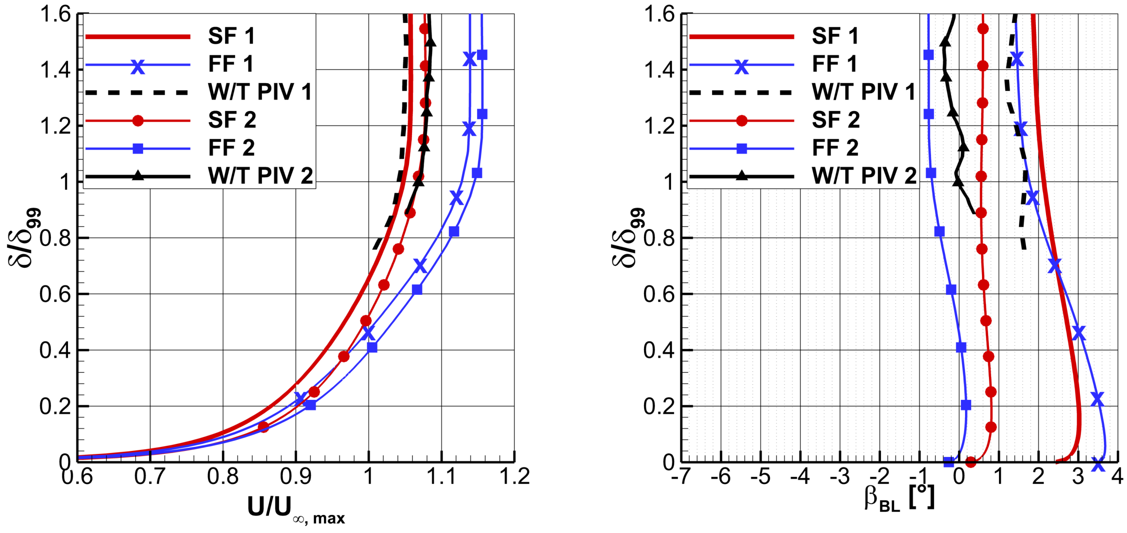

a) **b)**

Figure 5.10: Boundary layer profiles for the sectional fuselage case (SF), full fuselage case (FF) and W/T PIV measurement in two lateral positions, a) relative freestream velocity, b) crossflow angle β_{BL}.

The lower boundary layer PIV data is not included due to artefacts caused by reflections. At the outer portion of the boundary layer, the full fuselage case indicates an average velocity increase of 7.6 % compared to the sectional fuselage case (Figure 5.10a). The numerical result of the sectional case is nearly identical with respect to the PIV data. The deviations of the crossflow angles $\beta_{BL} = \arctan(V/U)$ of the two numerical cases are below 1.5° for both positions, indicating a minor influence of the fuselage truncation in terms of local flow direction. The difference of the sectional cases' crossflow angle and the PIV measurements is even smaller than 1°. In Section 5.1.2, the flow phenomena occuring in the sectional fuselage case have been discussed. Therefore, in the following, differences in the flow field characteristics of the sectional and the full fuselage cases directly downstream of the intake opening are regarded. Both surface streamlines at the front intake lip (see Figure 5.11) as well as projected 3D streamlines in a cut view at $\theta = 30°$ (compare Figure 5.12) are considered.

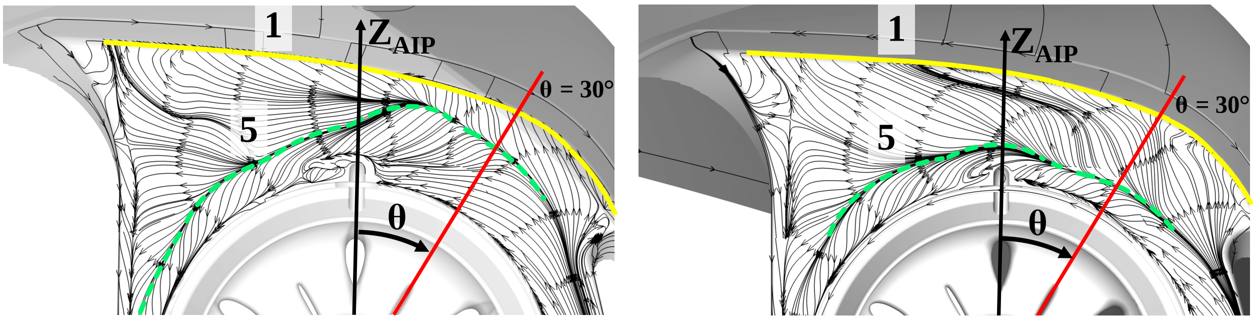

a) **b)**

Figure 5.11: Back view of front intake lip, surface streamlines, a) sectional fuselage case, b) full fuselage case.

The surface streamlines indicate qualitatively similar flow fields downstream of the front intake lip (Figure 5.11). Only in the region of 350° $< \theta <$ 360° and 0° $< \theta <$ 45°, differences are found that are discussed in the following, regarding Figure 5.12.

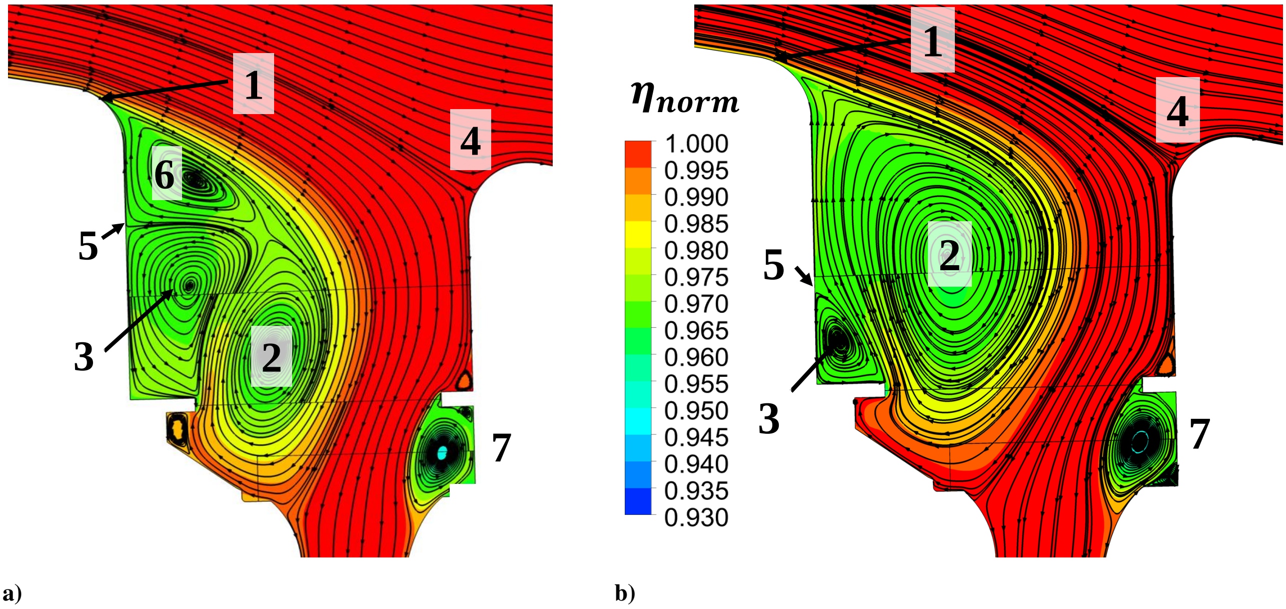

Figure 5.12: Cut view through EID and intake region at θ = 30° showing the distribution of the normalized total pressure ratio together with projected streamlines, a) sectional fuselage, b) full fuselage.

In both cases, the boundary layer separates from the front intake lip (label 1). Also in the full fuselage case a primary vortex with high vorticity rolls up from the shear layer (label 2). Furthermore, in both cases a counter-rotating secondary vortex (label 3) originates from the encounter of the primary vortex with the grid holder. Also for the full fuselage case this vortex reattaches at the back-facing wall of the intake (label 5). The vortex size and therefore also the reattachment line position is different in both cases. For the sectional fuselage case, between the shear layer and the secondary vortex, a third vortex (label 6) occurs, which is co-rotating with the primary vortex. Nevertheless, for both, between the stagnation line on the back intake lip (label 4) and the primary vortex, air from the outer flow with high total pressure is ingested into the EID region between θ = 270° and 60°. Both the primary intake vortex and the backside EID grid vortex (label 7) facilitate the transport of high momentum air to the inside of the EID, subsequently leading to high total pressures in the top part of the AIP. In Figure 5.13, the AIP η_{norm} distributions for the sectional fuselage and the full fuselage case simulations as well as the corresponding W/T experiment are depicted using the 96 measurement positions of the experiment (cp. Figure 3.17a).

Globally, the AIP distributions are in good agreement. Comparing the sectional fuselage and the full fuselage cases, small relative differences in $\bar{\eta}_{norm}$ of -0.06% and in $DC_{60,norm}$ of 2.12% are found. The relative difference of the sectional CFD and W/T AIP distribution of the coefficients $\bar{\eta}_{norm}$ and $DC_{60,norm}$ are 0.02% and 8.49%, respectively. Regions of high total pressure levels (330° $< \theta <$ 360° and 0° $< \theta <$ 60°), of low total pressures (60° $< \theta <$ 200°) and a mixed region (200° $< \theta <$ 330°) are identified. Even if flow topologies differ to some extent directly downstream of the intake opening, the main structure occurs, namely the primary vortex. Its transport effect of high total pressure fluid is found to be similar in both cases. Globally, the AIP total pressure distributions show that very similar crossflow angles

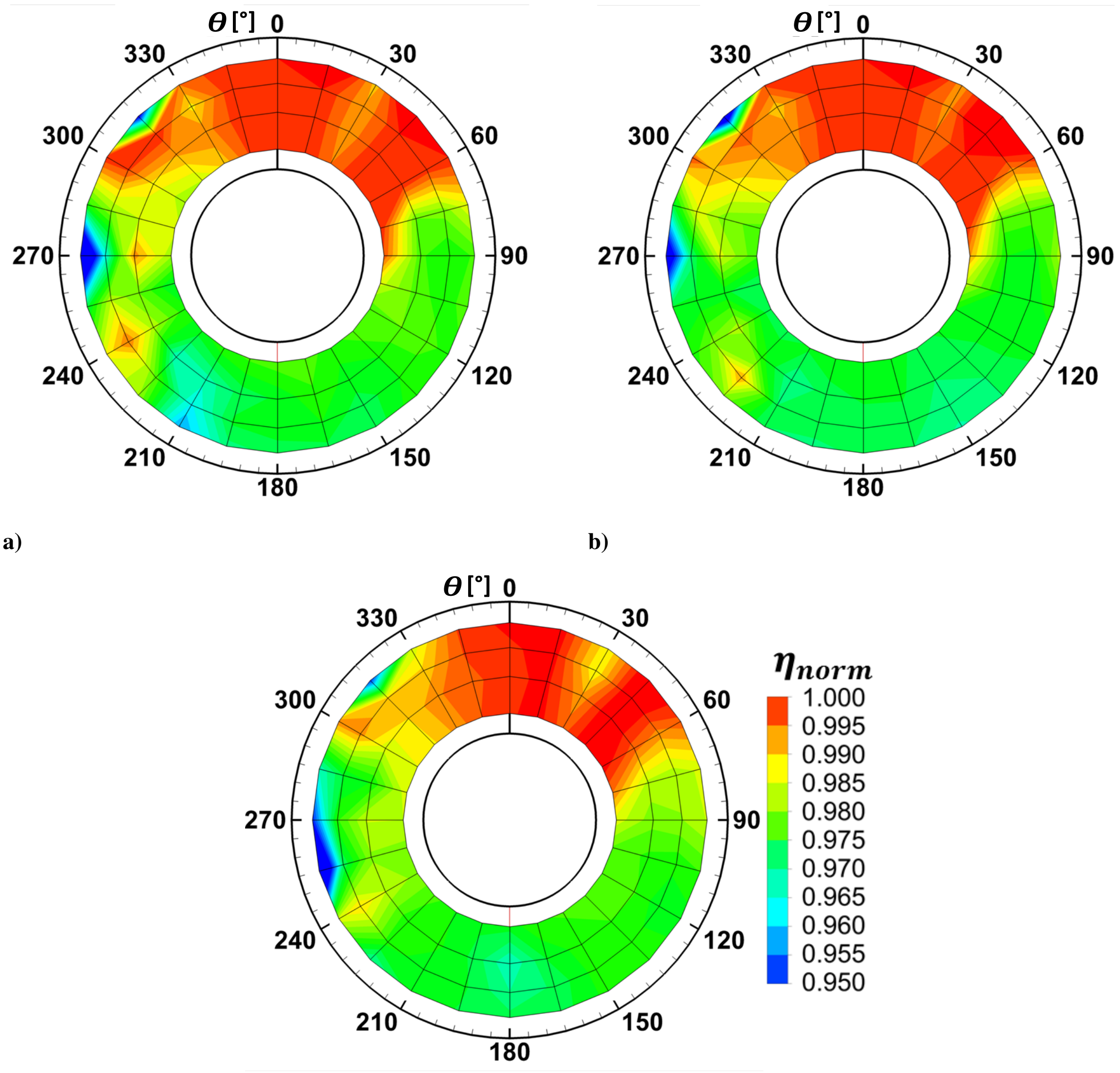

a)

b)

c)

Figure 5.13: Distribution of the normalized total pressure ratio in the AIP (96 points) for a) CFD simulation of sectional fuselage case, medium mesh, b) CFD simulation of full fuselage case, medium mesh, c) wind tunnel experiment, maximum relative freestream velocity, maximum mass flow rate ratio.

upstream of the intake opening lead to a similar downstream flow field, comparing the sectional fuselage and the full fuselage cases globally.

5.3 Synthesis

Local surface pressure distributions, PIV data of the flow field upstream of the intake opening and AIP total pressure distributions are used to validate the numerical modeling of the sectional fuselage case in comparison with wind tunnel data.

The analyses of the sectional fuselage case in fast forward flight condition identify the significant flow phenomena of the complex intake geometry which finally create a distorted AIP total pressure distribution.

Mainly two flow regions are unvealed by means of the aerodynamic interface plane total pressure distributions. The top part of the engine entry plane is characterized by high total pressures, whereas the lower part is dominated by low total pressures. A system of vortices emanates from the separated boundary layer at the strongly curved front intake lip, leading to a the region of high total pressures in the AIP (between $\theta = 330°$ and $\theta = 60°$).

Due to a flow separation at the right side intake lip, a region of separated flow of large extent is created inside the plenum chamber. As a consequence, lowered total pressures and velocity ratios persist in the angle regime of $60° < \theta < 200°$ throughout the entire EID.

In the AIP, for the angular regions of predominantly radial EID inflow direction, wakes of the EID guide vanes are identified.

In the angular region of $200° < \theta < 330°$, a more circumferential inflow direction at the EID entry leads to higher local incidence angles with respect to the guide vanes and thus the creation of small separation regions. The knowledge about the flow field is further used as a basis for the subsequent comparison of different intake shapes as well as the investigation of retrofit geometric modifications.

The comparison of a sectional and a full fuselage case indicates a very similar surface streamline pattern and local crossflow angles upstream of the intake opening. Even though the vortex system directly downstream of the front intake lip differs for both cases, the effect of high energetic fluid ingestion between the primary vortex and the intake back side stagnation region is very similar for both cases.

The very similar AIP total pressure distributions indicate that the most important flow phenomena occur for both cases and that similar crossflow angles with respect to the intake opening globally lead to a comparable flow field for such geometries, which justifies using the truncated model for the experimental investigations of different geometric gonficurations.

6 Analysis of Side Intake Configurations

The first part of the subsequent Chapter (Section 6.1 - Section 6.3) deals with the description of the aerodynamic characteristics of the basic intake variants, whereas in the second part (Section 6.4 - Section 6.5), the aerodynamic characteristics of retrofit modifications for the reference configuration are discussed. The reference geometry (I2 P3 IG2 EG2 RSP0 IGV0) refers to the configuration including intake 2 (I2), plenum chamber 3 (P3), intake grid 2 (IG2), engine grid 2 (EG2) and no retrofit modification (RSP0 IGV0). See also Refs. [36, 38, 40, 41].

6.1 Basic Intakes

Subsequently, the basic intake configurations I1 P1 IG1 EG2 RSP0 IGV0, I2 P3 IG2 EG2 RSP0 IGV0 and I3 P3 IG3 EG2 RSP0 IGV0 are investigated. For shortness, the basic configurations are abbreviated in this section as I1 P1, I2 P3 and I3 P3 or intake 1,2 and 3. In Figure 6.1, the corresponding geometries are depicted. To assess the aerodynamic characteristics of the three basic intake configurations, both the normalized total pressure ratio $\bar{\eta}_{norm}$ as well as the normalized total pressure distortion $DC_{60,norm}$ is presented in dependence of the relative freestream velocity, see Figure 6.2a and Figure 6.2b. The maximum mass flow rate ratio of $\dot{m}_{corr}/\dot{m}_{corr,max} = 1$ is chosen. The $\bar{\eta}_{norm}$ levels of intake 2 are higher than those of the static side intake 1. Firstly, this is due to the ram effect of the ramp. Secondly, the rounded plenum chamber P3 including the plenum splitter further increases total pressures especially in the lower part of the AIP, compare Figure 6.3a and 6.3b. The main relative differences of $\Delta\bar{\eta}_{norm,rel,1\rightarrow 2} \approx 0.5$ % are noticeable for $U_\infty/U_{\infty,max} = 1$. The influence of the ramp and the plenum chamber on $\bar{\eta}_{norm}$ is examined further in section 6.3. The additional scoop of the I3 intake variant leads to the best pressure recovery compared to the other intakes for $U_\infty/U_{\infty,max} > 0.6$. The large relative difference of $\Delta\bar{\eta}_{norm,rel,2\rightarrow 3} = 0.46$ % in comparison with the intake 2 variant appears for the highest velocity. In the low velocity regime, the intake variant 2 exhibits the highest $\bar{\eta}_{norm}$ levels. The total pressure losses due to the intake shapes are proportional to the freestream flow dynamic pressure. The covered intake entry and the resulting strong flow deflection around the scoop of the ingested air leads to the lowest total pressures of the I3 intake for $U_\infty/U_{\infty,max} \rightarrow 0$. As shown in Figure 6.2b, $DC_{60,norm}$ features a very similar curve progression in the low velocity regime for the intake 1 and 3 geometries. Here, the distortion level is the lowest for the intake 2. For the higher velocities, the trends for all intake variants are similar.

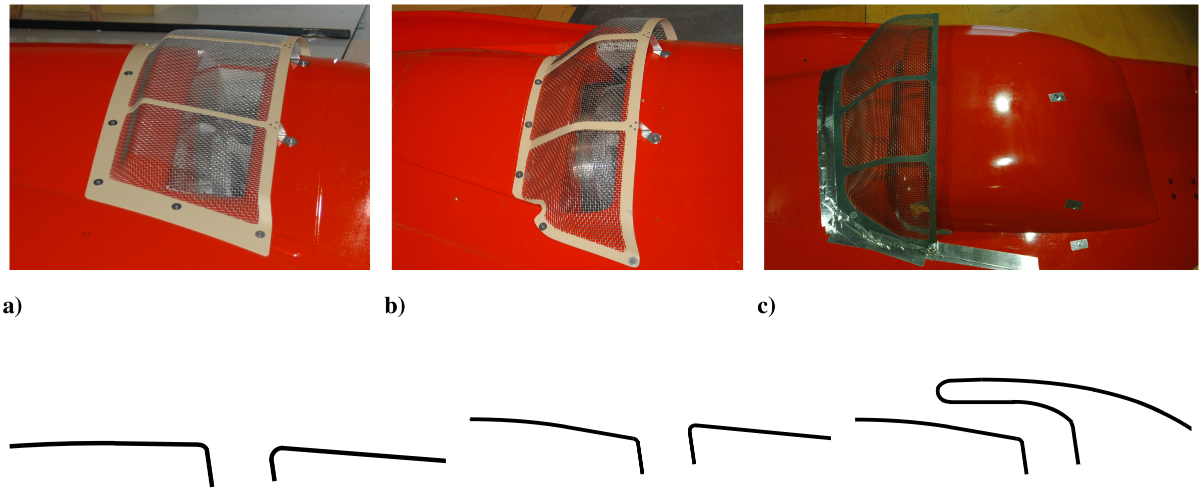

a) b) c)

d) e) f)

Figure 6.1: Representation of basic intakes a) I1, b) I2, c) I3, and schematic cut view of d) I1, e) I2 and f) I3.

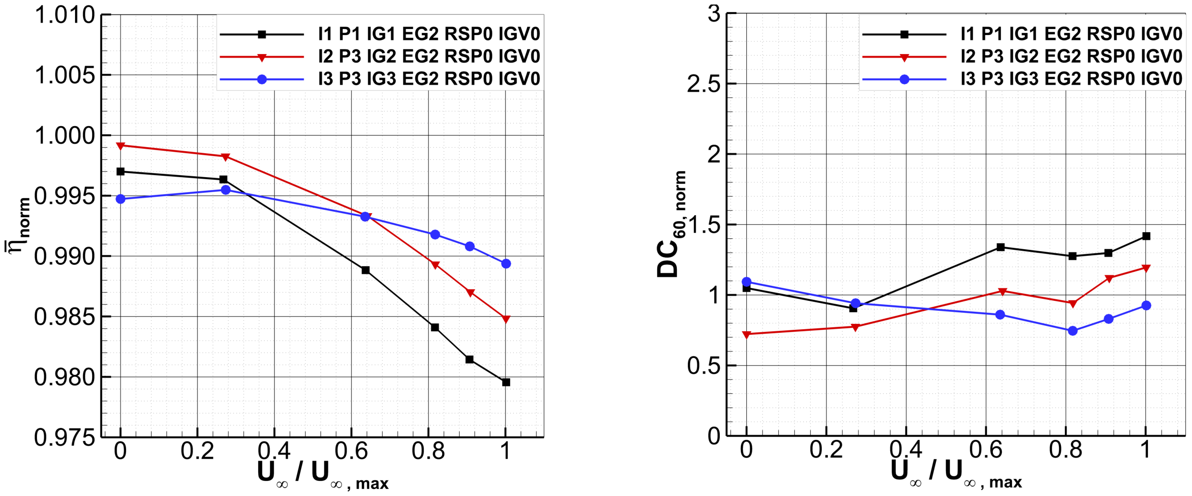

a) b)

Figure 6.2: Aerodynamic characteristics vs. relative freestream velocity of the geometries I1 P1, I2 P3 and I3 P3 for the maximum mass flow rate ratio, a) normalized total pressure ratio and b) normalized distortion coefficient.

Hereby, the intake 1 version shows the highest and the intake 3 the lowest levels of the AIP total pressure distortion, which can clearly be found in the AIP η_{norm} distributions, see Figure 6.3a and 6.3c.

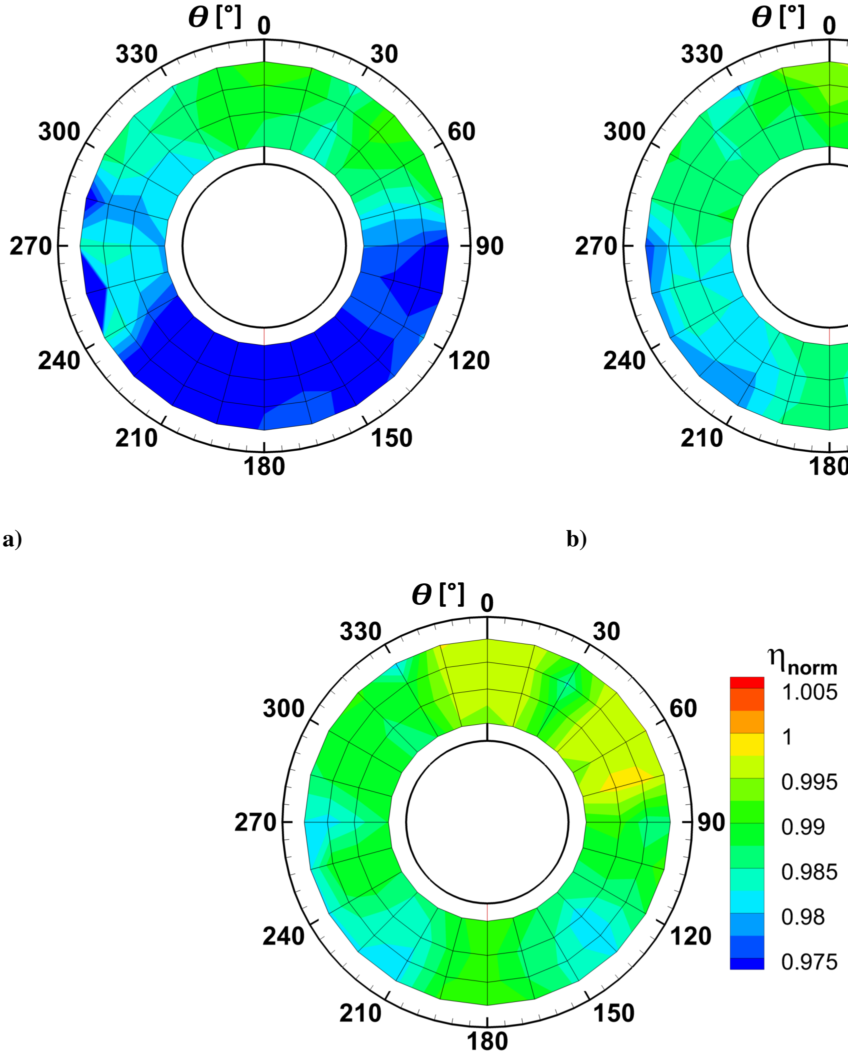

a)

b)

c)

Figure 6.3: Distribution of normalized total pressure ratio in AIP for a) I1 P1, b) I2 P3, b) I3 P3, at maximum relative freestream velocity, maximum mass flow rate ratio.

In Ref. [80], the same curve progression tendency as for the sideways facing intakes 1 and 2 has been found for another side intake configuration. From the $\bar{\eta}_{norm}$ as well as the $DC_{60,norm}$ perspective, a combination of the beneficial characteristics of the I2 variant for the low velocity regime and those of the I3 variant in the high velocity regime is desirable.

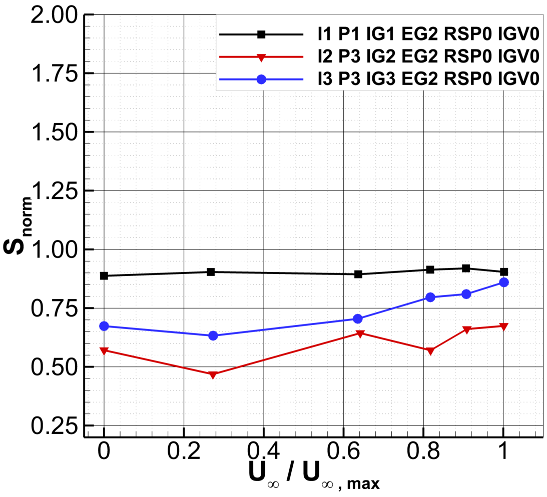

Figure 6.4: Normalized swirl coefficient vs. relative freestream velocity of the geometries I1 P1, I2 P3 and I3 P3 for the maximum mass flow rate ratio.

The normalized swirl angles of the three basic intakes are depicted in Figure 6.4. The swirl angles of the I1 configuration are nearly independent of the relative freestream velocity, whereas the intakes 2 and 3 feature a slight increase of the swirl coefficient with similar trends as their corresponding distortion characteristics. The intake 2 shows the lowest swirl angles and the intake 1 the highest swirl angles.

Considering the subsequent Figure 6.5, the estimated available engine power changes due to changes in η are presented for the intake 1 and 3 variants, in comparison to the variant I2 P3. Intake total pressure changes of 1 % are assessed to produce a change in engine power output of $\geq$ 2 %, according to Ref. [80]. From the total pressure ratio perspective, the basic intake 1 decreases available engine shaft power by $\Delta P_{avail} \approx 0.3 - 1.1$ %, comparing to the basic intake 2, see Figure 6.5a.

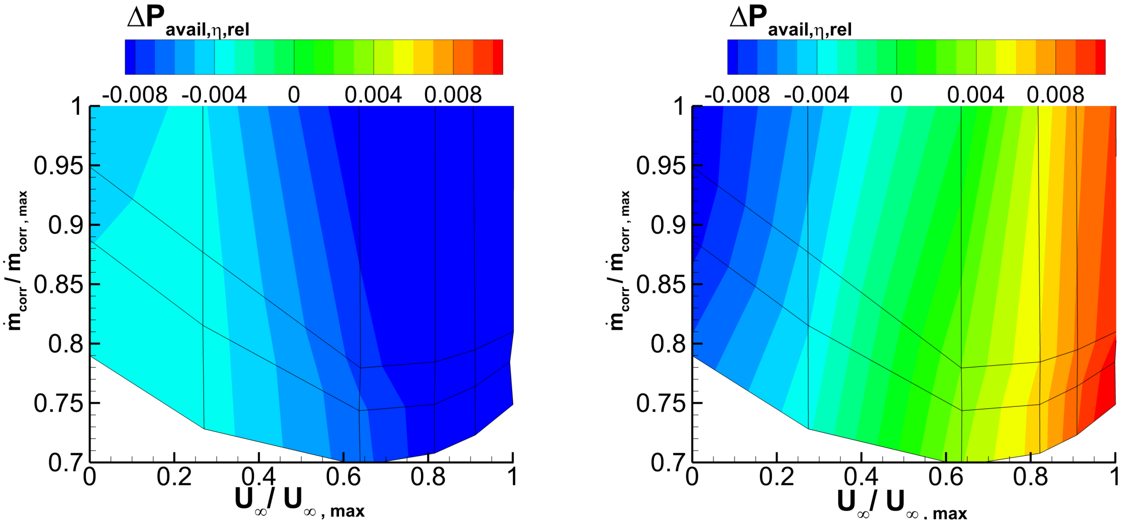

a) b)

Figure 6.5: Relative change of available engine power due to the total pressure ratio compared to the $I2P3$ configuration, vs. relative freestream velocity and mass flow rate ratio, a) I1 P1 and b) I3 P3.

Regarding Figure 6.5b, the basic intake 3 leads to a engine power change between $\Delta P_{avail} \approx -0.9 - (+1.1)$ %, increasing with increased velocity ratio. In both cases only minor influences due to engine mass flow rates are noticable. Engine power changes due to AIP flow uniformity are presented in Figures 6.6a and 6.6b, based on the findings of Ref. [77]. In case of the intake 1 variant, mainly small changes of the engine power output of $\Delta P_{avail} \approx -0.6 - (+0.09)$ % are determined. Hereby, no clear trend can be stated. Regarding the intake 3 geometry, changes of the available engine power of $\Delta P_{avail} \approx -0.7 - (+0.6)$ % are identified. For this configuration, in accordance with the $DC60$ progression, the intake 3 features higher engine power output levels for fast forward flight operation condition and lower engine power output levels for the low velocity regime, comparing to the intake 2 configuration.

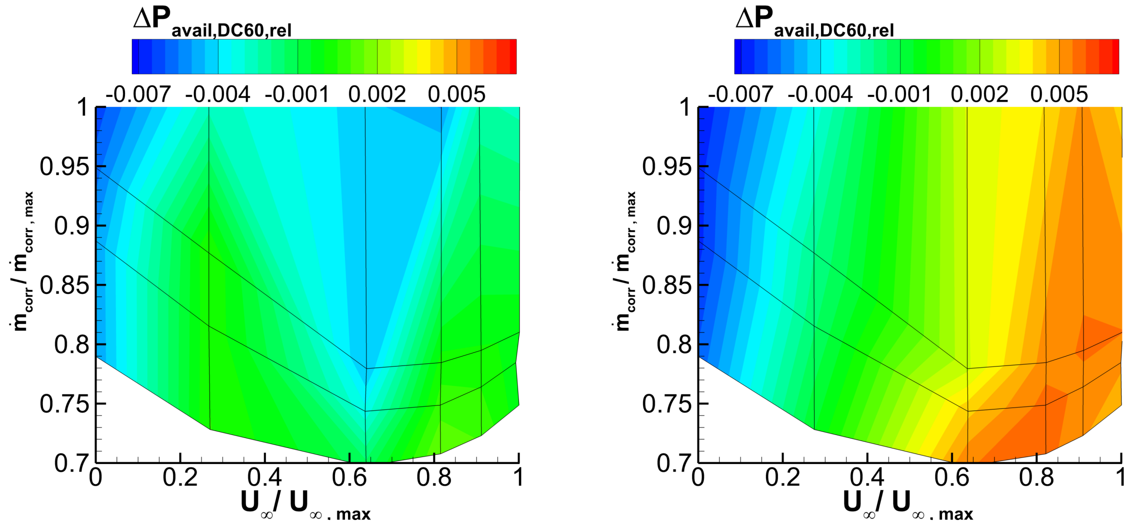

a) **b)**

Figure 6.6: Relative change of available engine power due to total pressure distortion compared to the I2 P3 configuration, vs. relative freestream velocity and mass flow rate ratio, a) I1 P1 and b) I3 P3.

In Figure 6.7, the combined engine power changes resulting from η and $DC60$ are presented for the intakes 1 and 3 in comparison to the intake 2. For velocity ratios of $U_\infty/U_{\infty,max} \leq 0.5$, the I1 P1 configuration leads to very low power changes compared to the I2 P3 configuration.

In the higher velocity regime, due to the lack of an cowling approach ramp, up to an engine power deterioration of $\Delta P_{avail} \approx -1.4$ % is expected. For the I3 P3 configuration, a gradual power progression from losses of $\Delta P_{avail} \approx -1.5\%$ for the zero velocity case to power gains of $\Delta P_{avail} \approx +1.6$ % in fast forward flight are estimated, in comparison to the I2 P3 variant.

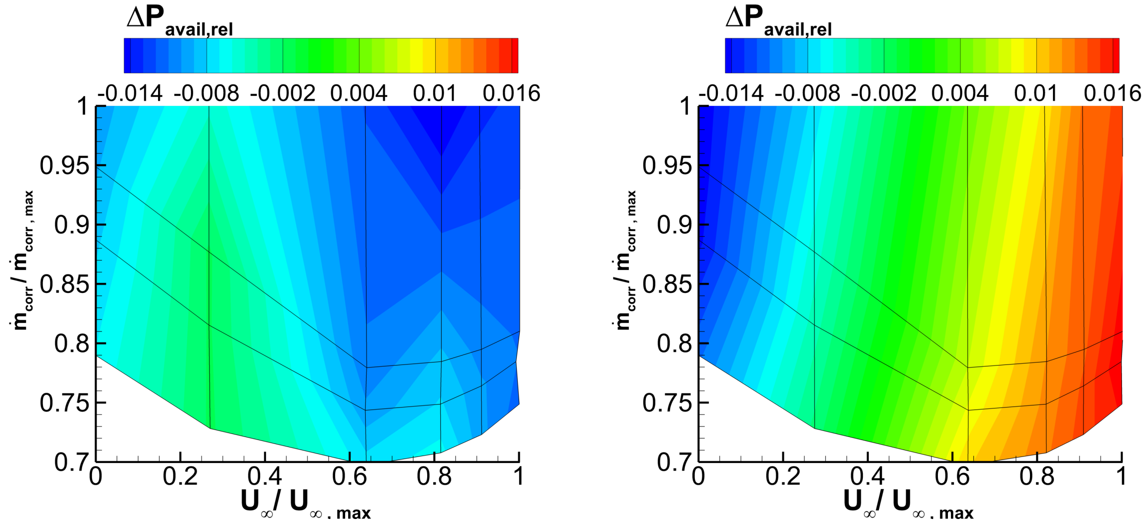

a) **b)**

Figure 6.7: Relative change of available engine power vs. relative freestream velocity and mass flow rate ratio, a) I1 P1, overall and b) I3 P3, overall.

6.2 Grid and Plenum Splitter

The intake 2 with the intake grid and the plenum chamber 3 including the splitter are displayed in Figure 6.8. The grid mount element as well as its installation are depicted in Figure 6.9. With the help of the $\bar{\eta}_{norm}$ $(U_\infty/U_{\infty,max})$ and the $DC_{60,norm}$ $(U_\infty/U_{\infty,max})$ characteristics (depicted in Figure 6.10 and Figure 6.12), the aerodynamic properties due to the plenum splitter, intake grid and the grid mount element are evaluated, at the example of the I2 intake and P2 plenum chamber combination for the maximum mass flow rate of $\dot{m}_{corr}/\dot{m}_{corr,max} = 1$.

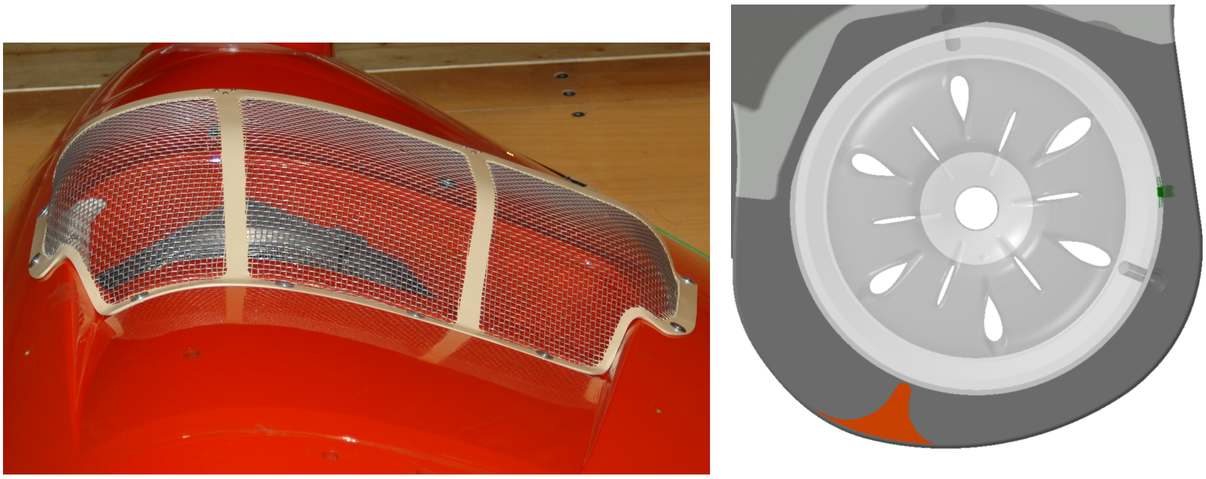

a) **b)**

Figure 6.8: a) I2 with intake grid, front view, b) plenum 3 (plenum 2 combined with plenum splitter).

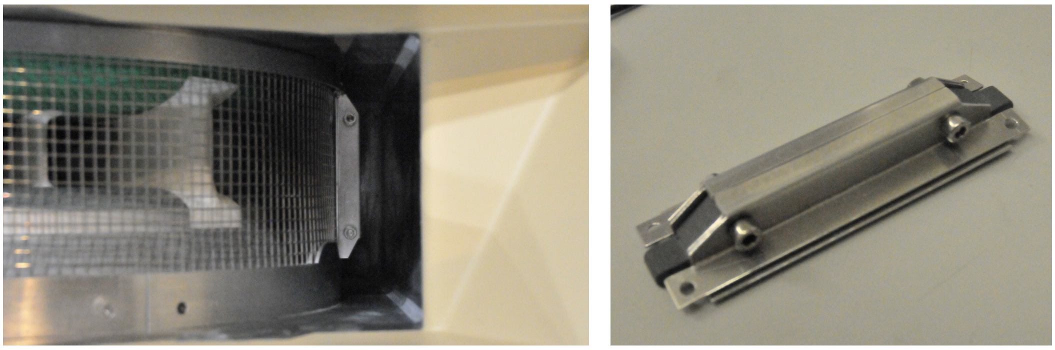

a) **b)**

Figure 6.9: a) Grid mount element installation, top view and b) grid mount element.

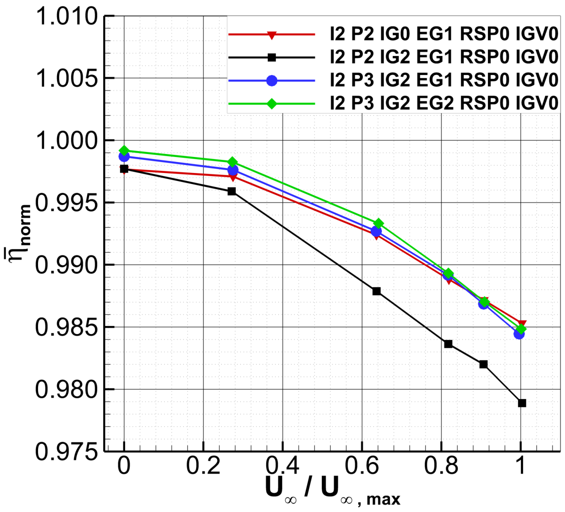

Figure 6.10: Normalized total pressure ratio vs. relative freestream velocity of the Intake 2 modifications for $\dot{m}_{corr}/\dot{m}_{corr,max} = 1$.

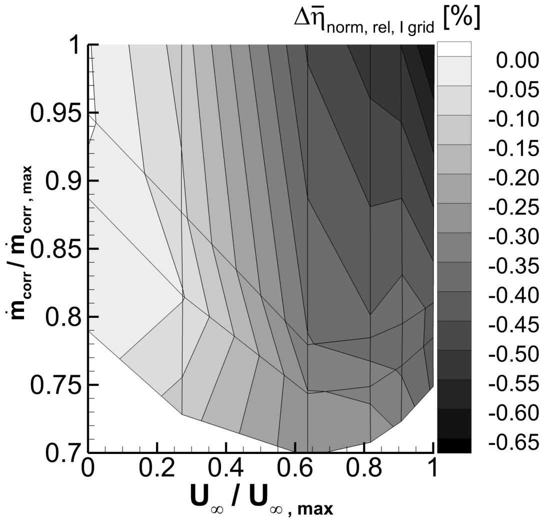

Figure 6.11: Relative difference in total pressure ratio due to intake grid vs. relative freestream velocity and mass flow rate ratio.

With an increase in relative freestream velocity, the intake grid reduces $\bar{\eta}_{norm}$. The maximum reduction is $\Delta\bar{\eta}_{norm,rel} = -0.6$ % for $U_\infty/U_{\infty,max} = 1$. This is due to the additional total pressure losses caused by the woven wire intake grid and the frame that is necessary to attach the grid to the cowling.

As depicted in Figure 6.10, total pressure losses $(1 - \bar{\eta})$ are nearly proportional to U_∞^2 which has been found in Ref. [80] for a similar static side intake. The relative difference of $\bar{\eta}_{norm}$ due to the intake grid (Figure 6.11) and thus additional total pressure losses satisfy the same tendency. An increase of mass flow rates has a minor effect.

For low freestream velocities, the AIP total pressure level is nearly not influenced by the intake grid.

The grid mount element is insignificant in terms of total pressure losses. As shown in Figure 6.12, the intake grid partly increases and decreases $DC_{60,norm}$ levels. The plenum splitter has a positive effect on the distortion in the entire velocity and mass flow rate range, see Figure 6.13. The plenum splitter diverts the flow at the bottom of the plenum chamber from the circumferential to a more radial direction. Thus, due to the improved inflow direction, in the EID region a further reduction of total pressure losses is achieved. In addition, the flow is straightened in the plenum chamber and losses in the lower part of the plenum chamber are markedly reduced, which is reflected also by a much more homogeneous AIP η_{norm} distribution, Figure 6.15. As a consequence, the splitter effectively compensates the intake grid's total pressure ratio reduction for the entire freestream velocity range.

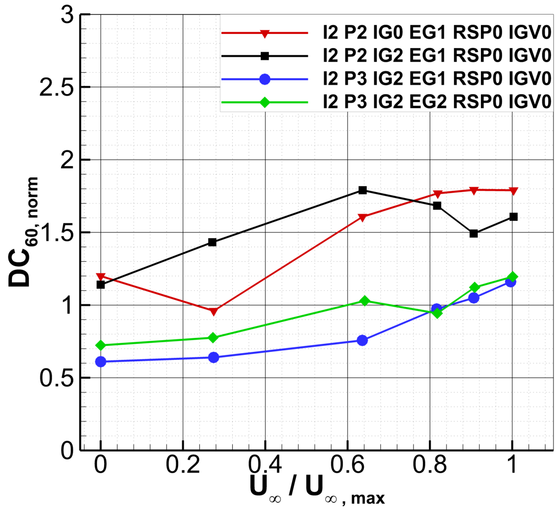

Figure 6.12: Normalized total pressure distortion vs. relative freestream velocity of the intake 2 plenum chamber and engine grid variants for the maximum mass flow rate ratio.

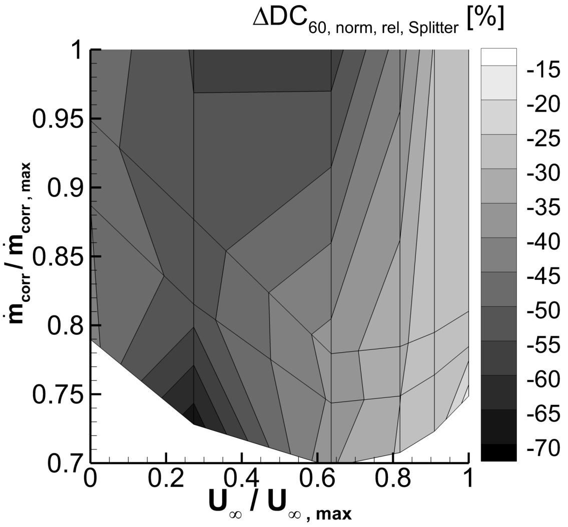

Figure 6.13: Relative difference in total pressure distortion due to plenum splitter vs. relative freestream velocity and mass flow rate ratio.

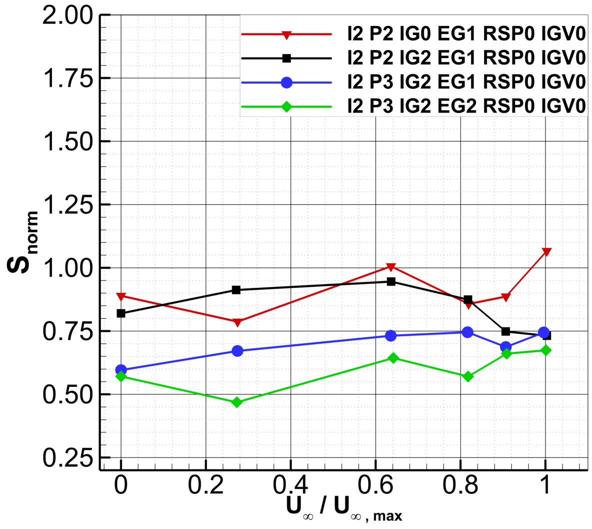

Figure 6.14: Normalized swirl coefficient vs. relative freestream velocity of the intake 2 plenum chamber and engine grid variants for $\dot{m}_{corr}/\dot{m}_{corr,max} = 1$.

Particularly in the low and mid velocity range, very low distortion levels occur. The grid mount element has only a slight effect on the AIP total pressure distortion. In the following, the configuration including intake 2, plenum chamber 3, intake grid 2, engine grid 2 and no retrofit modification (I2 P3 IG2 EG2 RSP0 IGV0) is the reference for the retrofit geometric variants.

In Figure 6.14, the normalized swirl coefficients of the intakte 2 variants are depicted. Again, the trends are similar to those of the distortion level characteristics. The application of the plenum splitter (P3 variants) reduces the swirl angles in the AIP by $\Delta S_{norm} \approx 20-30$ % in the entire operation range. In contrast to the distortion characteristics, the grid mount element further reduces the AIP swirl by $\Delta S_{norm} \approx 5-30$ %. For the velocity range, no clear trend of the swirl angle levels can be found. Nevertheless, as for the distortion characteristics, also for the average AIP swirl a slight increase with increasing velocities can be found.

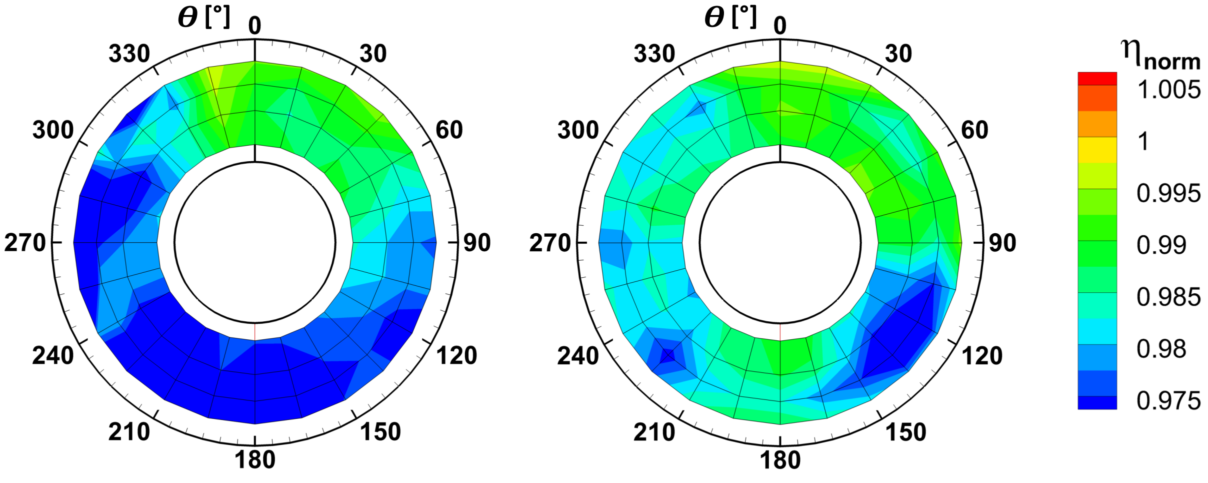

a) **b)**

Figure 6.15: Distribution of normalized total pressure ratio in AIP for a) I2 P2 IG2 EG1 RSP0 IGV0, b) I2 P3 IG2 EG1 RSP0 IGV0, maximum relative freestream velocity, maximum mass flow rate ratio.

In Figure 6.16, the assessed available engine power changes due to the application of an engine plenum chamber splitter and an intake grid are depicted at the example of the intake 2 version. Hereby, the parameters η and $DC60$ influence the available engine power. In both the change in engine power due to changed AIP total pressure levels and homogeneity, the splitter and intake grid feature an opposed trend.

As presented in Figure 6.16a, the local dynamic pressure of the oncoming flow creates an increase in total pressure loss due to the intake grid and also a similar behavior for the engine power output (compare Ref. [80]). Maximum engine power losses of $\Delta P_{avail,\eta,rel,grid} \approx -1.2$ % are expected in fast forward flight conditions. Due to the plenum splitter, the estimated engine power enhancement based on an increased AIP total pressure level increases with the freestream velocity as well as the engine mass flow rates (Figure 6.16b). The maximum expected enhancement is $\Delta P_{avail,\eta,rel,splitter} \approx +1.1$ %.
Regarding Figures 6.16c and d, due to changed AIP total pressure homogeneity, the intake grid leads to a slight increase in engine power output in the mid and low velocity regime and decreased engine power output in fast forward flight. The plenum splitter increases the total pressure homogeneity in the entire tested mass flow and velocity range, the highest increase in engine power output of $\Delta P_{avail,DC60,rel,splitter} \approx +1.6$ % is expected for the low and medium velocities.
Figures 6.16e and f represent the combined engine power change resulting from a superposition of the engine power change due to η and due to $DC60$. Considering the influence of the intake grid, a maximum deterioration of the engine power output of $\Delta P_{avail,rel,grid} \approx -0.9$ % is estimated for high velocities and a maximum power gain of $\Delta P_{avail,rel,grid} \approx 0.5$ % for low to medium velocities. The plenum splitter leads to an engine power output increase of $0.9\ \% \leq \Delta P_{avail,rel,splitter} \leq 2.4\ \%$. The splitter is a very effective means to increase engine power output of such plenum chamber type side intake configurations.

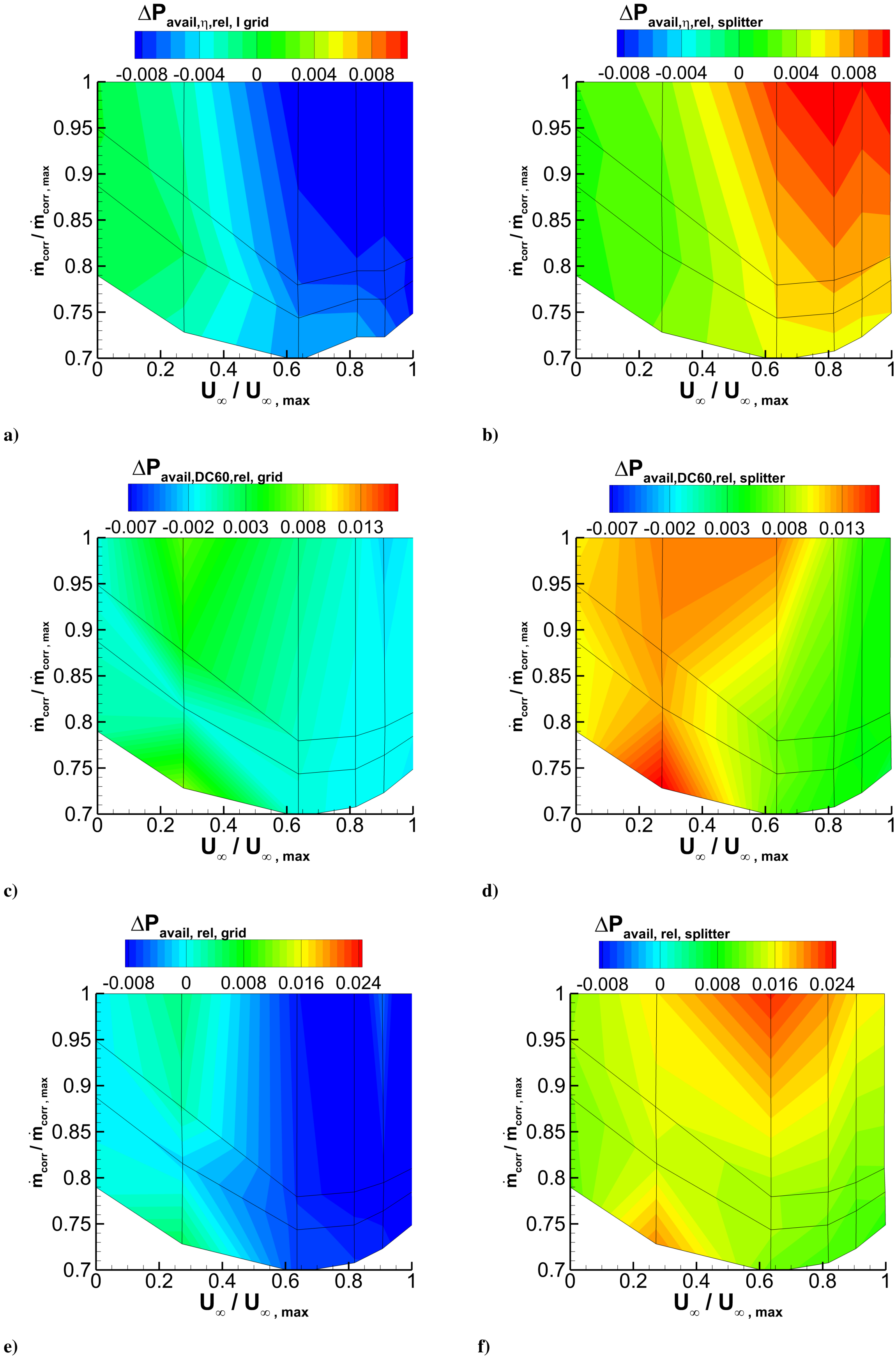

Figure 6.16: Relative change of available engine power vs. relative freestream velocity and mass flow rate ratio, a) grid influence, due to the total pressure ratio, b) splitter influence, due to the total pressure ratio, c) grid influence, due to total pressure distortion and d) splitter influence, due to total pressure distortion, e) grid influence, overall and f) splitter influence, overall.

6.3 Cowling Ramp and Plenum Chamber

In this section, the I1 P1 and I2 P3 configurations are compared with a configuration, which is a combination of the I1 intake and P3 plenum chamber. The related geometries are depicted in Figure 6.17. The aim is to distinguish clearly between the ramp's as well as the rounded plenum chamber's influence on the $\bar{\eta}_{norm}$, $DC_{60,norm}$ and S_{norm} characteristics, referring to Figure 6.18 and Figure 6.19. All following investigations are performed including intake grids.

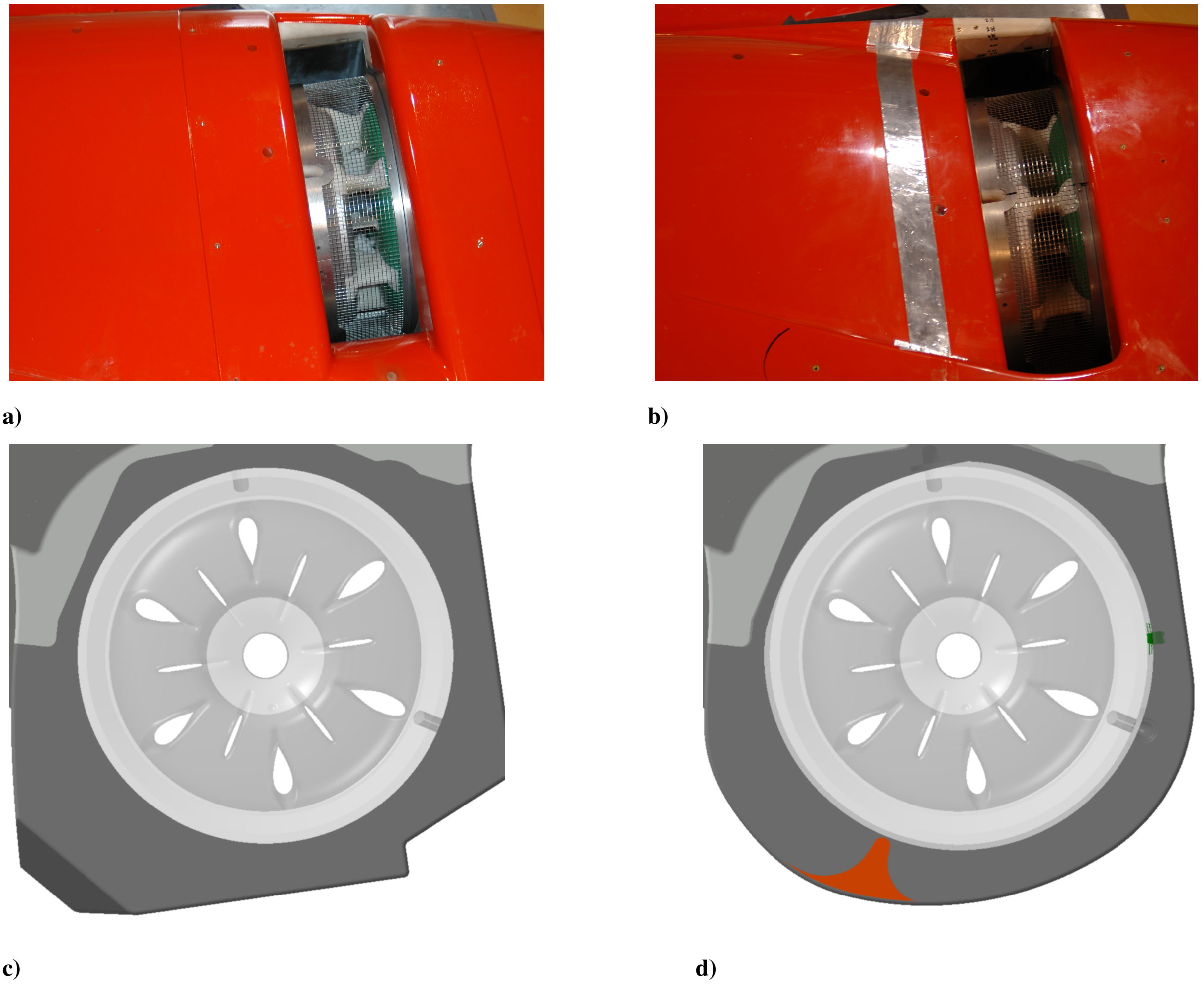

Figure 6.17: Geometry of I1 P1 and I2 P3 and its combinations, a) intake 1, top view, b) intake 2, top view, c) plenum 1 front view and d) plenum 3, front view.

At first, the $\bar{\eta}_{norm}$ characteristics are regarded, see Figure 6.18a. It is found that the rounded plenum chamber leads to an increase of the total pressure ratio by $\Delta\bar{\eta}_{norm}$= 0.12 - 0.26 %. The ram effect of the I2 intake variant leads to a further increase of $\Delta\bar{\eta}_{norm}$ of $0.06 - 0.42$ %. Especially for the higher freestream velocities, $\bar{\eta}_{norm}$ is mainly raised due to the ramp of the I2 intake.

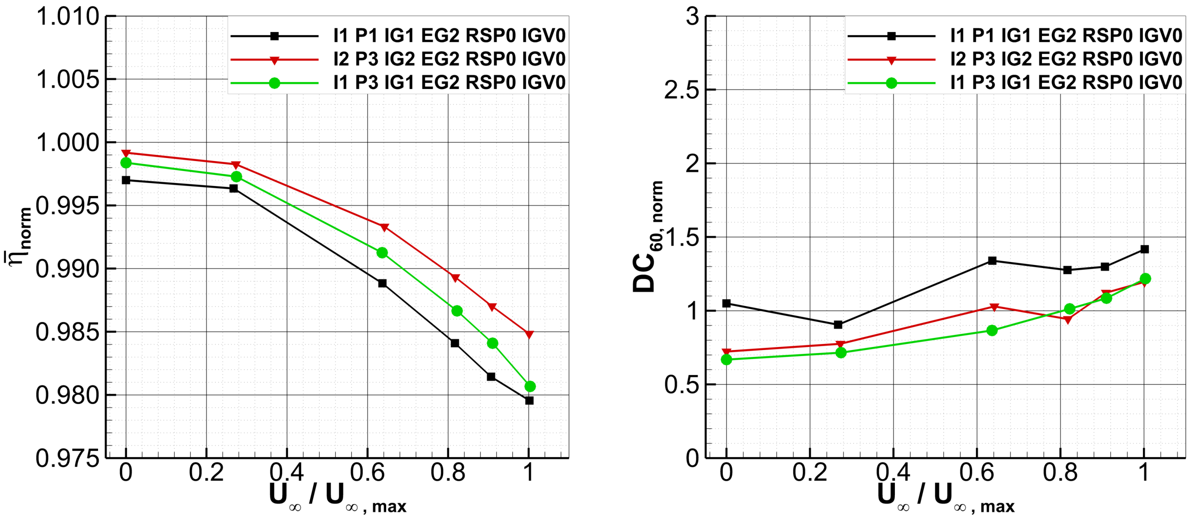

a) **b)**

Figure 6.18: Aerodynamic characteristics vs. relative freestream velocity of I1 P1, I2 P3 geometries and the combination I1 intake/ P3 plenum chamber, maximum mass flow rate ratio, a) normalized total pressure ratio and b) normalized distortion coefficient.

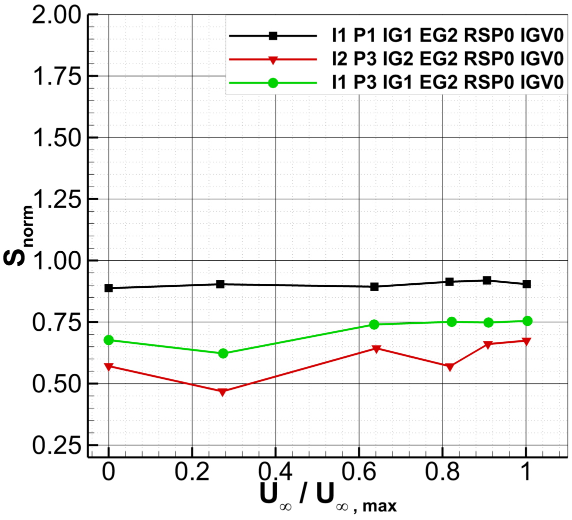

Figure 6.19: Normalized swirl coefficient vs. relative freestream velocity of the I1 P1, I2 P3 geometries and the combination I1 intake/ P3 plenum chamber for the maximum mass flow rate ratio.

As depicted in Figure 6.18b, the $DC_{60,norm}$ progression of the mixed geometry is very similar to the I2 P3 configuration over the entire velocity range tested. Thus, the plenum chamber has a main influence on the AIP total pressure distortion. The P3 plenum chamber including the splitter leads to a more homogeneous AIP total pressure distribution as already shown before in Figure 6.3.

Figure 6.19 represents the influences on the AIP swirl progression due to the cowling approach ramp and the rounded plenum chamber including a plenum splitter. The mean swirl in the AIP is reduced by $\Delta S_{norm} \approx 12 - 24$ % due to the cowling ramp, a smaller separation occurs for the I2 variant compared to the I1 variant and thus leading to lower flow angularity downstream. The rounded plenum chamber with the splitter (P3) is even more effective. It lowers the AIP swirl levels by $\Delta S_{norm} \approx 17 - 31$ %. The combination of both the rounded plenum chamber including a splitter and the cowling ramp, nearly a reduction of 50 % in AIP swirl is achieved.

In Figure 6.20a, the difference plot of $\Delta\bar{\eta}_{norm,rel,ramp}(U_\infty/U_{\infty,max}, \dot{m}_{corr}/\dot{m}_{corr,max})$ is given which results from calculating the relative difference of $\bar{\eta}_{norm}$ for the I2 P3 and the I1 P3 configuration. It is noticeable that the total pressure gain caused by the ramp on the cowling is mainly dependent on the freestream velocity and only slightly influenced by the mass flow rate. For $\dot{m}_{corr}/\dot{m}_{corr,max} = 1$, a nearly quadratic dependency of $\Delta\bar{\eta}_{norm,rel,ramp}$ can be found as presented in Figure 6.20b.

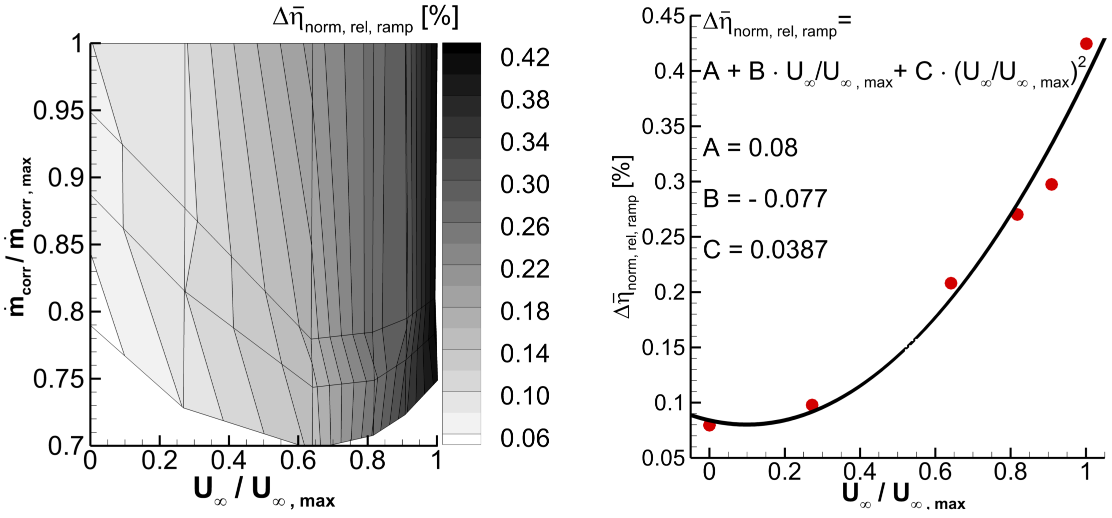

a) **b)**

Figure 6.20: Relative difference in total pressure ratio of I1 intake and I2 intake combined with P3 plenum chamber a) vs. relative freestream velocity and mass flow rate ratio and b) vs. relative freestream velocity, for the maximum mass flow rate ratio.

In Figure 6.21, the estimated engine power changes are presented to evaluate the distinct influence of the cowling approach ramp and the plenum chamber. Considering Figures 6.21a, also a quadratic increase in engine power with increase in velocity ratio as for the total pressure progression is valid. The contribution to the increase in engine power due to the rounded plenum chamber is smaller than the portion due to the approach ramp. Here, the enhancement of the engine power increases similarly with both the velocity ratio and engine mass flow rates. For the change of engine power due to changes in the DC_{60} coefficient, no clear trend is obtained. Nevertheless, the cowling ramp has just a small influence on DC_{60} and therefore originates engine power changes below $\Delta P_{avail,DC60,rel,ramp} \approx |0.2\ \%|$. On the other hand, the plenum chamber has a higher influence on AIP distortion and thus on engine power, especially in the lower and mid velocity regime. Figures 6.21e and 6.21f reflect the overall power changes due to the plenum chamber and the ramp, respectively. The cowling ramp mainly influences the pressure recovery and therefore engine power changes in the higher velocity regime, whereas the plenum chamber has a stronger effect on the AIP distortion and engine power changes due to DC_{60}.

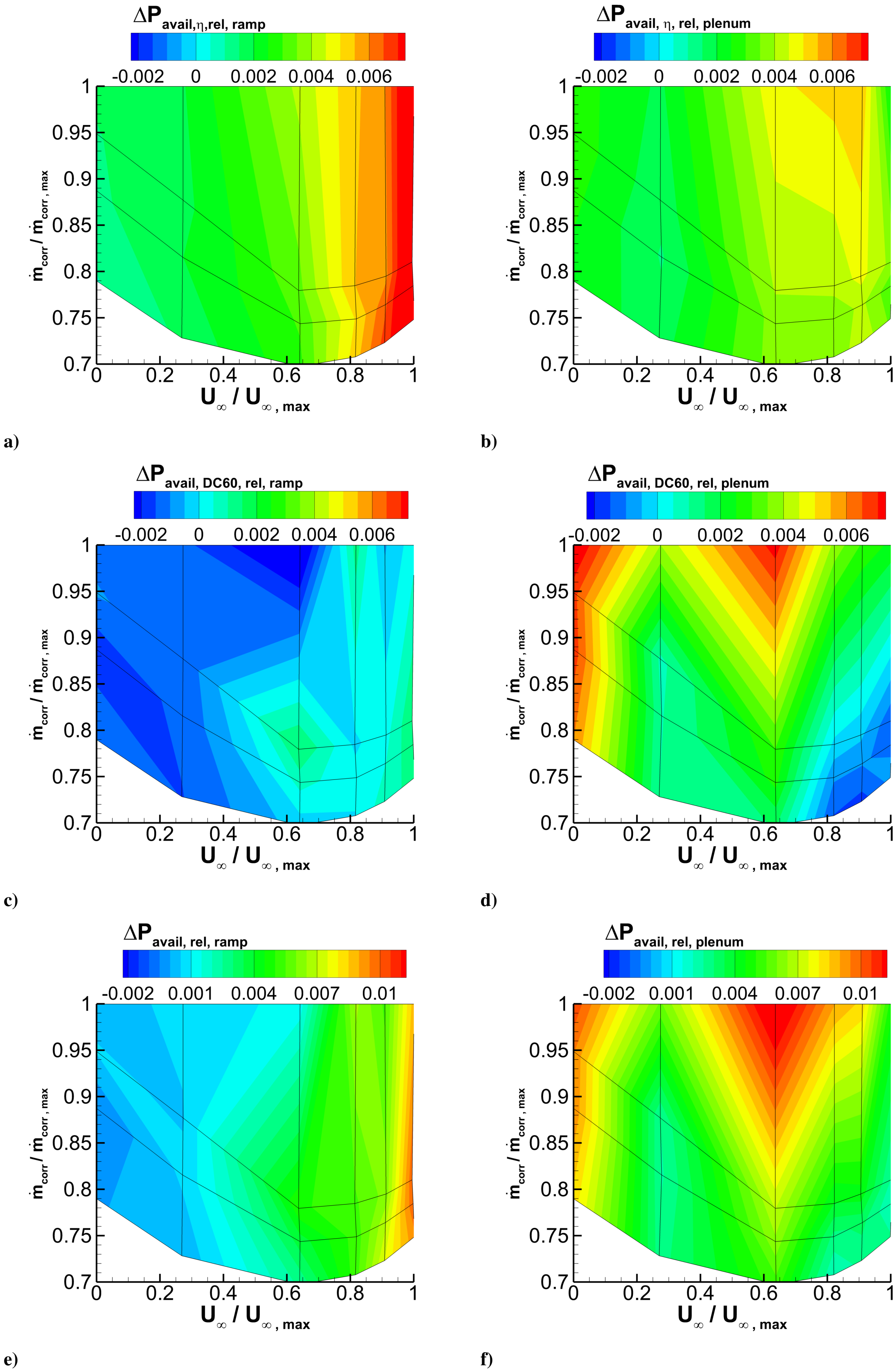

Figure 6.21: Relative change of available engine power vs. relative freestream velocity and mass flow rate ratio, a) ramp influence, due to the total pressure ratio, b) plenum influence, due to the total pressure ratio, c) ramp influence, due to total pressure distortion, d) plenum influence, due to total pressure distortion, e) ramp influence, overall and f) plenum influence, overall.

6.4 Retrofit Geometric Variants

In the subsequent section, main results of a parameter study of retrofit modifications for a reference side intake geometry (I2 P3 configuration) are investigated. The modifications include rear spoilers with variable heights and lengths and an intake guide vane at three different streamwise locations. Four different rear spoilers are tested in combination with the I2 intake to find the best combination of height and length of the rear spoiler, as shown in Figure 6.22. The intake overlapping ratio $R = l_{RSP}/l_I$ describes the relative overlapping of the intake opening (axial extend l_I) due to the rear spoiler length l_{RSP}. Furthermore, a relative height parameter $H_{rel} = h_{RSP}/h_{I2}$ defines the ratio of the rear spoiler height h_{RSP} and the back intake lip height of intake 2, h_{I2}, both measured from the front intake lip. The purpose of the rear spoilers is to increase the static pressure upstream of the intake opening (ram effect). The intake guide vane is meant to foster the deflection of the ingested air around the front intake lip (see Figure 6.22) to reduce the size of separated flow regimes directly downstream of the intake lip as achieved in Ref. [43]. The intake guide vane‘s relative position $P_{IGV} = (1 - l_{IGV})/l_I$ is defined by the relation of its trailing edge position from the back intake lip l_{IGV} relative to the overall axial extend l_I of the intake opening. All parameter values are listed in Table 6.1.

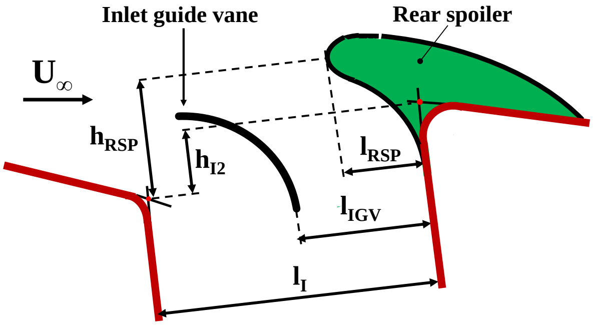

Figure 6.22: Schematic display of retrofit modifications and parametrization.

Retrofit variant	Parameter R	H_{rel}	P_{IGV}
RSP 1	0.29	1.47	-
RSP 2	0.5	1.75	-
RSP 3	0.29	1.91	-
RSP 4	0.5	2.19	-
IGV 1	-	-	0.43
IGV 2	-	-	0.5
IGV 3	-	-	0.57

Table 6.1: Rear spoiler parameter values and intake guide vane positioning.

Subsequently, Figures 6.23 - 6.25 are referring to the effect on $\bar{\eta}_{norm}$, $DC_{60,norm}$ and S_{norm} vs. relative freestream velocity. The variation of the engine mass flow rate has a minor influence on the effectiveness of the rather externally attached retrofit modifications. Therefore, only the results of the maximum mass flow rate are considered. As illustrated in Figure 6.23a, concerning total pressure recovery, the short rear spoiler variants ($R = 0.29$) are better suitable for low velocity conditions whereas the high variants ($1.91 < H_{rel} < 2.19$) are beneficial for fast forward flight conditions. In analogy with the results obtained for the intake 3 variant in Section 6.1, in the low velocity regime, additional total pressure losses occur. This is due to a stronger flow deflection and resulting regions of separated flow on the inside part of the rear spoiler.

Covering the intake opening (increasing R) thus deteriorates the total pressure recovery $\bar{\eta}_{norm}$. Due to an enhanced ram effect for fast forward flight, higher $\bar{\eta}_{norm}$ levels are achieved for the higher rear spoilers. Generally, the high and short rear spoiler is the best combination of the R and H_{rel} variation

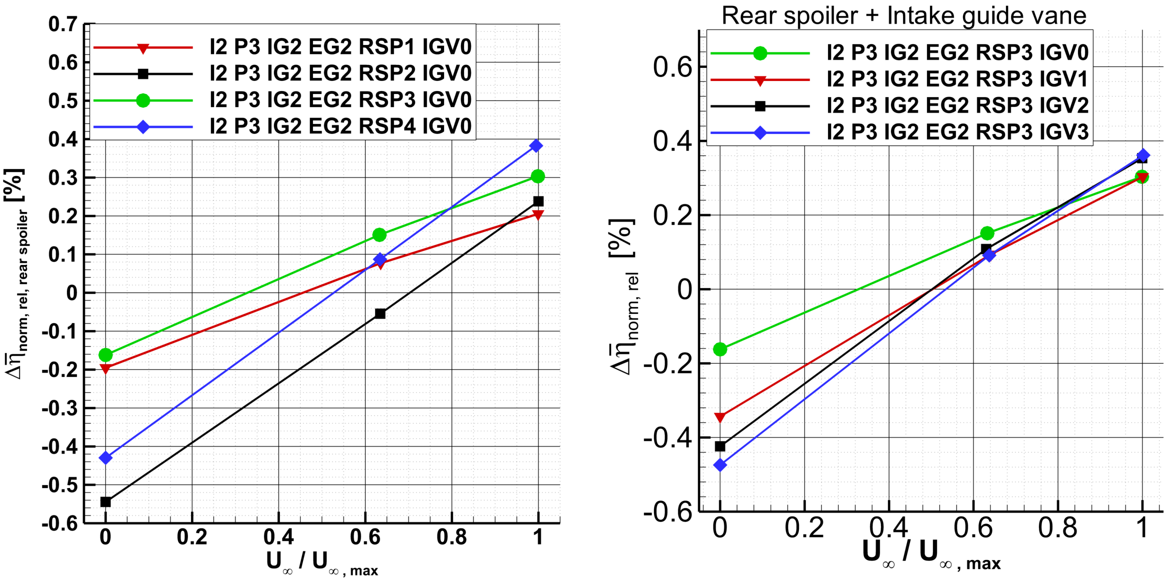

a) **b)**

Figure 6.23: Relative difference in normalized total pressure ratio of retrofit variants compared to the I2 P3 configuration vs. relative freestream velocity, maximum mass flow rate ratio, a) rear spoilers and b) rear spoilers and intake guide vane.

that features acceptable pressure losses in all flight conditions. Based on this configuration, an intake guide vane at three different positions P_{IGV} is investigated, cp. Figure 6.23b. Hereby, the front, middle and back positioning of the intake guide vane is denoted as "IGV1, 2 and 3". In terms of $\bar{\eta}_{norm}$, only minor AIP total pressure gains are achieved in fast forward flight due to the improved flow deflection around the front intake lip for all three positions compared to the "pure" rear spoiler configuration. As an effect of the increased blockage of the intake opening, the intake guide vanes significantly reduce $\bar{\eta}_{norm}$ for $U_\infty/U_{\infty,max} \rightarrow 0$, see Figure 6.23b. Regarding $DC_{60,norm}$ in Figure 6.24a, all rear spoiler variants reveal a higher level than the I2 P3 configuration without rear spoiler for low $U_\infty/U_{\infty,max}$. By contrast, the rear spoilers, specifically the high versions, reduce the total pressure distortion in the AIP at high $U_\infty/U_{\infty,max}$. Also in terms of total pressure distortion, short rear spoilers are advantageous in the low velocity regime. Referring to Figure 6.24b, the installation of the guide vanes leads to an increase of the $DC_{60,norm}$ coefficient at low relative freestream velocity. The total pressure distortion is reduced by the guide vanes at relative high velocities. In summary, the intake guide vane in the front position combined with the high and short rear spoiler provides the lowest levels of total pressure distortion.

The alteration of mean AIP swirl angles due to the retrofit modifications is illustrated in Figures 6.25a and 6.25b. Regarding the rear spoilers, the low and short variant induces the least changes over the entire velocity regime, close to zero. But generally, only minor influences are detected for all rear spoiler configurations. Regarding Figure 6.25b, due to the shielding of the intake, higher swirl angles are noticable in the lower velocity regime for all three rear spoiler and intake guide vane combinations, similar to the other coefficients. For the mid and high velocities, swirl angle changes close to zero occur. In the following, changes in available engine power are assessed based on the assumptions made in Ref. [80] for changes in total pressure ratio (i.e. changes in total pressure losses) as well as due to changes in the $DC60$ coefficient (i.e. AIP flow uniformity), based on Ref. [77].

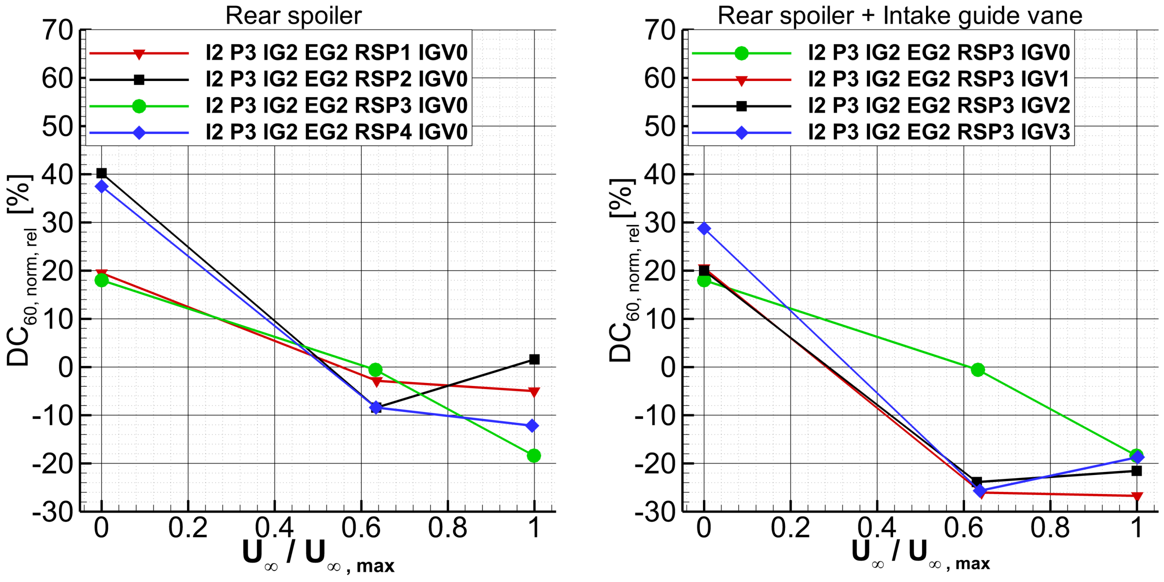

a) b)

Figure 6.24: Relative difference in normalized total pressure distortion of retrofit variants compared to the I2 P3 configuration vs. relative freestream velocity, maximum mass flow rate ratio, a) rear spoilers and b) rear spoilers and intake guide vane.

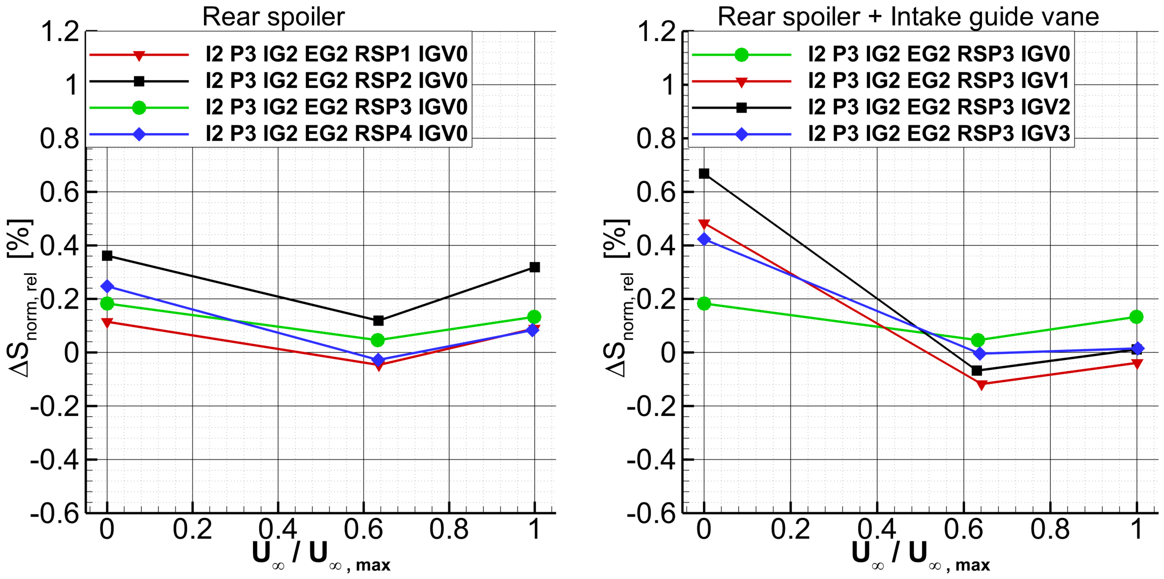

a) b)

Figure 6.25: Relative difference in normalized swirl coefficient of retrofit variants compared to the I2 P3 configuration vs. relative freestream velocity, maximum mass flow rate ratio, a) rear spoilers and b) rear spoilers and intake guide vane.

The available engine power changes due to the intake guide vane positioning are depicted in Figures 6.26a and 6.26b. The regarded configurations represent the combination of the intake guide vane with the high and short rear spoiler variant (R = 0.29 and H_{rel} = 1.91). For U_{max}, the increase in engine power due to changes in total pressure level as well as due to total pressure distortion are of similar magnitudes. Considering all engine power gains, for the fast-forward flight condition ($U_\infty/U_{\infty,max} = 1$ and $\dot{m}_{corr}/\dot{m}_{corr,max} = 1$), the foremost guide vane position is the best variant. Power gains due to higher total pressure of 0.6 % and due to a lowered distortion of 0.55 % can be estimated. For the zero velocity case, combined engine power output losses between 1 % and 1.4 % are assessed for the three guide vane positions, increasing from the foremost to the endmost position, corresponding to increasing intake shielding.

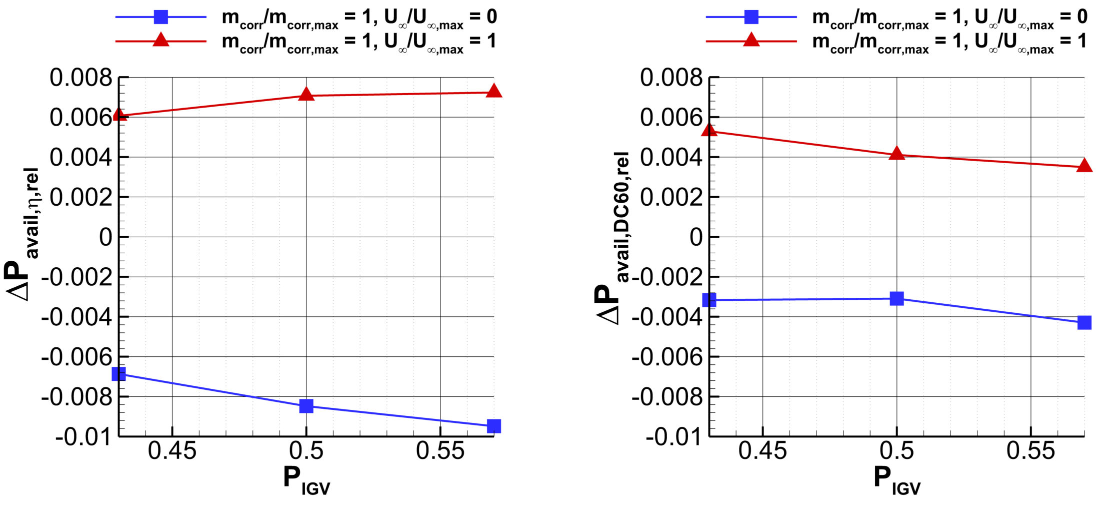

a) **b)**

Figure 6.26: Variation of intake guide vane position P_{IGV}, relative change of available engine power a) portion due to total pressure ratio, zero and maximum relative freestream velocity, maximum mass flow rate ratio and b) portion due to total pressure distortion, zero and maximum relative freestream velocity, maximum mass flow rate ratio.

Both due to increased total pressure losses and higher AIP total pressure distortion, for the zero velocity case, a reduction of the available engine power can be expected compared to the intake 2 plenum chamber 3 variant for all retrofit rear spoiler configurations, as depicted in Figures 6.27a and 6.27b. In accordance with the progressions of the total pressure ratio and the distortion coefficient, for the most shielded side intake configurations (R = 0.5), reductions in the available engine power of 0.8 – 1.1 % and 0.6 % can be assumed due to higher total pressure losses and higher distortion levels, respectively. The low and short rear spoiler variant originates approximate available engine power reductions of 0.3 % and 0.2 % due to higher total pressure losses and distortion, respectively. Considering Figures 6.27c and 6.27d, especially the high rear spoiler variants increase the available engine power. The high and short variant ($R = 0.29$ and $H_{rel} = 1.91$) leads to an increase of available engine power of 0.6 % and 0.34 % due to increase total pressure levels and reduced AIP distortion. For the high and long variant ($R = 0.5$ and $H_{rel} = 2.19$), engine power increases due to higher η and lowered $DC60$ levels of 0.76 % and 0.21 % are expected.

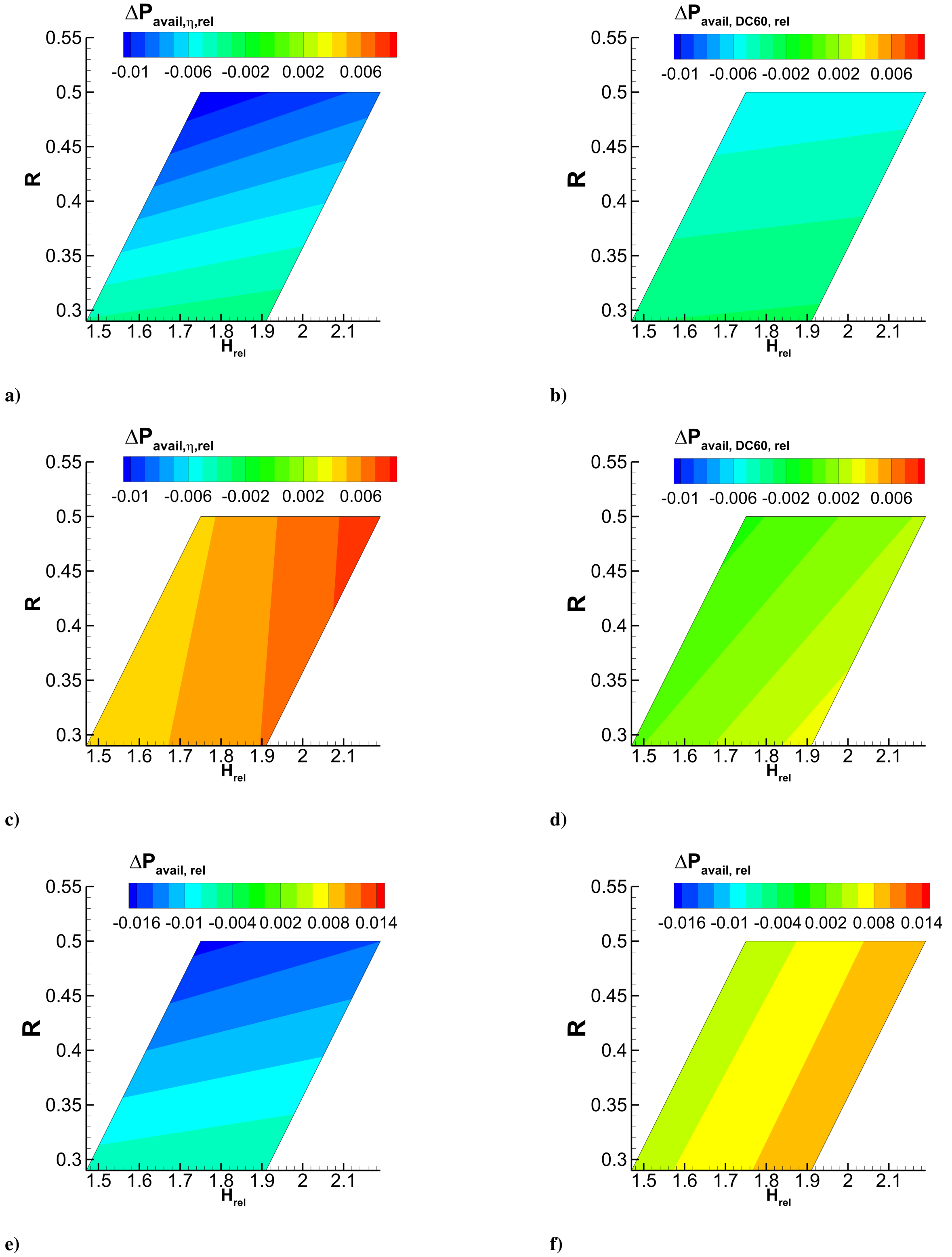

Figure 6.27: Variation of rear spoiler overlapping ratio R, and relative height H_{rel}, relative change of available engine power a) portion due to total pressure ratio, zero relative freestream velocity, maximum mass flow rate ratio b) portion due to total pressure distortion, zero relative freestream velocity, maximum mass flow rate ratio, c) portion due to total pressure ratio, maximum relative freestream velocity, maximum mass flow rate ratio, d) portion due to total pressure distortion, maximum relative freestream velocity, maximum mass flow rate ratio, e) combined power change, zero relative freestream velocity, maximum mass flow rate ratio and f) combined power change, maximum relative freestream velocity, maximum mass flow rate ratio.

6.5 Comparison of Basic and Best Retrofit Variants

In the following, considering Figures 6.28 - 6.31, the results of the best retrofit modifications are compared to the basic geometries I1 P1, I2 P3 and I3 P3 to summarize the influences on the $\bar{\eta}_{norm}$ and $DC_{60,norm}$ characteristics in dependence on the relative freestream velocity as well as on engine mass flow rate ratios.

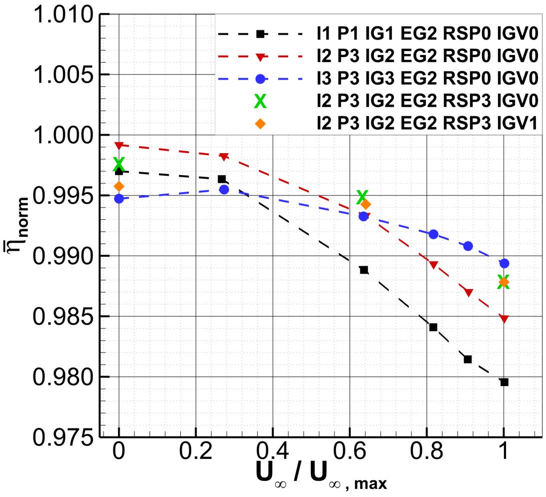

Figure 6.28: Normalized total pressure ratio vs. relative freestream velocity of the geometries I1 P1, I2 P3 and I3 P3 and best retrofit variants for maximum mass flow rate ratio.

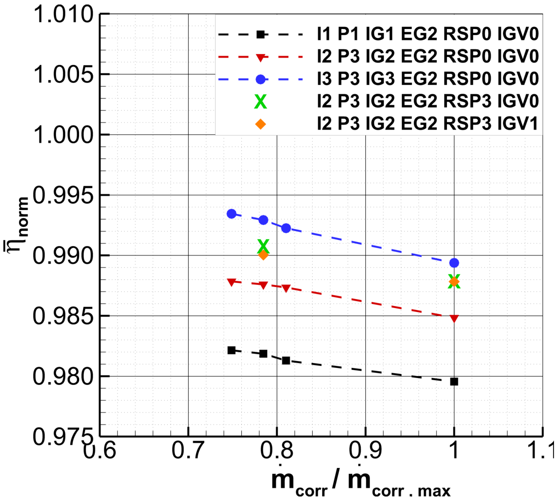

Figure 6.29: Normalized total pressure ratio vs. mass flow rate ratio of the geometries I1 P1, I2 P3 and I3 P3 and best retrofit variants for $U_{\infty,max}$.

For the highest velocities, the I3 intake features slightly higher total pressures caused by the scoops‘ larger cross section compared to the rear spoilers. In the low velocity regime, the I2 intake with its uncovered intake opening (cp. Figure 6.22) provides the highest total pressures followed by the retrofit variant without intake guide vane and the intake 1 variant. Figure 6.29 presents the levels of $\bar{\eta}_{norm}$ for all tested engine mass flow rates at the maximum relative freestream velocity. A nearly linear decrease in $\bar{\eta}_{norm}$ with similar gradients is noticeable for all intake geometries. Referring to the distortion characteristics in dependence of $U_\infty / U_{\infty,max}$, Figure 6.30, the retrofit variant including the intake guide vane combines the benefits of the I2 and I3 intake versions, for the entire operation range, thus, leading to the lowest variation and level of $DC_{60,norm}$.

In Figure 6.31 , the $DC_{60,norm}$ dependence on engine mass flow rate ratios at a constant relative freestream velocity of $U_\infty / U_{\infty,max} = 1$ is presented. For all intake shapes, a slight decrease in $DC_{60,norm}$ can be identified with an increase in mass flow rates. The total pressure distortion of the I3 intake as well as the retrofit variants are nearly identical and at the lowest level of all variants. Both the total pressure ratio and distortion characteristics prove the better suitability of the forward facing side air intakes (intake 3 and intake 2 with retrofit rear spoilers) for higher freestream velocities and the sideways facing engine air intakes (intake 1 and intake 2) for the lower velocity regime, which is in good agreement with Figure 2.15, Refs. [61, 65] as well as Figure 2.8, Ref. [80].

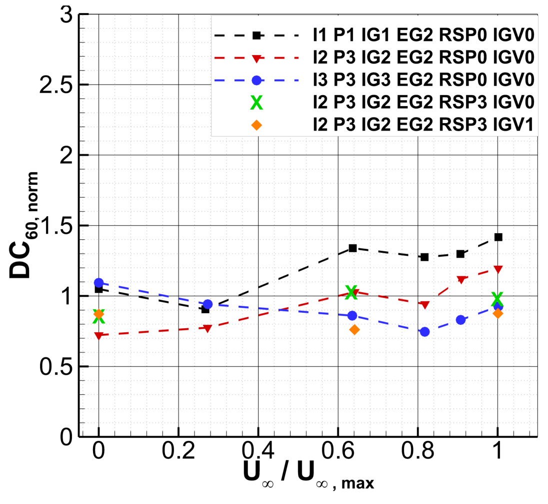

Figure 6.30: Normalized distortion coefficient vs. relative freestream velocity of the geometries I1 P1, I2 P3 and I3 P3 and best retrofit variants for maximum mass flow rate ratio.

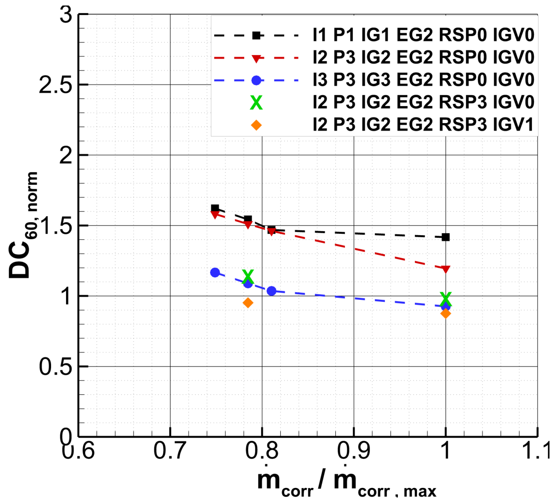

Figure 6.31: Normalized distortion coefficient vs. mass flow rate ratio of the geometries I1 P1, I2 P3 and I3 P3 and best retrofit variants for maximum relative freestream velocity.

6.5.1 AIP Detail Investigation

Further investigations of η_{norm} AIP distributions corresponding to the $\bar{\eta}_{norm}$ and $DC_{60,norm}$ trends of section 6.5 are presented. The I2 P3 configuration serves as the reference for the optimization and as geometrical basis for the retrofit modifications. Therefore, the corresponding AIP data is compared to that of the two best retrofit versions. Subsequently, two combinations of operating conditions of $U_\infty/U_{\infty,max}$ and $\dot{m}_{corr}/\dot{m}_{corr,max}$ are selected for which the largest differences in $\bar{\eta}_{norm}$ and $DC_{60,norm}$ occur. The first operation condition is $U_\infty/U_{\infty,max}$ =0, $\dot{m}_{corr}/\dot{m}_{corr,max} = 1$.

The η_{norm} distribution, as presented in Figure 6.32, clearly reflects the trend of Figure 6.28. For low freestream velocities air is ingested into the intake entry from all sides. The completely uncovered I2 intake is therefore advantageous compared to the partly covered configurations including a rear spoiler and intake guide vane. These elements promote local flow separation for $U_\infty/U_{\infty,max} \rightarrow 0$. Thus, the area of high η_{norm} values as well as the overall level increase in the order of c), b) and a), as depicted in Figure 6.32. Generally, η_{norm} is low in the area of the AIP between $90° < \theta < 270°$. The air which enters the EID in the related sector has passed through turbulent regions of the flow field in the upstream plenum chamber. As an affect, its total pressure level is reduced. Furthermore, significant deviation from a radial inflow direction at the EID entry leads to separations at the EID guide vanes (cp. Figure 3.17). As a consequence, further total pressure losses occur. In the top part of the AIP, the highest η_{norm} levels are noticeable due to the fact that air from the undisturbed freestream flow is particularly ingested here and enters the EID in the radial direction (Ref. also [38]). The numerical results obtained for the baseline configuration help to understand the corresponding phenomenology (Ref. section 5.2).

The regions corresponding to highest losses are located very similarly for the three configurations. The small differences in $DC_{60,norm}$ (cp. Figure 6.30) are not clearly identifiable from the η_{norm} AIP distributions. Particularly in the upper AIP region, characterized by overall high dynamic pressures, wakes of the EID guide vanes are visible for $\theta = 30°, 90°, 270°$ and $330°$. The corresponding η_{norm} deficits are

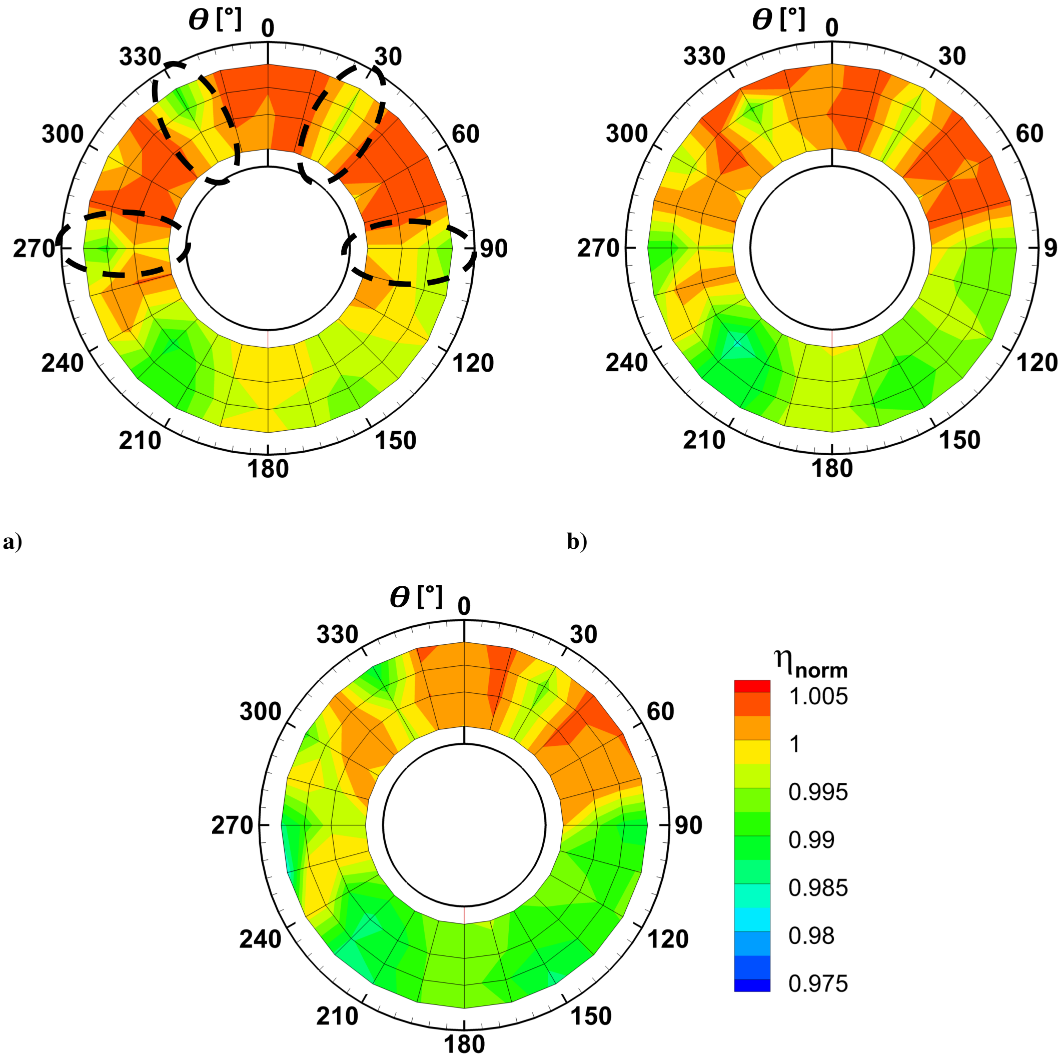

a)

b)

c)

Figure 6.32: Distribution of normalized total pressure ratio in AIP for a) I2 P3 IG2 EG2 RSP0 IGV0, b) I2 P3 IG2 EG2 RSP3 IGV0 c) I2 P3 IG2 EG2 RSP3 IGV1, zero relative freestream velocity, maximum mass flow rate ratio.

shown exemplarily in Figure 6.32a and marked with black dashed circles. The fact that the wakes are not transported in circumferential direction shows that in this regime the radial direction is the prevailing inflow direction at the EID entry. The second operation point is characterized by $U_\infty/U_{\infty,max}$ =1, $\dot{m}_{corr}/\dot{m}_{corr,max}$ = 1, see Figure 6.33. The trend is reversed for this operation point. The area of low η_{norm} in the regime of 90° $< \theta <$ 170° is clearly reduced due to the rear spoiler compared to the I2 intake, as depicted in Figure 6.33a and b. The intake guide vane leads to a different distribution with even higher η_{norm} levels in this area. The location of the region of decreased η_{norm} in between 200° $< \theta <$ 280° is similar for all three configurations, with the lowest level of η_{norm} for the I2 intake. Overall, the trend of the $\bar{\eta}_{norm}$ coefficient of Figure 6.28 is confirmed. The very homogeneous η_{norm} distributions for the two retrofit variants clearly reflect the decreased distortion levels in comparison to the I2 intake version.

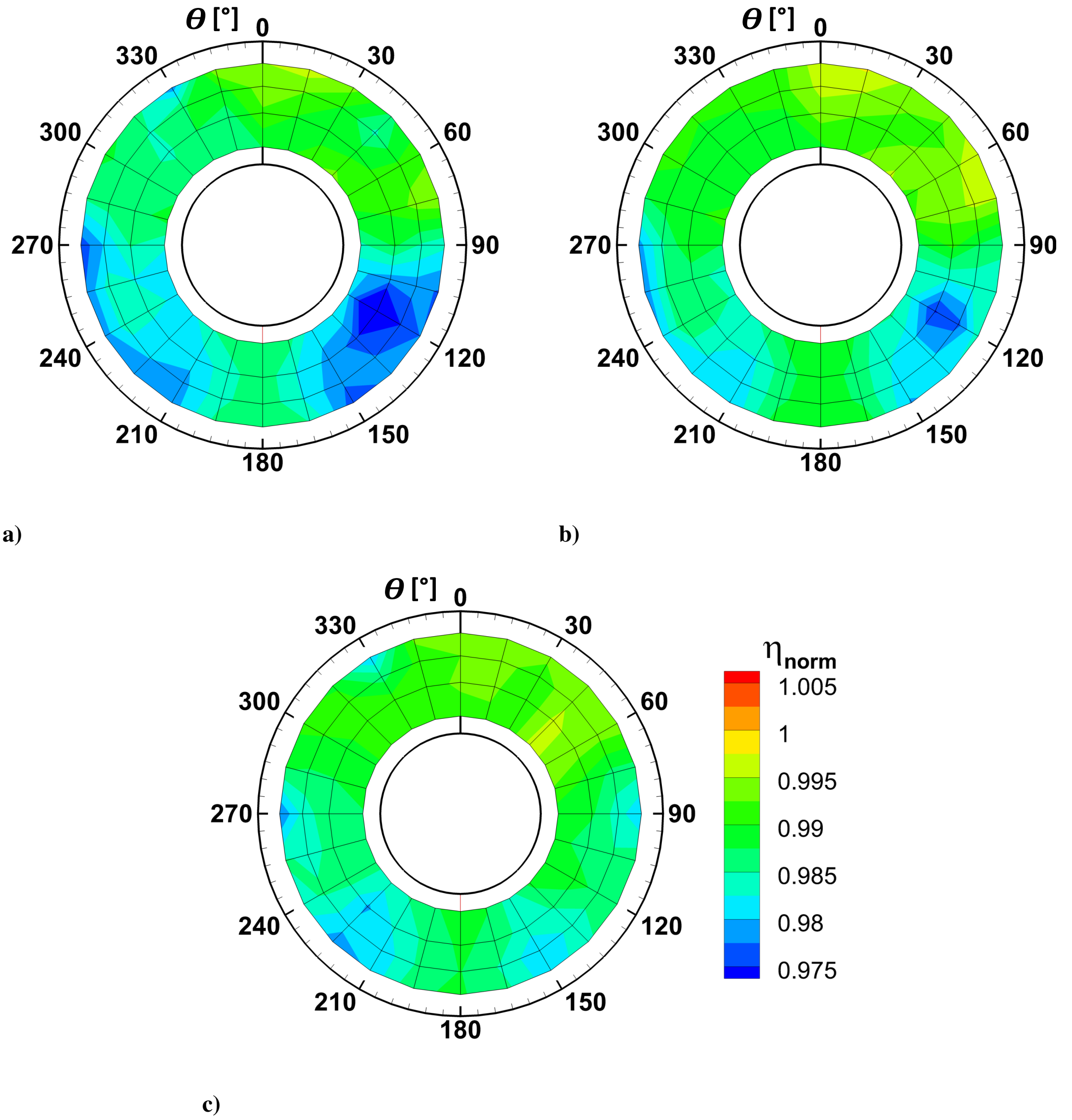

a)

b)

c)

Figure 6.33: Distribution of normalized total pressure ratio in AIP for a) I2 P3 IG2 EG2 RSP0 IGV0, b) I2 P3 IG2 EG2 RSP3 IGV0 c) I2 P3 IG2 EG2 RSP3 IGV1, maximum relative freestream velocity, maximum mass flow rate ratio.

6.5.2 Surface Pressures

Selected surface pressure distributions are presented for a better characterisation of the flow field in the fast forward flight operation condition ($U_\infty/U_{\infty,max}$ =1, $\dot{m}_{corr}/\dot{m}_{corr,max} = 1$) in reference to the $\bar{\eta}_{norm}$ and $DC_{60,norm}$ trends of section 6.5 as well as the η_{norm} AIP distributions of section 6.5.1. In Figure 6.34a, the cowling pressure distributions are given, represented by line 2 (see also Figure 3.20).

For the I3 intake, a part of the freestream dynamic pressure can be converted to static pressure between $S_2 = 0.6 - 0.94$ using a scoop ($c_p \approx -0.35 \rightarrow 0.5$), see Figure 6.34a. Therefore, already upstream of the beginning of the cowling ramp (dashed line) a pressure increase can be found. Increased static pressures are achieved ($c_p \approx -0.25 \rightarrow 0$) due to the ramp of the I2. In case of the I1 intake no re-compression on the cowling surface is noticeable. Therefore, the pressure level within the separation region ($S_2 = 0.92 - 0.98$) downstream of the front intake lip (cp. Figure 3.19 and Figure 3.20) is the

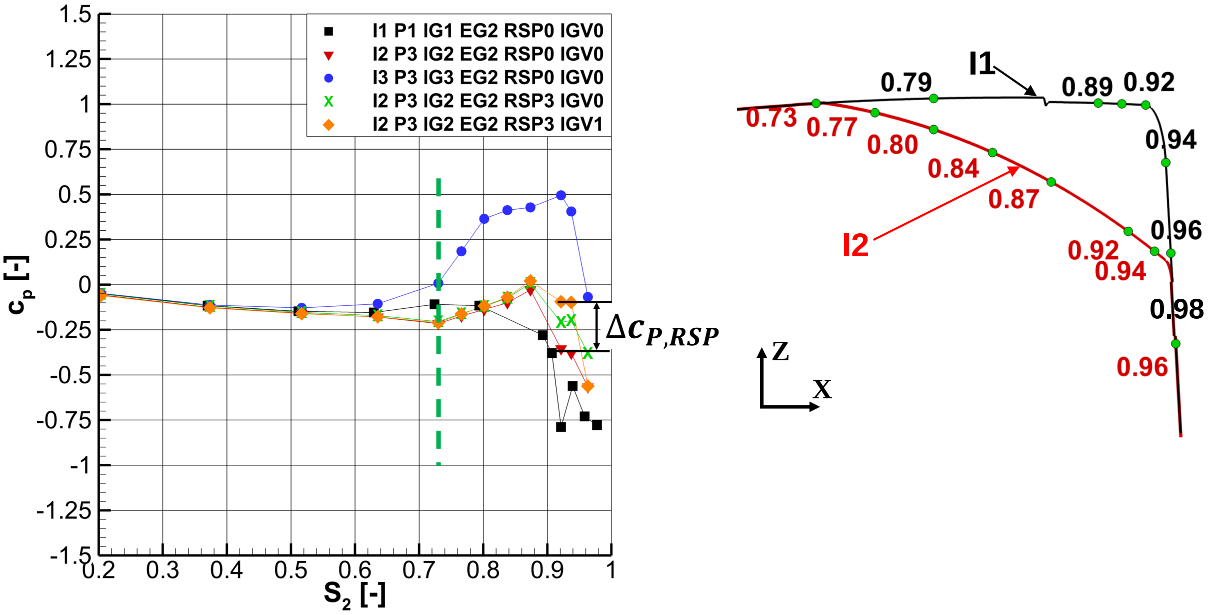

a) b)

Figure 6.34: a) Pressure distributions, line 2, basic intakes and best retrofit variants, maximum relative freestream velocity, maximum mass flow rate ratio and b) geometry and local curve length coordinate S_2 for line 2 of I1 and I2.

lowest. Directly downstream of the front intake lip, at the location $S_2 = 0.92 - 0.96$, the high and short rear spoiler increases the pressure level comparing to the I2 intake variant by $\Delta c_{P,RSP} \approx 0.16$, as illustrated in Figure 6.34a . The retrofit variant including the intake guide vane leads to a pressure gain of $\Delta c_P \approx 0.27$ indicating a less pronounced separation region at the front intake lip. As shown in Figure 6.35a, the pressure distributions imply a very complex plenum chamber flow field. Plenum chamber

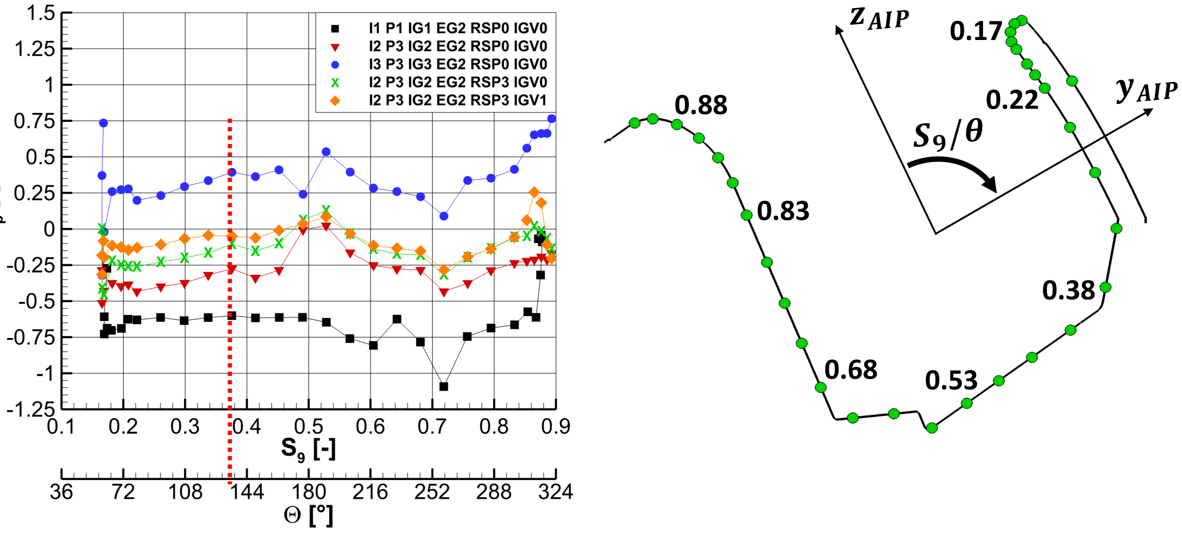

a) b)

Figure 6.35: a) Pressure distributions, line 9, basic intakes and best retrofit variants, maximum relative freestream velocity, maximum mass flow rate ratio and b) geometry and coordinate S_9 for line 9 in plenum 1.

pressure differences are similar to the entry cross section of the intake for all intake variants. Thus, the static pressure at the intake entry is crucial for downstream plenum chamber pressure levels. The retrofit modifications lead to an increase of static pressure over the entire plenum chamber, compared to the I2 P3 configuration. In the region around $S_9 = 0.49 - 0.53$, a pressure increase due to the splitter is clearly visible for all configurations except the I1 P1 variant. The fact that the increased surface pressure at the intake entry due to the guide vane compared to the "pure" rear spoiler is not entirely reproduced over the complete plenum chamber indicates differences in the local effectiveness of such a device interacting with a rear spoiler or scoop. For all intake geometries, the flow is accelerated around the right side intake lip at $\theta \approx 60°$ leading to a decrease of static pressure. In case of the I1 intake, shortly downstream, a nearly constant pressure level of $c_p \approx -0.67$ in between $0.2 < S_9 < 0.53$ ($70° < \theta < 190°$) indicates a region of separated flow, as depicted in Figure 6.35a. Comparable plateaus of constant c_p appear on much smaller scale in the other geometries‘ cases thus suggesting smaller separation areas in the rounded plenum chamber.

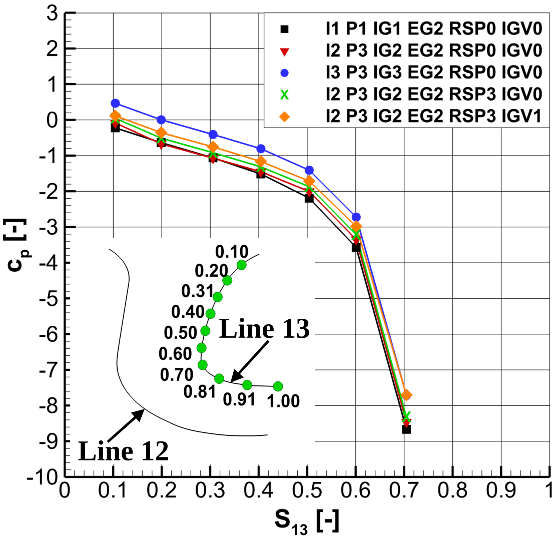

Figure 6.36: Pressure distributions, line 13, basic intakes and best retrofit variants, maximum relative freestream velocity, maximum mass flow rate ratio.

In Figure 6.36, the EID pressure distributions downstream are represented exemplarily by line 13. The lines 12 and 13 are located at the angular position $\theta = 135°$ and $S_9 = 0.375$, respectively. The EID is identical for all intakes and symmetrical around the engine axis. Corresponding to the EID entry pressures, the upstream engine plenum pressure values are highlighted using a dashed line in Figure 6.35a. The pressure curve progression is very similar for all intake variants. The EID operates as a nozzle with a strong area contraction from entry to exit (AIP), leading to a significant acceleration of the fluid as well as a strong decrease in static pressure. The concave curvature of the front part of the EID (line 12, see Figure 6.36) counteracts the pressure drop, whereas the convex curvature of the back side of the EID promotes flow acceleration, see Figure 6.36.

6.6 Angle of Attack

In this subchapter, the influence of different angles of attack between $-5° < \alpha < +5°$ is discussed for the retrofit variant with the high and short rear spoiler including the intake guide vane in the foremost position (I2 P3 IG2 EG2 RSP3 IGV1). At first, the influence on the total pressure ratio and the distortion coefficient is regarded in Figure 6.37.

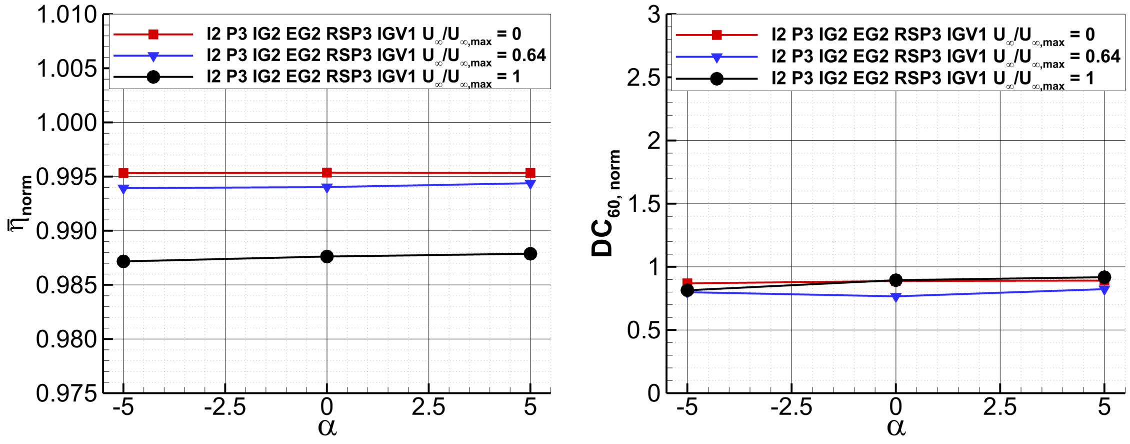

a) **b)**

Figure 6.37: Influence of α variation on aerodynamic characteristics of I2 P3 IG2 EG2 RSP3 IGV1, relative freestream velocities of $0; 0.64; 1$, maximum mass flow rate ratio, a) total pressure ratio and b) distortion coefficient.

As depicted in Figure 6.37, due to the regarded angles of attack, changes in the normalized total pressure ratio of merely $-0.046\ \% \leq \Delta\bar{\eta}_{norm} \leq 0.04\ \%$ occur for the three tested velocity ratios. Regarding the total pressure distortion, a higher sensitivity of the distortion coefficient to changes in angles of attack is found. At zero freestream velocity a variation of $-2.05\ \% \leq \Delta DC60_{norm} \leq 0.45\ \%$ is detected which represents the reproducibility of the measurement conditions and results. In the mid velocity regime ($U_\infty/U_{\infty,max} = 0.64$), a variation of $4.28\ \% \leq \Delta DC60_{norm} \leq 7.47\ \%$ occurs and in the high velocity regime ($U_\infty/U_{\infty,max} = 1$), a variation of $-8.96\ \% \leq \Delta DC60_{norm} \leq 2.58\ \%$ is found. For the investigated helicopter configuration, typical fast forward flight angles of attack are in the order of $\alpha \approx -2°$. The interpolated deviation for the $\alpha \approx -2°$ condition compared to the zero α case is $\Delta DC60_{norm} \approx -3.59\ \%$ for the maximum freestream velocity ratio. Nevertheless, all total pressure distortion levels are still low.

In terms of mean AIP swirl angles, higher differences are found for the mid and high velocity regime. For $U_\infty/U_{\infty,max} = 0.64$, an increase of the mean swirl is found for an increase in the angle of attack.

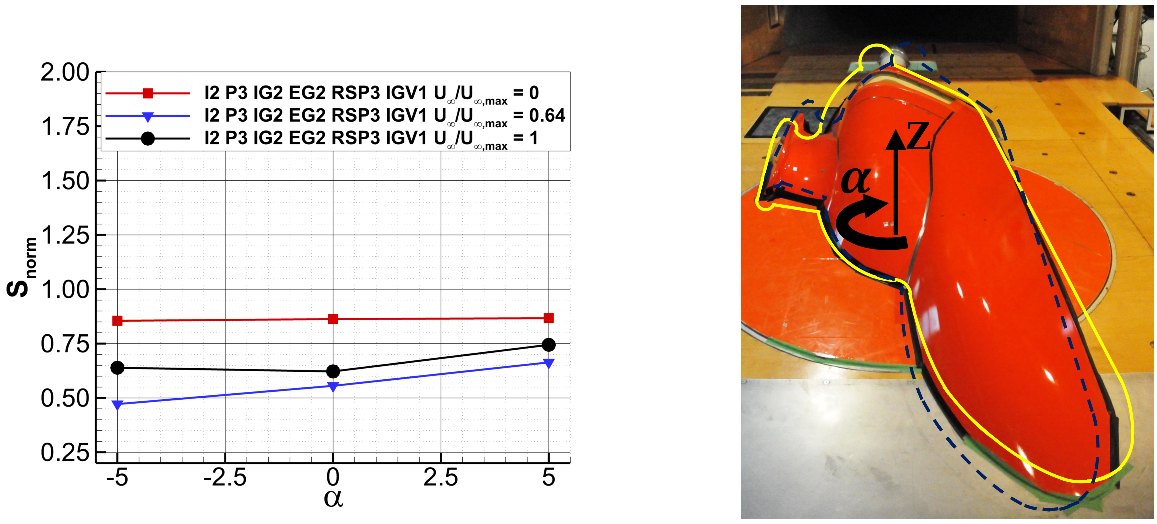

a) b)

Figure 6.38: a) Influence of α on aerodynamic characteristics of I2 P3 IG2 EG2 RSP3 IGV1, relative freestream velocities of 0; 0.64; 1, maximum mass flow rate ratio, normalized swirl coefficient, b) angle of attack adjustment.

The corresponding deviations from the zero AoA case are $-16.07\ \% \leq \Delta S_{norm} \leq 17.85\ \%$. For the high freestream velocity, deviations of $3.23\ \% \leq \Delta S_{norm} \leq 19.35\ \%$ are determined. The rather large differences of the mean swirl angles are partly due to the fact that the absolute AIP swirl angles are close to zero in the AIP. Thus, the deviations are unlikely to have a significant influence on stable engine operation due to swirl-induced flow separation at the compressor blades.

In Figure 6.39, the AIP η_{norm} distributions for the three angles of attack $\alpha = -5°, 0°$ and $+5°$ are presented for the forward flight case $U_\infty/U_{\infty,max} = 0.64$, $\dot{m}_{corr}/\dot{m}_{corr,max} = 1$. Qualitatively, all three distributions are similar. The extent and pressure level of the regions of lowered total pressure, i.e. wakes of the regions of separated flow, are too similar to clearly identify the origin of the deviations in $DC60$.

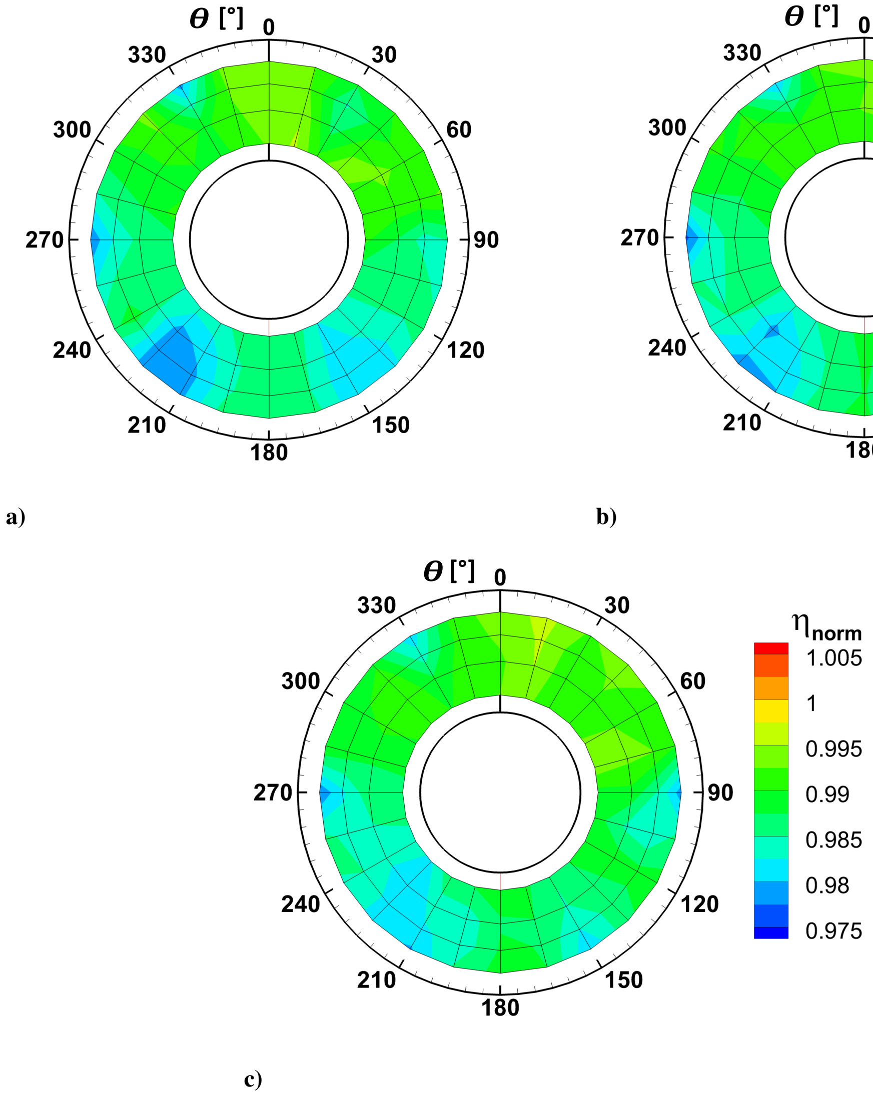

Figure 6.39: Distribution of normalized total pressure ratio in AIP for I2 P3 IG2 EG2 RSP3 IGV1, a) $\alpha = -5°$, b) $\alpha = 0°$ and c) $\alpha = +5°$, relative freestream velocities of 0.64, maximum mass flow rate ratio.

6.7 Synthesis

Significant differences in the aerodynamic characteristics of the three basic intakes are identified. In fast forward flight conditions, the intakes 2 and 3 are beneficial compared to the intake 1 regarding the AIP total pressure ratio, total pressure distortion, the mean swirl angle as well as the estimated engine power output. For low freestream velocities, due to flow deflection around the scoop, the total pressure levels and total pressure distortion of the intake 3 are worse than those of the intakes 1 and 2.

The effect of an intake grid and plenum chamber splitter are investigated based on the configuration intake 2 and plenum chamber 2. The configuration with an intake grid indicates lower total pressure ratios and higher total pressure distortion levels, for the major part of operation conditions. The AIP mean swirl shows no clear tendency. The plenum chamber splitter straightens the flow directions in the plenum chamber and creates a more radial engine duct inflow direction. Consequently, the freestream velocity dependent total pressure losses of the intake grid are compensated. For all operation conditions, the total pressure distortion and swirl angles are improved. An additional grid mount element has only a minor effect.

To differentiate the plenum chamber as well as the intake shape effect on engine inflow parameters, an additional investigation comprising combinations of the intake 1 and 2 as well as the plenum chambers 1 and 3 is performed. The cowling approach ramp (as part of intake 2) mainly improves the pressure recovery due to its ram effect, gains are proportional to the freestream dynamic pressure.

The rounded plenum chamber improves the pressure recovery but has an even higher effect on AIP distortion levels. Both measures strongly improve AIP swirl levels.

The intake 2 and plenum chamber 3 configuration is the basis for subsequent studies of retrofit modifications, to achieve a combination of the beneficial characteristics of the basic intake geometries.

Hereby, rear spoilers of different heights and forward protrusions are tested as well as an intake guide vane at three axial positions, relative to the intake opening. The high rear spoiler with small forward protrusion is assessed as best compromise of high and low velocity performance of the "pure" rear spoiler cases. In fast forward flight, pressure recovery is high due to the static pressure re-compression upstream of the intake opening as an effect of the rear spoiler height. A short forward protrusion leads to a large effective intake entry cross section and small flow deflection of the ingested air, thus creating high pressure recovery and lowest total pressure distortion levels.

In the subsequent intake guide vane study, highest total pressure and lowest total pressure distortion levels are indicated for the foremost position. The additional pressure recovery improvement, however, is limited to the highest freestream velocities and insignificant compared to "pure" the rear spoiler configurations. For low freestream velocities, a distinct deterioration of the pressure recovery, distortion and swirl levels is indicated, caused by the increased blockage of the intake entry section. In the mid and high velocity region, the intake guide vanes create a significant reduction of total pressure distortion.

Static pressure distributions of a fast forward flight case affirm the effective intake entry pressure enhancement due to the best retrofit modifications. The resulting increase in engine entry total pressure levels is most significant in the lower part of the AIP. The effective more homogeneous AIP total pressure distributions create lower total pressure distortion levels. Plenum chamber pressure distributions indicate variations of the local effectiveness of the intake guide vanes, combined with a rear spoiler.

An additional investigation of the model's angle of attack between $-5° < \alpha < +5°$ reveals only a minor effect on the pressure recovery as well as the total pressure distortion levels. The deviations in swirl are higher, but not critical with respect to the very low absolute swirl angles.

7 Numerical Optimization and Parameter Studies

The investigations performed for the basic intake shapes and the retrofit aerodynamic modifications on the basis of the reference configuration, as described in chapters 5 and 6, give a comprehensive overview of the aerodynamic characteristics of such plenum chamber type side intake configurations. For further assessment of the optimization potential and the identification of optimal solutions in terms of overall helicopter performance in fast forward flight conditions, further parameter studies and numerical optimization are performed for three different intake cases in the current chapter.
First of all, a brief summary of numerical optimization and parameter studies is presented followed by an explanation of the two tool chains, which are applied for subsequent investigations. In the following, three parameter cases and main findings are described.

7.1 Methods

Numerical optimization as well as parameter studies are crucial to improve the performance of typical engineering applications in various fields, amongst others in aeronautics, aerospace engineering, automotive design, civil engineering etc. Hereby, systematic alterations of shapes or structures are conducted. The systematic variation of the design variables x_i which constitute each design point x is aimed to find an optimal solution, evaluated by objective functions $f_z(x)$, compare equation (7.1).

$$\begin{aligned} & x = (x_1, x_2, ...x_n) && i = 1...n \\ & f_z(x) && z = 1...k \\ & {x_i}^l \leq x_i \leq {x_i}^u && \end{aligned} \tag{7.1}$$

Hereby, ${x_i}^l$ describes the lower and ${x_i}^u$ the upper limit for the range of permitted values of each design variable x_i, see Ref. [10].

For a general case of a constrained numerical optimization, further equality and inequality constraints are needed. Optimization techniques can be categorized in different ways. Either a single optimization algorithm is employed or an appropriate combination of different algorithms aimed at the unification of complementary advantages. Generally, algorithms can be subdivided into direct and indirect methods, Ref. [10]. In case of indirect methods, the equations describing the system should be available. Therefore, an explicit or implicit relation of the objective functions from design variables should be known a priori. For many engineering applications this relation is unknown a priori, thus direct optimization is preferred. Hereby, the system equations are evaluated for each single design point either by experiments or numerical simulations. Therefore, the direct methods are also referred to as search methods due to the systematic searching of the parameter space. Another way of classifying optimization methods is to distinguish between local and global methods. On the one hand, in case of a local method, starting from an initial combination of input parameters, a next local optimum is determined. On the other hand, the purpose of a global method is to search the entire parameter space. Hereby, multiple local optima can be detected. Often, the efficiency of local methods in finding optima is higher. Depending on the actual optimization case, the number of local optima can greatly differ. Especially for fluid mechanics applications, the objective functions (e.g. lift, drag or distortion parameters) can be strongly influenced by the interaction of separation regions, vortices or shocks. Therefore, a suitable combination of global and local methods is applied. For the current research, an emphasis is put on parameter studies.

7.1.1 Workbench Environment

For the optimization case of a 2D side intake geometry in this research (see Chapter 7.2.1), the ANSYS Workbench is employed. Therefore, the consecutive section gives an overview of the environment including information about its work flow, the included tools and the applied optimization algorithm. The ANSYS Workbench provides a framework to perform optimization projects effectively without separate scripts or macros. For this purpose, several ANSYS applications can be combined in a Workbench project. Here, the essential applications needed for the 2D optimization case are the *Design Modeler, ICEM and CFX*. Furthermore, Workbench inherent parameter analysis and optimization applications are used (*Parameter Set* and *Optimization*). Uni- or bidirectional connections for communication of applications can be set. Each combination of design variables x_i correspond to a set of input parameters for the geometry generation in the *Design Modeler*. The parametrized geometry is adapted accordingly and the new shape is transferred to ICEM CFD. Here, applying a tool command language mesh script file, a new volume mesh is created and transferred to CFX. Besides the case-dependent intake mesh, further unchanged meshes are created to represent the outer flow regime, compare Figure 7.1. As part of the pre-processing in CFX, all meshes are connected via interfaces, the boundary conditions and solver settings are defined. Hereafter, the simulation run is performed with CFX for the current design point. The objective function is transferred via the application *Parameter Set* and evaluated by the application *Optimization*. Here, a new set of design variables is defined and transferred via the application *Parameter Set* to the *Design Modeler* tool. As optimization algorithm, the Adaptive Single-Objective (ASO) Optimization is used. It is a hybrid global method and described in detail in Ref. [9].

7.1.2 Automated Aerodynamic Shape Development Environment

The Automated Aerodynamic Shape Development (AASD) environment, as applied for the current research, has been developed by Pölzlbauer, Ref. [51] and is based on Ref. [85]. The modular tool chain allows for geometric design optimization and parameter studies. Subsequently, a short description of the two parameter study cases of the current work is provided. The basis for the parameter variation and the optimization process is the Design Analysis Kit for Optimization and Terascale Applications (DAKOTA, Ref. [1]), including iterative analysis methods. The communication of the dedicated tools for CAD shape generation, meshing, CFD simulation, DAKOTA as well as post-processing is provided by Python routines. For the parameter studies, as part of Chapters 7.2.2 and 7.2.3, the parametrized geometries (.stp) are generated by macro-based design in CATIA V5R21 using the CATScript language. The respective parameters and resulting geometries are presented in the Chapters 7.2.2 and 7.2.3. Input parameters are provided by DAKOTA and delivered to CATIA via a design table. The surface and volume meshes are generated automatically applying tool command language scripts in ANSYS ICEM. The CATIA design tables (.txt) and ICEM scripts are manipulated by python routines for each design point. After the creation of the meshes (.msh), a flow computation is performed with ANSYS FLUENT. Hereby, the numerical set-up, execution of the simulations as well as output creation are controlled by a journal file. As the time scales for the different steps of design generation, meshing and CFD computation differ significantly, an aim is to avoid geometric and meshing failure cases, leading to unsuccessful and costly meshing and simulation. For the parameter studies, different pre-investigations are conducted. As a first step, the feasibility of geometric variants is analyzed aiming to avoid surface intersections for the complex test case of a side intake geometry, as illustrated in Chapter 7.2.3. Furthermore, concerning the parameter study of the side intake case, a multi-stage computation process in FLUENT is applied to achieve an efficient and stable convergence of the CFD computations.

7.2 Optimization and Parameter Study Cases

Subsequently, two simplified intake cases and a realistic helicopter side intake case are investigated, aimed at the aerodynamic improvement of helicopter engine side air intakes in fast forward flight conditions.

7.2.1 Optimization of a quasi two-dimensional Side Intake Geometry

The first case reflects a simplified quasi two-dimensional geometry of a side intake configuration, which is derived from a longitudinal cut section through the reference configuration. The corresponding investigation is aimed at the identification of the total pressure recovery optimization potential in dependence of variable ramp and scoop geometries. The crossflow angles β with respect to the front intake lip, especially in its central part, are close to zero degrees, compare Chapter 5.2, Figure 5.10b. Furthermore, throughout the entire EID, the highest total pressures and local velocities occur in the angle regime of $330^\circ < \Theta < 360^\circ$ as well as $0^\circ < \Theta < 30^\circ$, yielding only little distortion and cross flow velocity. Therefore, in a first study, a two-dimensional case is investigated to gain knowledge of the parameter influence of retrofit variants on the improvement of total pressure losses. The geometry for the current case is derived from a cut through the shape of the reference geometry (I2 P3 IG2 EG2 RSP0 IGV0, i.e. intake 2, plenum chamber 3, intake and engine grid installed, no retrofit aerodynamic modification, Figure 3.13). The resulting optimized shapes are similar to the experimentally tested retrofit geometric variants (I2 P3 IG2 EG2 RSPX IGVY), but not identical. Besides cross flow influence on the actual cases' results, also the upstream effect of intake shape variations is considered for further reduction of computational cost concerning the first numerical parameter study. For all experimentally tested geometries, the influence of different intake shapes on upstream positions of $S_2 \leq 0.5$ can be considered negligible, Figure 6.34a. To completely avoid intake upstream influences, the cowling geometry included in the 2D case starts at $S_2 = 0.37$. As depicted in Figure 7.1, the domain of the 2D optimization case consists of five part meshes (A-E), which are connected by interfaces in the pre-processing tool ANSYS CFX-Pre.

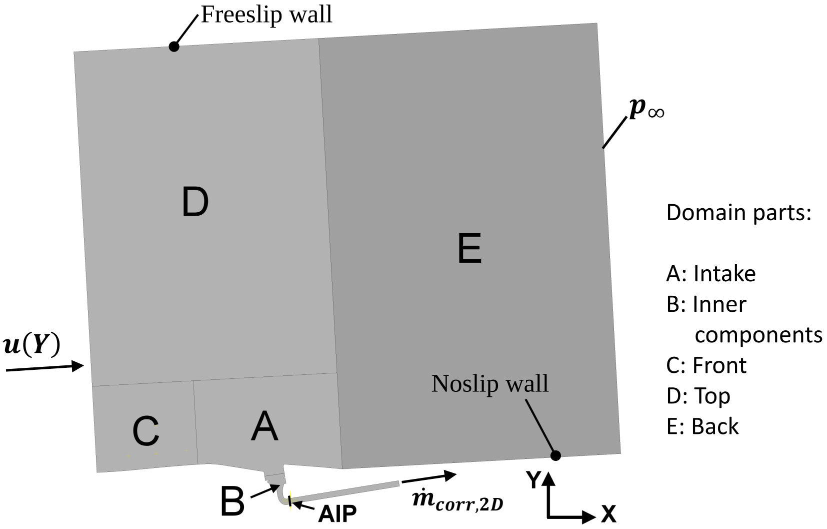

Figure 7.1: Complete 2D optimization domain.

Mesh A represents the intake mesh and is the only part mesh that incorporates an unstructured grid. Meshes B, C, D and E feature structured grids. Part A includes the parametrized geometry and therefore, its mesh needs to be newly generated for every optimization loop, whereas the other mesh parts remain unchanged. Thereby, mesh creation time is saved. The small lateral extent of the domain reflects the simulated two-dimensional case. Due to the boundary layer growth along the surface of the wind tunnel floor and the sectional fuselage, the $1/7-$power law $u = (y/\delta)^{\frac{1}{7}}\, U_\infty$ is applied for the turbulent boundary layer velocity profile at the domain inlet, Ref. [52]. The BL height δ_{99} is taken from PIV measurements, see Figure 5.10a. For $Y > \delta_{99}$, a constant velocity of U_∞ is chosen, reflecting the maximum experimental free stream velocity $U_\infty / U_{\infty,max} = 1$. The surfaces of the cowling, the intake and the inner components are modeled as smooth adiabatic no-slip walls. For the farfield top surface, a freeslip boundary condition is selected and at the outlet the ambient pressure p_∞ is set. The mass flow rate $\dot{m}_{corr,2D}$ which is imposed on the outlet surface of part mesh B, is scaled to reproduce a comparable Mach number as in the experimental case of $\dot{m}_{corr}/\dot{m}_{corr,max} = 1$. In the current optimization, the RANS equations are solved with the solver ANSYS CFX applying the shear-stress-transport turbulence model. The energy equation is solved to consider compressibility effects. In the CFD calculations, the maximum number of iterations is limited to 500, leading to residual levels of the momentum and continuum equations below 10^{-6}. The parametrization of the intake geometry is illustrated in Figure 7.2 b). The intake overlapping ratio $R = l_{RSP}/l_I$ and the relative height parameter $H_{rel} = h_{RSP}/h_{I2}$ have already been described in Chapter 6.4. New parameters are a relative ramp angle $\varphi_{rel} = \varphi/\varphi_{I2}$ and an intake lip radius r_i.

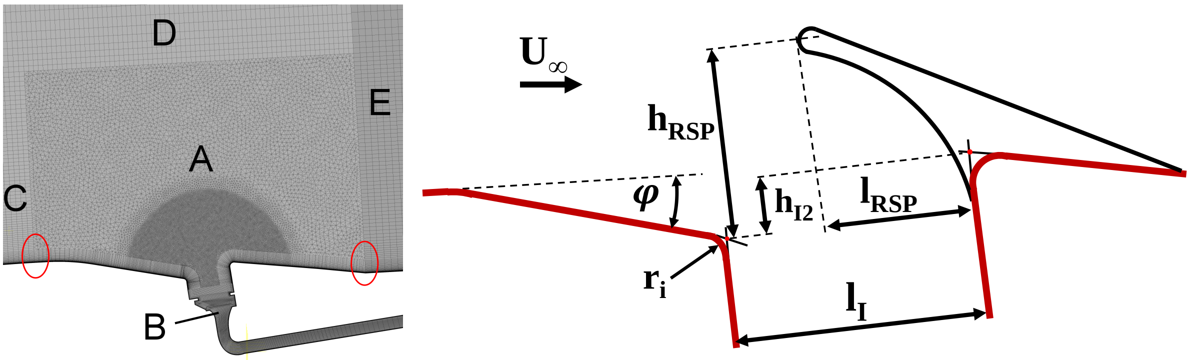

a) b)

Figure 7.2: a) Assembly of domain A, B, C, D, and E, b) Parameter definition

The 2D optimization is performed in three steps. The first run included the geometry of a slice through the reference side intake geometry, namely the shape of I2 P2 IG0 EG0 RSP0 IGV0 (cf. Figure 3.13). Two consecutive runs are conducted with different parameter limits. The corresponding parameters of the runs are listed in Table 7.1. In all three runs, the parameter values that are experimentally tested for R and H_{rel} are in the admissible parameter space.

Before the optimization, a sensitivity study was conducted. This study showed a minor effect for the intake lip radius, which is subsequently kept constant. The results of the final run are presented in Figure 7.3. As abort criterion a maximum number of 50 evaluations is selected. The progression in Figure 7.3a yields the highest η_{rel} values, which are about 0.3 % higher than those of the reference case. The corresponding geometry features a slightly lower ramp angle φ_{rel} than the reference geometry, compare

Run	*1st*	*2nd*	*3rd*
Ramp angle φ_{rel}	0.9 - 1.3	0.9 - 1.3	0.90 - 1.08
Overlapping ratio R	0 - 0.5	0.06 - 1	0.07 - 2.4
Scoop height H_{rel}	1 - 2.5	1.15 - 4.25	2.31 - 4.25

Table 7.1: Limits for the parametrizations, relative to the baseline configuration.

Figure 7.3b. The resulting scoop exhibits a distinctive overlapping of the intake opening and its height is 4.25 times the original height, see 7.3c and 7.3d, respectively. The optimum is achieved already at design point 23. Here, the parameter limits of R and H_{rel} are reached.

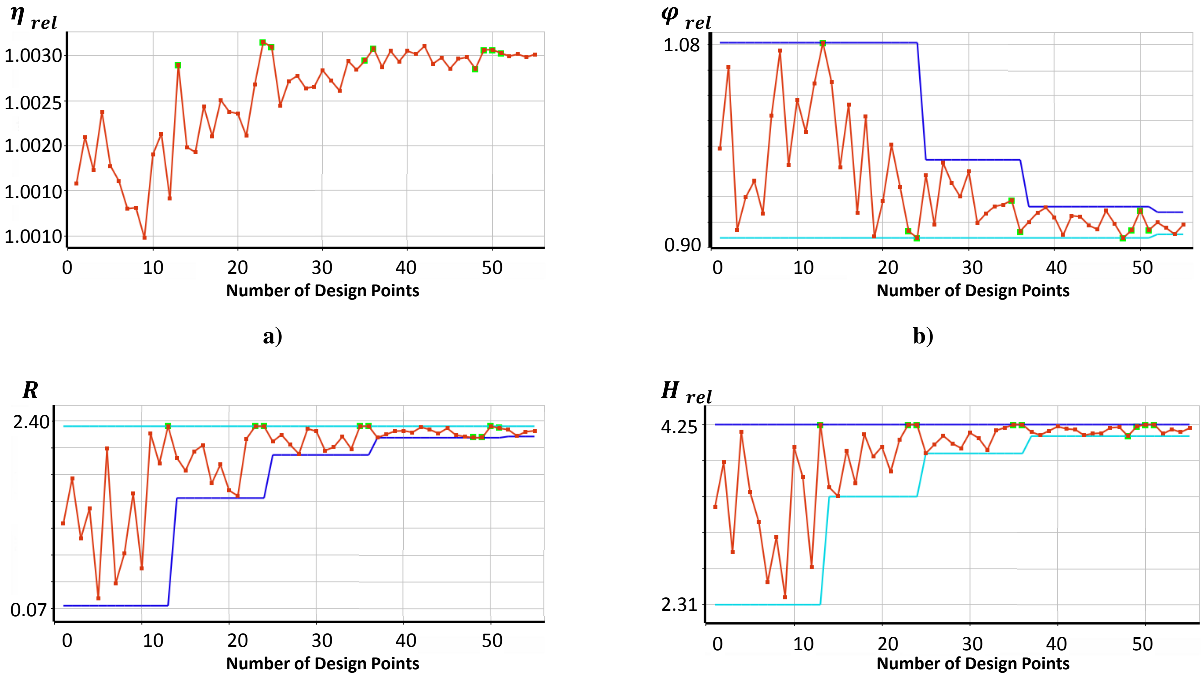

a) b)

c) d)

Figure 7.3: Development of the final 2D optimization run, a) η_{rel}, b) φ_{rel}, c) R and d) H_{rel}.

In Figure 7.4, the resulting η distributions in the flow field of the reference and optimized geometry are presented. The levels of the total pressure ratio are generally higher in case of the optimized geometry. This is caused by a more gradual pressure increase due to the scoop. The separation area at the front intake lip is increased and starts already at a more upstream location on the ramp.

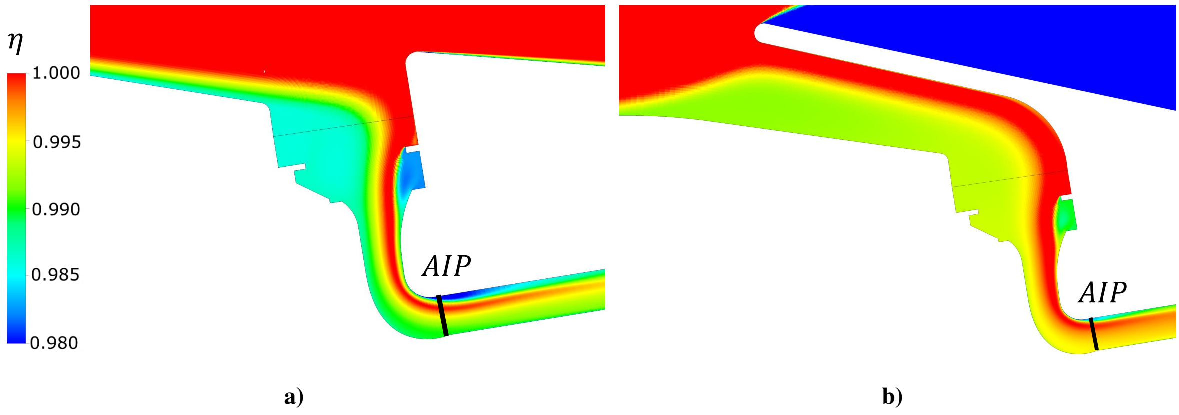

Figure 7.4: Distribution of η for a) reference geometry and b) optimized geometry.

Total pressure losses are significantly lower, as the deflection of the incoming flow is remarkably smoother in case of the optimized geometry. The "core flow" region with high η levels close to 1 is more extended up to the AIP. Therefore, the AIP total pressure level is higher. The 2D optimization case confirmed the beneficial effect of a high scoop related to fast forward flight conditions in terms of total pressure ratio in the AIP. The extent of the core flow region indicates, that for fast forward flight conditions a smaller effective intake area would be beneficial. Furthermore, a decrease of the intake ramp angle for such longitudinally and vertically protruded scoop geometries is advantageous concerning AIP total pressure levels in fast forward flight. For the optimized 2D geometry, a distinct separation region at the leeward side of the scoop is noticeable, which leads to an increased fuselage drag. The 2D investigations did not include a consideration of distortion levels as well as detrimental effects of additional drag due to the intake geometry. The latter influences are investigated in the course of Chapter 7.2.3.

7.2.2 Submerged Intake Parameter Case

The second case is based on the classical NACA-type submerged intake configurations. On the one hand it serves as testing case for the Automated Aerodynamic Shape Development environment and on the other hand it is meant to identify the total pressure recovery optimization potential due to planform parameter variations of the approach ramp upstream of the intake. The shape of the side intake configuration 2, which serves as the basis for the experimental and numerical optimizations, features a ramp on the cowling upstream of the intake. Thus, as a second test case, a generic submerged intake geometry is investigated, which is geometrically derived from the experiments of submerged intakes at subsonic freestream conditions, as presented in Ref. [44]. The aim is to investigate the effect of the ramp planform as well as the longitudinal section geometry on the AIP total pressure levels. The RANS equations are solved with the solver ANSYS FLUENT as part of the AASD environment. Hereby, the shear-stress transport turbulence model is applied. The meshes for each geometric variant are created with ICEM. Subsequently, the boundary conditions of the generic submerged intake test case are depicted in Figure 7.5.

As in the previous 2D optimization case, the law $u = (y/\delta)^{\frac{1}{7}}\, U_\infty$ is applied for the turbulent boundary layer velocity profile at the inlet of the domain. This represents the effective boundary layer height along the fuselage section model at $S_2 = 0.37$. Outside, the constant velocity of $55 m/s$ is set. The mass

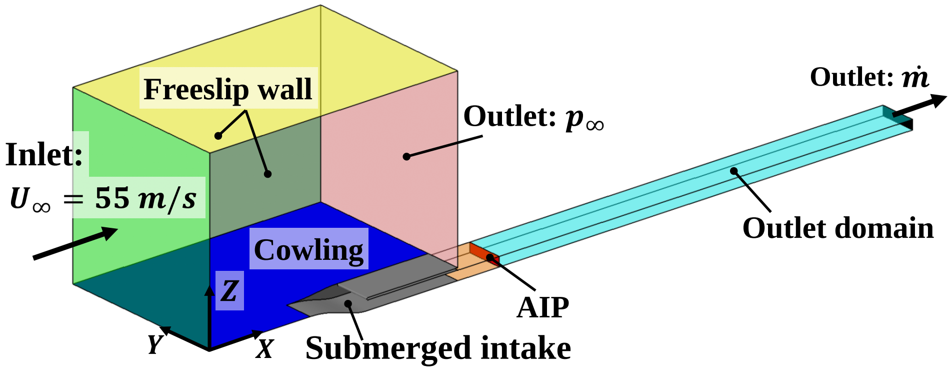

Figure 7.5: Boundary conditions of the submerged intake optimization case.

flow rate at the engine outlet $\dot{m}$ is adapted for each geometric variant to achieve a local Ma number of $Ma_{AIP} = 0.24$. Thus, the operation point reflects a velocity ratio of $U_{AIP}/U_\infty \approx 1.5$ which has also been tested in Ref. [44].

The vortex onset at the intersection of the cowling and the ramp side walls is considered to be mainly driven by geometric variations and not significantly by a variation of the subsonic AIP Mach number from 0.24 to 0.45 (as would be a typical AIP Ma number in the helicopter intake). Consequently, the case can be treated as incompressible and the energy equation does not have to be considered.

The design parameters as part of this parameter study are illustrated in Figure 7.6. The parameter dx_1 defines the ramp and side wall length. The parameter dx_2 defines the ratio of the inflection point position of the side wall and ramp profiles with respect to dx_1. The parameter b represents the width of the intake. The parameters φ and ψ describe the angles of the ramp and the side walls relative to the x-direction.

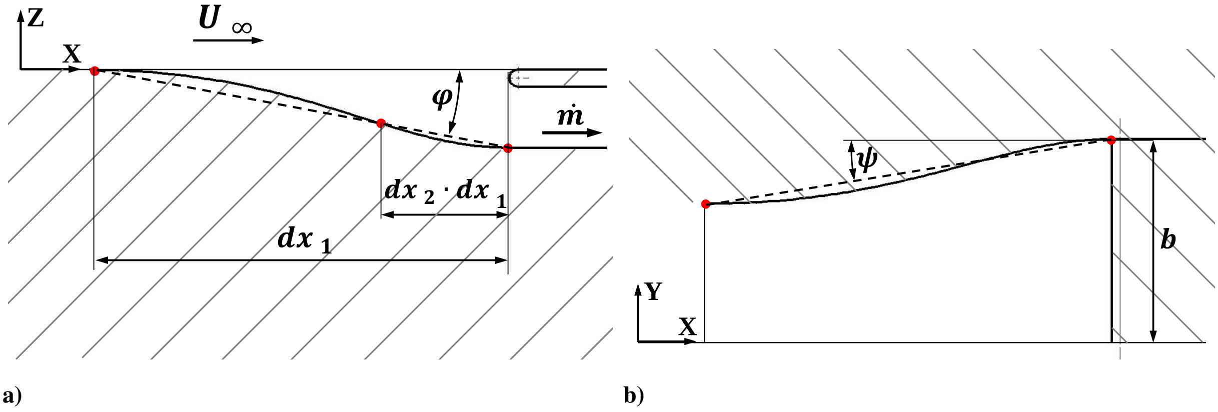

Figure 7.6: Parametrization of the submerged intake optimization case, a) side view, b) top view.

In the current parameter study, the purpose is not to find an exact combination of the parameters which lead to the optimal total pressure recovery. The identification of the main influences concerning the intake planform shape and ramp angle is desired for the subsequent parameter study of a side intake geometry. Thus, discrete values for the design parameters dx_2, φ and ψ are allowed. The parameters dx_1 and b are fixed at one value for a reduction of combinations with $b/dx_1 = 0.7$. For the relative inflection point position of the ramp and side walls contour, dx_2, values of 0.3, 0.35 and 0.4 are defined. Discrete ramp angles with a resolution of 1 degree between $5\ deg \leq \varphi \leq 12\ deg$ are simulated. Convergent side walls with angles $2deg \leq \psi \leq 12\ deg$, divergent side walls with angles $2\ deg \leq \psi \leq 8\ deg$ as well as parallel side walls are investigated. As main influential factors the parameters side wall angle and ramp angle are identified, see Figure 7.7a. The highest increase in AIP total pressure, relative to a ramp angle of $\varphi = 5\ deg$, can be obtained for ramp angles of $\varphi = 10\ deg$. Moreover the results are independent of the planform. The corresponding relative gain is $\Delta\eta_\varphi \approx 0.78\ \%$ for the convergent $\psi = 4$ deg planform case, other planforms featured similar results.

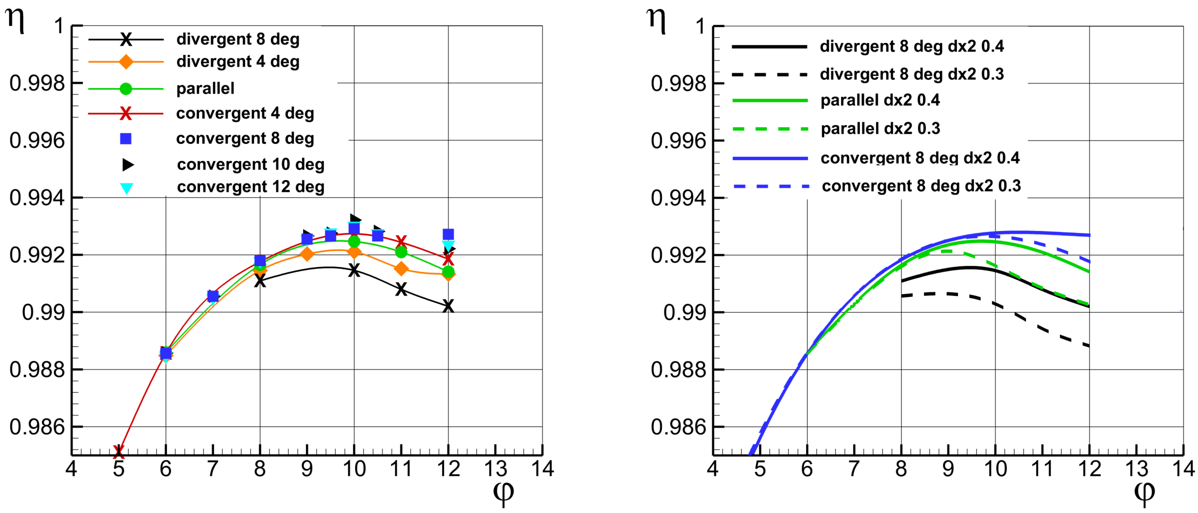

a) **b)**

Figure 7.7: Main parameter trends of the submerged intake case, a) $\eta(\varphi, \psi)$, $dx_2 = 0.4$, b) dx_2 influence on $\eta(\varphi, \psi)$.

The highest η levels arise for higher ramp angles compared to the results of Ref. [44]. This can be related to a different ramp geometry which is more curved in the current case. Further causes for deviations are the exact boundary layer state at the most upstream station of the intake, surface roughnesses in the experiments and differences in the Reynolds and Mach number, respectively. The current case should not exactly reflect the geometries and test conditions of Ref. [44]. The largest difference due to the planforms occurs between the $\psi = 10\ deg$ convergent and the $\psi = 8\ deg$ divergent case for a ramp angle φ of $10\ deg$, the relative difference hereby is $\Delta\eta_\psi \approx 0.18\ \%$. The trend which has been found in Ref. [44] in the comparison of planforms is confirmed here for $U_{AIP}/U_\infty \approx 1.5$, as the parallel planform leads to higher η levels than the divergent planform. Convergent planforms proceed the trend with even higher η levels.

The position of the inflection point relative to the intake longitudinal extend is also investigated, see Figure 7.7b. Generally, a more forward position of the inflection point leads to higher η levels. For the parallel and convergent planform cases this can be mainly related to flow separation occurring at the ramp walls. The corresponding position is farther away from the entry cross section and the dimension of the separation is smaller. The discrepancy between the two dx_2 limits 0.3 and 0.4 increases with ramp angles and thus, raised positive pressure gradients along the ramp wall. In case of the divergent planform, the effectiveness of the vortex emanating from the edge of the side walls is dependent on its shedding position. More upstream vortex shedding due to the sidewall contour (higher dx_2) leads to a larger vortex length upstream of the intake entry. Hence, more high energetic freestream fluid is transported to the ramp, originating higher intake entry total pressure. In the divergent planform case, the highest difference due to the inflection point position is $\Delta\eta_{dx_2} \approx 0.14$ %.

7.2.3 Parameter Study of a Side Intake Geometry

The third case is a synthesis of the first two parameter cases and reflects realistic plenum chamber type side intake configurations, which are very similar to those tested in the wind tunnel campaigns. The parametrization is partly based on the first optimization case (cf. Section 7.2.1) and the methodology as well as the tool chain of the current case are based on the submerged intake study, cf. Section 7.2.2. As the intakes are integrated into the fuselage of the helicopter of interest, the corresponding numerical simulations also reflect the intake's influence on the overall helicopter drag. A weighted sum approach is applied to quantify the performance of various designs based on the total pressure recovery, total pressure distortion and drag of the fuselage including the intake. Based on the results presented in Chapter 6 for retrofit geometric modifications, further geometrical parameter studies of a side intake geometry are performed numerically.

Numerical Setup

The numerical setup is based on the full fuselage case (cf. Figure 4.1b) which is compared to the sectional fuselage case in Chapter 5.2. In Figure 7.8, the flow domain and the boundary conditions are presented.

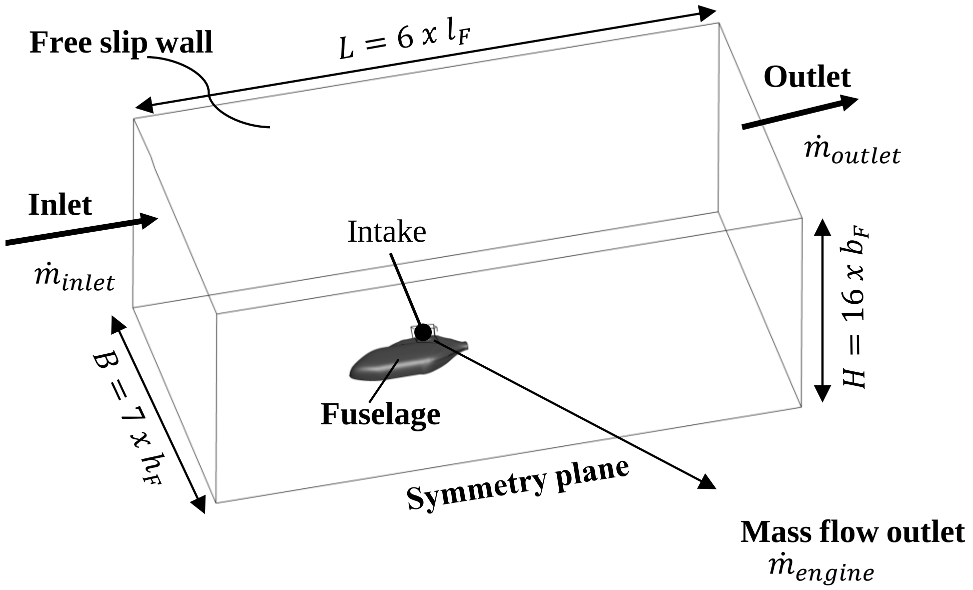

Figure 7.8: Side intake parameter study, domain representation.

The size of the flow domain is reduced representing a good compromize of computational costs and accuracy. The largest extent of the domain relative to the geometry is applied for the direction normal to the symmetry plane, as the side intakes are mainly orientated in this direction. The fuselage mesh, as represented in Figure 7.9, is identical to the full fuselage mesh shown in Chapter 5.2.

The intake geometries are spatially discretized by an unstructured tetrahedron mesh with approximately 6.2 *M* nodes and a prism boundary layer resolution of 28 layers with an expansion ratio of 1.22 and a total height of 35 *mm*. The same plenum chamber (plenum chamber 3) is incorporated in the numerical optimization setup as it is employed in the experimental investigation of retrofit geometries. In order to reduce the computational time of the single design points, some geometrical simplifications are applied. Therefore, in Figure 7.10, the original and the simplified geometry with the corresponding meshes of

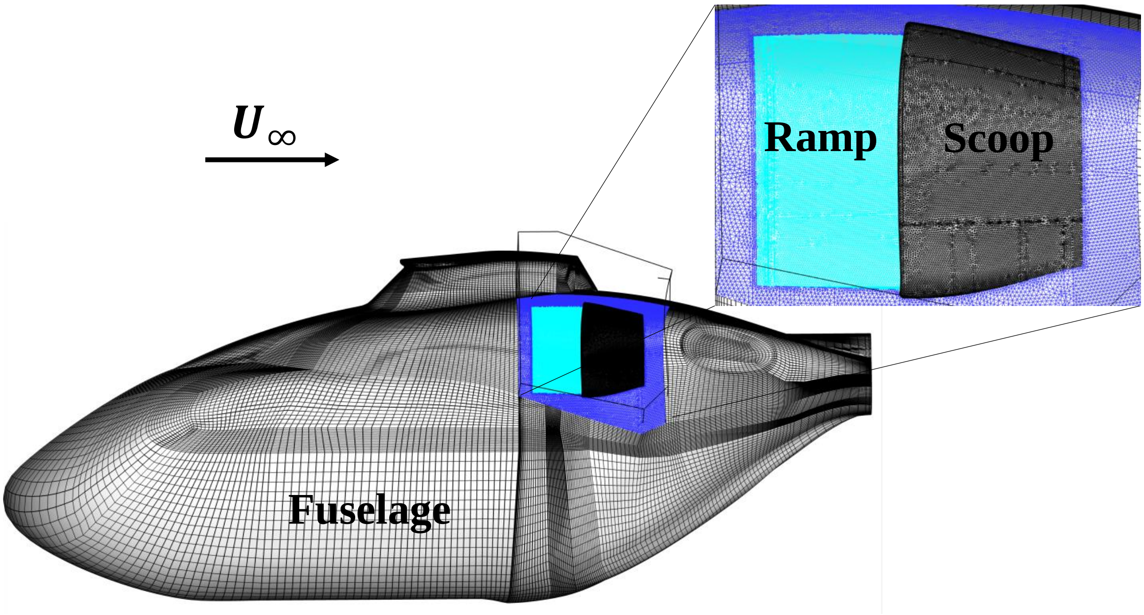
U_∞
Ramp
Scoop
Fuselage

Figure 7.9: Side intake parameter study, fuselage and intake surface meshes.

the EID are displayed together with the adjacent meshes. In the simplified case, the EID inner and outer guide vanes are not included. Furthermore, a single blocking is used for the geometry downstream of the plenum chamber and thus also the additional circular mesh is not necessary. In total, the simplifications leads to a reduction from 7.2 Mio nodes for the combination of the original EID mesh and the additional circular mesh to only 1.6 Mio nodes for the simplified EID mesh, without significantly changing the mesh resolution. Furthermore, the elimination of one grid interface further improves the computing time per design. In the longitudinal cut views through the EID region in Figure 7.11, further simplifications

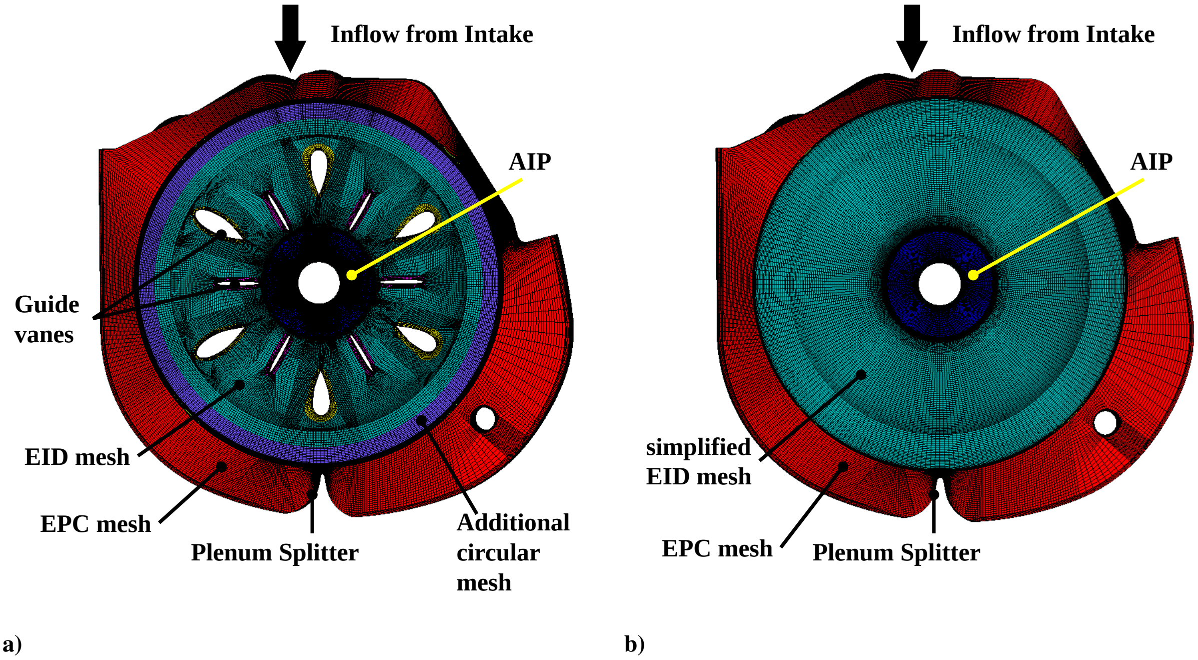
Inflow from Intake
AIP
Guide vanes
EID mesh
EPC mesh
Plenum Splitter
Additional circular mesh
a)
Inflow from Intake
AIP
simplified EID mesh
EPC mesh
Plenum Splitter
b)

Figure 7.10: Back view of a) Original EID mesh combined with EPC mesh and additional circular mesh, b) Simplified EID mesh combined with EPC mesh.

of the EID mesh are displayed. At the transition from the plenum chamber to the engine intake duct, the back-facing step of the foreign object damage grid as well as one step along the EID contour are not part of the simplified EID geometry.

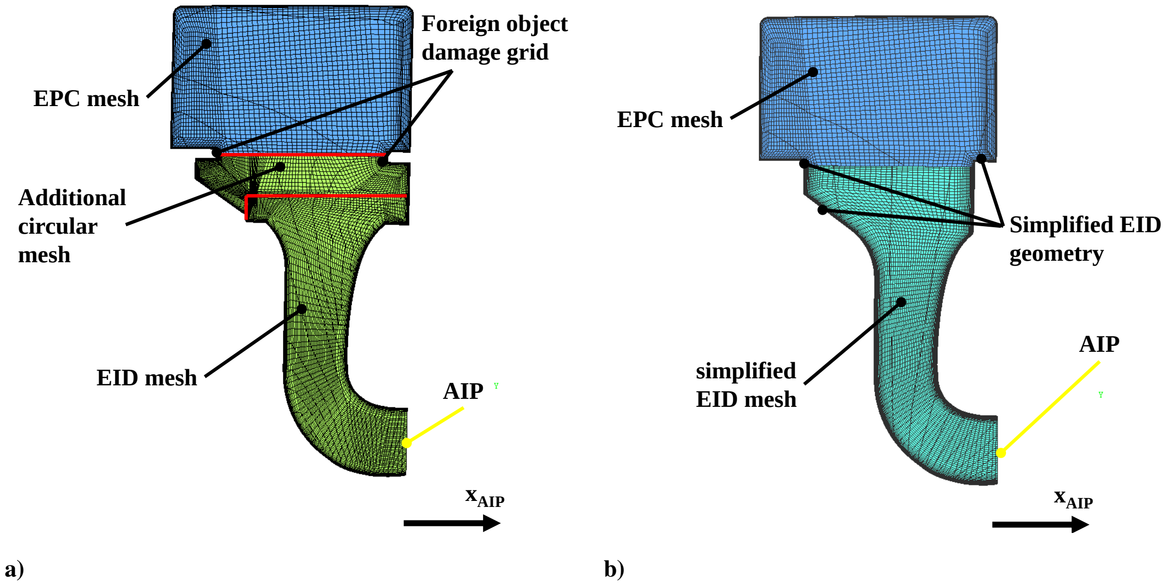

Figure 7.11: Cut view of a) Original EID mesh combined with EPC mesh and additional circular mesh, b) Simplified EID mesh combined with EPC mesh.

Objective Function

One purpose of the side intake parameter study is to reduce the power loss of the engine due to installation. Thus, the aerodynamic characteristics of the engine air intake are addressed. Hereby, as main influential parameters can be identified the AIP mean total pressure, represented by the coefficient η, the total pressure distortion, quantified by the parameter DC_{60}, the mean temperature at the engine entry face $\bar{T}_{SAIP}$ and the angularity of the flow with respect to the engine axis, described by the swirl coefficient SC_{60}. In the current investigation, the parameters η and DC_{60} are taken into account. The swirl angles in the AIP are not considered as they are very low. For the current case, a decrease in power output of 2 % is chosen per percent total pressure loss, based on an estimation from the literature (Ref. [80]). Reductions in power output in dependence of DC_{60} levels are taken from Ref. [78]. Another parameter that has to be considered for representation of a real flight case is the additional parasite drag due to the air intake Δc_D. For the consideration of intake drag, first of all the decomposition of helicopter power requirement in level flight is illustrated referring to Ref. [70]. The total required power P_{TOT} can be split into the induced power P_i, profile power P_o, parasite power P_p and tail rotor power P_{TR}, cf. Equation (7.2) left.

$$P_{TOT} = P_i + P_o + P_p + P_{TR} \qquad\qquad P_p = F_x \cdot U_\infty = 1/2 \cdot \rho \cdot A_{ref} \cdot C_D \cdot U_\infty^3 \tag{7.2}$$

According to Ref. [70], about 50 % of the power requirements are related to parasite power for light helicopters in level flight. In Equation (7.2) right, the relation of the parasite power and the drag coefficient is presented.

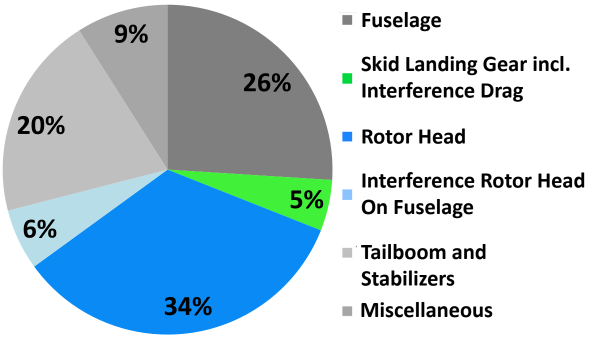

Figure 7.12: Decomposition of the drag coefficient for a lightweight helicopter configuration, Ref. [30].

As investigated in Ref. [30] for a very similar helicopter configuration, the drag coefficient can be decomposed as illustrated in Figure 7.12. The intake drag contribution is subsequently treated as part of the fuselage drag. Consequently, the drag associated to the fuselage accounts for approximately 13 % of the total helicopter power requirement. As presented in Equation (7.3), the available engine power is introduced in this case to quantify the efficiency of the intake, which is integrated between the airframe and the engine. It denotes the difference of the engine power $P_{engine}(x)$ and the total required power $P_{TOT}(x)$, at identical freestream and engine mass flow conditions. Due to an assumed balance of the total required power and the engine power for the reference configuration, $P_{TOT,Ref}$ equals $P_{engine,Ref}$ and therefore, $P_{avail,Ref} = 0$.

$$P_{avail}(x) = P_{engine}(x) - P_{TOT}(x) \tag{7.3}$$

Further can be applied Equation (7.4), by relating the difference of Equation (7.3) to $P_{engine,Ref}$:

$$\Delta P_{avail,rel}(x) = \left(\frac{P_{engine}(x) - P_{engine,Ref}}{P_{engine,Ref}}\right) - \left(\frac{P_{TOT}(x) - P_{TOT,Ref}}{P_{engine,Ref}}\right) \tag{7.4}$$

The first term can be subdivided into two terms, due to the relative contribution to the engine power changes caused by changes in η and DC_{60}, respectively. For the relative changes in the required power, only intake related drag contributions to the fuselage drag are considered. Thus, an objective function $F(x)$ can be formulated as illustrated in Equation (7.5).

$$F(x) = -(\Delta P_{avail,\ \eta,\ rel}(x) + \Delta P_{avail,\ DC60,\ rel}(x) - \Delta P_{avail,\ fuselage\ drag,\ rel}(x)) \tag{7.5}$$

The objective function $F(x)$ of the current parameter study represents a weighted sum approach and reads as presented in Equation (7.6). All assumptions from this chapter are included. Furthermore, "Ref" denotes the values obtained by simulating the reference configuration, integrated in the numerical setup as described before.

$$F(x) = -\left(2\cdot\left(\frac{\eta(x) - \eta_{Ref}}{\eta_{Ref}}\right) + \left(\frac{P_{engine,DC60}(x) - P_{engine,Ref}}{P_{engine,Ref}}\right) - 0.13\cdot\left(\frac{c_{D,fuselage}(x) - c_{D,fuselage,Ref}}{c_{D,fuselage,Ref}}\right)\right) \tag{7.6}$$

The separate contribution to engine power changes due to total pressure distortion are approximated by a polynomial of sixth order and based on the measured results from Ref. [78].

Comparison of the Original and the Simplified Reference Geometry

In this sub-chapter, the computational flow field result of the reference geometry is compared for the original and simplified EID geometries. In Figure 7.13, the qualitative flow separation at the front intake lip and its downstream effect are illustrated by total pressure iso surfaces. The main separation onset from the central part of the front intake lip is similar for both cases. However, the emanating structures that occur in the EPC and EID are considerably different.

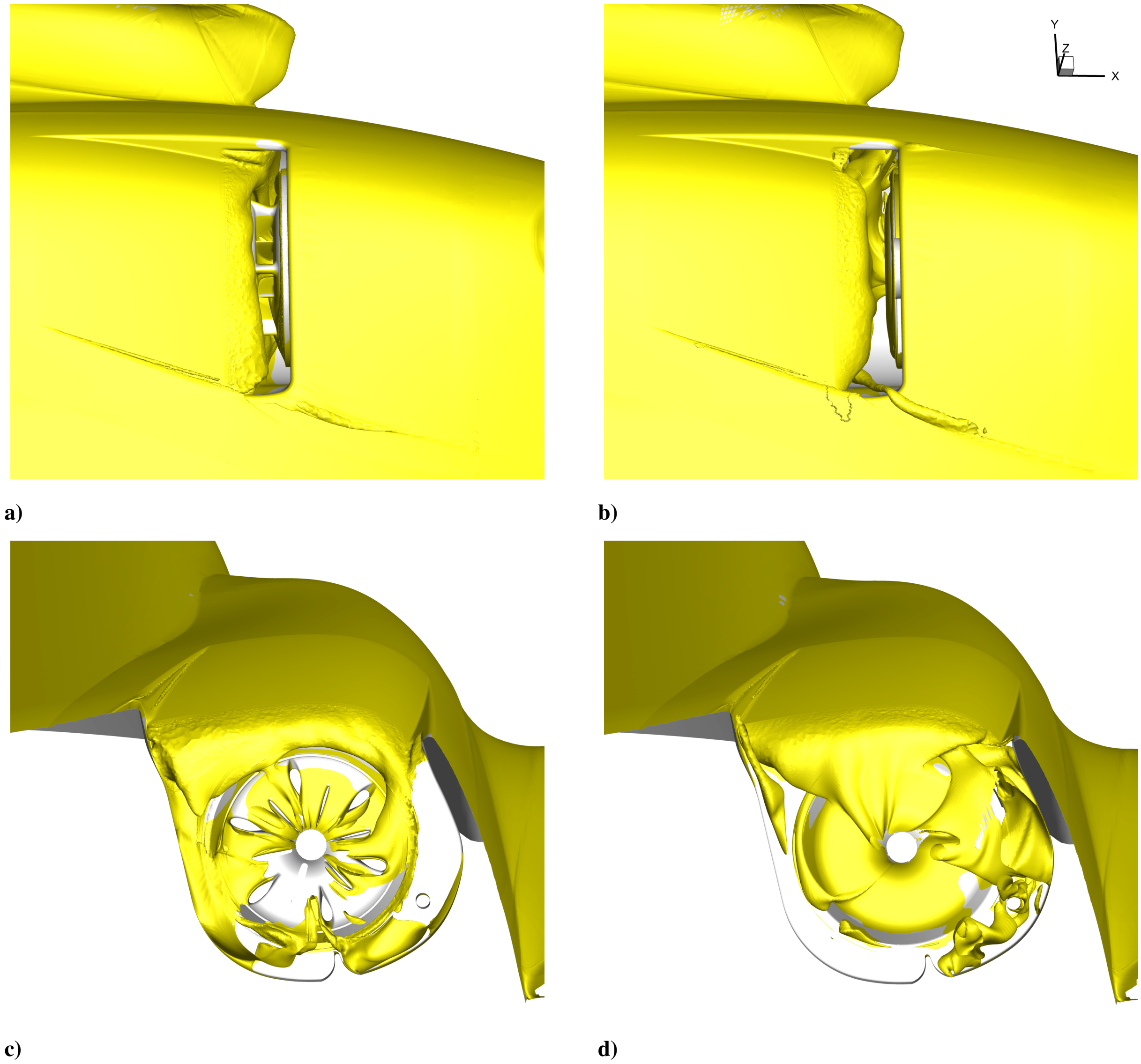

Figure 7.13: Total pressure iso surfaces for $\eta_{norm} = 0.988$, a) top view of the original reference geometry, b) top view of the simplified reference geometry, c) back view of the original reference geometry and d) back view of the simplified reference geometry.

Figure 7.14 presents the separation behavior at the front intake lip in more detail. Hereby, Figure 7.14a refers to a cut in the $X_{AIP} - Z_{AIP}-$ plane for the original reference case, including the influence of the central outer EID guide vane. Figure 7.14b shows a cut view through a plane at the circumferential angle $\theta = 15°$, representing the flow field between the outer and inner guide vanes for the original reference geometry. Figure 7.14c shows a cut in the $X_{AIP} - Z_{AIP}-$ plane for the simplified reference case. The flow separation onset location as well as the extent and total pressure level are very similar for both geometrical cases. The upstream effect of the simplifications only influences the local topology, the average total pressure levels are not affected significantly.

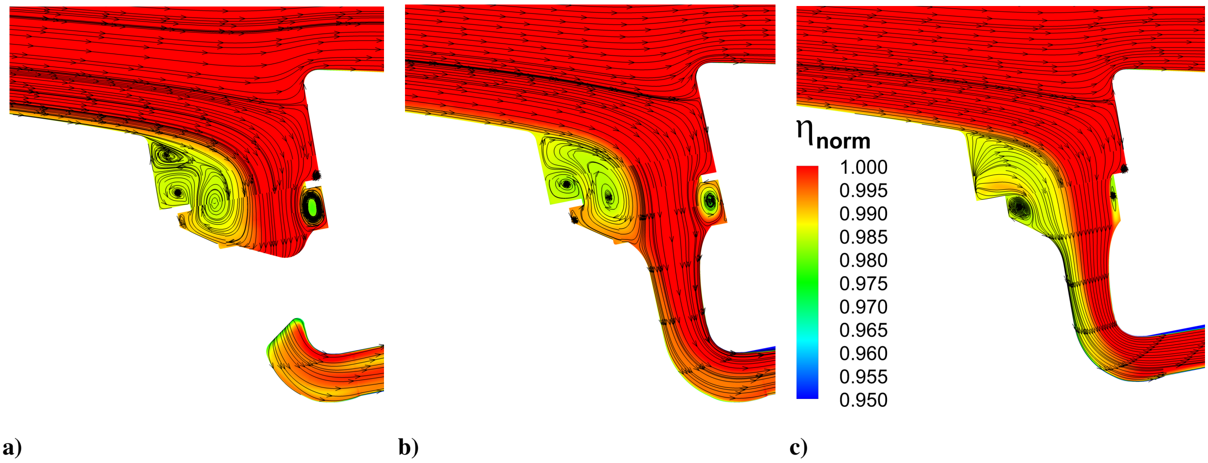

Figure 7.14: Normalized total pressure ratio distribution, a) sectional cut view in $X_{AIP}\ Z_{AIP}-$ plane of the original reference geometry, b) sectional cut view at $\theta = 15°$ of the original reference geometry and c) sectional cut view in $X_{AIP}\ Z_{AIP}-$ plane of the simplified reference geometry.

The AIP representations of the original and simplified cases in Figure 7.15 confirm the latter findings. Even if the AIP total pressure distributions are considerably different, the assessed engine power output loss due to the more complex original geometry is only $\Delta P_{avail,DC60,rel} \approx -0.24\ \%$. However, the average AIP total pressure level is very similar. The original geometry features a decrease of the total pressure level of $\Delta\eta_{norm,rel} \approx -0.29\ \%$, which is considered small enough for the use of the simplified geometry as reference for the subsequent parameter studies. Furthermore, the influence of the distortion on the engine power output is estimated to be one order of magnitude less important than the AIP total pressure level.

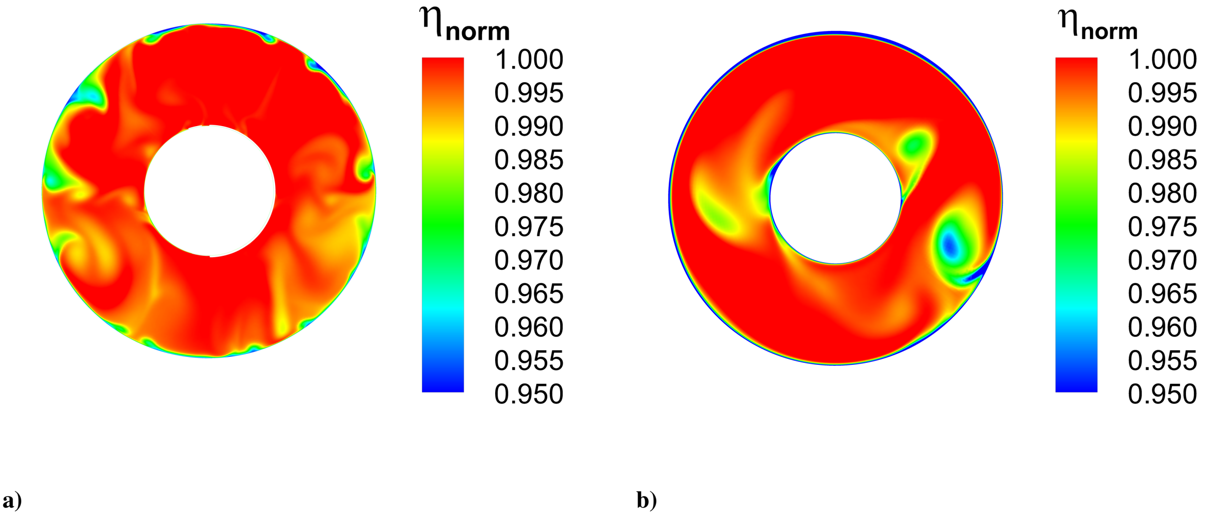

Figure 7.15: Normalized total pressure ratio distribution, a) AIP back view of the original reference geometry and b) AIP back view of the simplified reference geometry.

Regarding the alteration of the fuselage drag due to the intake geometry, Figure 7.16 illustrates regions of separated flow at the fuselage aft geometry by means of axial velocity iso surfaces for $U = -0.5\ m/s$. In addition, the surface pressure coefficients are displayed.

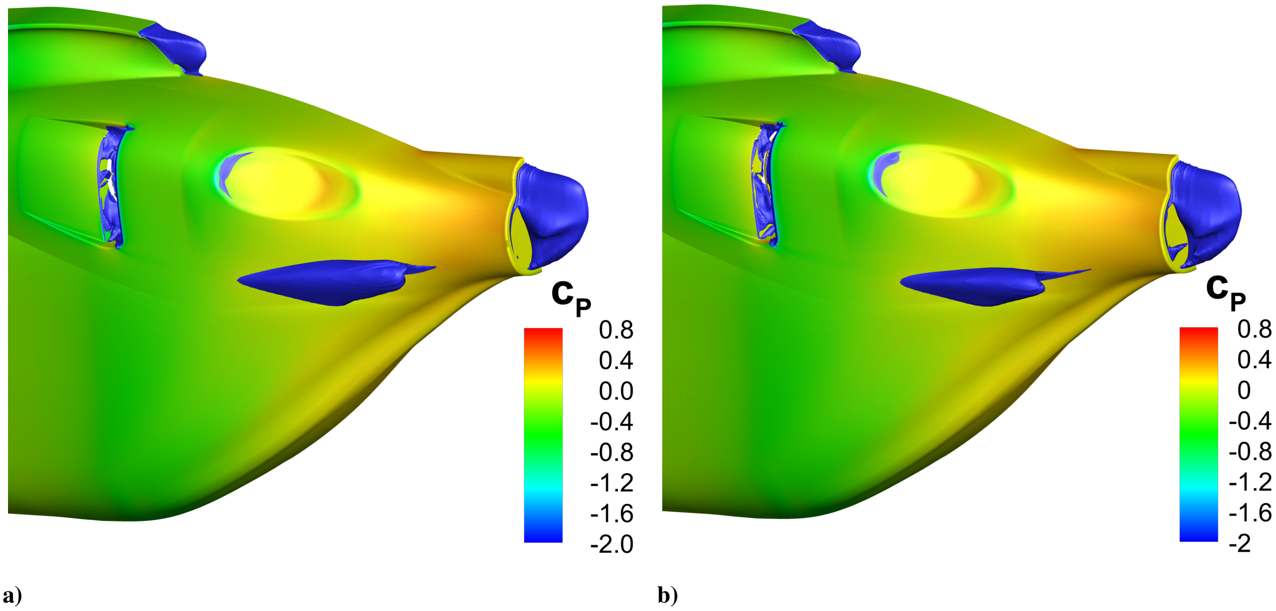

Figure 7.16: Display of aft-body separation regions at helicopter fuselage, indicated by green iso surfaces of the axial velocity $U = -0.5\ m/s$, a) perspective view of the original reference geometry and b) perspective view of the simplified reference geometry.

The drag contribution of to the outer components Fuselage, Cabin, Cowling and Ramp is $\Delta C_{D,outercomponents,rel} \approx +1.4\ \%$ higher for the simplified geometry, compared to the original geometry. The EID region leads to a suction force due to the prevailing strong acceleration along the back EID wall for the simplified geometry. This leads to an approximate relative component drag reduction of the EID of $\Delta C_{D,EID,rel} \approx 5\ \%$. The EPC contribution to the overall drag is one order of magnitude lower than that of the other geometrical regions. The overall drag coefficient of the simplified case is $\Delta C_{D,rel} \approx -1,5\ \%$ lower than that of the original geometry.

Consequently, the expected differences in the power requirement estimation due to the geometrical simplifications is assessed as acceptable for the scope of the following parameter studies.

Parameter Study

In Figure 7.17, an exemplary side intake geometry is presented in different views. The geometry of each design incorporates the parts cowling (green), ramp (blue) and scoop (orange).

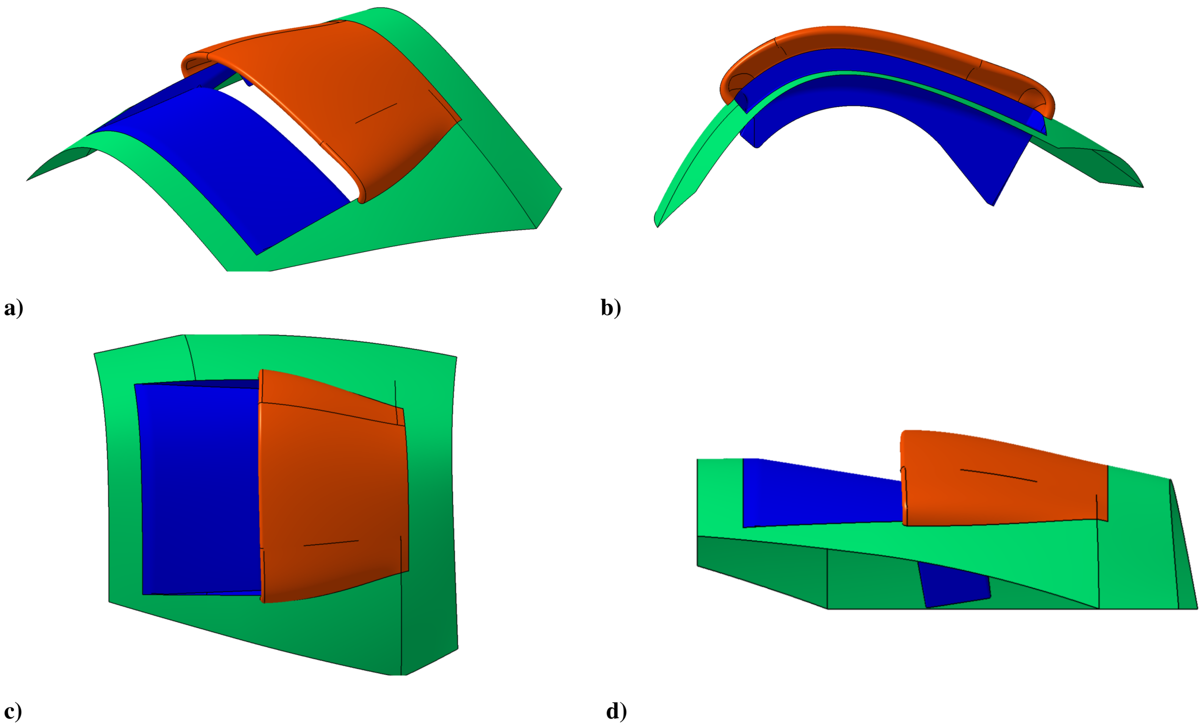

Figure 7.17: Exemplary side intake geometry in a) isometric, b) front, c) top and d) side view.

In Figure 7.18, the parametrization of the side intake geometry is presented. In analogy with the parametrization of Chapter 3.2, an intake overlapping ratio $R = l_{Sc}/l_I$ and a relative height parameter $H_{rel} = h_{Sc}/h_{I2}$ are defined. Furthermore, $r_{rel} = r_i/r_{I2}$ describes the relation of the radius at the end of the intake ramp to that of the reference geometry.

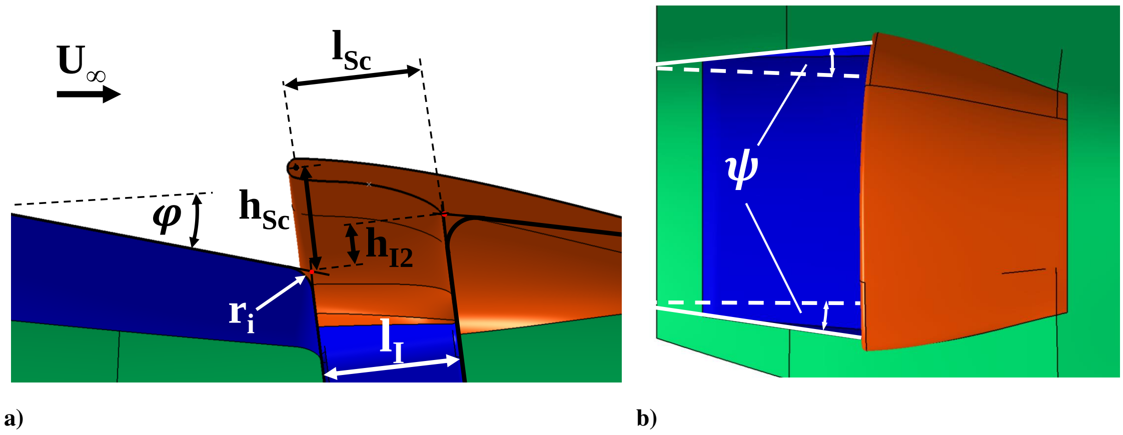

Figure 7.18: Parametrization of side intake geometry a) ramp and scoop geometry in sectional view, b) ramp parametrization in top view.

As in the 2D side intake parameter case, a relative ramp angle parameter $\varphi_{rel} = \varphi/\varphi_{I2}$ is varied. In addition to the parametrization of the 2D side intake case, the planform of the side intake is variable. Convergent, parallel and divergent intake ramps are realized by variation of the ramp side angle ψ. The subsequent parameter study is subdivided in three separate investigations dedicated to the sensitivity of the geometric parameters related to the scoop, ramp and planform in terms of their influence on available engine power. The corresponding parameter variations are presented in Table 7.2.

Run	*Scoop study*	*Ramp study*	*Planform study*
Ramp angle φ_{rel}	0.88	0.78 - 1.03	0.88
Ramp radius r_{rel}	2	0.25 - 4	2
Overlapping ratio R	0.25 - 1.4	1	0.6 - 1
Scoop height H_{rel}	1.315 - 2.89	1.94	1.94
Ramp side angle ψ	0	0	-6 deg - 6 deg

Table 7.2: Parameter limits of parameter studies, relative to the reference configuration, only ψ presented as absolute value.

In Figure 7.19, the influence of the variation of the parameters H_{rel} and R on the available engine power is presented. The objective function F is mainly affected by the change in total pressure ratio and fuselage drag due to the variation in scoop height and forward protrusion.

As illustrated in Figure 7.19a, for low scoop geometries with high overlapping of the intake, an increase in available engine power of 3.8 % is achieved. The available engine power enhancement is nearly equally caused by improved pressure recovery and drag levels. With an increased scoop height, the separation region at the downstream side of the scoop surface is enlarged, which creates higher fuselage drag. The available engine power is increased with an larger H_{rel} due to higher η levels. For $H_{rel} < 2$, a combination of both effects is expected to lead to an optimum design. Regarding the levels of $\Delta P_{avail,DC60,rel}$, the improved flow homogeneity in the AIP due to the scoop does not significantly influence the available engine power level. The changes due to DC_{60} are roughly one order of magnitude less compared to the influence of drag and total pressure level.

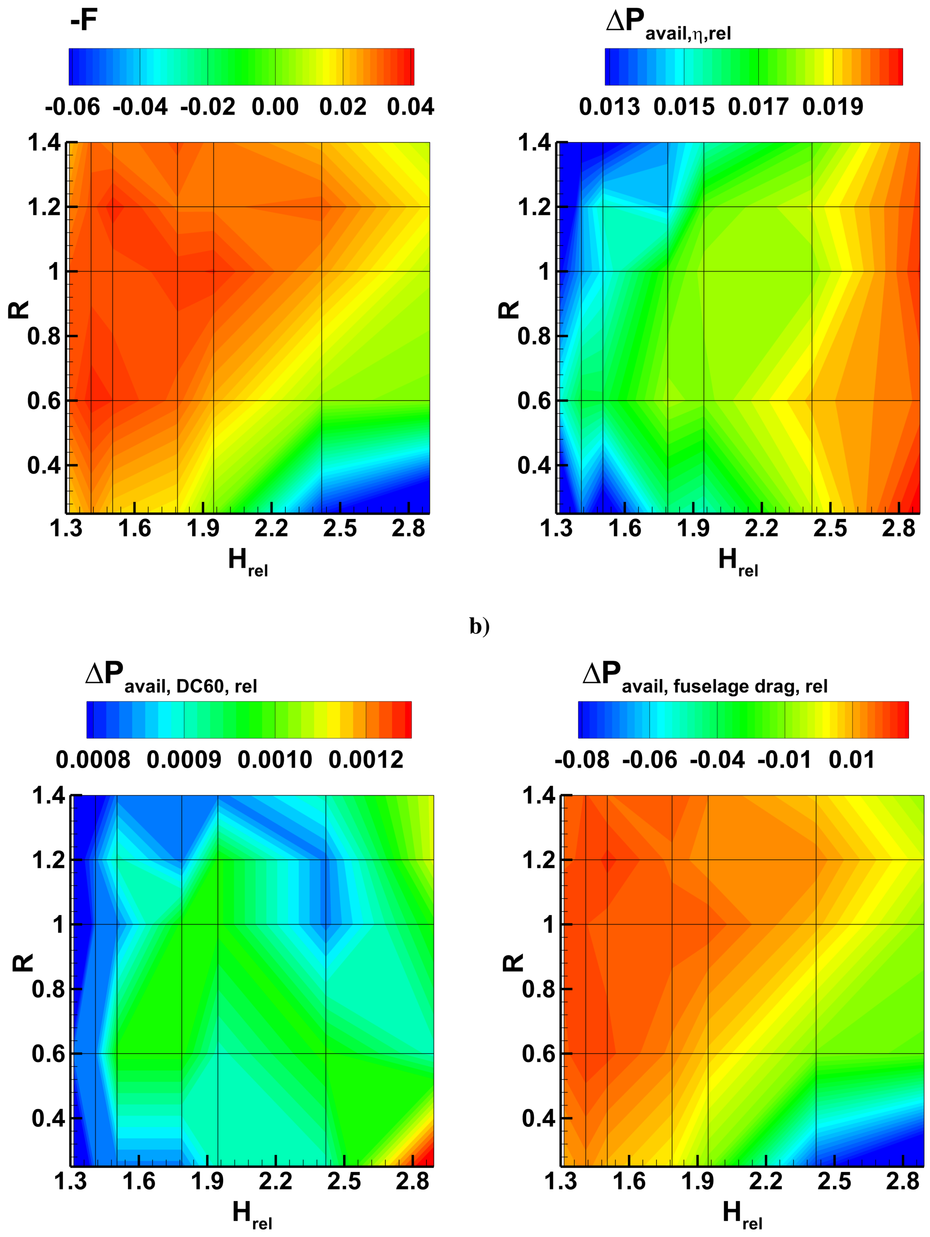

a) b)

c) d)

Figure 7.19: Variation of the relative scoop height H_{rel} and the scoop overlapping ratio R, $\varphi_{rel} = 0.88$, $r_{rel} = 2$, $\psi = 0\ deg$, relative change of the available engine power a) total change, b) portion due to η, c) portion due to $DC60$ and d) portion due to fuselage drag.

In Figure 7.20, the influence of the variation of the parameters φ_{rel} and r_{rel} on the available engine power is presented. A relative ramp angle of $\varphi_{rel} = 0.88 - 0.98$ leads to the highest levels of all three terms which constitute the available engine power. For $r_{rel} < 3$, the highest available engine power is predicted.

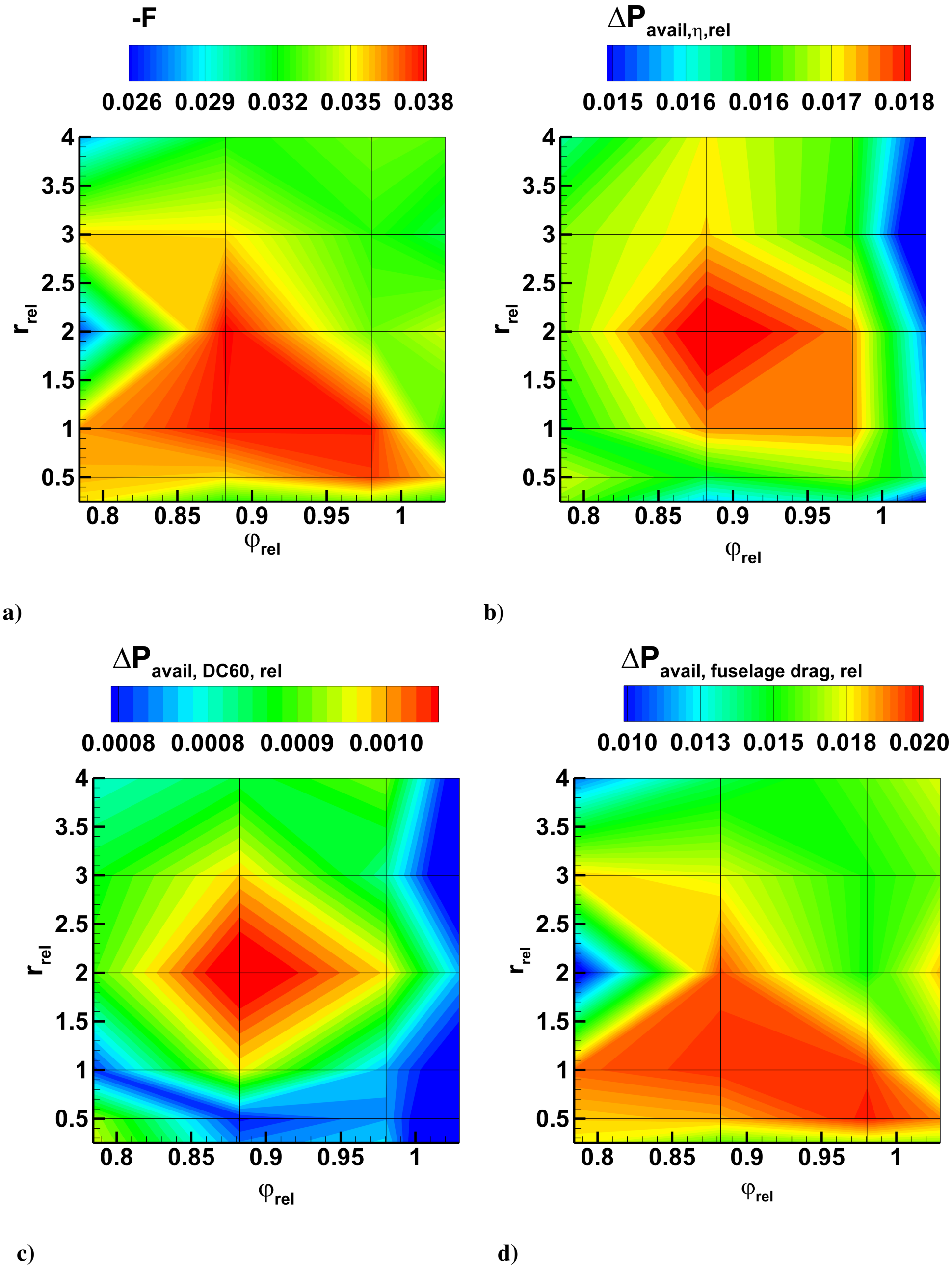

a) b) c) d)

Figure 7.20: Variation of the relative ramp angle φ_{rel} and the relative ramp radius r_{rel}, $H_{rel} = 1.94$, $R = 1.0$, $\psi = 0\ deg$, relative change of the available engine power a) total change, b) portion due to η, c) portion due to $DC60$ and d) portion due to fuselage drag.

Comparing the two first parameter studies, the variations of the parameters H_{rel} and R lead to considerably larger differences than the variations of the parameters φ_{rel} and r_{rel}. Again, DC_{60} is approximately one order of magnitude less important than drag and total pressure level.

In Figure 7.21, the influence of the variation of the parameters ψ and R on the available engine power is depicted. In terms of the influence due to all three evaluation parameters total pressure ratio, total pressure distortion and drag, a ramp plan form with parallel or slightly divergent side walls ($0 deg < \psi < 3\ deg$) is beneficial.

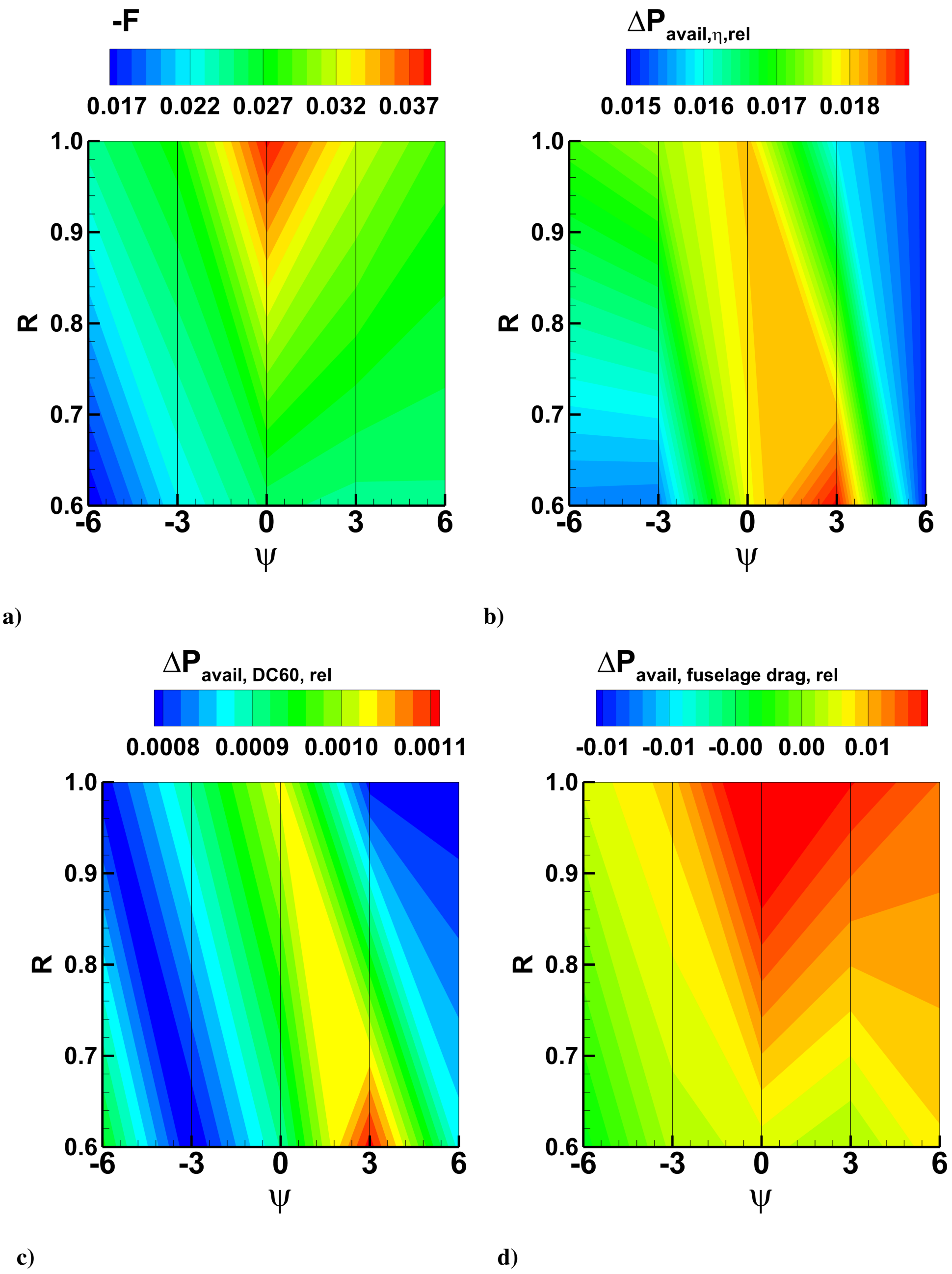

a) b) c) d)

Figure 7.21: Variation of the ramp side angle ψ and the scoop overlapping ratio R, $H_{rel} = 1.94$, $\varphi_{rel} = 0.88$, $r_{rel} = 2$, relative change of the available engine power a) total change, b) portion due to η, c) portion due to $DC60$ and d) portion due to fuselage drag.

Especially for the completely shielded intake opening ($R = 1$), the lowest fuselage drag occurs. Consequently, for the planforms combined with $R = 1$, the total available engine power is the highest. The latter findings of the three parameter studies are taken into account and the best design is analyzed subsequently.

Comparison of the Simplified Reference Geometry with the Best Parameter Case

In the following paragraph, the flowfield of the simplified reference configuration is compared to the configuration with the highest increase in engine power, namely the configuration defined by $R = 1.0$, $H_{rel} = 1.94$, $\varphi_{rel} = 0.88$, $r_{rel} = 2$ as well as $\psi = 0\ deg$. The corresponding configuration is displayed in Figure 7.22.

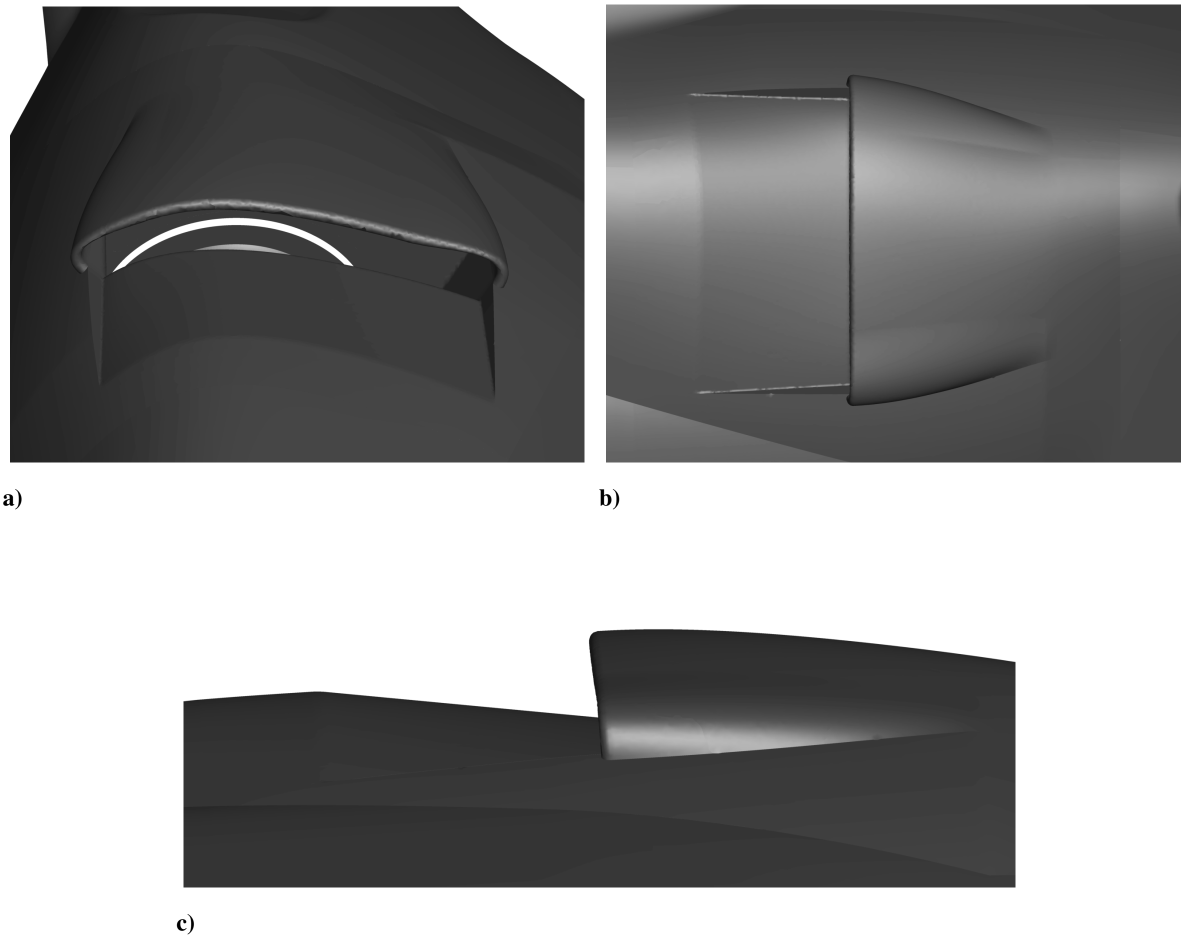

Figure 7.22: Geometric display of the configuration defined by $R = 1.0$, $H_{rel} = 1.94$, $\varphi_{rel} = 0.88$, $r_{rel} = 2$ as well as $\psi = 0 deg$ a) front view, b) top view and c) side view.

In order to asses the influence of the best geometry on the engine power output, first, the change of the total pressure is compared to the reference geometry. For this purpose, iso surfaces of $\eta_{norm} = 0.988$ are illustrated in the intake region, compare Figure 7.23. The best parameter case features significantly higher η_{norm} levels as the reference case. From a run length of $\approx 20\ \%$ along the cowling ramp to the AIP, nearly the entire flow field incorporates η_{norm} levels above 0.988.

The sectional views through the $X_{AIP} - Z_{AIP}-$ plane in Figures 7.24a and b exhibit the positive effect of the scoop. The parameters that define the scoop are chosen in a way, that the flow stays attached both on the inner and outer surfaces. Thereby, the oncoming flow is decelerated and the intake entry pressure is strongly increased. Simultaneously, no significant region of separated flow is evoked on the outer surface of the scoop. Consequently, the AIP total pressure level is increased distinctly leading to an engine power

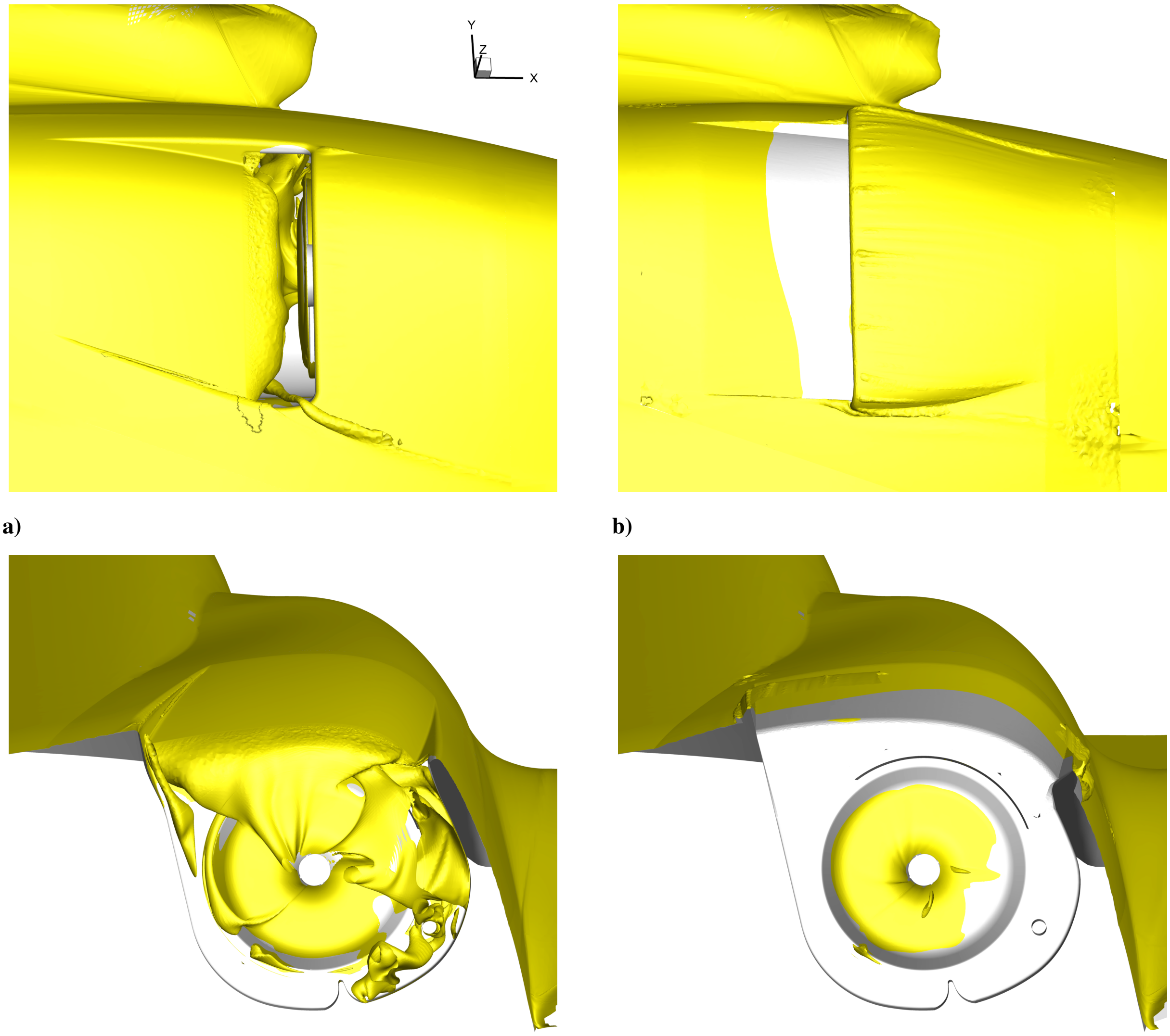

a)

b)

c)

d)

Figure 7.23: Total pressure iso surfaces for $\eta_{norm} = 0.988$, a) top view of the reference geometry, b) top view of the best parameter case, c) back view of the reference geometry and d) back view of the best parameter case.

enhancement of 1.8 %. The homogeneity of the flow field is also significantly improved as depicted in Figure 7.24 d.

In Figure 7.25, regions of separated flow are displayed for both the reference case and the best parameter case by means of negative axial flow velocity iso surfaces. The region of separated flow on the side of the fuselage aft body is significantly decreased, leading to a relative reduction of the overall drag of the geometry regarded in the CFD simulations. The higher pressure at the ramp and inside the intake also reduces the drag of the configuration. Despite the additional drag of the scoop, an effective overall reduction of $\Delta C_D \approx 14.5$ % is achieved.

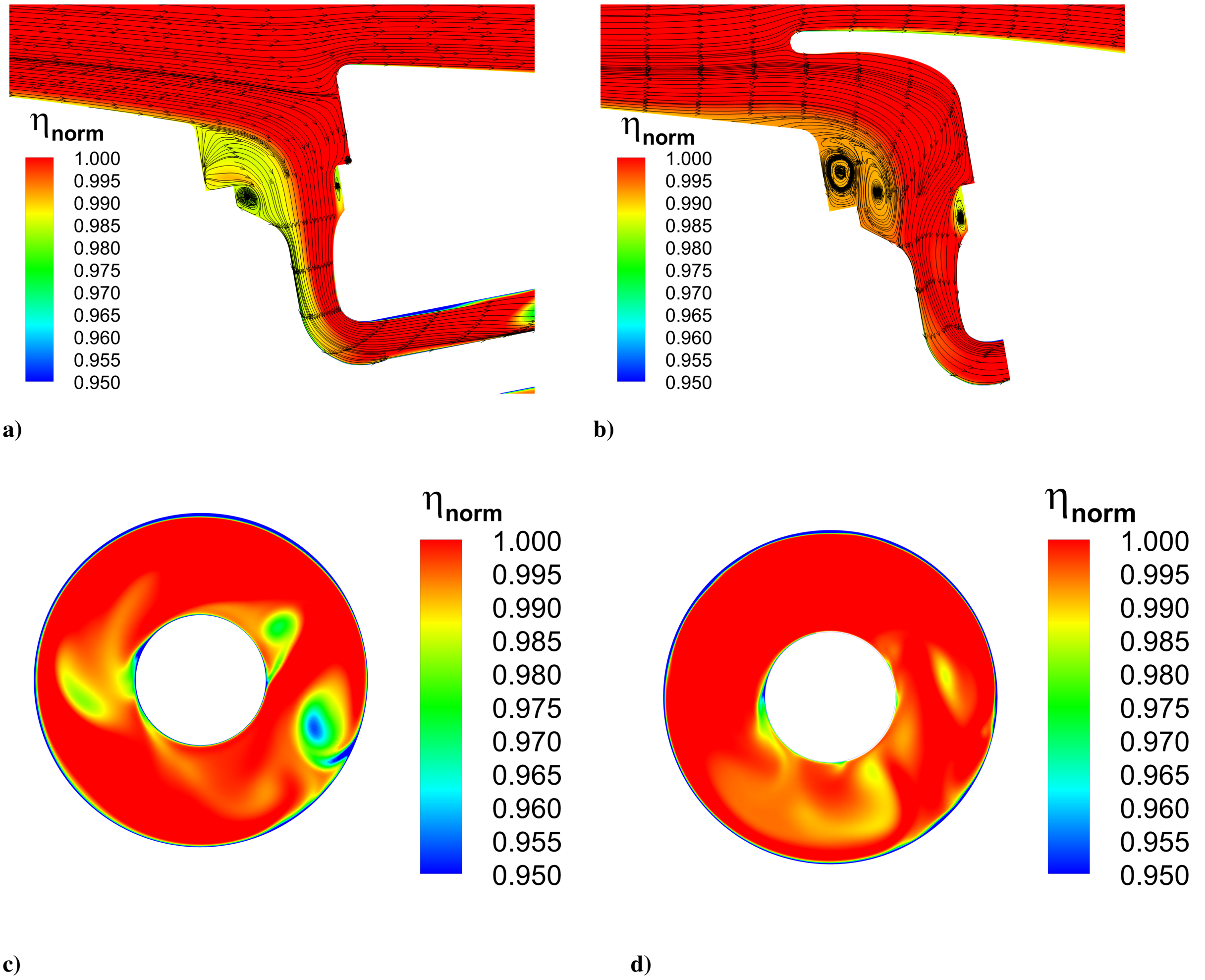

Figure 7.24: Normalized total pressure ratio distribution, a) sectional cut view in $X_{AIP} - Z_{AIP}-$ plane of the reference geometry, b) sectional cut view in $X_{AIP} - Z_{AIP}-$ plane of the best parameter case, c) AIP back view of the reference geometry and d) AIP back view of the best parameter case.

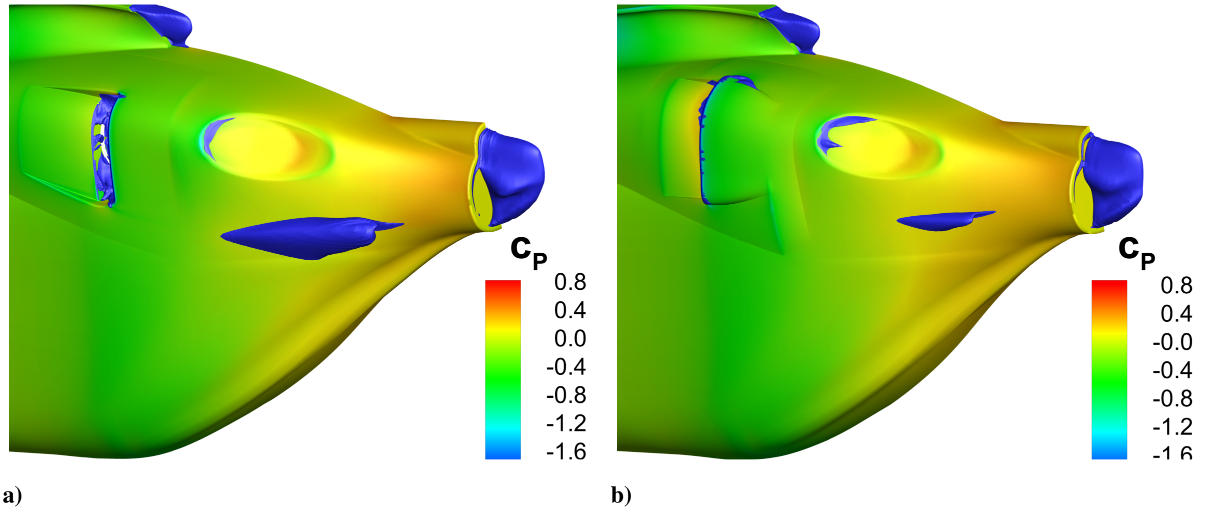

Figure 7.25: Display of aft-body separation regions at the helicopter fuselage, indicated by green iso surfaces of axial velocity $U = -0.5\ m/s$, a) perspective view of the reference geometry and b) perspective view of the best parameter case.

7.3 Synthesis

Based on the experimental results of three basic intakes and further retrofit aerodynamic modifications, parameter studies and optimization is performed. To improve the engine inflow conditions and the overall performance of the helicopter, a stepwise approach is applied. With the help of the ANSYS Workbench environment, as a first step, an optimization of the total pressure recovery upstream of the intake is conducted for a simplified two-dimensional intake geometry, derived from the reference configuration. The case mainly reflects the effect on the total pressure ratio in the top AIP region of the "real" three-dimensional plenum chamber type side intakes. Aerodynamic interface total pressure distortion and altered fuselage drag due to the intake are not considered in the first two parameter cases. Starting from the reference configuration, the approach ramp angle, the scoop height and forward protrusion as well as the upstream intake lip radius is varied. The effect of the intake lip radius is assessed to be of minor importance. A maximum increase of pressure recovery of 0.3 % is achieved by the best configuration. It features a slightly lowered ramp incidence angle compared to the reference case combined with a relative scoop height $H_{rel} = 4.25$ and an overlapping ratio $R = 2.4$. The effective smooth deflection of the core flow region leads to an increased pressure recovery. The extent of the core flow region indicates, that for fast forward flight, a smaller intake cross section would be sufficient.
As a second parameter case, a geometry derived from NACA-type submerged intakes is investigated. The Automated Aerodynamic Shape Development environment is applied to conduct parameter studies of an approach ramp with the purpose of pressure recovery optimization. Hereby, ramps with convergent, parallel and divergent side walls are investigated, in combination with different side wall and ramp angles. Furthermore, the axial position of the inflection point of the side walls and ramp are investigated. For the velocity ratio of $U_{AIP}/U_\infty \approx 1.5$, a ramp angle of $\varphi = 10\ deg$ is optimal, combined with parallel or slightly convergent side walls. The greatest difference related to the planform is found comparing a $\psi = 10\ deg$ convergent and $\psi = 8\ deg$ divergent geometry at constant ramp angle of $\varphi = 10\ deg$. The relative difference is $\Delta\eta_\psi \approx 0.18$ %. The improvement of engine entry total pressure due to a vortex, that emanates from a divergent side wall and transports highly-energetic fluid from the free stream flow to the wall, is of minor effect for the velocity ratios occuring in the current investigation. Generally, further upstream inflection points of the side walls and ramp are more beneficial.

Geometrically, the third parameter case is derived from the reference geometry and the retrofit modification cases, describing a realistic plenum chamber type side intake configuration. The parametrization is based on the first two parameter cases and the parameter studies are conducted applying the Automated Aerodynamic Shape Development environment. The numerical setup is very similar to the full fuselage case of Chapter 5.2, with a simplified engine intake duct geometry for computational cost reduction and an unstructured tetrahedron intake mesh for better script-based meshing. In order to quantify the intake performance integrated in the helicopter configuration compared to a reference case, an objective function is formulated as weighted sum. Hereby,changes of the available engine power in dependence of total pressure ratio, total pressure distortion as well as drag increments are taken into account. Before the actual parameter study, the influence of the simplifications made in the engine intake duct are assessed. The separation onset position and total pressure levels at the intake entry are very similar for the original and simplified reference configurations. The integral total pressure recovery differs by only $\Delta\eta_{norm,rel} \approx -0.29$ %. Even if the flow topologies in the plenum chamber and engine intake duct are different for both cases, only a slight change in the engine power due to the total pressure distortion of $\Delta P_{avail,DC60,rel} \approx +0.24$ % occurs. The drag is $\Delta C_{D,rel} \approx -1,5$ % lower for the simplified geometry, compared to the original reference case. Overall, the geometrical simplifications and resulting slight alterations in available engine power estimations are assessed as tolerable for the subsequent parameter studies.

Subsequently, three dedicated parameter studies are performed, to distinguish the effect of the parameters related to the scoop, the ramp and the ramp planform on the available engine power. The "scoop" parameter study indicates, that configurations with a low relative height parameter H_{rel} and high overlapping ratio R of the scoop achieve the highest enhancement of the available engine power of 3.8 %. The increase nearly equally originates from improved pressure recovery and lowered drag levels. For higher H_{rel}, the available engine power is increased due to higher η levels, but parasite drag increases disproportionately high. An optimal design is expected for $H_{rel} < 2$. The alterations of available engine power related to DC_{60} are roughly one order of magnitude less important compared to the changes due to drag and total pressure level.

The "ramp" parameter study indicates, that a relative ramp angle of $\varphi_{rel} = 0.88 - 0.98$ combined with a relative ramp radius of $r_{rel} < 3$ leads to the highest levels of available engine power. The relative ramp angle result confirms the findings of the two-dimensional side intake case. Generally, the differences in the "ramp" parameter study are smaller than those exhibited in the "scoop" parameter study. The "planform" parameter study reveales the highest available engine power level for parallel or slightly divergent side walls ($3deg < \psi < 0\ deg$).

The comparison of the flow fields of the best parameter case ($R = 1.0$, $H_{rel} = 1.94$, $\varphi_{rel} = 0.88$, $r_{rel} = 2$ as well as $\psi = 0\ deg$) and the reference configuration substantiates the findings of the parameter studies. From the intake entry to the aerodynamic interface plane, the best parameter case shows significantly higher total pressure levels. At the same time, the flow is attached on the inner and outer surfaces of the scoop. The combination of no additional regions of separated flow and higher pressure levels on the ramp and in the plenum chamber leads to a significant decrease of parasite drag.

8 Conclusions

The main scope of the current thesis is the aerodynamic investigation of plenum chamber type side intake configurations as typically used in helicopter configurations. Hereby, an emphasis is placed on a light weight utility helicopter in fast forward flight conditions. As part of the CLEANSKY research project ATHENAI, a full-scale engine air intake wind tunnel setup was realized. With the help of this setup, comprehensive experimental studies are performed and complemented by numerical investigations. The theoretical basis and an overview is provided by a brief summary of essential parameters to assess aerodynamic intake characteristics such as aerodynamic interface plane total pressure distortion, total pressure recovery and swirl, related to different intake geometries and operating conditions.

For the experiments, a full-scale wind tunnel model of a helicopter fuselage section is designed including all essential intake components, for testing at realistic Reynolds and Mach numbers. The model allows for a simple exchange of the intake shape and plenum chamber geometry. For total pressure and velocity field characterization at 96 locations in the aerodynamic interface plane, a circumferentially adjustable 5-hole probe system is designed and integrated. To achieve an accurate mass flow reproduction in the wind tunnel, a duct system and Venturi meter are integrated and operated in combination with a suitable fan. In addition, surface pressure as well as particle image velocimetry measurements are performed to provide information about the local flow characteristics and the oncoming flow velocities, respectively.

In the experimental research for this thesis, basic intake variants and retrofit variants based on one basic reference geometry are distinguished. The three basic intake configurations include three different geometrical approaches. The first is a classical "static" sideways-facing side intake in combination with a square-cut plenum chamber, the "baseline" configuration. The second basic intake, also referred to as "semi-dynamic", includes a cowling approach ramp and a rounded-shaped plenum chamber. The third basic intake, also referred to as "dynamic", is based on the second geometry complemented with a scoop, thus creating a forward-facing plenum chamber type side intake.

Derived from the results of the basic intake configurations, further retrofit geometries such as an intake guide vane and an intake rear spoiler are tested on the basis of the second basic intake, which serves as the "reference" configuration. In addition, plenum chamber splitters and intake grids are tested. To complement the experimental intake testing, numerical investigations at two different geometrical setups are performed, solving the unsteady Reynolds-averaged Navier-Stokes equations with ANSYS CFX and the shear-stress transport turbulence model. The first setup is related to the sectional fuselage case, flush-mounted to the wind tunnel floor, as tested in the wind tunnel, including all essential intake components and the wind tunnel nozzle as well as the collector. The second geometry is a representation of the he-

licopter with its fuselage comprising the intake in free flight, however without rotor and rotor head. For both cases, a high emphasis is placed on the mesh quality, thus leading to a purely block-structured grid approach.
The numerical results of the sectional fuselage case including the baseline intake are validated against experimental surface pressure distributions, particle image velocimetry data and aerodynamic interface plane total pressure distributions.

The sectional and free flight fuselage cases lead to very similar engine entry conditions, the normalized total pressure coefficient differ by merely -0.06 % and the normalized distortion parameter by 2.12 %. In combination with the similar cross-flow angles identified upstream of the intake opening, the truncation assumption is therefore assumed to be justified.
For the sectional fuselage case, detailed investigations of the flow field from the intake entry to the aerodynamic interface plane are conducted for a fast-forward flight condition. The main large-scale and some small-scale flow phenomena of the intake flow field are identified, that originate a complex engine entry total pressure pattern. By means of the local vorticity distributions and surface streamlines, a vortex incorporating high positive vorticity is found that rolls up from the shear layer downstream of the front intake lip separation line. Between the vortices and the stagnation line at the downstream intake wall, high momentum air is ingested from the undisturbed freestream flow, which subsequently leads to a region of high total pressures in the aerodynamic interface plane (between $\theta = 330°$ and $\theta = 60°$). A region of separated flow of large extent is identified inside the plenum chamber, originating from an additional flow separation at the right side intake lip. Consequently, lowered total pressures and velocities persist in the angle regime of $60° < \theta < 200°$, throughout the entire engine intake duct up to the aerodynamic interface plane. In the angular region of $200° < \theta < 330°$, small-scale separation regions are detected, resulting from high local incidence angles of the guide vanes in the duct.
The investigation of the aerodynamic characteristics of the basic intakes clearly shows benefits in the total pressure ratio, total pressure distortion and the mean swirl angles of the second and third intakes over the baseline intake, especially in fast forward flight conditions. For low freestream velocities, the corresponding expected engine power output is very similar for the baseline and the second intake configuration. For the higher freestream velocities, up to an engine power reduction of $\Delta P_{avail} \approx -1.4$ % is expected for the static baseline intake. The third intake configuration is estimated to lead to engine power losses of $\Delta P_{avail} \approx -1.5$ % for zero freestream velocity case and to power enhancements of $\Delta P_{avail} \approx +1.6$ % in fast forward flight conditions, compared to the second intake configuration. The deterioration of total pressure levels for low freestream velocities is due to the scoop's shielding of the intake entry and thus strong flow deflection of the ingested air. The variation of the mass flow rate does not significantly change the trends referring to the total pressure and total pressure distortion coefficients for the basic geometries. On the basis of the second basic intake configuration, the influence of an intake foreign object damage grid and a plenum chamber splitter device are evaluated. The woven wire intake grid produces additional total pressure losses and leads to a deterioration in the total pressure ratios and total pressure distortion levels, nearly over the complete freestream and mass flow rate range. The splitter straightenes the plenum chamber flow and conditioned the engine duct inflow direction, thus markedly improving the total pressure ratios, total pressure distortion levels and swirl in the aerodynamic interface plane. Thereby, the losses due to the intake grid are compensated. An effective gain of engine power

output of 0.9 % $\leq \Delta P_{avail,rel,splitter} \leq$ 2.4 % is estimated over the freestream velocity range. This configuration is used as the basis and reference case for further retrofit modifications.
Additionally, geometric combinations of the "static" baseline intake and the "semi-dynamic" intake as well as the square-cut baseline plenum chamber and the rounded plenum chamber including a splitter are compared. Hereby, the effect of the plenum chamber and intake shape on the total pressure ratio, total pressure distortion and swirl can be distinguished. The cowling ramp (as part of the second intake) strongly influences the pressure recovery and leads to engine power gains which increase with increasing relative freestream velocities. The plenum chamber, however, has a stronger effect on the total pressure ratio distortion and corresponding engine power changes, which are both dependent on relative freestream velocities and mass flow rate ratios. Related to the cowling ramp a decrease of $\Delta S_{norm} \approx 12 - 24$ % is indicated. The rounded plenum chamber with the splitter originates a swirl level decrease of $\Delta S_{norm} \approx 17 - 31$ %, compared to the square-cut baseline plenum chamber.

Retrofit modifications, fitted to the semi-dynamic intake configuration, are investigated, aimed at the combination of the beneficial characteristics of the basic static, semi-dynamic and dynamic intake geometries. The corresponding investigations include rear spoilers of different heights and forward protrusions as well as an intake guide vane at three different positions, relative to the intake opening. Two geometric variants are selected as best retrofit modifications. The high rear spoilers indicate best static pressure recompression upstream of the intake entry section, especially for the fast forward flight conditions. The short rear spoilers are most beneficial for low freestream velocities related to the small flow deflection of the ingested air and their larger effective intake entry cross section. Therefore, the high rear spoiler with least forward protrusion is evaluated as the best rear spoiler configuration. In fast forward flight, a total pressure improvement of 0.3 % and a decrease in total pressure distortion of almost 20 % leads to a noticeable engine power enhancement. In typical helicopter missions , a substantial portion is constituted by fast forward flight. Hence, with reasonable effort, a considerable reduction in fuel consumption can be achieved by the application of retrofit geometric modifications.
The intake guide vane study unveils best total pressure and total pressure distortion levels in the foremost position. Nonetheless, the total pressure improvements due to the guide vane only occur for high freestream velocities and are not significant comparing to "pure" rear spoiler configurations, even if improved flow deflection around the front intake lip is indicated by surface pressure distributions. Due to the increased blockage of the intake opening, the intake guide vanes markedly reduce total pressures for the low speed test points. For the mid and high freestream velocities, a considerable reduction of total pressure distortion of 10 – 20 % is achieved by the implementation of an intake guide vane. The plenum chamber pressure distributions reveal variations of the local effectiveness of the intake guide vanes, interacting with a rear spoiler. Therefore, for future investigations, an intake guide vane with adapted twist angles and camber or a slotted two-element device could significantly improve flow deflection around the intake lip of such sideways-facing side air intakes. Such investigations are out of the scope for the current research. For the best retrofit modifications, the static pressure distributions substantiate the increase of static intake entry pressure and effectively higher engine entry total pressures. Thereby, the functionality of external retrofit geometric modifications is assured. In analogy with the basic intake geometries, also for the retrofit modifications configurations, two main flow regions are exhibited in the aerodynamic interface plane total pressure distributions. The higher part of the engine entry plane fea-

tures high total pressures, whereas the lower part is dominated by low total pressures. Especially in the lower part, the best retrofit modifications significantly increase total pressure levels in fast forward flight conditions. Furthermore, more homogeneous total pressure distributions substantiate the improvement of total pressure distortion levels. The influence for angles of attack between $-5° < \alpha < +5°$ at the example of the retrofit variant with the high and short rear spoiler including the intake guide vane in the foremost position, is only marginal in terms of total pressure levels in the aerodynamic interface plane. Based on a realistic angle of attack of the corresponding helicopter configuration, a deviation of $\Delta DC_{60,norm} \approx -3.59$ % is determined for the maximum freestream velocity ratio. The swirl results deviate considerably, for both tested freestream velocities, but were not assessed critical as the absolute swirl angles are close to zero.

For further performance improvements of the plenum chamber type side intake geometries, two parameter studies and an optimization are conducted. Applying the ANSYS workbench and an in-house Automated Aerodynamic Shape Development environment, mainly the same parameters are varied as in the experimental retrofit geometric modifications studies. The first case, an optimization of a quasi two dimensional intake section, is based on the reference geometry. The objective is to investigate the effect of the ramp angle and scoop height as well as protrusion on engine entry total pressure level, without regarding detrimental effects due to total pressure distortion and additional drag, related to the intake shape. The hereby achieved best configuration leads to an increase of the total pressure ratio by 0.3 %. The geometry features a relative ramp angle of $\varphi_{rel} = 0.9$ and an extensively increased overlapping ratio of $R \approx 2.4$ as well as a scoop height of $H_{rel} \approx 4.2$. Due to the increased forward protrusion and height of the scoop, a smoother deflection of the flow is achieved. The submerged intake parameter study is aimed at the investigation of the ramp planform as well as the ramp longitudinal section effect on engine entry total pressure levels. The case is geometrically similar to the early NACA submerged intake studies, and so are the trends for total pressure levels. For the investigated velocity ratio of $U_{AIP}/U_{\infty} \approx 1.5$, parallel and convergent planforms are more beneficial for engine entry total pressure than divergent ramp planforms. Compared to the early NACA work, higher ramp angles of $\varphi \approx 10\ deg$ lead to the highest total pressure levels. Especially for these high ramp angles, a more forward inflection point position of the side wall and ramp contour originates higher total pressure levels.

The third case, namely a parameter study case of an engine side air intake, is based on the reference intake geometry. It incorporates a parametrized ramp and scoop, located in the fuselage of the full fuselage case, representing free flight conditions. To reduce the computational effort and allow more parameter variations, the engine intake duct is simplified. For automated script-based mesh generation, an unstructured intake mesh is applied. To realistically evaluate the effect of the parameter variation on the overall helicopter cruise flight efficiency, an objective function is defined which estimates the engine excessive shaft power in relation to the reference case. Hereby incorporated are power output changes in dependence of the engine entry total pressure mean level and distortion. Furthermore, the change of the helicopter fuselage drag is accounted for in the power output balance. As a first step, the flow field solutions of the full fuselage case, including the reference intake geometry, are compared for the original and the simplified engine intake duct. The upstream effect of the duct's simplifications are small and so are the effects on the aerodynamic interface plane total pressure level as well as the fuselage drag. Even if the total pressure distortion in the aerodynamic interface plane is different, due to its minor effect on the engine power output, the geometry including the simplified engine intake duct is assessed to be suitable for the parameter studies. The subsequent parameter studies are subdivided into a dedicated scoop, ramp, as well as a planform study. The parameters are the ramp angle φ_{rel}, the ramp radius r_{rel}, the overlapping ratio R, scoop height H_{rel} as well as the ramp side angle ψ. All three studies indicate an approximately one order of magnitude less significant effect on the power output due to total pressure distortion compared to the influence related to the mean total pressure level or drag. The scoop study indicates, that an increased scoop height increases the engine entry total pressure, but also leads to an extensive region of separated flow on the scoop's downstream surface and thus higher drag. The overlapping ratio has no significant effect on the total pressure levels at the aerodynamic interface plane but features an optimal region between $0.7 < R < 1.3$ in terms of drag. The ramp study shows, that in agreement with the quasi 2D intake optimization case, a ramp angle of $\varphi_{rel} \approx 90\ \%$ compared to the reference geometry leads to the best total pressure levels. In combination with a ramp radius of two times the original radius, highest overall power output levels are generated. The planform study reveales the parallel ramp configuration as best compromise of total pressure as well as drag and leads to the highest overall engine power output. The effect on the engine power output due to the scoop height and overlapping ratio dominates over the other parameters thus implicitly confirming the correctness of the parameter choice for the experimental testing of retrofit geometric variants in terms of effectiveness. As the best parameter case with highest increase in engine power of $\Delta P_{avail} \approx 3.8\ \%$ compared to the reference geometry, the configuration defined by $R = 1.0$, $H_{rel} = 1.94$, $\varphi_{rel} = 0.88$, $r_{rel} = 2$ as well as $\psi = 0\ deg$ is identified. The configuration shows significantly higher total pressure levels from the intake entry to the aerodynamic interface plane, attached flow on the scoop downstream surface and decreased extent of the separation regions on the fuselage aft-body surfaces.

The investigations and testing procedures are applied for a detailed characterization of the inner flow field and identification of improvement potential, especially for the fast forward flight performance of helicopters, including sideways and forward-facing plenum chamber type side intakes.

For detailed investigations and further research of the real behavior of the installed PW206B engine, intake measurement data from the current investigation and the ATHENAI project were provided to the Chair of Turbomachinery and Flight Propulsion. In current and future investigations, the data of the basic intake shapes helps to simulate the total pressure losses, distortion and swirl by application of dedicated screens in a test stand, mounted upstream of the real helicopter engine. By this approach, the aerodynamic interface plane conditions can be reproduced and the resulting performance and stability of the engine can be analyzed.

Furthermore, two of the three basic intake configurations were tested in the flight test campaigns of the Airbus Bluecopter Demonstrator. The wind tunnel tests at high technology readiness level helped to decrease the uncertainty of the engine behavior, in combination with the novel intake configurations. In future comparisons, the data base from this research, the research from the Chair of Turbomachinery and Flight Propulsion as well as the flight test data could be compared.

Experimental and numerical approaches similar to those used in the current research can be a basis for the development process of other novel helicopter intakes, leading to valuable information in the early design phase of the engine-airframe integration process. The concrete testing facility, including the fan, mass flow as well as five-hole probe measurement, can also be used for the investigation of inlet barrier filters, scavengers or other subsonic intake configurations, operating at similar conditions.

Bibliography

[1] Adams, B., Ebeida, M., Eldred, M., Jakeman, J., Maupin, K., and Monschke, J. *Dakota, a multilevel parallel object-oriented framework for design optimization, parameter estimation, uncertainty quantification, and sensitivity analysis, User Manual.* Sandia National Laboratories, Albuquerque, NM, USA. v6.4, ID: SAND2014-4633, 2016.

[2] Aeroprobe Corporation. Five-Hole Pitch and Yaw Probe Manual. Blacksburg, VA, USA, v3.1, 2010.

[3] Ahn, G. B., Jung, K. Y., and Myong, R. S. Numerical and Experimental Investigation of Ice Accretion on Rotorcraft Engine Air Intake. *Journal of Aircraft.* Vol. 52, No. 3, DOI: 10.2514/1.C032839, 2015, pp. 903 - 909.

[4] Airbushelicopters.ca. Airbus Helicopters h225. `https://www.airbushelicopters.ca/product/h225/`. Accessed: 2018-23-12.

[5] Airliners.net. Airbus Helicopters Bluecopter Demonstrator. `https://www.airliners.net/photo/Airbus-Helicopters/Airbus-Helicopters-H-135-Bluecopter/3869937/L`. Accessed: 2019-03-09.

[6] Anderson, B. H. and Gibb, J. Vortex-Generator Installation Studies on Steady-State and Dynamic Distortion. *Journal of Aircraft.* Vol. 35, No. 4, DOI: 10.2514/3.46666, 1998, pp. 513 - 520.

[7] Anderson, B. H., Reddy, D. R., and Kapoor, K. Study on Computing Separating Flows Within a Diffusing S-Duct. *Journal of Propulsion and Power.* Vol. 10, No. 5, DOI: 10.2514/3.23777, 1994, pp. 661 - 667.

[8] Ansys Inc. Ansys CFX Solver Theory Guide. Cannonsburg, PA, USA, v16.0, 2015.

[9] Ansys Inc. Design Exploration User's Guide. Cannonsburg, PA, USA, v15.0, 2013.

[10] Arora, J. S. *Introduction to Optimum Design.* Elsevier Academic Press, third edition. ISBN: 978-0-12-381375-6, 2012.

[11] Aulehla, F. Intake Swirl - a Major Disturbance Parameter in Engine / Intake Compatibility. In *13th Conference of the International Council of the Aeronautical Sciences.* International Council of the Aeronautical Sciences. Paper ID: ICAS-82-4.8.1, 1982.

[12] Barone, D., Loth, E., and Snyder, P. Efficiency of an Inertial Particle Separator. *Journal of Propulsion and Power.* Vol. 31, No. 4, DOI: 10.2514/1.B35276, 2015, pp. 997-1002.

[13] Berrier, B. L. Carter, M. B. and Allen, B. G. High Reynolds Number Investigation of a Flush-Mounted, S-Duct Inlet With Large Amounts of Boundary Layer Ingestion. Technical report, NASA Langley Research Center. NASA Technical Memorandum NASATP-2005-213766, 2005.

[14] Bojdo, N. and Filippone, A. Comparative Study of Helicopter Engine Particle Separators. *Journal of Aircraft*. Vol. 51, No. 3, DOI: 10.2514/1.C032322, 2014, pp. 1030 - 1042.

[15] Bojdo, N. and Filippone, A. Performance Prediction of Inlet Barrier Filter Systems. *Journal of Aircraft*. Vol. 48, No. 6, DOI: 10.2514/1.C031335, 2011, pp. 1903 - 1912.

[16] Bouldin, B. and Sheoran, Y. Inlet Flow Angularity Descriptors Proposed for Use With Gas Turbine Engines. *SAE Technical Paper*. Paper ID: 2002-01-2919, DOI: 10.4271/2002-01-2919, 2002.

[17] Braithwaite, W. M. and Soedert, R. H. Combined Pressure and Temperature Distortion Effects. *Journal of Aircraft*. Vol. 17, No. 7, DOI: 10.2514/3.57927, 1980, pp. 468 - 472.

[18] Bräunling, W. J. G. *Flugzeugtriebwerke*. Springer-Verlag Berlin Heidelberg, third edition. Vol. 11, No. 3, DOI: 10.1007/978-3-642-34539-5, 2009.

[19] Campanardi, G. and Gibertini, G. Nacelle air intake preliminary wind tunnel tests. Technical report, HIT09. 2010.

[20] Campbell, J. and Ellis, S. Inlet-Engine Compatibility Analysis, AIAA Paper 70-941. In *AIAA 6th Propulsion Joint Specialist Conference, San Diego*. DOI: 10.2514/6.1970-941, 1970.

[21] Clean Sky Joint Undertaking. Tiltop, Efficient Shape Optimization of Intake and Exhaust of a Tiltrotor Nacelle, publishable summary. 2011, Accessed: 2017-05-18.

[22] Colin, F. and Agarwal, R. K. Simulation of Secondary and Separated Flow in Diffusing S-Ducts. *Journal of Propulsion and Power*. Vol. 31, No. 1, DOI: 10.2514/1.B35275, 2015, pp. 180 - 191.

[23] de Bruin, A. C., Fatigati, G., and Shin, H. B. Kai SURION Helicopter Full-Scale Air Intake Testing at CIRA Icing Wind Tunnel. In *Proceedings of the 30th Congress of the International Council of the Aeronautical Sciences, Daejeon, Korea*. Paper ID: 2016_0496, 2016.

[24] Delot, A.-L., Berens, T. M., Tormalm, M. H., Saeterskog, M., and Ceresola, N. des computations for a subsonic uav configuration with a highly integrated s-shaped intake duct. In *Proceedings of the 52nd Aerospace Sciences Meeting, AIAA SciTech Forum, National Harbor, Maryland*. Paper ID: AIAA 2014-0723, DOI: 10.2514/6.2014-0723, 2014.

[25] Deutsches Institut für Normung e.V., D. *DIN EN ISO 5167-4*. Beuth Verlag GmbH, Berlin. 2004.

[26] Dudzinski, T. J. and Krause, L. N. Flow Direction Mmeasurement with Fixed-Position Probes. Technical report, NASA, NASA Lewis Research Center. NASA-TM-X-1904, 1969.

[27] Fabris, A., Garavello, A., Russo, M., Ponza, R., and Benini, E. Multiobjective and Multipoint Optimization of a Heavy Class Helicopter Engine Installation using Evolutionary Algorithms. In *VI International Conference on Adaptive Modeling and Simulation, ADMOS, Lisbon, Portugal, 2013.*

[28] Garavello, A., Benini, E., Ponza, R., Scandroglio, A., and Saporiti, A. Aerodynamic Optimization

of the ERICA Tilt-Rotor Intake and Exhasut System. In *37th European Rotorcraft Forum, Ticino Park, Italy, Paper ID: 191, 2011.*

[29] Goldsmith, E. L. and Seddon, J. *Practical Intake Aerodynamic Design.* Blackwell Scientific Publications, Cambridge, first edition. ISBN: 0-632-03103-4, 1993.

[30] Grawunder, M. *Aerodynamic Design Optimisation for Utility Helicopter Drag Reduction, Dissertation.* Verlag Dr. Hut, Technische Universität München. 2017.

[31] Group for Aeronautical Research and Technology in Europe. Garteur AD/AG-46 Highly Integrated Subsonic Air Intakes. Technical report, GARTEUR. 2014.

[32] Hall, C. F. and Frank, J. L. Ram Recovery Characteristics of NACA Submerged Inlets at High Subsonic Speeds. Technical report, NASA, Ames Aeronautical Laboratory. RM A8129, 1948.

[33] Heise, R., Meyer, C. J., and von Backström, T. W. Evaluation of Helicopter Intakes in the Presence of a Rotor. In *Proceedings of the 32th European Rotorcraft Forum, Maastricht.* 2006.

[34] Hövelmann, A. *Analysis and Control of Partly-Developed Leading-Edge Vortices, Dissertation.* Technische Universität München. ISBN: 978-3-8439-2807-6, 2016.

[35] Johansen, E. S., Rediniotis, O., and G., J. The Compressible Calibration of Miniature Multi-Hole Probes. *Journal of Fluids Engineering.* Vol. 123, No. 1, DOI: 10.1115/1.1334377, 2001, pp. 128 - 138.

[36] Knoth, F. and Breitsamter, C. Aerodynamic Analysis of Helicopter Side Intake Variants by Full Scale Wind Tunnel Measurements. In *41st European Rotorcraft Forum, Munich, Paper ID: ERF2015_0041, 2015.*

[37] Knoth, F. and Breitsamter, C. Aerodynamic Testing of Helicopter Side Intake Retrofit Modifications. *Aerospace.* Vol. 4, No. 3, DOI: 10.3390/aerospace4030033, 2017.

[38] Knoth, F. and Breitsamter, C. Flow Analysis of a Helicopter Engine Side Air Intake. *Journal of Propulsion and Power.* Vol. 33, No. 5, DOI: 10.2514/1.B36285, 2017, pp. 1230 - 1244.

[39] Knoth, F. and Breitsamter, C. Aerodynamic Characteristics of Helicopter Engine Side Air Intakes. *Aircraft Engineering and Aerospace Technology.* Vol. 90, No. 9, DOI: 10.3390/aerospace4030033, 2018, pp. 1355-1363.

[40] Knoth, F. and Breitsamter, C. Numerical and Experimental Investigation of a Helicopter Engine Side Intake. In *New Results in Numerical and Experimental Fluid Mechanics XI*, chapter 1. Springer, Cham, Switzerland. ISBN: 978-3-319-64518-6, 2018, pp. 27-37.

[41] Knoth, F., Stuhlpfarrer, M., and Breitsamter, C. Numerical and Experimental Investigation of Helicopter Engine Air Intakes. In *64. Deutscher Luft - und Raumfahrt Kongress, Rostock, 2015.*

[42] Kurzke, J. Effects of Inlet Flow Distortion on the Performance of Aircraft Gas Turbines. *Journal of Engineering for Gas Turbines and Power.* Vol. 130, No. 4, DOI: 10.1115/1.2901190, 2008.

[43] Liao, C. C. and Liou, T. L. Flows in a Curved Combustor Inlet with and without a Guide Vane. *Journal of Propulsion and Power.* Vol. 11, No. 3, DOI: 10.2514/3.23866, 1995, pp. 464 - 472.

[44] Martin, N. J. and Holzhauser, C. A. An Experimental Investigation at Large Scale of Several Configurations of an NACA Submerged Air Intake. Technical report, NASA, Ames Aeronautical Laboratory. RM A8F21, 1948.

[45] Menter, F. R. Two-Equation Eddy Viscosity Models for Engineering Applications. *AIAA Journal*. Vol. 32, No. 8, DOI: 10.2514/3.12149, 1994, pp. 1598 - 1605.

[46] Miste, G. A., Nibale, T., Garavello, A., and Benini, E. Assessment of the Engine Installation Performance of a Redesigned Tilt-rotor Intake System. In *68th Annual National Forum, American Helicopter Society, Fort Worth, Texas, 2012.*

[47] Nichols, M. R. and Pierpont, P. K. Preliminary Investigation of a Submerged Air Scoop Utilizing Boundary- Layer Suction to Obtain Increased Pressure Recovery. Technical report, NASA, Langley Aeronautical Laboratory. TN 3437, 1950.

[48] Pagano, G. and Ballard, J. Development and Testing of the A129 Air Intake. In *Ninth European Rotorcraft Forum, Stresa, Italy, 1983.*

[49] Paul, A. R., Upadhyay, R. R., and Jain, A. A Novel Calibration Algorithm for Five-Hole Pressure Probe. *International Journal of Engineering, Science and Technology*. Vol. 3, No. 2, DOI: 10.4314/ijest.v3i2.68136, 2011, pp. 89 - 95.

[50] Pearson, H. and McKenzie, A. B. Wakes in Axial Compressors. *Journal of the Royal Aeronautical Society*. Vol. 63, No. 583, DOI: 10.1017/S0368393100071273, 1959, pp. 415 - 416.

[51] Pölzlbauer, P., Desvigne, D., and Breitsamter, C. Aerodynamic Design Optimization of a Helicopter Rotor Blade-Sleeve Fairing. *Council of European Aerospace Societies*. Paper ID: 2018_0070, 2018.

[52] Prandtl, L. *Über den Reibungswiderstand Strömender Luft*. Ergebnisse der Aerodynamischen Versuchsanstalt in Göttingen, third edition. 1927.

[53] Rae, W. H. and A., P. *Low-Speed Wind Tunnel Testing*. Wiley, second edition. 1984.

[54] Rediniotis, O. K., Hoang, N. T., and Telionis, D. P. Seven-Hole Probe: It's Calibration and Use. In *Forum on Instructional Fluid Dynamics Experiments: Presented at the Fluids Engineering Conference, Washington, D.C., June 20-24*. ASME. ISBN: 978-0-7918-0960-0, 1993, pp. 21 - 26.

[55] Reid, C. The Response of Axial Flow Compressors to Intake Flow Distortion. In *ASME 1969 Gas Turbine Conference and Products Show, Cleveland, Ohio, USA, 1969.*

[56] Rein, M. and Koch, S. experimental study of boundary-layer ingestion into a diverterless s-duct intake. *AIAA Journal*. Vol. 53, No. 11, DOI: 10.2514/1.J053902, 2015, pp. 3487 - 3492.

[57] Aerodynamic Testing of HElicopter Novel Air Intakes. `http://www.cleansky-projects.tum.de/athenai/`. Accessed: 2017-11-13.

[58] Cleansky Joint Technology Initiative. `http://www.cleansky.eu`. Accessed: 2017-11-13.

[59] Homepage of the Chair of Aerodynamics and Fluid Mechanics. `http://www.aer.mw.tum.de/windkanaele/windkanal-a/`. Accessed: 2017-12-01.

[60] Seventh Framework Programme for Research and Technological Development. `https://ec.europa.eu/research/fp7/pdf/fp7-inbrief_en.pdf`. Accessed: 2017-11-13.

[61] Roesch, P. Aerodynamic Design of the Aerospatiale SA 365 N Dauphin 2 Helicopter. In *Sixth European Rotorcraft and Powered Lift Aircraft Forum, Bristol, 1980.*

[62] Rolls, L. S. A Flight Comparison of a Submerged Inlet and a Scoop Inlet at Transonic Speeds. Technical report, NASA, Ames Aeronautical Laboratory, Moffett Field. RM A53A06, 1953.

[63] Sacks, A. h. and Spreiter, J. R. Theoretical Investigations of Submerged Inlets at Low Speeds. Technical report, NASA, Ames Aeronautical Laboratory. TN 2323, 1951.

[64] Sóbester, A. Tradeoffs In Jet Inlet Design: A Historical Perspective. *Journal of Aircraft*. Vol. 44, No. 3, DOI: 10.2514/1.26830, 2007, pp. 705 - 717.

[65] Seddon, J. and Goldsmith, E. L. *Intake Aerodynamics*. Collins Professional and Technical Books, London, first edition. ISBN: 0-00-383048-9, 1985.

[66] Smith, C. F. Podleski, S. D. and Barankiewicz, W. S. Comparison of F/A-18A High Alpha Research Vehicle Inlet Flow Analysis Results with Flight Data: Part 1. In *Proceedings of the 31st AIAA/ASME/SAE/ASEE Joint Propulsion Conference and Exhibit, San Diego, California*. DOI: 10.2514/6.1995-2758, 1995.

[67] Society of Automotive Engineers. Aerospace Recommended Practice 1420 - Gas Turbine Engine Inlet Flow Distortion Guidelines. Technical report, Society of Automotive Engineers. 2017.

[68] Squires, P. K. and Warmbrodt, W. Correlation of Full-Scale and Small-Scale Wind-Tunnel Tests of a Helicopter Fuselage. In *Proceedings of the AIAA Applied Aerodynamics Conference, Danvers, Massachusetts*. 1983.

[69] Steenken, W. G. *Aircraft Propulsion Systems Technology and Design*. AIAA, Washington, DC. DOI: 10.2514/4.861499, 1989, pp. 338 - 369.

[70] Stroub, R. H. and Rabbott, J. P. J. Wasted Fuel - Another Reason For Drag Reduction. In *31st Annual National Forum, American Helicopter Society, Washington,D.C., 1975.*

[71] Tamigniaux, T. L. B. and Oates, G. C. An Experimental Investigation of the Effect of a Nearby Solid Surface on a Five-Hole Pressure Probe. In *Proceedings of the 23rd Aerospace Sciences Meeting*, Reno, Nevada. 1969.

[72] Taskinoglu, E. S., Jovanovic, V., Knight, D. D., and Elliott, G. S. Design Optimization for Submerged Inlets - Part i. In *21st AIAA, Applied Aerodynamics Conference*. AIAA. DOI: 10.2514/6.1998-2810, 2002.

[73] Taskinoglu, E. S. and Knight, D. D. Multi-Objective Shape Optimization Study for a subsonic Submerged Inlet. *Journal of Propulsion and Power*. Vol. 20, No. 4, DOI: 10.2514/1.5809, 2004, pp. 620 - 633.

[74] Telionis, D., Yang, Y., and Rediniotis, O. Recent Developments in Multi-Hole Probe (mhp) Technology. In *Proceedings of the 20th International Congress of Mechanical Engineering*, volume 21. 2009.

[75] Tormalm, M. Design and Analysis of Compact UAV Ducts. In *Proceedings of the 24th Applied Aerodynamics Conference, San Francisco*. 2006.

[76] Tormalm, M. flow control using vortex generators or micro-jets applied in an ucav intake, aiaa 2014-0724. In *Proceedings of the 52nd Aerospace Sciences Meeting, AIAA SciTech Forum, National Harbor, Maryland*. DOI: 10.2514/6.2014-0724, 2014.

[77] van der Walt, J. P. and Nurick, A. Life Prediction of Helicopter Engines Fitted with Dust Filters. *Journal of Aircraft*. Vol. 32, No. 1, DOI: 10.2514/3.45299, 1995, pp. 118-123.

[78] van der Walt, J. P. and Nurick, A. Static Pressure Distribution in the Inlet of a Helicopter Turbine Compressor. *Journal of Aircraft*. Vol. 31, No. 6, DOI: 10.2514/3.46666, 1994, pp. 1411 - 1413.

[79] Vogel, F. *Aerodynamische Analysen an Helikopter Zellen-Ausleger Konfigurationen, Dissertation*. Verlag Dr. Hut, Technische Universität München. ISBN: 978-3-8439-2696-6, 2016.

[80] Vuillet, A. Aerodynamic Design of Engine Air Intakes for Improved Performance. In *Sixth European Rotorcraft and Powered Lift Aircraft Forum, Bristol, 1980.*

[81] Wellborn, S. R., Reichert, B. A., and Okiishi, T. Study of the Compressible Flow through a Diffusing S-Duct. Technical report, NASA, Ames Aeronautical Laboratory. TM 106411, 1993.

[82] Welte, D. Experimental Analysis of a Pitot-Type Air Intake. *Journal of Aircraft*. Vol. 23, No. 4, DOI: 10.2514/3.45299, 1986, pp. 266-274.

[83] Wikipedia. Eurocopter EC135 IBF. `https://commons.wikimedia.org/wiki/File:Inlet_barrier_filter.jpg`. Accessed: 2017-11-08.

[84] Wikiwand. Eurocopter AS365 Dauphin. `http://www.wikiwand.com/en/Eurocopter_AS365_Dauphin`. Accessed: 2017-11-08.

[85] Winkler, A. *Automatisiertes Verfahren zur Aerodynamischen Formentwicklung*. Verlag Dr. Hut, Technische Universität München. ISBN:978-3-8439-0137-6, 2011.

[86] You, J. H. *Aeroacoustic Characteristics of a Shrouded Helicopter Tail Rotor, Dissertation*. Technische Universität München. ISBN: 978-3-8439-3636-1, 2017.